

Understanding the relaxation spectra of neat and mixed ionic liquids

Zum Verständnis der Relaxationsspektren purer und gemischter ionischer Flüssigkeiten

Zur Erlangung des Grades eines Doktors der Naturwissenschaften (Dr. rer. nat.)

Genehmigte Dissertation von Florian Pabst aus Offenbach am Main

Tag der Einreichung: 24.01.2022, Tag der Prüfung: 21.02.2022

1. Gutachten: apl. Prof. Dr. Thomas Blochowicz

2. Gutachten: Prof. Dr. Michael Vogel

Darmstadt – D 17



TECHNISCHE
UNIVERSITÄT
DARMSTADT

Physics Department
Institute of Condensed
Matter Physics
AG Blochowicz

Understanding the relaxation spectra of neat and mixed ionic liquids
Zum Verständnis der Relaxationsspektren purer und gemischter ionischer Flüssigkeiten

Accepted doctoral thesis by Florian Pabst

1. Review: apl. Prof. Dr. Thomas Blochowicz
2. Review: Prof. Dr. Michael Vogel

Date of submission: 24.01.2022

Date of thesis defense: 21.02.2022

Darmstadt – D 17

Bitte zitieren Sie dieses Dokument als:

URN: urn:nbn:de:tuda-tuprints-208851

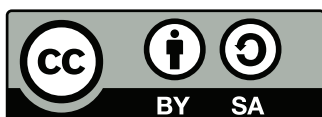
URL: <http://tuprints.ulb.tu-darmstadt.de/id/eprint/20885>

Dieses Dokument wird bereitgestellt von tuprints,

E-Publishing-Service der TU Darmstadt

<http://tuprints.ulb.tu-darmstadt.de>

tuprints@ulb.tu-darmstadt.de



Veröffentlicht unter CC BY-SA 4.0 International

<http://creativecommons.org/licenses/>

Erklärung gemäß §9 Promotionsordnung

Hiermit versichere ich, dass ich die vorliegende Dissertation selbstständig angefertigt und keine anderen als die angegebenen Quellen und Hilfsmittel verwendet habe. Alle wörtlichen und paraphrasierten Zitate wurden angemessen kenntlich gemacht. Die Arbeit hat bisher noch nicht zu Prüfungszwecken gedient.

Darmstadt, 24.01.2022

F. Pabst

Abstract

Due to their unique properties, ionic liquids are promising candidates for various applications. The possibility to combine cations and anions almost arbitrarily leads to a virtually infinite number of different ionic liquids. The hope is that one could tailor an ionic liquid for a specific need in this way. However, to achieve a particular property, it would be essential to understand the ionic liquids on a microscopy level and not rely on trial and error. One crucial point is the dynamics of the ions, for example, concerning reaction media or electrolytes. However, the ion dynamics are quite complex due to the balanced interplay between Coulomb, hydrogen-bonding, and van der Waals interactions. Furthermore, in cases where cations are equipped with long, non-polar chains, it was found that nanosized aggregates form in neat ionic liquids. In this way, rotational and translational motions of cations and anions together with motions of aggregates possibly show up in the spectra of dynamical measurements. This has led to dynamic processes in the spectra being interpreted differently in the literature with respect to their microscopic origin.

Therefore, this work aims to combine dielectric spectroscopy and depolarized light scattering to disentangle the rotational and translational contributions found in the relaxation spectra of ionic liquids. This is done for various neat ionic liquids, where the cations are equipped with non-polar chains of different lengths, thus varying the size ratio between cations and anions. Measurements are performed from far above room temperature down to the glass transition. In the case of dielectric spectroscopy, also pressures up to 550 MPa are applied. In this way, it could be shown that the dynamics of cations and anions separate in the case of a large size difference between the two ion species. Rotational motions of the cations are revealed to be the origin of a slow dielectric relaxation process, which was formerly often ascribed to motions of aggregates. It could be shown that such aggregates show up only in rare cases in the light scattering spectra at low frequencies, not accessible by dielectric spectroscopy. Furthermore, mixtures of an ionic liquid with water or 1-propanol are considered. The rotational contribution of the admixtures is discriminated from the ion dynamics and from signatures of hydrogen-bonding mediated orientational cross-correlations. Additionally, an ionic gel is prepared by mixing an ionic liquid with water and gelatin, and it is shown that the rotational and translational dynamics of the ions are hardly affected by the presence of the gelatin, although macroscopically, mechanical rigidity is introduced. More fundamental questions regarding the intensity of the scattered light and the shape of the rotational spectra, which have arisen during this work, are also addressed based on non-ionic systems.

Zusammenfassung

Aufgrund ihrer einzigartigen Eigenschaften sind ionische Flüssigkeiten vielversprechende Kandidaten für verschiedene Anwendungen. Die Möglichkeit, Kationen und Anionen fast beliebig zu kombinieren, führt zu einer praktisch unendlichen Anzahl verschiedener ionischer Flüssigkeiten. Die Hoffnung ist, dass man auf diese Weise eine ionische Flüssigkeit für einen bestimmten Bedarf maßschneidern kann. Um eine bestimmte Eigenschaft zu erreichen, wäre es jedoch wichtig, die ionischen Flüssigkeiten auf mikroskopischer Ebene zu verstehen und sich nicht auf Versuch und Irrtum zu verlassen. Ein wichtiger Punkt ist die Dynamik der Ionen, zum Beispiel in Bezug auf Reaktionsmedien oder Elektrolyte. Aufgrund des ausgewogenen Zusammenspiels von Coulomb-, Wasserstoffbrücken- und van-der-Waals-Wechselwirkungen ist die Ionendynamik jedoch recht komplex. Darüber hinaus wurde festgestellt, dass sich in Fällen, in denen Kationen mit langen, unpolaren Ketten ausgestattet sind, in reinen ionischen Flüssigkeiten nanoskalige Aggregate bilden. Auf diese Weise zeigen sich in den Spektren der dynamischen Messungen möglicherweise sowohl Rotations- als auch Translationsbewegungen von Kationen und Anionen sowie Bewegungen von Aggregaten. Dies hat dazu geführt, dass dynamische Prozesse in den Spektren der Literatur hinsichtlich ihres mikroskopischen Ursprungs unterschiedlich interpretiert werden.

Ziel dieser Arbeit ist es daher, dielektrische Spektroskopie und depolarisierte Lichtstreuung zu kombinieren, um die Rotations- und Translationsbeiträge in den Relaxationsspektren ionischer Flüssigkeiten zu entflechten. Dies geschieht für verschiedene pure ionische Flüssigkeiten, bei denen die Kationen mit unpolaren Ketten unterschiedlicher Länge ausgestattet sind, wodurch das Größenverhältnis zwischen Kationen und Anionen variiert. Die Messungen werden von weit oberhalb der Raumtemperatur bis hin zum Glasübergang durchgeführt. Bei der dielektrischen Spektroskopie werden auch Drücke bis zu 550 MPa angewendet. Auf diese Weise kann gezeigt werden, dass sich die Dynamik von Kationen und Anionen im Spektrum trennt, wenn der Größenunterschied zwischen den beiden Ionenspezies ausreichend groß ist. Rotationsbewegungen der Kationen erweisen sich als Ursache für einen langsamen dielektrischen Relaxationsbeitrag, der in der Literatur häufig auf Bewegungen von Aggregaten zurückgeführt wurde. Es wird gezeigt, dass solche Aggregate nur in seltenen Fällen in den Lichtstreuungsspektren bei niedrigen Frequenzen zu sehen sind, die jedoch für die dielektrische Spektroskopie nicht zugänglich sind. Außerdem werden Mischungen einer ionischen Flüssigkeit mit Wasser oder 1-Propanol betrachtet. Der Rotationsbeitrag der Beimischungen wird von der Ionendynamik und von Signaturen wasserstoffbrückenvermittelter Orientierungskreuzkorrelationen abgegrenzt. Es wird anhand eines ionischen Gels gezeigt, dass die Rotations- und Translationsdynamik der Ionen durch das Vorhandensein von Gelatine kaum beeinträchtigt wird, obwohl makroskopisch eine mechanische Steifigkeit hervorgerufen wird. Grundlegendere Fragen zur Intensität des gestreuten Lichts und zur Form der Rotationsspektren, die sich im Laufe dieser Arbeit ergeben haben, werden ebenfalls anhand von nicht-ionischen Systemen behandelt.

Contents

1. Introduction	1
2. Background	5
2.1. Dynamics in (supercooled) liquids	5
2.2. Dynamics in ionic liquids	13
3. Methods	19
3.1. Light scattering	19
3.1.1. Photon correlation spectroscopy	25
3.1.2. Tandem-Fabry-Pérot interferometry	28
3.1.3. Raman spectroscopy	32
3.2. Dielectric spectroscopy	36
3.3. Differential scanning calorimetry	40
3.4. Quantum chemical calculations	45
4. General aspects of rotational dynamics in non-ionic liquids	48
4.1. The intensity of light scattered by molecular liquids	49
4.1.1. Comparison of DFT calculations with experiments	52
4.1.2. Mixtures of non-ionic liquids	60
4.2. The shape of the structural relaxation	65
5. Molecular dynamics in neat ionic liquids	74
5.1. Modeling of translational dynamics	74
5.2. Chain length dependent separation of ion dynamics	83
5.2.1. Light scattering	83
5.2.2. Dielectric spectroscopy and differential scanning calorimetry	94
5.2.3. The special case $[P_{14,6,6,6}][Cl]$	100
5.3. Dynamics of nanoscale aggregates	106
5.4. Origin of the low-frequency relaxation in dielectric spectra	114
5.4.1. High pressure measurements	115
5.4.2. Dipolar relaxation	121

6. Molecular dynamics in ionic liquids with admixtures	130
6.1. Mixtures with water	130
6.2. Mixtures with alcohol	141
6.3. Mixtures with water and gelatin	155
7. Summary	164
A. Samples and Preparation	167
B. Additional data	169
Bibliography	177
Supervised student theses	205
Publications and conference contributions	206
Acknowledgment	209

1. Introduction

It feels like the introduction to most studies on ionic liquids starts with a sentence such as "ionic liquids are salts which are liquid below 100 °C". Therefore, and because this temperature is chosen arbitrarily, such an opening should be avoided here. In fact, when heating, for example, table salt, i.e., sodium chloride, to about 800 °C, it melts, and one ends up with a liquid entirely composed of ions, namely [Na] cations and [Cl] anions. Thus, it can be justifiably called an ionic liquid (IL). However, it is more common to talk about a molten salt in this case, while what is usually understood by the term ionic liquid is a substance composed of an organic cation and mostly an inorganic anion. Such organic cations are usually larger and have markedly lower symmetry than the [Na] cation, sticking with this example. This results in a significantly reduced melting point, which happens to be commonly below 100 °C, often even below room temperature; thus, the name room temperature ionic liquid (RTIL) can also be found. These organic ILs are the subject of this work, and two common sorts of cations are shown in figure 1.1 to illustrate their chemical structure.

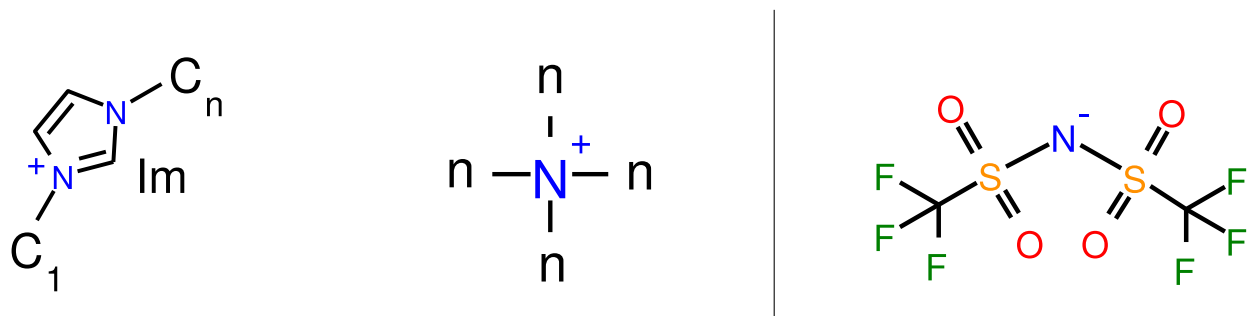


Figure 1.1.: Schematic representation of an imidazolium-based cation $[C_1C_n\text{Im}]$ on the left hand side and an ammonium based cation $[N_{n,n,n,n}]$ in the middle. On the right hand side the most complex anion of this study is shown, namely $[\text{NTf}_2]$

An imidazolium-based cation is shown on the left-hand side, which could be equipped with an alkyl-chain of n carbon atoms; thus, these cations are written as $[C_1C_n\text{Im}]$. In the middle, an ammonium-based cation is shown, which is written as $[N_{n,n,n,n}]$. Anions in this work range from small ones such as $[\text{Cl}]$ to complex ones like $[\text{NTf}_2]$,¹ which is shown on the right hand side of figure 1.1.

It seems that the first report of an IL with a melting point below room temperature was already made in 1914 by Paul Walden [1], but it took until the 1990s that air and moisture stable ILs were synthesized, which fueled the interest in this research area. Finally, around the turn of the

¹A synonym for $[\text{NTf}_2]$ is $[\text{TFSI}]$.

millennium, ILs became commercially available, which opened the possibility for researchers not familiar with the synthesis of ILs to take part in this field. From then on, the interest in ILs exploded, which can be seen for example by the increasing number of papers with "ionic liquid(s)" in the title that appeared after that time, which is shown in figure 1.2.

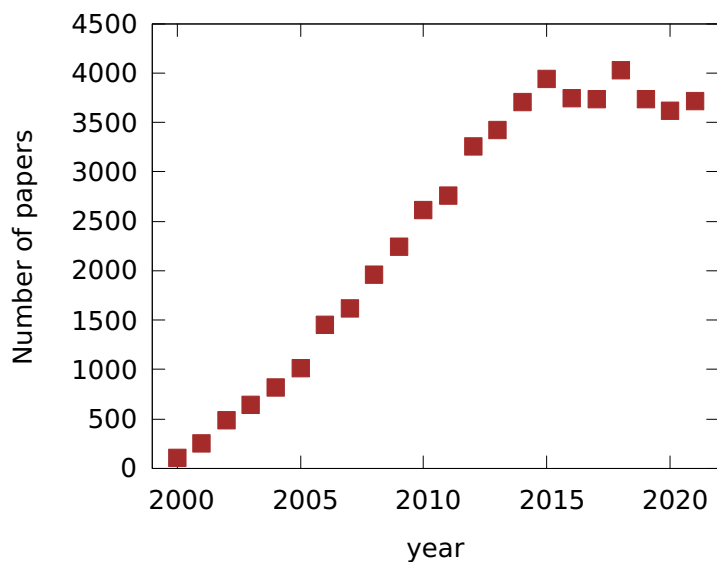


Figure 1.2.: Number of papers with "ionic liquid" or "ionic liquids" in the title depending on the year of publication.

This was also because high hopes were placed in ILs for several kinds of application due to their unique properties [2]. For example, ILs were found to be good solvents, and together with their negligible vapor pressure caused by the strong Coulomb interaction, they are regarded as reusable and thus as "green" solvents. Because of the high conductivity of ILs combined with the low flammability, they seem very well suited for replacing other electrolyte materials, for example, in batteries. But also the possibility to include ILs in a gel matrix, so-called ionogels, are promising in this respect, since in this way additionally the problem of leakage is prevented, which might lead to a new type of solid-state battery. It seems that most large-scale applications of IL can be found today in the chemical industry. However, also fancy applications were proposed, like a metal coated IL to be used as a mirror in a large telescope on the moon [3]. Moreover, the first lady of Finland once wore a dress made from cellulose, which was extracted from wood pulp by an IL [4].

But also, the scientific interest in the structure and dynamics of the ILs from a microscopic perspective arose, fueled by the discovery that nanostructuration occurs in some neat ILs. This happens when the alkyl chains of the cations are long enough, resulting in their segregation into non-polar domains. Such observations led to an increasing number of studies that were concerned with the balanced interplay of Coulombic, van der Waals, and hydrogen-bonding interactions, which leads to such aggregation behavior. Due to the asymmetry of many cations, it is often possible to supercool ILs, i.e., to avoid crystallization at temperatures below the melting point. This is useful for dynamic investigations since different motional processes of the ions, which are highly merged in experimental spectra at high temperatures, start to separate

on lowering the temperature, simplifying the assignment of their different microscopic origins. If crystallization is prevented at all temperatures, the supercooled liquid eventually becomes a glass, upon further cooling. Since, despite decades of research in this area, the glass transition is still an open problem in condensed matter physics, one has naturally to deal with this topic when investigating ILs at low temperatures. The glass transition can not be classified as a first or second-order phase transition since its position, i.e., the glass transition temperature T_g depends on the thermal history, often defined by the cooling rate. The glass is an out of equilibrium state, and the glass transition is usually regarded as a dynamic phenomenon. A dramatic increase of the time constants characterizing the structural rearrangement of the molecules from the picosecond regime at high temperatures to some hundred seconds near T_g can be seen. This behavior is directly mirrored in the increase of the viscosity of the liquid. It is important to note that no discontinuity of the viscosity or the correlation time occurs at the glass transition, and both quantities steadily increase for temperatures below T_g , this temperature regime, however, is experimentally challenging to access, since measuring times would easily exceed weeks or months, even only few Kelvin below T_g . Also, structurally nothing happens at the glass transition. The lack of long-range order as present in the liquid state persists unaltered below T_g . But how is the glass transition temperature defined? There are several definitions, but one is based on calorimetric data, i.e., temperature-dependent heat capacity $C_p(T)$ measurements. A step in C_p is observed when the correlation time of the liquid exceeds the one imposed by the experimental cooling rate. This is because the dynamic degrees of freedom freeze in and no longer contribute to the heat capacity. Thus, the temperature at which such a step appears can be used as a definition of T_g , but, as mentioned above, it still depends on the cooling rate.

Monitoring the molecular dynamics over the whole temperature range, i.e., over 14 orders of magnitude in time, is experimentally challenging. Two experimental methods are used in this work, which are suited for this task. The first one is broadband dielectric spectroscopy (BDS), which is sensitive to the rotational motions of molecules with a permanent dipole moment. In the case of ILs, also translational motions of the ions, i.e., conductivity, can be monitored. On the other hand, depolarized light scattering (DLS) measurements give access to rotational motions of optical anisotropic molecules. Thus, the combination of both methods is well suited to disentangle translational and rotational dynamics in the spectra. Although both methods have been used before to study the dynamics of ILs, there is no consistent interpretation of the relaxation spectra regarding the molecular origin of the different dynamic features. Therefore, the main goal of this work is to resolve these controversies and understand the relaxation spectra of ILs from a microscopic point of view.

This work is organized as follows: In chapter 2, at first, the basics of molecular dynamics in liquids are described. The features expected for neat, simple supercooled liquids and for mixtures of non-ionic liquids are discussed. Basic equations, used later to describe experimental data, are also explained. Then, a literature survey on dynamic measurements of ionic liquids is given. The focus is on the spectra from experimental methods used in this work and extends slightly beyond them.

In chapter 3, the theoretical background for the different experimental techniques is described as well as the different setups. Some basics of quantum chemical calculations are also given, which are used in this work to calculate molecular properties.

Chapter 4 deals with fundamental questions which the author encountered during the work on ionic liquids. On the one hand, this is the question of whether information about the intensity of the light scattering spectrum can be used to disentangle different dynamic contributions, which would be useful for the case of ILs, where always two molecular species are present. In dielectric spectroscopy, the dielectric strength of the spectra is not only recorded routinely but also evaluated by comparison with the magnitude of the permanent dipole moments of the molecules. In analogy, the intensity of the light scattering spectrum should be connected to the optical anisotropy of the molecules under study. However, it seems that the intensity information was so far not connected with dynamic spectra. The other question discussed in this chapter is the different appearances of the relaxation spectra in BDS and DLS measurements. Almost all measurements in this chapter were performed on van der Waals liquids to discuss all effects in the most simple cases.

In chapter 5, the results from measurements on neat ionic liquids are discussed. By using temperatures from far above room temperature down to the glass transition and high pressure measurements, the different dynamic contributions to the BDS and DLS spectra are carefully disentangled. This leads to a consistent picture of the molecular origin of the various relaxation processes in neat ILs.

Measurements on an ionic gel are shown in chapter 6, which is prepared by mixing an ionic liquid with water and gelatin. In order to understand the complex dynamics of such a system, at first a mixture of water and ionic liquid is addressed. Since at high water concentrations this system crystallizes upon supercooling, water is replaced by 1-propanol to be able to explore the regime of low ionic liquid concentrations. In this way it is possible to disentangle the ion dynamics from the dynamics of the admixture.

All substances under study are listed with full names in the appendix, where also some additional data can be found.

2. Background

2.1. Dynamics in (supercooled) liquids

The dynamics of molecules comprising a liquid could be roughly categorized in vibrational, translational, and rotational motions. Vibrational motions are only considered peripherally in this work. The main focus is on the translational and rotational motions of the molecules. What is meant by rotational dynamics is the reorientation of a molecule when it leaves its cage of surrounding molecules. This process is commonly termed α - or structural relaxation, where the term α -process refers to the fact that this relaxation is in most cases the slowest and most prominent one. The term structural relaxation emphasizes that a structural rearrangement occurs during this process, and both terms are commonly used interchangeably.

Naturally, when a molecule leaves its cage of surrounding molecules, a translational displacement of the molecule is involved, leading to macroscopic diffusion of the molecule through the liquid via consecutive translational steps. When considering the molecule as spherical, the translational and rotational diffusion coefficients can be determined with the Stokes-Einstein equation [5, 6]

$$D_{\text{trans}} = \frac{k_B T}{6\pi\eta r} \quad D_{\text{rot}} = \frac{k_B T}{8\pi\eta r^3} \quad (2.1)$$

where r is the radius of the molecule, T the temperature, k_B the Boltzmann constant and η the viscosity. When introducing the rotational correlation time τ_{rot} from the Debye model as $\tau_{\text{rot}} = 1/(6D_{\text{rot}})$ [6], one ends up with the so called Debye-Stokes-Einstein (DSE) equation:

$$D_{\text{trans}}\tau_{\text{rot}} = \frac{2r^2}{9} \quad (2.2)$$

This means that the translational and rotational motions are coupled, as expected in the simple "escaping the cage" picture, and have the same temperature dependence. This is confirmed experimentally for temperatures above $1.2T_g$, where T_g denotes the glass transition temperature [7].

The translational diffusion is commonly measured using nuclear magnetic resonance (NMR) spectroscopy on lengthscales of approximately $1\text{ }\mu\text{m}$ [8], or on intermolecular distances with quasielastic neutron scattering. Rotational dynamics can also be monitored with NMR techniques, but also with dielectric spectroscopy probing the reorientation of permanent dipole moments or with depolarized dynamic light scattering probing the reorientation of optical anisotropic molecules. A sketch of typical relaxation spectra, as could be obtained by the latter two methods, is shown in figure 2.1. In the upper row, the data at a high temperature far above T_g is presented and at a temperature near T_g the data is shown in the lower row. On the

left-hand side, the data is presented in the susceptibility representation in the frequency domain and on the right-hand side in the time domain as correlation decays, the interconnection of which is detailed in chapter 3. In each case, the orange shaded area is the α -relaxation, and the blue shaded area is intermolecular vibrations, which are subsumed under the term microscopic dynamics in the following. Intramolecular vibrations appear at even higher frequencies, as Raman or infrared absorption lines are not shown in this figure.

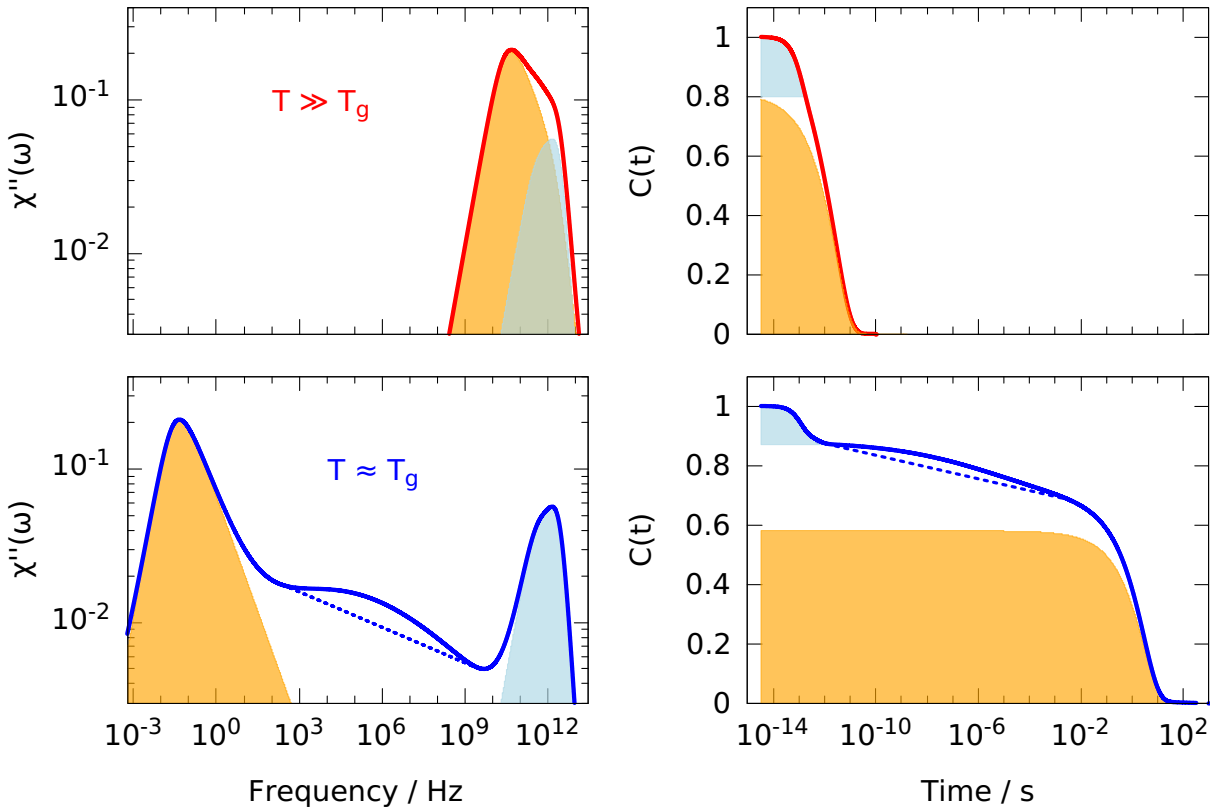


Figure 2.1.: Visualization of typical spectra of molecular dynamics. On the left hand side in susceptibility representation in the frequency domain and on the right hand side in the time domain as correlation decays. In the upper row, typical high temperature data is shown and in the lower row a low temperature near the glass transition temperature. Dashed line symbolizes the so called high frequency wing.

As can be seen at the high temperature, the α -process and the microscopic dynamics are merged, making it hard to separate them by eye, and the correlation decay appears almost as a single step. This picture is typical for the liquid state. Since the microscopic dynamics is hardly temperature-dependent, the α -relaxation separates from it upon cooling by several orders of magnitude in frequency or time until the glass transition temperature is reached. Thus, the shape of the α -relaxation at low temperatures can be examined best since no or only little overlap with other dynamic processes interferes. It is found experimentally that the correlation decay is not mono-exponential or, equivalently, when Fourier transformed to the

frequency domain, not Lorentzian. When first addressing dielectric relaxation, Peter Debye predicted a Lorentzian shape of the dielectric loss peak, which is why it is also called Debye-peak in the field of dielectric spectroscopy. However, the experimental spectra are broadened as compared to an exponential decay or a Debye-peak and are therefore often modeled with a Kohlrausch-Williams-Watts (KWW) function or a Cole-Davidson (CD) function, respectively, which are both empirical functions:

$$C(t) = \exp\left(-\left(\frac{t}{\tau_{\text{KWW}}}\right)^{\beta_{\text{KWW}}}\right) \quad (2.3)$$

$$\Phi(\omega) = \frac{1}{(1 + i\omega\tau_{\text{CD}})^{\beta_{\text{CD}}}} \quad (2.4)$$

The stretching exponents β take values between 0 and 1, and τ denotes the correlation time. The non-exponentiality is one of the three "Nons" of the glass transition [9], which are three experimental facts found in glass-forming liquids, which are not fully understood up to date. The probably most common explanation attempt for the non-exponentiality is the concept of dynamic heterogeneity, which is sketched in figure 2.2.

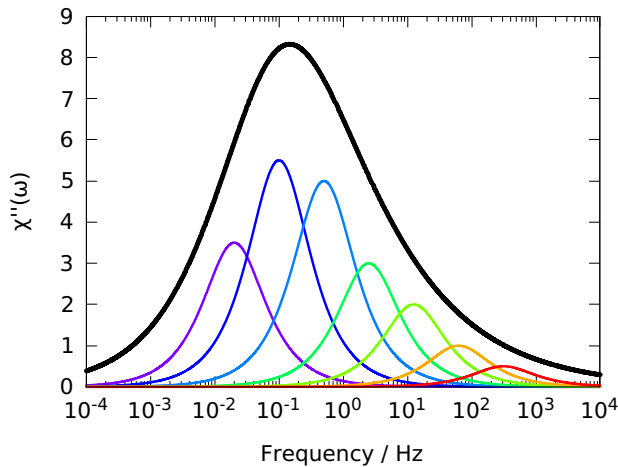


Figure 2.2.: Sketch of the common picture explaining the reason for non-exponential relaxation functions. In different regions of the sample, shown in different colors, the relaxation rate is different, leading to a superposition of Debye-processes, which together end up as a broadened peak (shown in black). Adapted from [10].

It is assumed that in supercooled liquids, distinct regions exist in which the molecules have different mobilities, i.e., the molecules in certain regions relax faster than in others. Each region contributes with a Debye shape to the total spectrum, leading to an overall broadening of the peak. Over time, the slow regions become fast and vice versa. This exchange is supposed to happen on the time scale of the slowest time scale contributing to the spectrum [10]. This concept could be contrasted by the homogeneous scenario, where an intrinsic broadening of the relaxation function of each molecule is assumed. However, it seems that most experimental and computer simulation data points into the direction of the heterogeneous scenario [11],

[12]. Nevertheless, it is surprising that mono-exponentiality is often not recovered at high temperatures, as the dynamic heterogeneity is thought to be a feature of the supercooled state. But instead, stretching exponents below unity are found in the liquid state by dielectric spectroscopy [13, 14, 15] and by depolarized dynamic light scattering [16, 17]. Even more, for some liquids, it was shown that the shape of the α -relaxation does not change at all from the glass transition temperature to near the boiling point [18, 19]. This might be a hint in the direction that although dynamic heterogeneity exists in supercooled liquids, its influence on the broadening of dielectric or light scattering spectra is not as straightforward as implied by figure 2.2, or other effects may affect the shape as well. In Section 4.2 this topic is addressed in detail.

The region between the α -relaxation and the microscopic dynamics developing upon cooling is filled with what is usually called secondary relaxations, which might show up either as a broad β -relaxation peak or as a high-frequency wing of the α -process (dashed line in figure 2.1) [20]. The microscopic origin of secondary relaxations is still debated in the literature. Besides the trivial case of movements of some side groups, for example, in polymers, it was found by Johari and Goldstein that β -relaxations show up also in rigid molecules [21]. Such relaxations are named in their honor, which they explained with the concept of islands of mobility, meaning that molecules in some regions of the sample are more mobile than in other regions, thus performing the β -relaxation. Contrary, it was later found by NMR measurements that basically all molecules participate in the β -process via small-angle reorientations [22]. It is observed experimentally that the β -process is usually not only broadened at the high-frequency side but also at low frequencies. In order to model such peaks, it is convenient to use a Havriliak-Negami (HN) function (equation 2.5) or a Cole-Cole (CC) function, which is a special case thereof where $\gamma_{\text{HN}} = 1$.

$$\Phi(\omega) = \frac{1}{(1 + (i\omega\tau_{\text{HN}})^{\alpha_{\text{HN}}})^{\gamma_{\text{HN}}}} \quad (2.5)$$

This results in the case of the CC function in a symmetrically broadened peak and in the case of the HN function in an asymmetric broadened peak. Besides the fitting of β -processes with such functions in some substances of this work, no deeper discussion of secondary relaxations will be performed. In order to compare time constants obtained by different fitting functions, in this work only correlation times at the peak maximum are considered, i.e., $\tau = 1/\omega_{\max}$.

The origin of the high-frequency wing (dashed line in figure 2.1), which is present in some liquids instead of a β -peak, was very recently tackled by computer simulations, and it was found that a model combining dynamic heterogeneity and kinetic facilitation is able to produce a high-frequency wing [23, 24]. In this view, the excess wing is intimately connected to the α -relaxation. The concept of facilitation describes a scenario where the relaxation of a molecule triggers the relaxation of neighboring molecules [12]. Experimentally, a peak underlying the excess wing is discussed, which could be made visible under certain circumstances [25, 26]. In order to model a high-frequency wing, for example, a so-called extended gamma distribution can be used as described in detail in reference [20]. However, no modeling of excess wings will be performed in this work.

When it comes to visualizing the correlation times τ from the different dynamic processes, it is

most common to display them in a so-called Arrhenius plot. There, the correlation times are plotted logarithmically versus the inverse temperature, as shown exemplified in figure 2.3. As mentioned before, the microscopic dynamics is hardly temperature-dependent, with a very slight shift to shorter correlation times for lower temperatures [27]. The β -relaxation usually follows the Arrhenius law

$$\tau_\alpha = \tau_0 \exp \frac{E_a}{k_B T} \quad (2.6)$$

where E_a is the activation energy and the value of the pre-exponential factor τ_0 is often in the range of the microscopic correlation times. This gives a straight line in the Arrhenius plot, which explains its name.

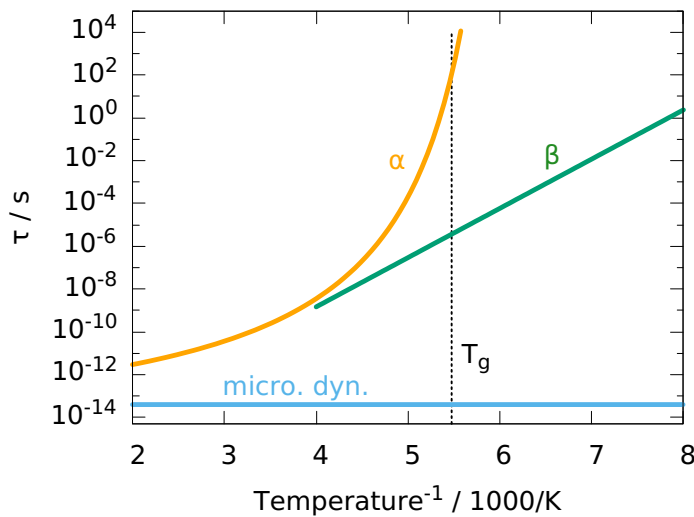


Figure 2.3.: Schematic representation of the temperature dependence of the relaxation times for the α - and β -relaxation as well as for the microscopic dynamics.

However, the correlation times of the α -relaxation might be described with an Arrhenius law at very high temperatures only. At low temperatures, a more or less strong bending is observed for all glass formers, leading to a dramatic increase of the correlation times over a rather limited temperature range. This super- or non-Arrhenius behavior is the second unresolved "Non" of the glass transition, and it is probably the most striking one. Empirically, the temperature dependence of τ_α is commonly described by the Vogel-Fulcher-Tamman (VFT) equation

$$\tau_\alpha = \tau_0 \exp \frac{B}{T - T_0} \quad (2.7)$$

where B is a material-dependent parameter, and T_0 is the Vogel temperature at which the correlation times diverge and which is usually located some tens of Kelvin below the glass transition temperature. It is debated whether such a divergence actually exists, with experimental hints into the direction that this might not be the case [28]. However, the VFT equation usually describes experimental data above T_g rather well, if not too large a temperature range

is considered. The concept of cooperative dynamics is probably the most common picture to rationalize the non-Arrhenius behavior of the α -relaxation times. In this view, at high temperatures, i.e., low densities, the molecules have enough room to move without the need for neighboring molecules to make way. At low temperature, i.e., higher densities, however, for a molecule to move, it is necessary that surrounding molecules also move, i.e., the dynamics gets cooperative. The correlation length, which is the distance over which molecular movements are correlated, is assumed to increase with decreasing temperature and eventually diverges at a temperature well below T_g [29, 30].

It should be noted in passing that it is not only possible to obtain a glass by cooling a liquid but also by isothermal compression, thus by solely increasing its density. Since upon decreasing temperature, the density of a liquid increases as well, the comparison of temperature and pressure-induced glass transitions can be used to disentangle the influence of both variables. However, it is also possible to produce a glass isochorically, indicating that neither temperature nor density alone is responsible for the glass transition [31]. In fact, it is possible to scale dynamic quantities of the substance under study, measured at different thermodynamic conditions, using a single material constant γ [31, 32, 33, 34, 35]. Thus, one can write for the relaxation times $\tau = f(TV^\gamma)$, where f is a function and V the specific volume. It has been shown that the scaling exponent γ can be related to the steepness of the intermolecular potential [33, 36, 37] and moreover that its value corresponds in the case of a dominating repulsive part to an exponent $n = 12$ in the Lennard-Jones potential, which is the value most commonly employed [38].

Due to their different temperature dependencies, the α - and β -relaxation times approach each other at high temperatures and eventually merge, as indicated in figure 2.3, meaning that at high temperatures, only one process is observed in the spectra, which is the α -process. A different view, as proposed by Ernst Donth [27], is that the α -and β -process occur below the merging region where cooperative motions take place, whereas at high temperatures, a different single process, the "a-process", is present. Since the merging often occurs in the MHz to GHz range, it is experimentally difficult to monitor the merging with high precision since, in dielectric spectroscopy, two different experimental setups have to be combined to cover this frequency range. In the case of depolarized light scattering, there is a gap precisely in this frequency range between the two commonly employed setups. Nevertheless, there are indications that the temperature dependence of the β -relaxation times differs in the merging region from the one observed at low frequencies, following approximately the one of the α -relaxation times [39, 40].

In some substances, mostly monohydroxy-alcohols, it was reported that an additional dynamic process slower than the α -relaxation is present in dielectric spectra with a mono-exponential shape, therefore usually called Debye-process. From the dielectric spectrum alone, it is usually not apparent that two processes are present since the Debye process often has a markedly higher dielectric strength than the α -relaxation. Only with a combination of other experimental methods can it be shown that the dielectric Debye process is not the α -relaxation. For example, the time scale of the Debye-process is not connected to the glass transition step as measured by differential scanning calorimetry and also disagrees with the timescale of the main process from light scattering, and rheology [41, 42, 43, 44, 45, 46]. Gainaru and co-workers put forward the illustrative transient-chain model to explain the Debye-process in monohydroxy-alcohols

[47]: Chain-like supramolecular structures are formed due to H-bonding between neighboring molecules. The total dipole moment of such a chain is the sum of the single-molecule dipole moments along the backbone of this chain. The movement of these supramolecular structures takes place through successive detaching of molecules on the one end and attaching on the other end, leading to an overall reorientation of the chain on timescales slower than a single molecular reorientation. Due to the length of the chain, these movements average over several heterogeneous regions, thus appearing mono-exponential itself [48]. However, a recent theory by Pierre-Michel Déjardin can reproduce the temperature-dependent static dielectric constants, which are dominated by the strength of the Debye-process, of several monohydroxy alcohols by just considering dipole-dipole interactions without the need for explicitly taking H-bonds into account [49, 50]. Moreover, this theory predicts a collective dynamic process in addition to the single molecular reorientation in cases where dipole-dipole interactions lead to a preferred parallel alignment of neighboring dipole moments. In fact, it will be shown in this work that the Debye process might be more ubiquitous in dielectric spectra than previously thought and is not a unique feature of hydrogen-bonding materials.

The third "Non" of the glass transition should also be briefly noted. It is nonlinearity, meaning that the relaxation is dependent on the departure from equilibrium. For example, a temperature jump of the same magnitude from below or above to a certain end temperature will result in a slower relaxation toward equilibrium in the former case [27]. Most measurements in well-equilibrated systems are considered in this work, except for differential scanning calorimetry experiments, where the cooling or heating runs can be considered as a series of small successive temperature jumps.

Up to now, only single-component liquids have been considered. However, since ionic liquids are naturally comprised of two species of molecules, binary mixtures of non-ionic liquids should be briefly addressed in the following: When it comes to the appearance of the dynamic spectra of binary mixtures, one decisive point is the dynamic asymmetry of the two components, which is given by the difference in the glass temperatures or the molar masses M of the two species, respectively. Simplified speaking, this means that small molecules have a low T_g , resulting in fast dynamics at a given temperature $T > T_g$ compared to a large molecule with a high T_g . It was shown that T_g and M are correlated by $T_g(M) \propto M^\alpha$ with $\alpha \approx 0.5$ [51]. The other decisive point for the appearance of the relaxation spectrum is the magnitude of the contribution of each species to the measured signal. For example, if a mixture of a polar and a low-polar molecule is investigated by dielectric spectroscopy, the signal from the low-polar component is usually neglected, and the spectrum is assumed to arise solely due to the dynamics of the polar molecules [52, 53]. These are, however, influenced by the presence of the second component. In the case of a small T_g contrast, the spectrum broadens upon addition of the second component, but the width decreases again when increasing the concentration beyond an equimolar composition [54, 53]. This behavior is usually ascribed to concentration fluctuations leading to a broader distribution of relaxation times [55]. In these cases, a single glass transition step is found in differential scanning calorimetry, the width of which also broadens in dependency of the composition in analogy to the dielectric α -peak [55]. However, when a high T_g -contrast in a mixture of polar and low-polar molecules is present, a bimodal spectrum can be observed, where the slower peak is ascribed to the dynamics of the high- T_g component and the faster one to the low- T_g component [56]. The first is broadened

on the high-frequency side and the latter on the low-frequency flank, leading to extremely heterogeneous dynamics in this system. Two α -processes were also reported for a mixture of two polar substances with a T_g difference of only 41 K [57]. However, it was speculated that this behavior is due to the fact that one component is a monohydroxy alcohol, which segregates at mesoscopic scales from the second component due to H-bonding, leading to the observed separation in time scales. Regarding the temperature dependence of the time scales of the two α -processes in binary mixtures, it is usually found that the high- T_g component follows a VFT law, while the low- T_g component either exhibits a VFT slope or an Arrhenius behavior depending on its concentration [58]. From the above examples, it becomes clear that mixing two liquids increases the already high complexity of molecular dynamics even further. However, in ionic liquids, at least the concentration of cations to anions naturally stays constant at 50:50. That this does not imply a simple dynamic pattern becomes clear in the next section, where results from the literature on the dynamics of ionic liquids are compiled.

2.2. Dynamics in ionic liquids

An ionic liquid in the broader sense, the dynamics of which has been extensively studied since the 1960s, is calcium potassium nitrate (CKN), investigated most often in the composition $2\text{Ca}(\text{NO}_3)_2 \cdot 3\text{KNO}_3$. Thus, it is an inorganic mixture of ions, which is in the glassy state at room temperature, with a glass transition temperature of approximately 60°C [59, 60]. The dynamics of the ions has been studied by dielectric spectroscopy [61, 59, 60], light scattering [62, 17], rheology [59, 63] and NMR [63]. The reason why CKN got so much attention is manifold:

At first, it consists only of spherical or near-spherical ions; still, crystallization is easily circumvented, and the supercooled liquid or glassy state is accessible. Due to the shape of the ions, none of them has a permanent dipole moment, and only the nitrate ion has an optical anisotropy, which is rather low. The former is essential for interpreting dielectric spectra since no contribution from dipolar reorientation can be expected, as is the case in polar substances. The latter was exploited mostly in the 1990s in the attempt to experimentally confirm predictions from mode-coupling theory (MCT) by light scattering measurements. Since MCT is concerned with density fluctuations, light scattering measurements on molecules with a large optical anisotropy, where orientation fluctuations are probed, can not be compared to MCT in a straightforward manner. For molecules with a small optical anisotropy, it was believed that the scattered light is mainly originating from a dipole-induced-dipole mechanism, which could be related to density fluctuations and thus be compared to MCT predictions. However, since the nitrate ion in CKN has a non-vanishing optical anisotropy, this view is challenged by the findings presented in section 4.1.

Second, it was found early that the dynamics probed by dielectric spectroscopy decouples from the shear mechanical time constants at low temperatures, but already above T_g [59]. Due to this decoupling of structural relaxation and charge transport, dielectric spectroscopy can monitor ion dynamics even well below T_g . The temperature dependence of the conductivity relaxation time follows an Arrhenius law, in contrast to a VFT behavior above T_g . This can be interpreted as a movement of some more mobile ions through a solid structure [59]. This fact was exploited to measure the structural relaxation time of CKN well below T_g by monitoring the change of conductivity relaxation during physical aging [60]. It was found by NMR measurements that the molecules taking part in the slow structural relaxation are the nitrate ions [64], while the mobile ones are the alkali (i.e., potassium in the case of CKN) ions [63].

Many of these findings in the course of CKN research, some of them dating back more than 50 years, are still highly relevant in the field of ionic liquids nowadays, and some of them are not fully understood yet. For example the decoupling of charge transport from structural relaxation is found for neat ILs [65, 66, 67] and polymerized ILs [68, 69, 70]. Also, the step in the real part of the permittivity as observed by dielectric spectroscopy, which is reminiscent of dipolar relaxation, is commonly found in various ILs, just like in CKN. Its origin is still highly debated and will thus be the topic of section 5.4.2.

The microscopic structure of molten salts with structural simple ions like CKN is determined by charge alternation due to the attraction of anions and cations and the repulsion of like-charged ions [2]. In the case of ionic liquids in the narrower sense, the molecular structures of the ions, especially of the cations, are much more complex. Therefore the microstructure of these ILs

might be more diverse due to a balanced interplay of Coulomb and dispersion forces, $\pi - \pi$ interactions as in imidazolium-based cations or also hydrogen bonds between cations and anions [71]. In fact, for the case of imidazolium-based ILs, it was shown by an all-atom molecular dynamics simulation study in 2006 that for cations with alkyl-chains with four or more carbon atoms, the alkyl chains segregate in nonpolar domains, separated from the polar domains of imidazolium head groups and anions [72]. This finding was experimentally confirmed a year later by an X-ray study, where a pre-peak was found in the spectrum of imidazolium-based ILs with alkyl tails equal or longer than four carbon atoms, indicating structurization on the nanometer scale [73]. These findings have attracted tremendous attention, as can be seen by more than 1800 and 1200 citations of the two works by the time of writing, respectively. Indeed, an increasing slope of the number of published papers with "ionic liquid" in the title after these years can be seen in figure 1.2. Whether or not this could be traced back to these findings is unclear. However, they certainly fueled the interest in searching for nanostructures in ILs. After that, pre-peaks were found with X-ray or neutron scattering in several classes of ionic liquids with long enough alkyl chains, and sometimes even complex structures like lamellas or micelles were proposed to rationalize the findings [74, 75]. In contrast, it was emphasized by others that it is usually sufficient for a pre-peak to appear that the charged groups are spaced by the alkyl-chains [76]. In each case, the dynamics of such an IL is supposed to be more complex than that of an ordinary liquid, and a tremendous body of work followed to explore either the heterogeneous nature of the dynamics or find dynamic signatures of long-lived aggregates. Since ILs with fairly asymmetric but not too long alkyl chains are often supercoolable, the whole dynamic range from temperatures near the decomposition temperature down to the glass transition temperature could be accessed. However, the workhorse in this respect – dielectric spectroscopy – is faced with serious problems in the case of ILs, since the signal is dominated by DC-conductivity, which renders the imaginary part of the permittivity, where a clear peak is seen in polar systems, quite featureless, complicating the interpretation of the spectra. Moreover, several relaxation processes might be active in dielectric spectroscopy, which must be appropriately disentangled. This will be done in chapter 5 by combining different experimental techniques. Here, studies from the literature will be discussed in the following. In dielectric spectra, there could be up to four relaxational processes detectable, in principle, stemming from three different motional mechanisms:

- At first, molecular reorientations will be active if the ions are equipped with permanent dipole moments. In common ILs, the anions are often symmetric; thus, they do not have a permanent dipole moment. But of course, there are various non-symmetric anions, like the $[NTf_2]$ anion used in this work. Cations are mostly asymmetric, especially in ILs, which can be supercooled, and equipped with a more or less strong permanent dipole moment. As it was discussed above for the mixtures of non-ionic liquids, this might lead to a bimodal spectrum, stemming from the dynamically separated reorientations of cation and anion, in cases where their sizes are sufficiently different, or due to the dynamical heterogeneity imposed by the aggregation of the cations, just like it was discussed for mixtures with monohydroxy alcohols. Such a bimodality of the dielectric spectrum due to separate cation and anion reorientation is only rarely reported for experimental [77], and simulation studies [78]. A single reorientational process, on the other hand, was reported

in several dielectric studies. Around room temperature, i.e. in high frequency dielectric measurements, dipolar reorientation is usually interpreted as the main contribution to the spectrum [79, 80, 81, 82, 83, 84]. In contrast, it was shown by comparison of two similar ILs, one of which containing a symmetric cation and the other one an asymmetric cation, where in both cases the anion was the same and symmetric, that the spectra hardly differ, indicating that dipolar reorientation has a negligible effect to the spectrum [85]. Instead, the relaxation was attributed to translational motions of ions. In simulation studies, both motional mechanisms are found to contribute to the spectrum [78, 86]. In some of the works mentioned above, the assignment of dielectric relaxation modes to the reorientation of the cations has been made by comparison with spin-lattice relaxation times T_1 obtained from ^{13}C or ^2H -NMR (nuclear magnetic resonance) [77, 82]. In fact, different NMR techniques are highly useful for the determination of rotational relaxation times of ionic liquids since the possibility to probe different nuclei can be exploited to obtain information only about the cation or anion dynamics selectively [87]. However, it seems that only very recently correlation functions and susceptibilities of ILs measured by NMR became available [88, 89], which provides the opportunity of a more direct comparison of NMR data with dielectric or light scattering spectra that goes beyond that of comparing mere correlations times. In fact, it has been shown that correlation decays measured by ^2H stimulated-echo experiments compare favorably to correlation decays measured by depolarized light scattering [8]. However, although it is possible to obtain correlation times from the combination of different NMR experiments over more than ten orders of magnitude [89], information about the spectral shape is confined to relatively narrow frequency/time windows and rely in some cases of field-cycling measurements on the validity of frequency-temperature superposition. Additionally, the spectra can be strongly influenced by intramolecular dynamics at high frequencies.

At low temperatures, i.e., at frequencies below the MHz-regime, the relaxational processes observed in the dielectric spectrum are only rarely attributed to dipolar reorientations. In cases where it is done, the assignment was based on comparisons with depolarized light scattering measurements, where solely reorientational motions are probed [90, 91]. Instead, the dielectric process is most often attributed to conductivity relaxation in low-temperature measurements, which leads to the next point:

- Due to the diffusive motion of the ions in an electric field, a conductivity relaxation process can be expected. Its step-like nature in the real part of the permittivity might be reminiscent of dipolar relaxation. However, it also occurs in cases where none of the ions has a permanent dipole moment, like in CKN, as discussed above. Therefore, sometimes a reorientation of ion pairs is used to rationalize the permittivity step [69]. However, the formation of long-lived ion pairs is doubted in the literature [92, 93], and conductivity relaxation is also observed when one ion species is immobile like in CKN below T_g or in polymerized ILs and also in dilute electrolytes, where the counter-ions are not necessarily in close proximity [94]. Hence, this view is not adopted in this work. Instead, models for translational transport of ions are used to describe the conductivity relaxation in dielectric spectra. This is described in detail in section 5.1. From these models, which are usually used to describe dielectric data in the conductivity representation, a step

in the real part of the permittivity emerges very naturally when transformed from the conductivity representation. Such models have been used in the literature to describe conductivity relaxation in ILs at low-temperature [95, 96, 69, 97], but also empirical models usually used to describe dipolar reorientations were employed and ascribed to ion hopping [98]. Although cations and anions might possess different translational mobility even for non-polymeric ILs far above T_g , only one conductivity relaxation is expected to occur, probably dominated by the faster ions, which might facilitate charge transport even below T_g , as seen for example in CKN as discussed above. Of course, several NMR techniques are routinely used for measuring translational self-diffusion coefficients of ILs, and a comparison with those calculated from DC-conductivity obtained by dielectric spectroscopy usually yields relatively good agreement [99, 100, 101, 69]. However, it has to be kept in mind that NMR measures the mass transport, while in dielectric spectroscopy, information about the charge transport is obtained. Naturally, each ion is charged, but nevertheless, for example, through correlated forward and backward movements, an ion might exhibit mass transport but does not contribute to the overall charge transport [102]. Therefore, the differences in the diffusion coefficient can be quite large, and thus it is important to choose the experimental technique depending on what diffusional mechanism one is interested in. Again, as it was the case for rotational dynamics, NMR can address the diffusion coefficients separately for cations and anions. Interesting in this respect are studies on ILs where the alkyl-chain length of the cation is varied, thus changing the cation and anion size ratio since this is also done in the present work. However, for example, for the case of imidazolium-based cations with $[\text{NTf}_2^-]$ anion, there seems to be no conclusive picture in the literature. It has been found on the one hand that the cation diffuses faster than the anion up to a chain length of $n = 8$, even though the cation is markedly larger than the anion in this case [103]. On the other hand, almost identical diffusion coefficients for cations and anions have been reported for $n = 6$, while cations with even longer alky-chains diffuse slower than the anions [8]. Surprisingly, the difference is small even for chain lengths as large as $n = 12$, also in the case of an ammonium-based cation [104].

- As an additional relaxational process, the dynamics of aggregates could come into play: For ILs equipped with long alkyl-tails, where an X-ray scattering pre-peak is observed, one could speculate that the aggregated cations perform translational and rotational motions slower than that of single ions. This view might be inspired by the case of monohydroxy alcohols, where the slow Debye process is often attributed to the movement of supramolecular structures. And in fact, bimodal spectra were found in dielectric spectroscopy [105, 98, 95], light scattering [106, 107], rheology [98], and optical Kerr-effect measurements [108, 79], where in all these cases the slowest relaxation process was attributed to the dynamics of aggregates. The attribution was performed upon different reasoning: For example, the hydrodynamic radius associated with the slow relaxational contribution in light scattering measurements was found to compare with the structural length corresponding to the X-ray scattering pre-peak [106, 107]. But also, the appearance of the slow dielectric process was reported to be dependent on the size of the supramolecular structures as probed by the X-ray pre-peak [105].

Also, the comparison of the spectra of different experimental methods has proven useful to assign one of the processes of a double peak spectrum to the α -relaxation, or the aggregate dynamics, respectively [108, 79, 106]. However, little help comes from NMR measurements when identifying the aggregates' relaxation. It seems that there is no direct observation of a dynamic feature reported in NMR data, which was assigned to dynamics of supramolecular structures. Only indirect evidence is obtained through the breakdown of the Stokes-Einstein equation for long-chained cations, which was attributed to a restriction of the translational dynamics due to the aggregates, while the rotational motion is unaffected [89].

Thus, it can be seen that the disentanglement of the different dynamic contributions to the experimental spectra is highly involved. Moreover, the assignment of spectral features to their microscopic origin is not consistent in the literature and sometimes seems to depend on the authors' community. An example is a dielectric relaxation, which is most often attributed to a dipolar reorientation in the high-frequency community, while it is usually assigned to conductivity relaxation by the glass community, as discussed above.

The situation gets even more complicated when mixtures of non-ionic substances with ILs are considered since an additional relaxational contribution is expected in the experimental spectra. However, such mixtures might also help in some instances to separate the conductivity relaxation from dipolar processes in dielectric spectroscopy when an IL is diluted in a non-ionic liquid, and thus the conductivity shifts to lower frequencies. The most natural admixture to ILs is undoubtedly water. ILs are often hydrophilic, so uptake of water from air can lead to not only a change in physicochemical properties, such as viscosity [109] or glass transition temperature [110], i.e., it affects the molecular dynamics, but also differences in the crystallization behavior of the liquid [111]. Therefore, ILs are usually dried in a vacuum oven before characterization to ensure the absence of water. Conversely, intentionally added water can alter the properties of the IL in the desired direction, for example, to enhance the diffusion coefficient or the conductivity [112, 113, 114]. Mixtures of water and ILs have been investigated with dielectric spectroscopy [115] and especially a combination of dielectric spectroscopy with molecular dynamics simulation has proven useful for disentangling the dipolar contributions of water molecules, and ions [116, 78]. Additionally, it was found that in some IL-water mixtures, nanoscale water clusters form, which are sometimes also called water pocket [117]. They were experimentally observed by small-angle neutron scattering (SANS) [117, 118], Raman spectroscopy [119, 120] and NMR measurements [121], but also by molecular dynamics simulations [122, 123]. However, dynamic information on these systems, especially from light scattering measurements, are not reported so far. Those experiments might give information about the diffusion of such water pockets through the IL network. A drawback of IL-water mixtures is that water crystallizes in an IL-water mixture upon supercooling for too high water concentrations. This means that not the full concentration range could be investigated at low temperatures, where different dynamic processes are best separated. This can hinder the full understanding of such mixtures, which might be overcome by choosing another admixture structurally similar to water but easily supercoolable. As such, alcohols are suited, and the dynamics of such mixtures have been addressed in some studies [124, 125, 126].

As a next step, IL-water mixtures can be mixed with gelatin to form a gel often called "Ion

"Jelly" (IJ). Such gels have been shown to exhibit similar DC-conductivity as the liquid without gelatin but are mechanical rigid [127]. This makes them interesting for various applications such as electrolytes [128], gas sensors [129], fractionation of mixtures [130], electrochromic windows [131] and biosensing [131]. Among the experimental methods used to investigate the properties of IJs in the literature is differential scanning calorimetry (DSC), where it was shown that some IJs do not crystallize upon cooling despite the considerable amount of contained water [127]. Naturally, the ionic conductivity of ionogels is among the properties studied the most. For example, the influence of the gelling agent on ion dynamics was addressed in the literature [127, 132]. Usually, dielectric spectroscopy is used for such investigations [133], sometimes also combined with NMR spectroscopy to probe diffusive ionic motion [134, 127]. Structural information was obtained by X-ray scattering[128] and scanning electron microscopy [135]. However, the complex interplay of microscopic translational and rotational dynamics with macroscopic dynamics of the gel matrix was not investigated in great detail up to now. Especially measurements of IJ with dynamic light scattering were not reported so far in the literature.

3. Methods

In this chapter, the different experimental and computational methods are addressed. The theoretical background, which is needed in the course of this work, is outlined, and the experimental setups are described. The largest part concerns light scattering, as this is the method used most comprehensively in this work. After that, dielectric spectroscopy and differential scanning calorimetry are discussed. At last, quantum chemical calculation methods are addressed, which are used to calculate molecular properties.

3.1. Light scattering

Already about 150 years ago, light scattering attracted the attention of researchers such as Tyndall or Lord Rayleigh in an effort to explain the blue color of the sky [136]. In honor of his explanation of the intensity of light scattered by molecules being proportional to the inverse of the fourth power of its wavelength [137], the elastic scattering by particles much smaller than the wavelength of light is named Rayleigh scattering.

Later, it was observed by Robert Strutt, who followed his father as the 4th Lord Rayleigh, that the light scattered by gas at right angles to the direction of the incident unpolarized light is not fully polarized as it would be expected for spherical particles [138]. The expectation of full polarization can be easily seen when considering an unpolarized ray traveling from left to right impinging on a spherical molecule. Since unpolarized light can be thought of being a superposition of a ray polarized vertically and a ray polarized perpendicular to the drawing plane, the scattered light observed by the reader will be just the component induced in the molecule by the vertically polarized ray [136]. The observation of scattered light, which is not fully polarized, thus implies that the molecule has a preferred direction of polarization [138], i.e., it is not spherical. This fact has been exploited, for example, by Gans to determine the shape of gas molecules by measuring the ratio of the intensity of scattered light polarized in the direction of the incident light and perpendicular to it [139].

Regarding light scattering in liquids, Einstein derived in 1910, based on the ideas of critical opalescence by Smoluchowski [140], a quantitative equation for the intensity of light scattered due to density, or equivalently, refractive index fluctuations [141]. The derivation is based on Boltzmann's principle and on Maxwell's equations, and with this, it is not only possible to describe the scattered light of binary mixtures near demixing (critical opalescence), but also light scattered by neat liquids due to density fluctuations. For the case of an ideal gas, Einstein's equation reduces to the one found by Lord Rayleigh explaining the blue color of the "Luftmeer" [141].

In addition to this elastic scattering, two different types of inelastic scattering of light were

reported some years later, one of them being rewarded with the Nobel Prize. The scattering of light by acoustic waves in the medium was predicted by Brillouin and named after him [142]. It was first observed experimentally for different liquids eight years later by Gross, manifesting as two symmetrically spaced lines around the elastic line with a very small separation [143]. The experimentally observed separation was in accordance with the one predicted by Brillouin, where the speed of sound and light in the respective substance and the scattering angle enter in the calculation. In order to resolve the Brillouin lines, a Fabry-Pérot interferometer is commonly used today. Thus the term "Brillouin spectroscopy" can be found in the literature for measurements performed with a Fabry-Pérot interferometer, also in cases where only the depolarized scattered light is detected, resulting in the suppression of the fully polarized Brillouin lines. Therefore, this term is not used in this work in order to exclude confusion as no Brillouin lines are observed here.

The second type of inelastic light scattering was discovered on 28.02.1928 by Raman and co-workers, after its prediction by Smekal in 1923 [144], when studying the light scattered from benzene and other liquids [145]. They found lines in the scattered spectrum, markedly separated from the incident wavelength but strongly polarized, thus excluding fluorescence as their origin. Although similar observations were made a week earlier by Landsberg and Mandelstam (but published only later) [146], the new radiation was named after Raman, and also the Nobel Prize was awarded to him two years later [147]. Today it is well known that the Raman effect is due to a coupling of the light with the intramolecular vibrational degrees of freedom in a molecular liquid, and Raman spectroscopy is routinely used, for example, to identify molecules based on their characteristic inelastic spectrum.

Around that time, another observation was made when spectroscopically investigating scattered light: The central line of incident light after scattering in a liquid was accompanied by a nebulous intensity on both sides, which was called the "wings" [148, 149]. Two essential features of these wings were observed: Its intensity depends on the degree of optical asymmetry of the molecule under study, and the scattered light in this spectral region was depolarized [150]. These findings pointed into the direction that rotations of the molecule might be responsible for the wings. However, it was found some years later by Gross and Vuks that the wings did not broaden upon increasing the temperature of the liquid, as would be expected in the case they were due to the rotations of the molecules [151]. Instead, they identified a portion of the wings very close to the central line, the intensity of which increased upon increasing temperature, while the outer parts of the wings stayed unaltered. Hence, they speculated that only the inner part might stem from molecular rotations. In the late 1960s, Fabelinskii remarked in his comprehensive book, reviewing the light scattering results up to that time, that "Although 35 years have passed since its discovery, the nature of the wing is still not completely explained, both in theoretical and experimental aspects" [152], a statement which still holds today more than fifty years later. The basic idea that the inner part of the wings is due to relaxational processes in the liquid, like those responsible for the dispersion of electromagnetic waves in polar liquids, which was traced back by Fabelinskii to Landau and Plasczek [153], is still prevalent today, although alternative explanations were discussed in the meantime. Likewise, the division into an inner and outer part of the wings was still practiced many years later when evaluating light scattering data [154], although details of the spectrum are overlooked in this way. Theoretical models were also developed by that time. For example, Starunov explained the inner part of the wing by

rotational diffusion and the outer part by rotational oscillations of the molecules (see [152] and references therein). In that light, Fabilinskii obtained rotational relaxation times in the 1950s, thus without a laser and with a prism spectrograph and recordings performed on a photographic plate. The relaxation times were determined by the half-width $\delta\nu$ of the inner wings via [152]

$$\tau = \frac{1}{2\pi\delta\nu}. \quad (3.1)$$

For example, for the cases of toluene and water, these relaxation times are in good agreement with up-to-date measurements and data evaluation methods as employed in this work. This relaxational process is identified with the α -relaxation discussed in section 2.1 and thus of main interest for this work.

A sketch of a typical depolarized light scattering spectrum of a liquid comprised of optical anisotropic molecules obtained with a combination of a diffraction spectrometer and an interferometer is shown in figure 3.1. The part shown as black lines symbolizes the spectral portion obtainable with a Raman spectrometer as described in detail in section 3.1.3 and the colored lines indicate the part of the spectrum obtained with a Tandem-Fabry-Pérot interferometer (TFPI) utilizing different mirror spacings. The incident wavelength determines the zero on the frequency axis, and the frequency shift of the scattered light relative to that frequency is shown. Please note that the intensity is plotted on a logarithmic scale. In the area highlighted by the shading, the wings are clearly visible and are shown magnified in the inset. This part of the spectrum will be called quasi-elastic and is the main focus of this work. At frequencies further apart from the central line, sharp Raman lines can be observed. The fact that the intensity of the Raman lines is lower on the right than on the left-hand side is discussed later.

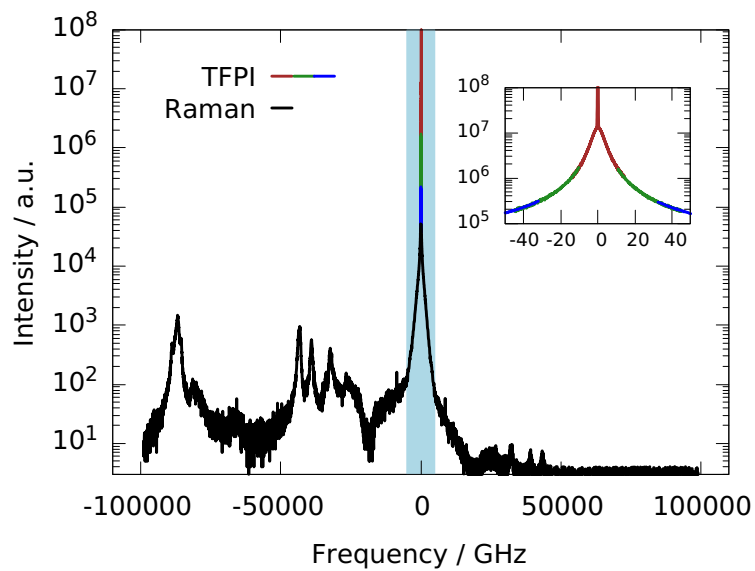


Figure 3.1.: Sketch of a light scattering spectrum obtained with a combination of a Raman spectrometer (black lines) and a Tandem-Fabry-Pérot interferometer (colored lines). The shaded area highlights the quasi-elastic part of the spectrum or, in older terms the wings of the Rayleigh line.

When lowering the temperature, it is immediately apparent by equation 3.1 that the width of the rotational part of the wing narrows. This means that this process can eventually no longer be resolved for low temperatures, even with a modern interferometer. Therefore, a third spectroscopic technique has to be employed to measure the rotational relaxation at low temperatures, namely photon correlation spectroscopy (PCS). This technique is nowadays mainly used to determine the size of nanoscale objects in solution. It seems that only a handful of workgroups worldwide use it actively for rotational spectroscopy of molecular liquids at the time of writing. Therefore, and also because a strict differentiation between PCS, TFPI, and Raman measurements is often made in the literature, it is important to realize that all three techniques have access to one and the same signal, just on very different frequency (time) scales. Since the spectra from Raman and TFPI overlap in a certain frequency region, as seen in figure 3.1, it is immediately evident that both measure the same signal. The situation is less evident in the case of photon correlation spectroscopy, which measures the time correlation function of the intensity of the scattered light. However, the connection to the spectral density $S(\omega)$ as measured by TFPI or Raman spectroscopy is established because the field correlation function and the spectral density are Fourier-transform pairs, i.e., [155]

$$S(\omega) = \frac{1}{2\pi} \int_{-\infty}^{\infty} dt' \langle E^*(t)E(t+t') \rangle \exp(-i\omega t') \quad (3.2)$$

The connection between the field correlation function $\langle E^*(t)E(t+t') \rangle$ and the intensity correlation function, which is the one actually measured, will be discussed with all other details of photon correlation spectroscopy in section 3.1.1.

The main challenge is now to relate the macroscopically measured spectral densities or field correlation functions, respectively, to microscopic motions of the molecules. While theoretical models exist which are able to predict the total intensity of the light scattered by density fluctuations and also for the case of rotational motions of optically anisotropic molecules in good accordance with experiments (see section 4.1), there is no model which can describe the shape of the wings quantitatively. This, however, is not merely due to a lack of an adequate theory for depolarized light scattering but is inherent to all dynamical measurements of liquids and directly related to the incomplete understanding of the relaxation processes as discussed in section 2.1. Therefore, a qualitative picture, which is able to capture the essence of the molecular dynamics underlying the wing, is sketched below, following Berne and Pecora [155]: Assuming an incident monochromatic beam with polarization \vec{n}_i acting on a molecule with polarizability tensor $\underline{\alpha}$. Then, a dipole moment is induced in the molecule, given by $\vec{\mu}(t) = \underline{\alpha}\vec{E}(t)$. The polarizability tensor can be written in a diagonal form as

$$\underline{\alpha} = \begin{pmatrix} \alpha_{xx} & 0 & 0 \\ 0 & \alpha_{yy} & 0 \\ 0 & 0 & \alpha_{zz} \end{pmatrix}$$

with respect to the principal axis of the molecular polarizability, which is directly connected to the nuclear frame of the molecule. If $\alpha_{xx} = \alpha_{yy} = \alpha_{zz}$ then a molecule is optical isotropic, i.e. a spherical top molecule, and optical anisotropic otherwise. This means that for the induced

dipole moment $\vec{\mu}(t)$ in the general case of anisotropic molecules, its direction is not necessarily parallel to the electric field of the incident light. Therefore, the light radiated by the dipole, i.e., the scattered light, is fully polarized in the same direction as the incident light only if the molecules are isotropic. It can be shown that the scattered field with polarization \vec{n}_f is proportional to the sum of amplitudes from molecules in the scattering volume, i.e.

$$\sum_j \vec{n}_f \underline{\alpha}(t) \vec{n}_i \exp(i\vec{q}\vec{r}_j(t)) \quad (3.3)$$

where

$$\vec{q} = \frac{4\pi n}{\lambda} \sin\left(\frac{\theta}{2}\right) \quad (3.4)$$

is the scattering vector, n the refractive index, θ the scattering angle and $\vec{r}_j(t)$ is the position of the j th molecule. The time correlation function of the scattered field is thus proportional to

$$C_{if}(\vec{q}, t) = \sum_{j,k}^N \left\langle \alpha_j^{if}(0) \alpha_k^{if}(t) \exp[i\vec{q}(\vec{r}_j(0) - \vec{r}_k(t))] \right\rangle \quad (3.5)$$

and the spectral density is

$$S_{if}(\vec{q}, \omega) = \frac{1}{2\pi} \int_{-\infty}^{\infty} dt e^{-i\omega t} C_{if}(\vec{q}, t) \quad (3.6)$$

where $\alpha^{if} = \vec{n}_f \underline{\alpha} \vec{n}_i$.

Two quantities in equation 3.5 are time-dependent: The polarizability tensor with respect to the laboratory frame and the molecular position. While the latter describes diffusional motions, the fluctuation of the polarizability tensor can be categorized in three different time regimes: On time scales of femtoseconds, vibrational displacements of atoms give rise to Raman lines. At times in the order of tenths of picoseconds, oscillatory libration motions and collision-induced distortion of the molecular frame are present, resulting in the broad part of the wing, as described above. At even longer time scales, which are strongly dependent on the temperature, the rotation of the polarizability tensor, i.e., of the molecules, gives rise to the narrow part of the wings.

Regarding the term dependent on the translational displacements of the molecules $\exp[i\vec{q}(\vec{r}_j(0) - \vec{r}_k(t))]$, some considerations are in order: As mentioned above, it is known from Einstein's theory that light is scattered due to fluctuations of the refractive index, which in the case of neat liquids arise due to fluctuations of the density [141], implying translational displacements of the molecules. However, these fluctuations occur on intermolecular length scales, whereas at length scales determined by the scattering vector \vec{q} , which are on the order of the wavelength, the refractive index appears stationary. Thus, no time dependence of these translational motions in neat liquids can be detected by measuring the scattered light. In contrast, when considering, for example, large molecules in a solvent, the refractive index contrast between the two kinds of molecules fluctuates on length scales matching the accessible \vec{q} range due to the diffusion of the large molecules. This is routinely used today for the determination of

particle sizes [156, 157]. It is clear from equation 3.5 that the translational displacements are not detected in depolarized measurements as long as the particles are isotropic. Otherwise, the translational part could, in principle, contribute to the depolarized spectrum. However, usually, the translational diffusion of the particle takes place on a time scale several orders of magnitude slower than the rotational motions due to the small scattering vector. Thus, the depolarized correlation function decays entirely due to rotational motions, and the translational dynamics acts only as a stationary multiplicative factor.

It should be noted that equation 3.5 contains the self ($j = k$) and the distinct ($j \neq k$) part of the correlation function. Usually, the distinct part is neglected, which, however, is only justified in dilute solutions, and it will be discussed later that in certain cases, dynamic contributions of cross-terms might be detected in light scattering spectra.

The experimental details of the different light scattering setups, which are used to obtain either the time correlation function (equation 3.5) or the spectral density (equation 3.6) of the scattered light, are discussed in the following subsections.

3.1.1. Photon correlation spectroscopy

The photon correlation spectroscopy (PCS) setup is shown in the configuration as present at the end of this work in figure 3.2. The experiment was first set up several years ago and considerably improved during a preceding doctoral thesis. More details of the optical components and their alignment can thus be found in references [158], and [159].

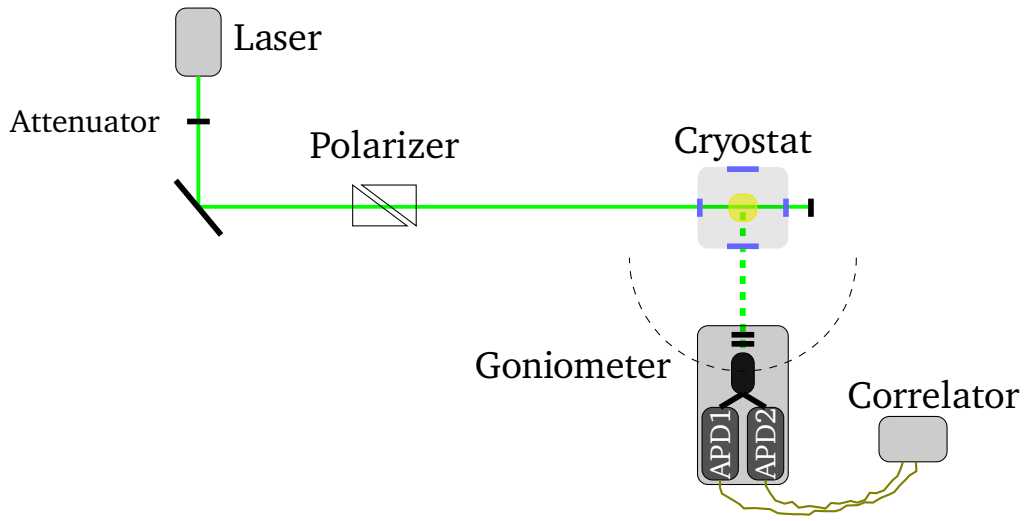


Figure 3.2.: PCS setup: After passing the attenuator and the polarizer, the beam impinges on the sample. The scattered light passes a narrow band pass filter and a polarizer before being collected by the fiber optics and split up into two avalanche photo diodes.

The laser is a Cobolt Samba type single frequency solid-state laser with a wavelength of 532 nm and a maximum power of 500 mW. It is mounted on an active cooling plate, which employs a Peltier element for vibration-free cooling of the laser. It is possible to adjust the power of the laser between 1 and 500 mW. However, the intensity is most stable when the maximum power is chosen. Therefore, in order to be able to reduce the power on the sample while operating at the maximum power, a half-wave plate in combination with a polarizer is used as an attenuator: The vertically polarized light of the laser is rotated by the wave-plate, and the polarizer transmits only vertically polarized light. For an even better extinction ratio, the beam is passed through a second polarizer and impinges on the sample, mounted in a cold finger cryostat. Several different designs of sample cells were developed over the years. The most recent one is a cylindrical one made of blackened aluminum, which allows for high cooling rates. The sample is surrounded by a vacuum shroud, where the isolating vacuum is maintained during measurements by an ion getter pump, which operates vibration-free. The cold finger cryostat can be operated with liquid nitrogen or helium, depending on temperature needs. In this work, only liquid nitrogen is used, which is fed into the cryostat in gaseous form due to the special design of the transfer line in order to avoid vibrations from boiling nitrogen. The light scattered by the sample is collected by a detection unit, which is mounted

on a goniometer, giving access to different scattering angles and which contains the following parts: A polarizer from Bernhard Halle with an extinction ratio of 1×10^7 and a bandpass filter, centered at 532 nm with a bandwidth of 2 nm in order to cut out fluorescence light, which is present in some ionic liquids. Behind that, coupling optics from ALV GmbH are used to couple the scattered light into a single-mode fiber, which is directly connected to a 50:50 fiber splitter. Both signals are fed into one COUNT T100 avalanche photodiode from LaserComponents each. The intensity signals of the two detectors are cross-correlated by an ALV 7004 hardware correlator in order to suppress after-pulsing effects, and the resulting normalized intensity correlation function is recorded by the ALV software on a computer, which can be written as

$$g_2(t) = \frac{\langle I(0)I(t) \rangle}{\langle I \rangle^2} \quad (3.7)$$

where the angle brackets denote the time average. As detailed above, the information about the molecular dynamics are, however, contained in the field autocorrelation function $g_1(t) = \langle E(0)E^*(t) \rangle / \langle E \rangle$. Thus, a connection between the autocorrelation function of the intensity and the electric field has to be established. The way it is done in this work has been published previously in reference [90].

The intensity of the light at the detector is assumed to result from a superposition of the scattered field and a static field, mainly stemming from reflexes in the sample cell, which is also called the local oscillator, i.e., $I(t) = |E_{LO}(t) + E_s(t)|^2$. Thus, the signal is called partially heterodyne, while it would be called homodyne if only the scattered light would be detected. Assuming that $E_{LO}(t)$ and $E_s(t)$ are statistically independent and that the latter is a zero-mean Gaussian variable, one can apply the Siegert relation [160] $g_2(t) = 1 + \Lambda|g_1(t)|^2$ to obtain for the mixed signal [161, 162, 163]

$$g_2(t) = 1 + \Lambda C^2|g_1(t)|^2 + 2\Lambda C(1 - C)|g_1(t)| \quad (3.8)$$

where Λ is the spatial coherence factor, ideally being unity, which depends on the geometry of the experimental setup and determined here with a suspension of latex spheres to be approximately $\Lambda = 0.98$. The constant $C = \langle I_s \rangle / (\langle I_{LO} \rangle + \langle I_s \rangle) = \langle I_s \rangle / \langle I \rangle$ depends on the time-averaged intensities of the scattered light by the sample I_s , and the local oscillator I_{LO} , respectively. Equation 3.8 includes the homodyne case if $C \approx 1$ and the heterodyne limit if $C \ll 1$ so that C^2 becomes negligible compared to C .

Solving equation 3.8 in the limit $t \rightarrow 0$ for C , where $g_1(0) = 1$ per definition and $A = g_2(0) - 1$ is the intercept, one gets:

$$C = 1 - \sqrt{1 - A/\Lambda} \quad (3.9)$$

However, care has to be taken due to the fact that the intercept may be reduced because of fast dynamics appearing on a time scale not captured by the correlator. Thus, at the shortest correlation time t_0 , the field correlation function yields:

$$g_1(t_0) = 1 - A_{\text{fast}} = \lambda. \quad (3.10)$$

By substituting into equation 3.8 and solving again for C , one gets:

$$C = \frac{1 - \sqrt{1 + A/\Lambda - 2A/(\lambda\Lambda)}}{2 - \lambda} \quad (3.11)$$

A_{fast} , i.e., the intensity of the microscopic dynamics can be measured by TFPI/Raman measurements. However, then, the influence of the band-pass filter employed in the PCS, cutting some of the short time intensity, has to be taken into account additionally, which renders this procedure complicated. Therefore, in the present work an estimation is used: The minimum value of λ , i.e., the maximum of the microscopic dynamics A_{fast} that is possible for a given intercept A of the measured data can be calculated by equating the radicand of eq. 3.11 with zero. The errors of the correlation times τ made due to this estimation of λ_{\min} and $\lambda_{\max} = 1$ were found to be around 15 %, leading to errorbars in the typical Arrhenius plot smaller than the size of the symbols.

In order to be able to compare the so obtained field correlation functions with data from the other light scattering setups, i.e., TFPI and Raman, which operate in the frequency domain, the PCS correlation functions are Fourier transformed to yield the spectral density, as given by equation 3.2. This is done by employing the Filon algorithm [164], which is especially suited for performing a Fourier transformation for logarithmically spaced discrete data. Details of this procedure can be found in reference [20]. After that, the data is transferred into the susceptibility representation via the fluctuation-dissipation theorem as outlined in the next subsection. This is done since it is the most common representation for dielectric data and thus well known, and additionally, different dynamic contributions can be separated best by eye in this representation.

3.1.2. Tandem-Fabry-Pérot interferometry

For the detection of the scattered light in a frequency range from approximately 0.3 GHz to 3 THz, a Tandem-Fabry-Pérot interferometer (TFPI) manufactured by JRS Optical Instruments is employed. The technical details in this section are based on the work of John Sandercock, the designer of this machine [165, 166]. As the name TFPI already suggests, the centerpiece of this apparatus are two Fabry-Pérot interferometers (FPI) operated in series. Each of them consists of two parallel highly reflective mirrors with separation L , through which only light is transmitted obeying the relation $L = \frac{1}{2}m\lambda$, where λ is the wavelength of the light, and m is an integer. The frequency interval between two successive transmission orders is given by $\Delta\nu = c/(2L)$ and is called the free spectral range (FSR). The FPI could be readily used as a spectrometer by varying the mirror spacing. This, however, is not suited when signals with a broad range of frequencies should be measured, as intended here, since then the signal within an FSR is the sum of the intensity of all frequencies satisfying the relation $L = \frac{1}{2}m\lambda$. To solve this problem, a second FPI is used in series to the first one, with a slightly different mirror spacing L_2 . Thus, for wavelengths, which are transmitted through both FPIs, the relation $L_1/L_2 = m_1/m_2$ must be fulfilled. From this, it is immediately clear that when both FPIs are adjusted in such a way that a certain wavelength is transmitted at the same time by both, then the next order is blocked. Now, both FPIs have to be scanned simultaneously in such a way that the change of the mirror spacing δL_i satisfies the relation $\delta L_1/\delta L_2 = L_1/L_2$. This is done by mounting one of the mirrors of each pair on a piezoelectric-driven stage, where one of the FPIs lies with its axis at a certain angle to the scan direction. This is illustrated in figure 3.4. In the present case, the angle is 18.2° , which leads to a ratio of the mirror spacings of $L_2/L_1 = 19/20$, i.e., each 20th order is transmitted again with full intensity. Thus, the transmission function of the TFPI can be written as

$$I_T = I_0 / \left[\left(1 + \frac{4F^2}{\pi^2} \sin^2 \left(\frac{\pi\nu}{\Delta\nu} \right) \right)^3 \cdot \left(1 + \frac{4F^2}{\pi^2} \sin^2 \left(0.95 \cdot \frac{\pi\nu}{\Delta\nu} \right) \right)^3 \right] \quad (3.12)$$

where F can be regarded as the quality of the mirrors regarding reflectivity and flatness and is called finesse. By fitting equation 3.12 to an experimental transmission spectrum of the laser line, the finesse of the TFPI is determined to be $F = 120$. Such an experimental spectrum together with the fit is shown in the lower panel of figure 3.3. There, it can be seen how higher transmission orders are suppressed and how each 20th order is again fully transmitted. In order to additionally reduce the influence of these higher orders, a bandpass filter can be mounted in the TFPI, which is centered at the laser line and which has a bandwidth of 1 nm. It is indicated as a dashed line in the lower panel of figure 3.3. It has been shown in the literature that the usage of such a filter is necessary to avoid artificial features in the resulting spectra [167, 168, 169]. In the upper panel, the transmission functions of the two individual FPIs are shown in the region indicated in the lower panel. There, the shift in the transmission frequency between the two FPIs can be seen, resulting in the high suppression of intensity in this frequency range when operated in series. In this way, it is assured that higher orders influence the intensity in the FSR of interest only negligibly, and it is thus possible to measure broad rotational spectra of liquids.

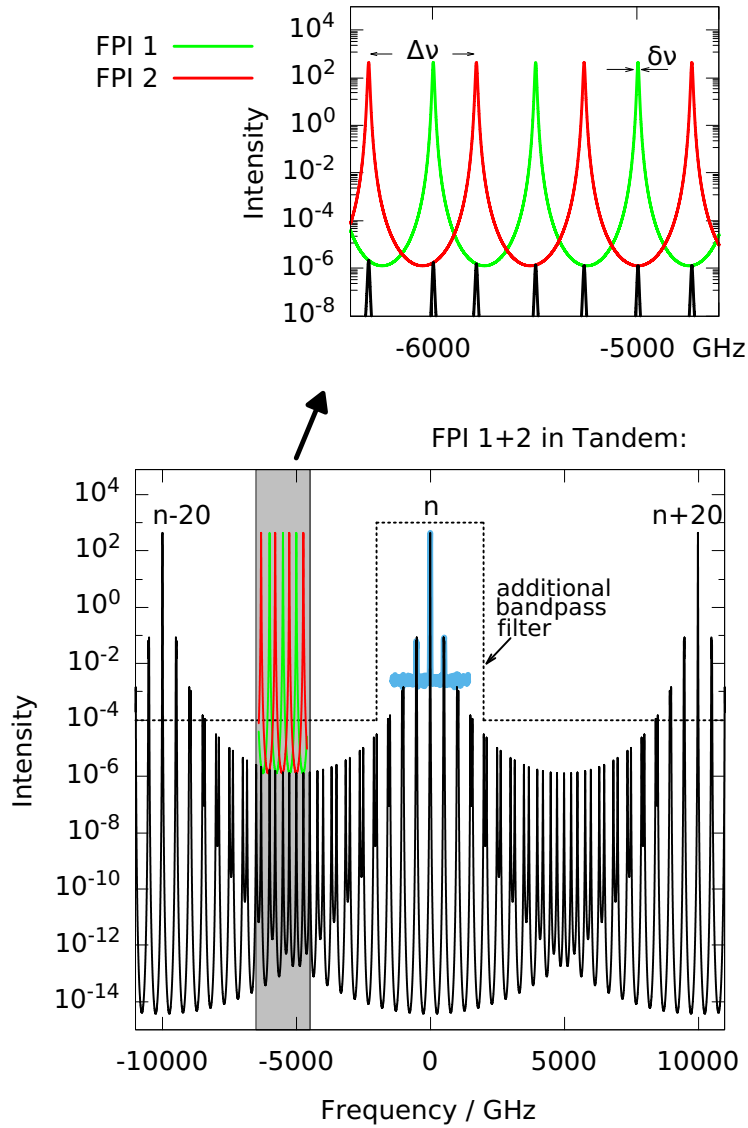


Figure 3.3.: Transmission function of a Tandem-Fabry-Pérot interferometer. Upper part shows the transmission lines of each single FPI, lower part the combined transmission function. The blue line is experimental data for mirror spacing $L_1 = 0.3$ mm and $L_2 = 0.95L_1$. Full transmission in tandem mode would again occur at orders $n \pm 20$, which is suppressed by an additional bandpass filter

In order to be able to measure frequency scans over several hours, the two FPIs must stay perfectly adjusted to each other over the whole time. Therefore, on the one hand, the mirrors are mounted on an actively stabilized platform, which reduces vibrations. Furthermore, sufficient temperature stability in the laboratory has to be assured. But most importantly, the transmission of the laser line through both FPIs simultaneously is actively stabilized. This is done by maximizing the intensity of the reference beam (see figure 3.4) through the piezoelectric adjustment of the mirror positions via an electronic feedback loop. Thereby, the scanning of

the mirror spacings over several hours without interruption is possible, which is needed for some measurements, for example, when the relative intensities of different samples should be determined, as it is done in section 4.1.

However, the mirror spacing range, which is scanned piezoelectrically, as mentioned above, is usually only $0.5 \mu\text{m}$, i.e., approximately one FSR. This gives only access to a relatively narrow frequency range. Therefore, different coarse mirror spacings can be set manually, for each of which the automatic scan is performed. When choosing these spacings appropriately, the spectrum obtained with one spacing overlaps with the one from the next spacing, and in this way, a continuous spectrum can be formed. Here, 30, 10, 3, 0.75 and 0.15 mm are chosen. The bandpass filter discussed above is used for the first three spacings. It is clear that errors made during the adjustment of these spacings are most significant for the mirror distance of 0.15 mm . Moreover, the TFPI has a built-in bandpass consisting of a prism and a pinhole, which might influence the highest frequency measured with the 0.15 mm spacing. Therefore, it is more appropriate to use the Raman spectrometer, as described in the next subsection, for measuring the highest frequencies.

The different spectral densities obtained for the mirror spacings are transformed into the susceptibility representation individually. This is done in the following way: Since both sides of the laser line are measured, i.e., the Stokes and the anti-Stokes side, which contain the very same information and are identical except for the Boltzmann factor, which accounts for the fact that some dynamic modes are not occupied on the anti-Stokes side. Thus, the average of the spectrum on the Stokes side and the one on the anti-Stokes side, the latter multiplied by the Boltzmann factor, is used as the spectral density $S(\omega)$. The light scattering susceptibility $\chi''_{\text{LS}}(\omega)$ is then calculated via the fluctuation-dissipation theorem [170, 171], i.e.,

$$\chi''_{\text{LS}}(\omega) = \frac{1}{\hbar} \frac{S(\omega)}{n(\omega, T) + 1} \approx \frac{\omega}{k_b T} S(\omega) \quad (3.13)$$

with $n(\omega, T) = (\exp(\hbar\omega/k_B T) - 1)^{-1}$ being the Bose factor. The indicated approximation holds in the classical limit of $k_B T \gg \hbar\omega$ and is only used in the case of PCS data. Subsequently, the different mirror spacings are scaled vertically in the susceptibility representation so that they overlap. This procedure is visualized in [172]. In this way, a continuous spectrum over the whole frequency range accessible with the TFPI is obtained. In cases where additional Raman measurements are performed, these spectra are transformed and shifted vertically, in the same way, to overlap with the TFPI data. Examples of such spectra are shown later in figure 4.7.

Finally, the experimental setup outside the TFPI should be considered, as shown in figure 3.4. A Verdi V2 solid-state laser operating at a wavelength of 532 nm is used. The output power can be varied up to 2 W . Here, usually 400 mW and 200 mW are used for mirror spacings with or without the bandpass filter, as the latter reduces the detected intensity by approximately 50 %. As mentioned above, a beam splitter is used to feed a part of the beam via an attenuator into the TFPI, which is used as a reference beam for stabilization. The main beam is directed via mirrors through a polarizer, which selects vertically polarized light, then further to a small prism, and is then focused by a lens onto the sample. The sample is either mounted in an optical cryostat or in a custom-made oven. One of these ovens holds standard cuvettes and is designed to operate up to temperatures of 450 K . The other one is isolated and able to reach sample temperatures as high as 570 K . In this case, the sample is flame sealed in cylindrical

glass flasks. The scattered light is collected in either case in backscattering geometry by the same lens, which focuses the beam onto the sample. The scattered light is fed through a polarizer, which selects horizontally polarized light and focused onto the entry pinhole of the TFPI. After passing the TFPI, as described above, the light is detected by a photodiode with a dark count rate of approximately 10 counts/s and recorded with the "Ghost" software, which belongs to the TFPI.

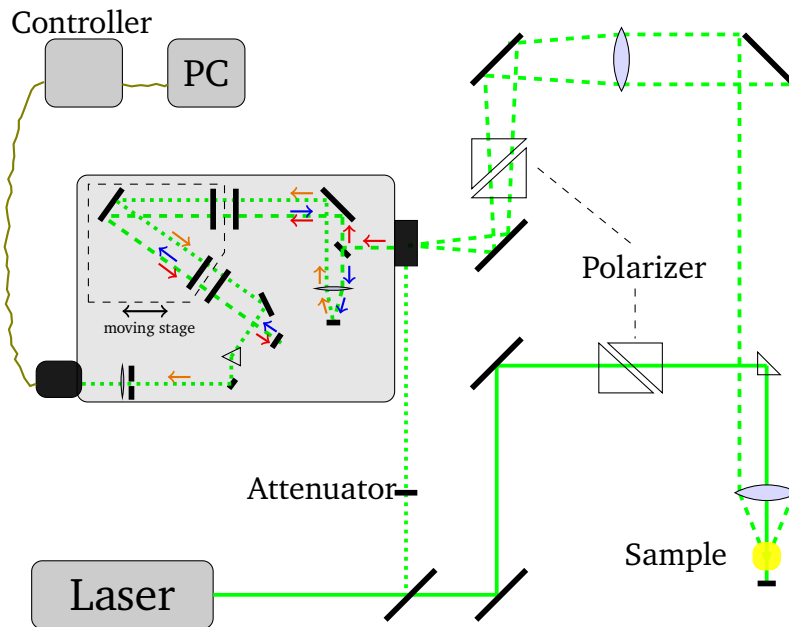


Figure 3.4.: Schematic representation of the Tandem-Fabry-Pérot setup. Inside the TFPI the optical path is simplified, each FPI is passed three times by the scattered light, as indicated by the arrows, and the wavelength is selected according to the respective mirror plate separation.

3.1.3. Raman spectroscopy

The Raman spectrometer setup was created basically from scratch as part of this work. A Horiba Jobin Yvon Raman spectrometer, type U1000, was acquired from Prof. Rößler, University of Bayreuth, with a photo-multiplier tube (PMT) and an output amplifier from the same manufacturer. The U1000 is a double monochromator, equipped with two 2400 grooves/mm gratings, and has a focal length of 2×1 m. It is designed for high stray light rejection and is therefore well suited for measurements near the laser line, which is necessary here in order to obtain overlap to the TFPI spectrum. The frequency range is scanned by tilting the gratings in such a way that only light of a specific wavelength reaches the output pinhole and is detected by the PMT. To this end, a state-of-the-art stepper motor from National Instruments was installed in the spectrometer, controllable via LAN from the computer, to move the gratings. Its power supply and the high voltage supply for the PMT were constructed and built into a common box by the electronic workshop of the institute. This box also contains the connector to set up an automatic shutter, which provides the possibility to automatically block the laser beam. Furthermore, the amplified signal from the PMT is fed into the box, which is connected to a computer through which all these functionalities can be controlled with a LabView program written during the master thesis of Stephan Bock, supervised by the present author. The PMT is cooled by a refrigerated circulator, pumping a water-alcohol mixture of 15 °C through the PMT. By this, a dark count of approximately 3 couts/s can be achieved.

The optical setup in front of the spectrometer is shown in figure 3.5. The laser is a Cobolt Samba type single frequency solid-state laser with a wavelength of 532 nm with a maximum power of 400 mW. It is passively cooled and mounted vertically so that the polarization of the emitted light is horizontal with respect to the table. This is done for the following reason: Most of the measurements with this setup are intended to be performed in depolarized geometry, and since only vertically polarized light can pass the spectrometer due to the orientation of the gratings, the least optical components are needed when operating in horizontal-vertical (HV) geometry. This is identical to the VH-geometry used in TFPI, and PCS measurements [155]. In cases where a VV-geometry should be used, a $\lambda/2$ plate is introduced into the beam, adjusted in such a way that the polarization is rotated by 90°. Thus, the laser is first passed through a polarizer selecting horizontally polarized light and then directed via mirrors from the optical table up to the height of the entrance of the Raman spectrometer. All other optical components are mounted at this height on a specifically designed mounting plate manufactured by the mechanical workshop of the institute. It consists of two parts, where one part holds the sample oven and is detachable for cases where instead of an oven, a cryostat should be used. As described above, the oven holds standard cuvettes and is constructed similar to the one used at the TFPI setup. The cryostat is the same one used for TFPI measurements; however, due to the different heights of the beam path of these two experiments, a different mounting had to be constructed to use it at the Raman setup, which was also built by the mechanical workshop. The laser beam is deflected by a prism and focused by a lens onto the sample. The scattered light is collected by the same lens in backscattering geometry and then focused by another lens onto the entrance slit of the Raman spectrometer after passing a polarizer selecting vertically polarized light. The focal length of this lens is chosen so that the first mirror at the back of the spectrometer is fully illuminated. When needed, additional optics can be inserted easily into

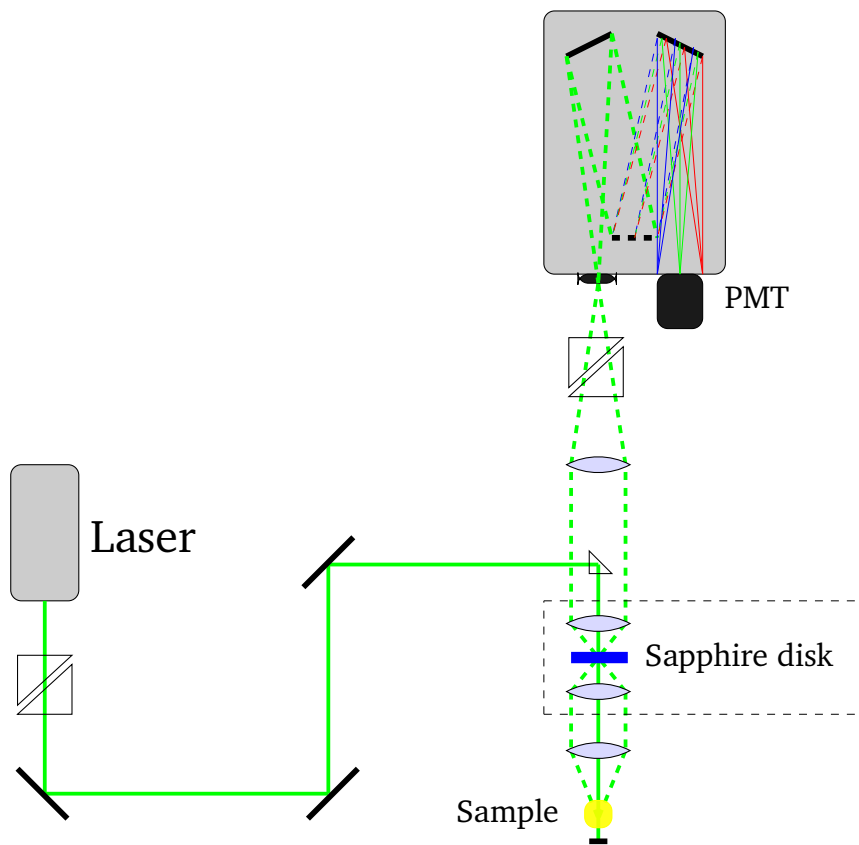


Figure 3.5.: Schematic representation of the Raman setup. Inside the U1000 the optical path is simplified and only one diffraction grating is indicated, while there are actually two.

the beam path between the prism and the lens near the sample, as indicated by the dashed lines in figure 3.5 by a quick-mount mechanism. These consist of a sapphire window and two lenses and can be used as an external intensity standard in the following way, which is adapted from reference [173]: By employing the two lenses on each side of the sapphire window in such a way that it is located in the focal point of both lenses, the spectrum of sapphire is recorded alongside with the one of the sample. Such measurements can then be normalized to the height of a sapphire Raman line, resulting in spectra that can be safely compared in intensity. This might otherwise not be the case since a drift in the laser intensity or drift in the room temperature can influence the intensity of subsequently measured spectra. These sources of error are eliminated when the sapphire window is used as an external standard. In figure 3.6, two example measurements are compared, where in one case, no sample was present, i.e., only the Raman lines of sapphire show up, and in the other one, cyclohexane was measured.

This comparison makes it immediately clear which lines in the cyclohexane spectrum are due to sapphire and thus could be used for normalization. It is then possible to subtract the sapphire measurement from the data and end up with a spectrum of only cyclohexane, normalized in

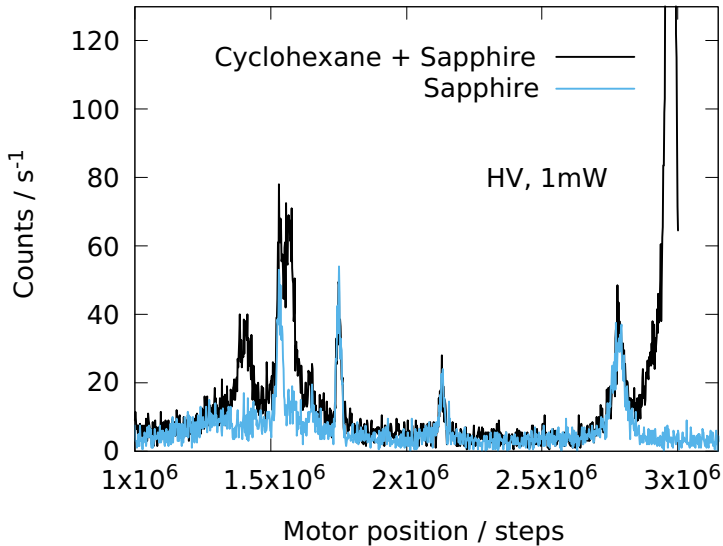


Figure 3.6.: Comparison of a spectrum of the sapphire disk without any sample and with cyclohexane.

intensity to the external standard.

Furthermore, cyclohexane is used for calibration of the position of the stepper motor to actual frequencies. This is done by obtaining a cyclohexane spectrum over the whole frequency range, fitting the Raman lines, and comparing the peak positions to the literature [174]. This is shown in figure 3.7, where the peak position in step units of the motor are shown on the y-axis and literature values of the wavenumber (cm^{-1}) of these peaks on the x-axis. From a linear fit, it is found that approximately 3750 steps are equal to one wavenumber. The reproducibility of this value is very good and therefore used throughout this work. The intercept of this fit depends on the relative position of the motor in respect to the laser line and has no general validity. When high precision in the absolute frequencies is needed, it has to be checked before the measurement. This is due to the following reason: After switching the laser off and on again, its wavelength is not necessarily exactly the same as before. Furthermore, if the power fails at the motor, its internal position is set to zero, no matter what it was before. Therefore, it is necessary to routinely check the motor position, which corresponds to the laser line, especially if low-frequency measurements are performed, where it is crucial to have exact frequencies. This is most easily and reliably done by massively attenuating the laser beam and measuring the reflection of an empty cuvette over the stepper motor range of the laser line. Then, everything is at hand, which is needed to calculate accurate frequencies from the stepper motor position. The laser line can also be used in the same way to obtain the resolution of the spectrometer in dependency on the size of the input and output slits.¹ This is shown in figure 3.8.

Naturally, the resolution worsens upon increasing the slit openings, and the intensity increases. Thus, one must find a compromise between the resolution and the obtained intensity individually for each measurement, depending on the specific needs. For the low-frequency

¹The line-width of the laser is specified by the manufacturer to be below one megahertz.

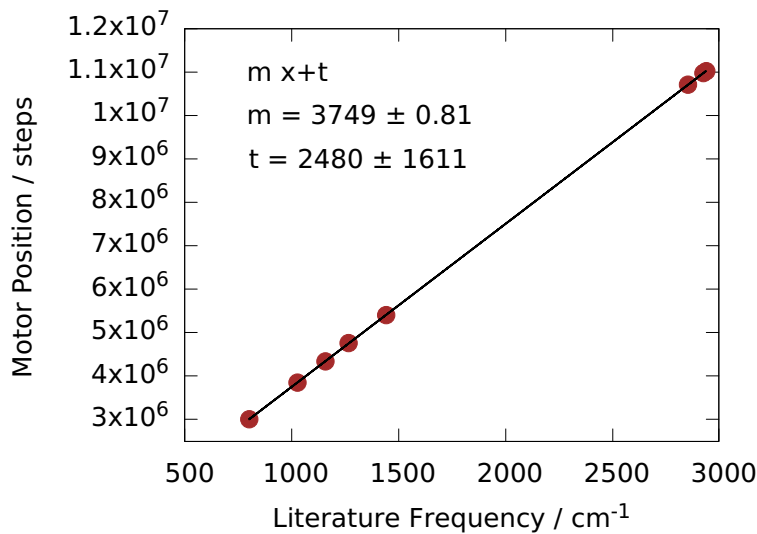


Figure 3.7.: Calibration of the stepper motor with literature values of the Raman frequencies of cyclohexane

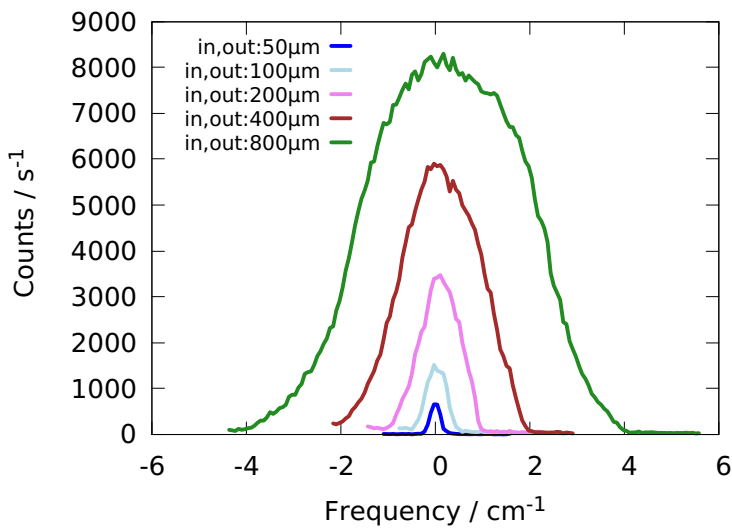


Figure 3.8.: Resolution of the Raman spectrometer at different openings of the entrance and exit slit as indicated, measured with the attenuated laser line.

measurements performed in this work, the input and output slits were set to 250 µm, for which it can be approximated by figure 3.8 that the laser line influences the spectra up to approximately 1 cm^{-1} , which corresponds to 30 GHz.

In reality, an influence can be seen up to approximately 100 GHz, so that data is used starting from this frequency on. These frequencies are still low enough to assure sufficient overlap with the TFPI spectra to form a composite spectrum.

3.2. Dielectric spectroscopy

Dielectric spectroscopy is a far more widespread experimental method to monitor the reorientational motions of molecules than depolarized light scattering. Therefore, excellent comprehensive books are available like the ones from Böttcher [175, 176] covering all details of dielectric spectroscopy. However, also the textbook of Kremer and Schönhals [177] is widely used to give an introduction into the field. Thus, these books are followed in this section unless stated otherwise.

The polarization of a material subjected to a time-dependent electrical field (Maxwell field), is given by

$$\vec{P}(t) = (\epsilon^*(t) - 1) \epsilon_0 \vec{E}(t) \quad (3.14)$$

where ϵ_0 is the vacuum permittivity and $\epsilon^*(t) = \epsilon'(\omega) - i\epsilon''(\omega)$ is the complex dielectric permittivity with the real and imaginary parts ϵ' and ϵ'' , which will be of main interest here. It is now possible to relate the macroscopic polarization to microscopic dipole moments p_i of the molecules via

$$\vec{P}(t) = \frac{1}{V} \sum \vec{p}_i(t) \quad (3.15)$$

The dipole moments p_i consists of an induced part and, in the case of polar molecules of a permanent part. The latter, usually denoted by $\vec{\mu}$, can be oriented by an external field and is thus the one of interest here. The microscopic correlation function of the permanent dipole moment can be written as

$$\Phi_\mu(t) = \frac{\langle \vec{\mu}_i(0) \cdot \sum_{j=1}^N \vec{\mu}_j(t) \rangle}{\langle \vec{\mu}_i(0) \cdot \sum_{j=1}^N \vec{\mu}_j(0) \rangle} = \frac{\langle \vec{\mu}_i(0) \cdot \vec{\mu}_i(t) \rangle + \langle \vec{\mu}_i(0) \cdot \sum_{j \neq i}^N \vec{\mu}_j(t) \rangle}{\langle \vec{\mu}_i(0) \cdot \sum_{j=1}^N \vec{\mu}_j(0) \rangle} \quad (3.16)$$

These microscopic fluctuations of the dipole moments can be related to the complex dielectric permittivity in the frequency domain in the following way:

$$\frac{\epsilon^*(\omega) - \epsilon_\infty}{\Delta\epsilon} = \int_0^\infty \frac{d\Phi_\mu(t)}{dt} e^{-i\omega t} dt = 1 - i\omega \int_0^\infty \Phi_\mu(t) e^{-i\omega t} dt \quad (3.17)$$

There, ϵ_∞ is the high-frequency limit of the real part of the permittivity and is determined by the induced polarizability. It is related to the refractive index via $n^2 = \epsilon_\infty$. $\Delta\epsilon = \epsilon_s - \epsilon_\infty$ is the dielectric strength, and ϵ_s is the static permittivity, i.e., the low frequency limiting value of the real part of the permittivity. Thus, a connection between the microscopic reorientational dynamics of the dipole moments to the macroscopic complex permittivity, which is measured in experiments as detailed below, is established. However, a comment on the dipole correlation function is in order:

The first term on the right-hand side equation 3.16 is the self part of the correlation function since the same dipole moment is correlated with itself at different times. The second term is the cross-correlation part, where different dipole moments are correlated. Usually, dynamical cross-correlations are neglected when considering dielectric spectra. This is done because it is usually argued that the cross-correlations relax on equal time scales as the self part [178]. It

will, however, be shown in section 4.2 that this view is an oversimplification and is not valid in general.

The fact that *static* orientational cross-correlations can have a large impact on the dielectric spectra is well known and accounted for in the Kirkwood-Fröhlich equation by introducing the Kirkwood correlation factor g_K :

$$g_K \mu_{\text{gas}}^2 = \frac{9\epsilon_0 k_B T M_{\text{mol}}}{N_A \rho} \frac{(\epsilon_s - \epsilon_\infty)(2\epsilon_s + \epsilon_\infty)}{\epsilon_s(\epsilon_\infty + 2)^2} \quad (3.18)$$

where M_{mol} is the molecular weight and ρ the density of the substance under study. This means that the apparent dipole moment of a liquid, calculated from the measured ϵ_s and ϵ_∞ , might differ from the one obtained in the gas phase by a factor $\sqrt{g_K}$, which arises due to orientational cross-correlation in the dense medium. It is instructive to consider the Kirkwood factor as a function of the angle between pairs of molecules θ_{1j} , i.e.

$$g_K = 1 + \sum_{j \neq 1} \langle \cos(\theta_{1j}) \rangle \quad (3.19)$$

From this equation, it is clear that g_K values obtained from experiments are usually compared with unity to determine whether the dipole moments tend to align parallel or anti-parallel. This is because $g_K > 1$ in the case of $\langle \cos(\theta_{1j}) \rangle$ being positive, i.e. when pairs of dipoles have a trend to orient parallel, and $g_K < 1$ implies the trend to orient anti-parallel as $\langle \cos(\theta_{1j}) \rangle$ is negative. However, it was shown in recent developments of the theory by Pierre-Michel Déjardin that this picture is an oversimplification since it neglects the contribution of induced dipole moments [49].

It should be noted that although up till now, only the complex permittivity is considered, other data representations are often used, especially for ionic liquids. These are the complex conductivity and the complex dielectric modulus, which, however, can be calculated from the complex permittivity via

$$\epsilon^*(\omega) = \frac{\sigma^*(\omega)}{i\epsilon_0\omega} = \frac{1}{M^*(\omega)} \quad (3.20)$$

Thus, no new information is contained in these representations, but some features will be seen more easily in one or the other, as discussed below in detail. For example, in the case of conducting materials, the DC-conductivity can directly be read off the plateau showing up in $\sigma'(\omega)$. Then, it is directly clear from equation 3.20 that this DC-conductivity appears in the dielectric loss as $\epsilon''(\omega) = \sigma_{DC}/(\epsilon_0\omega)$, which in highly conducting materials, like ILs, results in the fact that this contribution overshadows relaxational processes. Furthermore, a parasitic effect called electrode polarization is present in the dielectric spectra of conducting materials. It arises due to the separation of charges, blocking the electrodes of the sample capacitor, which leads to a large polarization, showing up at low frequencies and causes values in $\epsilon^*(\omega)$, which are often several orders of magnitude higher than relaxational processes. It is possible to a certain degree to shift the electrode polarization to lower frequencies, thus covering less of the relaxation spectrum, by choosing a sample capacitor with a larger plate spacing and polishing the plates.

The dielectric spectra are measured in this work utilizing an impedance analyzer from Novocontrol Technologies GmbH & Co. KG, the so-called Alpha-Analyzer. The sample is contained in a custom-made stainless steel plate capacitor, where two different types are used. One can be sealed airtight and is therefore suited for measurements of volatile substances. The other type consists of two polished stainless steel electrodes spaced by a quartz glass ring, and it thus easily polished, which makes it suitable for measurements of ILs.

Using a sinusoidal electric field, the complex impedance $Z^*(\omega)$ of the sample cell is measured by the Alpha-Analyzer, which can be transformed to the complex permittivity via

$$\epsilon^*(\omega) = \frac{1}{i\omega Z^*(\omega)C_0} \quad (3.21)$$

where C_0 is the capacitance of the empty cell. In this way, dielectric spectra are obtained in the frequency range of 1×10^{-2} Hz to 1×10^7 Hz. The temperature was controlled utilizing a Novocontrol Quatro cryosystem.

High-pressure dielectric measurements were performed in the laboratory of Marian Paluch, University of Katowice. A Teflon-shrouded, polished stainless steel capacitor was used with an electrode distance of $50 \mu\text{m}$, kept by a kapton spacer. The sample was placed inside a high-pressure chamber and compressed by a Unipress setup utilizing silicone oil. The high-pressure chamber was located inside a Weiss fridge for temperature control. The maximum pressure was limited by the crystallization of the silicon oil and was thus dependent on temperature.

Before concluding this section, a comment on the comparison of dielectric and depolarized light scattering data is in order [179]. Since both methods have access to the reorientational dynamics of the molecules, as can be seen by equations 3.6 and 3.17, this is possible in principle. However, differences in the spectra are expected since a vectorial quantity (the permanent dipole moment) is probed in dielectric spectroscopy and a tensorial quantity (the polarizability) in light scattering. Thus, the single-molecule reorientational correlation functions related to both experiments can be expressed as

$$C_\ell(t) = \langle P_\ell(\cos \theta(t)) \rangle \quad (3.22)$$

where P_ℓ is the Legendre polynomial of rank ℓ and $\ell = 1$ for dielectric spectroscopy and $\ell = 2$ for light scattering, respectively. Since there are no general relations between these two correlation functions, only considerations dependent on the motional mechanism of the observed dynamics can be made. For example, the ratio of the correlation times τ_1/τ_2 is three for the case of isotropic rotational diffusion, while it is unity for random large angle jumps [155]. However, it was found that under circumstances $\tau_1/\tau_2 = 1$ holds in both cases [180]. A factor of three can also be found between the relaxation strength of both methods if small angle rotations are present like it is the case for secondary processes [181, 182, 183]. It should, be noted that some assumptions are underlying these considerations, like, for example, that the dipole moment is oriented along the principal axis of the polarizability tensor. Also, only the single-molecule correlation functions are considered, and it will be seen later that cross-correlations can have an even larger impact on the spectra than the one due to the $\ell = 1, 2$ difference.

On the experimental side, it is crucial for the comparability of spectra obtained by different techniques that the temperature in the experimental setups match. Therefore, great care is

taken to calibrate the sample temperatures of the different setups in respect to each other. This is done by placing PT100 temperature sensors, calibrated against each other, inside the respective sample cell and recording the sample temperature in dependency of the set temperature over the whole temperature range. In this way, a compatibility of the temperatures of the different setups within ± 0.5 K is achieved.

3.3. Differential scanning calorimetry

The aim of differential scanning calorimetry (DSC) measurements is to obtain the temperature-dependent amount of energy, which is released (exothermic reaction) or taken up (endothermic reaction) by a sample, for example, during a phase transition. This is usually done by scanning the temperature of interest linearly, either during a heating or a cooling run. To this end, the commercial power compensated DSC apparatus DSC8000 from PerkinElmer is used in this work. The sample, which is contained in an aluminum sample pan, is placed in the sample furnace, and an empty pan in the reference furnace. If, during the predefined measurement protocol, a difference between the temperatures of the furnaces is detected, differential thermal power is used to retain the desired sample temperature [184]. The amount of this thermal power $\Delta P(T)$ is recorded in dependence of the temperature and also called the heat flow from or to the sample. From that, the specific heat capacity trace of the sample can be calculated via

$$c_p(T) = \frac{\Delta P(T)}{m q} \quad (3.23)$$

where m is the sample mass and q is the heating or cooling rate. In order to obtain meaningful results in this way, several measures must be taken.

At first, it has to be assured that the recorded heat flow is entirely determined by the sample, i.e., that it is not influenced by the sample pans or by some contribution inherent to the apparatus. Therefore, an empty pan measurement is performed with the same measurement protocol as the sample measurement and subtracted from the latter. Since the empty pan measurement will rarely have the exact same slope as the sample measurement, this is accounted for in the following way: Isothermal steps of 3 minutes are performed before and after each temperature scan. Then, after subtracting the empty pan data from the sample measurement, the isothermal steps before and after the scanning should be identical. Since this is usually not the case, a linear interpolation between these points is performed and then subtracted from the data, thus rectifying the difference in slope between the sample and the empty pan measurement. This procedure is also implemented in the same way in the DSC software, as ensured by consulting with a PerkinElmer employee.

Furthermore, in order to obtain correct heat capacity traces via equation 3.23, a calibration of the instrument has to be performed properly. On the one hand, this includes the calibration of the temperature and, on the other hand, the calibration of the heat flow. This could also be done in the PerkinElmer software. However, it is done in this work via a Python script for the following reasons: The calibration procedure in the DSC software is quite tedious and has to be performed for each heating/cooling rate one wants to use separately. Since five of them are used here for each sample, for reasons detailed later, and the calibrations have to be switched manually upon changing the cooling/heating rate, this is rather impractical for the measurements intended here. To this end, cyclohexane is measured as a standard each time when starting a new measurement series. Cyclohexane has a solid-solid transition at 186.09 K with a change in enthalpy of $\Delta H = 79.58 \text{ J/g}$ and a melting point of 279.69 K.² By comparing these transition temperatures with the one measured for each cooling/heating rate, linear

²These values are adapted from the PerkinElmer software

calibration laws are obtained over a large temperature range, which is used in the subsequent measurements to correct the temperatures. The heat flow is calibrated by comparing the area of the solid-solid transition peak divided by the sample mass to the literature ΔH value. In this way, properly calibrated heat capacity traces are obtained from the raw data.

On the experimental side, all measurements were performed with hermetically sealed sample pans manufactured by TA Instruments since they showed superior behavior in baseline noise and reproducibility than the one from PerkinElmer. The DSC apparatus is equipped with a liquid nitrogen cooling system, and ultra-pure helium (99.999%) was used as a purge gas, which together gives access to temperatures down to approximately 120 K.

The main focus of the DSC measurements in this work is the glass transition step, which occurs when the relaxation dynamics of a liquid become slower than the time defined by the cooling rate, i.e., the liquid falls out of equilibrium and is considered as glassy below this step. Thus, it can be considered freezing of rotational and translational dynamics. This is seen as a decrease in c_p since these dynamic degrees of freedom no longer contribute to the heat capacity. However, common practice is to evaluate the glass transition step upon heating, and this is also done in this work. Most often, the only information deduced from such measurements is the glass transition temperature, which can be defined in several ways, as discussed below. When comparing this temperature to dynamic data, e.g., from dielectric measurements, it is common practice to assign a relaxation time of 100 s to the glass transition temperature. Often, the dielectric α -relaxation time is then in good accordance with this value at that temperature [185]. However, it must be noticed that the value of 100 s is arbitrary, and also sometimes 1000 s is used instead [186]. Contrary, it is also possible to deduce actual calorimetric time constants from cooling rate-dependent DSC measurements. One of these methods is the one by Hodge, based on the following equation [187]:

$$\tau_{\text{Hodge}} = \frac{R T_g^2}{q_c \Delta E_a} \quad (3.24)$$

where R is the gas constant and ΔE_a is the apparent activation energy, which is usually obtained by a fit of

$$\ln q_c = A - \Delta E_a / (R T_g) \quad (3.25)$$

to the glass transition temperatures measured at different cooling rates q_c [188, 189]. Thus, it is possible with this model to obtain calorimetric time constants by just measuring the glass transition temperature in dependency of different cooling rates. The fact that the glass transition temperature varies upon changing the cooling rate is immediately clear from the origin of the glass transition step mentioned above, i.e., that the relaxation time of the liquid becomes slower than the time scale defined by the cooling rate. Thus, the T_g will be higher for higher cooling rates and vice versa. However, several definitions of how T_g should be deduced from a measured glass transition step exist. Some of them are indicated in figure 3.9 on an example of a glass transition step. The black lines are fits to different regions of the heat capacity trace, and the intersection points of these lines mark the different definitions of T_g . An exception is T_g^{half} , which is defined as located at the increasing part of the step at the half-height between the glass and the liquid line. The fictive temperature T_f , sometimes also used as a definition for T_g , is explained below. Since it is not a priori clear which of the T_g definitions

should be used in equation 3.24 (Hodge uses T_g^{half}), the results for the different T_g are shown in the insets of figure 3.9. In the upper inset, the determination of the activation energies via equation 3.25 are shown. The different symbols represent the different T_g definitions as indicated in the main panel. In the lower inset, the solid symbols are the calorimetric time constants calculated via equation 3.24 for the different T_g definitions. It is clear that they are located at dramatically different positions in the Arrhenius plot. This renders this approach too arbitrary to compare these values of τ_{cal} with those obtained from different experimental methods.

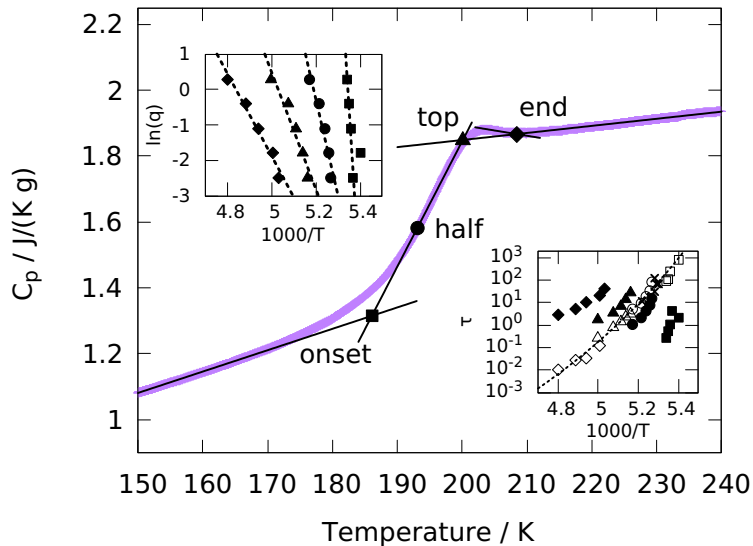


Figure 3.9.: Glass transition step with different definitions of the glass transition temperature indicated by different symbols. Upper inset: Cooling/heating rate dependent values of the glass transition temperatures. Dashed lines are fits with equation 3.25. Lower inset: Calorimetric time constants from the Hodge equation (equation 3.24, solid symbols) and from the TNMH model (equation 3.27, open symbols). Dashed line is a VFT-fit (equation 2.7).

Another approach, however, yields consistent correlation times for all definitions of T_g , which are shown as open symbols in the lower inset of figure 3.9, and which are located on a single VFT curve. This model, proposed by Tool, Naranayashwamy, Moynihan, and Hodge (TNMH) [190, 191, 192, 193] is described in the following:

As a first step, the temperature-dependent fictive temperature $T_f(T)$ has to be obtained from the experimental data. The fictive temperature can be thought of as the temperature at which a supercooled equilibrium liquid would have the same structure as the out-of-equilibrium glass under consideration. Here, T_f is obtained via Moynihan's area matching method, which is given by

$$\int_{T^*}^{T_f} (C_{pl} - C_{pg}) dT'_f = \int_{T^*}^T (C_p - C_{pg}) dT' \quad (3.26)$$

where T^* is any temperature above the glass transition in the equilibrium region, and T' is any temperature well below the glass transition [194]. The heat capacities of the glass $C_{p_g}(T)$ and the liquid $C_{p_l}(T)$ are obtained by fits to the respective region and extrapolated beyond these regions. The method is visualized in figure 3.10. Figuratively speaking, the fictive temperature is found by moving the vertical line, denoted with T_f , horizontally until the sum of the green shaded areas is equal to the blue shaded area. The temperature where this is the case is the fictive temperature.

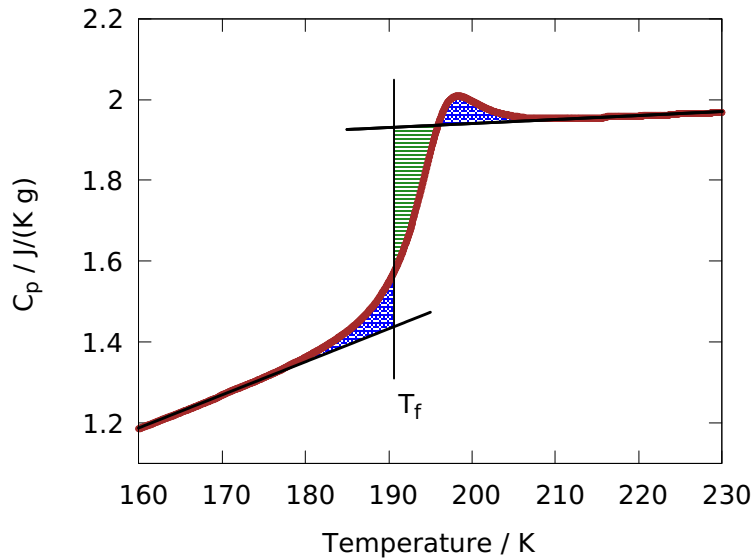


Figure 3.10.: Visualization of Moynihan's area matching method for determination of the fictive temperature T_f .

When determining $T_f(T)$, i.e. changing the integration limit on the right hand side in equation 3.26 starting from high temperatures in the equilibrium liquid, it is clear that $T_f(T) = T$ and this changes when T reaches the glass transition step. Finally, in the glassy state $T_f(T) = \text{const.}$ Now, the TNMH-model, which is an application of the Boltzmann superposition principle [193], and which is given by

$$T_{f,n} = T_0 + \sum_{j=1}^n \Delta T_j \left[1 - \exp \left[- \left(\sum_{k=1}^n \frac{\Delta T_k}{q \tau_k} \right)^{\beta_{\text{TNMH}}} \right] \right] \quad (3.27)$$

can be fitted to the fictive temperature in dT_f/dT representation, which can be regarded as a normalized, dimensionless heat capacity representation. In eq. 3.27, T_0 is a starting temperature above the glass transition, from which the temperature is decreased with steps of size ΔT to below the glass transition and subsequently increased again to T_0 . Only the heating process is fit to the experimental heating curve. The non-exponentiality of the relaxation process is accounted for by the stretching exponent β_{TNMH} and the correlation time at step k is given by [195]

$$\tau_k = \tau_0 \exp \left[\frac{x\Delta E_a}{R T_k} + \frac{(1-x)\Delta E_a}{R T_{f,k-1}} \right] \quad (3.28a)$$

$$= \tau_g \exp \left[\frac{x\Delta E_a}{R T_k} + \frac{(1-x)\Delta E_a}{R T_{f,k-1}} - \frac{\Delta E_a}{R T_g} \right] \quad (3.28b)$$

where x is the non-linearity parameter , τ_0 is the Arrhenius prefactor and τ_g is the correlation time at temperature T_g . The advantage of eq. 3.28b over the more common eq. 3.28a is as follows: While both equations incorporate an Arrhenius-type behavior of the correlation time τ_k , which is a good approximation in a narrow temperature range around the glass transition temperature, it leads to an unphysical low value of τ_0 , which is the high temperature limiting value of τ_k . This also leads to very unstable fits. These shortcomings can be circumvented by using eq. 3.28b. By inserting the third term in the exponential function, τ_0 is replaced by the correlation time τ_g at the reference temperature T_g . This readily provides the calorimetric correlation time at the glass transition temperature. When inserting the different values of T_g marked in figure 3.9 as full symbols, the τ values shown as open symbols in the lower inset of the same figure are obtained, as mentioned above. Since they are all located on a single VFT-curve (eq. 2.7), they are independent of the choice of the T_g definition used. Thus, this procedure is used to obtain calorimetric time constants throughout this work.

3.4. Quantum chemical calculations

Quantum chemical calculations are used in this work as a tool to compute the polarizability tensor of molecules mainly. From that, the optical anisotropy of a molecule is readily obtained, which is decisive for the intensity of light scattered from this kind of molecular liquid. It should be emphasized that only single molecular, gas-phase polarizabilities are obtained via such calculations in this work. Mainly density functional theory (DFT) methods are used, which are well established and readily available in free software packages, such as ORCA [196, 197], that was used in this work. Only a brief overview of the theoretical aspects of such calculations should be given below since the calculations are used only as a tool for obtaining the desired molecular information. The presentation below follows the textbook of Koch and Holthausen [198] unless stated otherwise.

When a molecule is subjected to an external electrical field \vec{F} , its energy E will change as the charge density responds to the applied field. Since the polarizability is a measure of how easy the field distorts the charge density, it is instructive to write the energy of the system as a Taylor expansion

$$E(\vec{F}) = E(0) + \sum_i \frac{\partial E}{\partial F_i} \Big|_0 F_i + \frac{1}{2} \sum_{i,j} \frac{\partial^2 E}{\partial F_i \partial F_j} \Big|_0 F_i F_j + \dots \quad (3.29)$$

where higher order terms, including hyperpolarizabilities are omitted for the sake of brevity. The first and second partial derivatives are the dipole moment and the polarizability, respectively, i.e.

$$\mu_i = - \frac{\partial E}{\partial F_i} \Big|_0 \quad \text{and} \quad \alpha_{ij} = - \frac{\partial^2 E}{\partial F_i \partial F_j} \Big|_0 \quad (3.30)$$

where the values are taken at zero field, i.e. the static values.

The first step - and the main goal in quantum chemical calculations - is thus to find the ground state energy of the system. This could, in principle, be done by solving the time-independent Schrödinger equation

$$\hat{H} \Psi_0 = E_0 \Psi_0 \quad (3.31)$$

where the Hamilton operator \hat{H} can be written in the Born-Oppenheimer approximation as

$$\hat{H}_{\text{elec}} = -\frac{1}{2} \sum_{i=1}^N \nabla_i^2 - \sum_{i=1}^N \sum_{A=1}^M \frac{Z_A}{r_{iA}} + \sum_{i=1}^N \sum_{j>1}^N \frac{1}{r_{ij}} = \hat{T} + \hat{V}_{\text{ext}} + \hat{V}_{ee} \quad (3.32)$$

There, Z_A are the charges of the M nuclei, and r are the distances between nuclei and electrons or between the N electrons, respectively. The approximation made here is that the electrons move in the field of fixed nuclei since the electron mass is markedly lower than that of a nucleus. In wave function-based methods, approximations are induced to handle the N -electron wave functions Ψ_0 . For example, in the famous Hartree-Fock (HF) method, Ψ_0 is approximated by an antisymmetric product of N one-electron wave functions, known as the Slater determinant. In contrast, DFT methods make use of the two Hohenberg-Kohn theorems, which state that the external potential $V_{\text{ext}}(\vec{r})$ is a unique functional of the electron density $\rho(\vec{r})$ and that the functional $G[\rho]$ that gives the ground state energy of the system, delivers the lowest energy if

and only if the input density is the true ground state density ρ_0 . However, although with these theorems at hand, the $3N$ spatial variables of the N -electron wave function reduce to 3 spatial variables in the case of the electron density and the ground state energy could be found via the variational principle, no hint is given how the functional that delivers the ground state energy can be constructed. Therefore the Kohn-Sham approach is used:

The functional $G[\rho(\vec{r})] = T[\rho(\vec{r})] + J[\rho(\vec{r})] + E_{\text{ncl}}[\rho(\vec{r})]$ contains the kinetic energy, the classical Coulomb interaction and the non-classical part due to self-interaction correction, exchange and electron correlation effects. Since only the Coulomb-term is known, Kohn and Sham set up a non-interacting reference system in order to be able to calculate at least a portion of the kinetic energy exactly, whereas the deficit between the true kinetic energy T and the non-interacting kinetic energy T_S , which is denoted as T_C , is incorporated into the exchange-correlation energy $E_{\text{XC}}[\rho(\vec{r})] = T_C[\rho(\vec{r})] + E_{\text{ncl}}[\rho(\vec{r})]$. The resulting Kohn-Sham equation, which has to be solved iteratively with the so called self-consistent field (SCF) technique, reads

$$\left(-\frac{1}{2} \nabla^2 + \left[\int \frac{\rho(\vec{r}_2)}{r_{12}} d\vec{r}_2 + V_{\text{XC}}(\vec{r}_1) - \sum_A^M \frac{Z_A}{r_{1A}} \right] \right) \varphi_i = \epsilon_i \varphi_i \quad (3.33)$$

where $\varphi_i(\vec{r})$ are the orbitals of the non-interacting system, with $\sum_i^N \sum_s |\varphi_i(\vec{r}, s)|^2 = \rho_0(\vec{r})$ and $V_{\text{XC}} = \partial E_{\text{XC}} / \partial \rho$. All that is unknown is contained in the exchange-correlation functional $E_{\text{XC}}[\rho]$, and it is the goal of different DFT approaches to find approximations to that functional which give highly accurate ground-state energies with respect to experimental values. Probably the most commonly used is the hybrid-functional called B3LYP, which is also used in this work, where the letters stand for the name of the authors and the number 3 for three semiempirical coefficients used to weight different contributions as there are the exchange part by Becke and the correlation functional by Lee, Yang, and Parr. It is called a hybrid functional since a portion of the exchange energy is calculated exactly via the HF approach.

Although it would be possible to solve equation 3.33 numerically, this procedure is too demanding, and thus, the Kohn-Sham orbitals are linearly expanded with a set of L basis functions η_μ , which are usually Gaussian-type orbitals:

$$\varphi_i = \sum_\mu^L c_{\mu i} \eta_\mu \quad (3.34)$$

Thereby the optimization problem has been reduced to a linear one, where the only variables are $c_{\mu i}$ and which can be efficiently solved by computer programs. The nomenclature of basis sets should be explained on the example of the one mostly used in this study, namely def2-TZVPP. The def2 family of basis sets was developed by the Ahlrichs group in Karlsruhe, where the "def" stands for default because they are the default basis sets in the Turbomole program, and the 2 denotes the second generation [199]. "TZV" is short for triple zeta valence, meaning that each valence orbital is represented by three Gaussian functions, while the core electrons are described by only one. Polarization functions "PP" are introduced, which are functions of higher angular momentum than the valence orbital, in order to allow for distortion from the original atomic symmetry. Together, this means for the example of the hydrogen atom that three functions for the s-, 2 for the p- and 1 for the d-orbital are used [199].

Although the ground state energy of a molecule can be calculated as outlined above, it might be that the molecular geometry used is not the most stable one, i.e., there might exist a geometry that has lower energy. Therefore, starting from an initial guess geometry, obtained in this work by the program Avogadro [200], a geometry optimization is performed where the energy of repeatedly altered geometries is calculated until the change in energy meets a predefined convergence criterion. Since this is extremely time-consuming for large molecules using the B3LYP/def2-TZVPP method and since in the case of non-rigid molecules a conformer ensemble is needed, as detailed below, a different approach was chosen for the conformer search and geometry optimization, namely the so-called GFN2-xTB semiempirical tight-binding DFT model [201]. It was constructed, i.a., for the fast calculation of accurate molecular geometries for large systems. This approach is incorporated in the program CREST by Grimme and co-workers [202], where the acronym stands for Conformer–Rotamer Ensemble Sampling Tool. It automatically explores the chemical structure space of a given molecule by repeatedly performing short molecular dynamic simulation runs and geometry optimizations of the so obtained conformers and gives, as a result, an ensemble of low-energy conformers up to a chosen energy threshold, here 1 kcal/mol.

4. General aspects of rotational dynamics in non-ionic liquids

In the course of the work on ionic liquids, some general questions arose regarding the light scattering spectrum and its spectral differences to the dielectric spectrum, as already mentioned in the introduction. One of these questions is whether it is possible to deduce from the intensity of the light scattering spectrum or from parts of it the dynamics of which molecules are responsible for that particular part of the spectrum. This would be especially useful in the case of such ionic liquids, where two spectral contributions are visible in the light scattering spectrum in order to discriminate between the dynamic contributions of the ions and the aggregates. In dielectric spectroscopy, the dielectric strength of rotational processes is routinely evaluated and compared to the permanent dipole moment of the molecules, for example, via equation 3.18. In the same manner, it should be possible in principle to relate the depolarized scattering intensity of relaxation processes to the optical anisotropy of the molecules under study. Static light scattering measurements have been performed routinely in the 1960s in order to determine the shape, or more precisely, the optical anisotropy of various molecules, as will be seen below. However, primarily only the total intensity of the depolarized scattered light was considered without obtaining spectral information. In cases where spectra were measured, for example, with a TFP, this was done to separate the rotational contribution from the so-called collision-induced scattering (CIS). The discovery of the CIS mechanism leads to modification of the original equations relating the scattering intensity to the optical anisotropy of molecules. Today, it is often assumed, at least for sufficiently anisotropic molecules, that the rotation of the molecules dominates the depolarized scattered light and that CIS plays a minor role. However, different variations of the equations which relate the intensity of the scattered light to the optical anisotropy have been proposed, and it is unclear which of them should be used. Therefore, the first step in section 4.1 is to compare values of the optical anisotropy parameters from the literature, obtained with either taking CIS into account or not, to DFT-calculated optical anisotropies, to determine the equations which give experimental values in accordance with the calculated ones. Since these literature values were obtained by highly diluting the molecules under consideration, the next step is to examine the differences when considering neat liquids. To this end, a test set of 13 different non-ionic liquids are chosen, and own measurements of the intensity are compared with DFT calculations. After that, bridging the gap to ionic liquids, binary mixtures are considered, and the attempt is made to relate the intensity of the two contributions of the two molecular species to their respective anisotropy parameters.

After that, in section 4.2, a second topic concerning the rotational spectra of molecules is addressed. As discussed in section 2.1, the structural relaxation is non-exponential, and it

is known from a tremendous body of dielectric work that the stretching exponent can differ significantly among different substances. On the other hand, by comparing light scattering spectra of different liquids obtained near the glass transition temperature, it is found that they seem to exhibit similar α -relaxation shapes, although the molecules are highly different. This is surprising since a recent explanation of the dielectric shape would imply a similar behavior for the light scattering spectra [203]. Therefore, dielectric and light scattering spectra are compared for various substances, and a possible explanation of the difference in the spectra is worked out, also by considering dielectric dilution measurements of a polar substance.

4.1. The intensity of light scattered by molecular liquids

As discussed in section 3.1, it has been known for over a century that the light scattered by gas molecules is not fully polarized as it would be expected for spherical particles, [204, 139] which is explained by the anisotropy of the gas molecules. Thus, by measuring the ratio of the intensities of polarized and depolarized light, information about the shape of the gas molecules can be obtained [139]. More precisely, one can define the anisotropic part of the molecular polarizability for arbitrarily shaped molecules from the polarizability tensor (see equation 3.3) by

$$\beta = \sqrt{\frac{3}{2} [(\alpha_{xx} - \alpha_0)^2 + (\alpha_{yy} - \alpha_0)^2 + (\alpha_{zz} - \alpha_0)^2]} \quad (4.1)$$

$$= \sqrt{\frac{1}{2} [(\alpha_{xx} - \alpha_{yy})^2 + (\alpha_{yy} - \alpha_{zz})^2 + (\alpha_{zz} - \alpha_{xx})^2]} \quad (4.2)$$

where the isotropic polarizability is given by $\alpha_0 = \frac{1}{3}\text{Tr}(\underline{\underline{\alpha}})$ [205].

The relative anisotropy factor $\kappa = \frac{\beta}{3\alpha_0}$ is directly related to the ratio of the intensity of depolarized and polarized scattered light by [205]

$$\rho_{\text{VH}} = \frac{I_{\text{VH}}}{I_{\text{VV}}} = \frac{3\kappa^2}{5 + 4\kappa^2} \quad (4.3)$$

Thus, when α_0 is determined independently, e.g., via the Lorentz-Lorenz equation from refractive index measurements, the optical anisotropy β of the gas molecules is readily obtained from such intensity measurements.

The total intensity of the scattered light by molecules in the gas phase can be written as

$$I_{\text{VV}} = I_0 \frac{V}{r^2} \left(\frac{2\pi}{\lambda} \right)^4 N \left(\alpha_0^2 + \frac{4}{45} \beta^2 \right) \quad (4.4)$$

$$I_{\text{VH}} = \frac{1}{15} I_0 \frac{V}{r^2} \left(\frac{2\pi}{\lambda} \right)^4 N \beta^2 \quad (4.5)$$

where I_0 is the intensity of the incident light, V is the scattering volume, r the distance of the detector from the scattering volume, λ the wavelength of the incident light, and N the number

density of the molecules [155]. Thus, according to equation 4.5, it would be sufficient for the determination of β to measure the intensity of the depolarized scattered light. However, the experiment-specific parameters, like the scattering volume or the incident intensity, which are difficult to determine with the necessary accuracy, render this equation rather impractical. Thus, the so-called Rayleigh ratio [206]

$$R_{\text{VH}} = \frac{I_{\text{VH}} r^2}{I_0 V} = \frac{1}{15} \left(\frac{2\pi}{\lambda} \right)^4 N \beta^2 \quad (4.6)$$

is introduced, from which – by a comparison with the known Rayleigh ratio of a standard via equation 4.7 – the optical anisotropy can be obtained [207, 154].

$$R_{\text{VH}} = \frac{I_{\text{VH}}}{I_{\text{ref}}} \left(\frac{n}{n_{\text{ref}}} \right)^2 R_{\text{VH}}^{\text{ref}} \quad (4.7)$$

Since no measurements in the gas but in the liquid phase are performed in this work, the next step is to consider highly diluted solutions with an isotropic solvent like carbon tetrachloride to exclude orientational correlations between the molecules of interest.

However, when going from the gas to the liquid phase, equation 4.6 has to be modified by the contribution of the internal field, which arises due to the polarization of the surrounding molecules. Several models of the local field have been proposed, see reference [208] and references therein, but here the discussion is restrained to the one from Lorentz [209] since it seems to be the one used most often in light scattering, it only needs the knowledge of the refractive index to be calculated, and other models seem not to provide significantly different values by the expense of more parameters. However, the exponent of the local field factor is debated in the literature being either second-power [210, 211, 207] or fourth-power [212, 213, 154], which leads to a significant difference of its value.

Additionally, a finding by McTague and coworkers at the end of the 1960s caused a stir in the light scattering community [214]: They found that liquid argon scatters depolarized light and resolved the spectral broadening of the laser line with a Raman spectrometer. The same was done shortly before for gaseous argon and krypton [215]. At first glance, this seems surprising since the spherical molecules of noble gases are not expected to scatter depolarized light. However, already 40 years earlier, this was observed for gaseous argon [138], and Kielich predicted this effect for liquid argon based on his theory of molecular interactions [216]; thus, this effect is also called dipole-induced-dipole (DID) in the literature. Nevertheless, the term "collision-induced scattering" (CIS) is mostly used in later light scattering literature due to the explanation of this scattering by the distortion of the electronic structure of colliding molecules [217]. After that, most researchers in the field tried to get rid of the CIS in their measurements, thought to be present in all liquids. Therefore, either filters were used to cut out higher frequencies where the CIS was supposed to happen [218, 219, 220], or when spectra of the scattered light were recorded, a fit with a sum of two Lorentzian was employed, the narrower one attributed to the reorientation of the anisotropic molecule and the broad one attributed to CIS and thus discarded [154].

As a result of the above discussion about the internal field and CIS, equation 4.6 has to be modified for the case of anisotropic molecules diluted in an isotropic solvent, as follows:

$$R_{\text{VH}} = \frac{1}{15} \left(\frac{2\pi}{\lambda} \right)^4 \underbrace{\left(\frac{n^2 + 2}{3} \right)^m}_{\text{Lorentz local field}} N \beta^2 + R_{\text{CIS}}^{\text{VH}} \quad (4.8)$$

with $m = 2$ or $m = 4$. It has been assumed that the CIS contribution is additive to the reorientational contribution.

As a next step, when going from the dilute solution to the neat liquid, orientational correlations of the molecules have to be considered. This effect is probably best known from the work of Kirkwood on dielectric spectroscopy [221], as discussed above. In the case of light scattering, the second rank orientational parameter g_2 has to be used due to the tensorial character of the polarizability, which is given by

$$g_2 = 1 + \sum_{j \neq 1} \frac{1}{2} \langle 3 \cos^2 \theta_{1j} - 1 \rangle \quad (4.9)$$

where θ_{1j} is the angle between neighboring molecules [213]. Furthermore, when considering that if not rigid, molecules exist as different conformers, the anisotropy parameter has to be the mean value ($\langle \cdot \cdot \cdot \rangle$) of the conformer ensemble. Thus, β^2 in equation 4.8 has to be replaced by $\langle \beta_{\text{eff}} \rangle^2 = g_2 \langle \beta \rangle^2$ when considering neat liquids of non-rigid molecules.

Altogether, the most general expressions (accepting the Lorentz internal field and the additivity of the CIS contribution) of the depolarized (or anisotropic) Rayleigh ratio reads as follows:

$$R_{\text{VH}} = \frac{1}{15} \left(\frac{2\pi}{\lambda} \right)^4 \left(\frac{n^2 + 2}{3} \right)^m N \langle \beta_{\text{eff}} \rangle^2 + R_{\text{CIS}}^{\text{VH}} \quad (4.10)$$

In order to be able to use this equation, it is necessary at first to determine the exponent m and how to handle the CIS contribution. This is done in the following by comparing experimental β values of highly diluted rigid molecules from the literature to DFT-calculated values. After that, non-rigid molecules are considered to check whether averaging over calculated β -values of different conformers leads to values in accordance with experimental literature values. Finally, the influence of the g_2 correlation factor in neat liquids is discussed.

4.1.1. Comparison of DFT calculations with experiments

At first, optical anisotropy parameters obtained in the literature for rigid molecules in solution are considered, where measures were taken to exclude the CIS contribution in determining the scattering intensity used for calculating β . As mentioned above, this was done either by filters or only considering the central Lorentzian in the TFPI spectra. For each of the molecules under investigation in these studies, the β -value was determined here by DFT-calculations, as described in section 3.4. The experimental β -values are compared to the one calculated by DFT in figure 4.1, where the solid black line indicates the equality of both values $\beta_{\text{exp}} = \beta_{\text{DFT}}$.

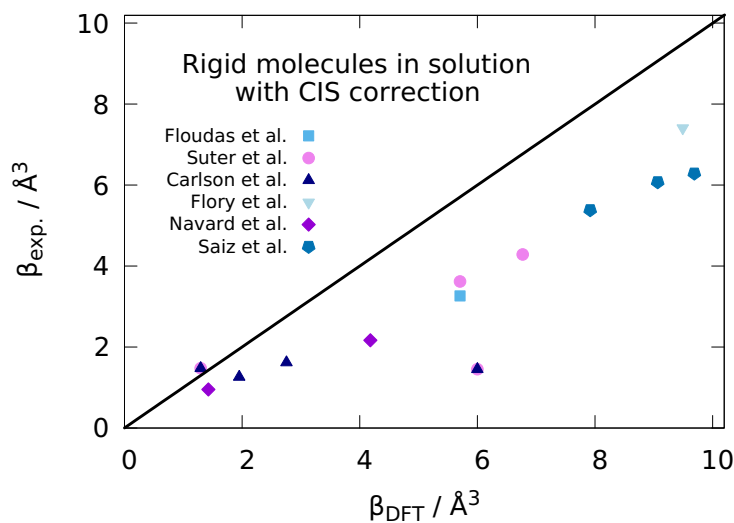


Figure 4.1.: Experimental anisotropy parameters from references [207, 219, 220, 222, 223, 224] compared to calculated ones for rigid molecules in solution where measures were taken in the experiments to exclude CIS. Black solid line indicates the equality $\beta_{\text{exp}} = \beta_{\text{DFT}}$.

As one can see, almost all of the experimental values fall below this line, and the deviation from the DFT values increases with increasing β . In all studies from which the values are shown in the figure, the authors used the quadratic Lorentz field to determine the experimental β -values. If they had used the fourth power instead, the values would have been even lower, as can be easily seen when inspecting equation 4.8. Thus, the power of the local field can not be the reason for the discrepancy. Instead, since the squared anisotropy parameter is proportional to the intensity of the scattered light, from which a portion was subtracted to account for CIS, it points into the direction that this subtraction is not justified when using equation 4.8.

Therefore, as a next step, measurements of rigid molecules in solution from literature are considered, mostly from before the 1970s, where the anisotropy parameters were calculated from the measured total depolarized scattering intensity, without subtracting any contribution from CIS, i.e., $R_{\text{CIS}}^{\text{VH}} = 0$ in equation 4.8. The parameters are shown again against the values from DFT calculations in Figure 4.2.

The experimental and calculated anisotropy factors agree very well over a large range of

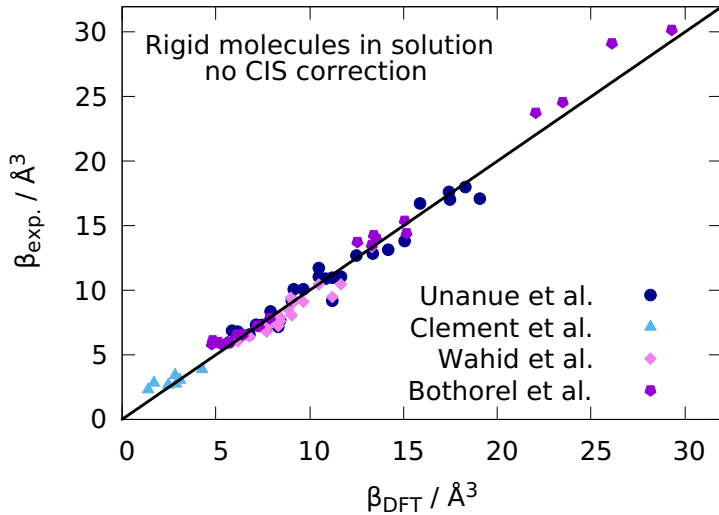


Figure 4.2.: Experimental anisotropy parameters from references [225, 226, 227, 228, 229, 230, 231] compared to calculated ones for rigid molecules in solution where no measures were taken in the experiments to exclude CIS. Some values from Bothorel *et al.* are outside the plot range and are up to 100% higher than the calculated ones. It is assumed that these substances were not fully dissolved.

different substances, from almost isotropic to highly anisotropic ones. Thus in setting $R_{\text{CIS}}^{\text{VH}} = 0$ in equation 4.8, a markedly better agreement of the experimental and calculated β values can be obtained than by subtracting some portion of the intensity which is assumed to arise from CIS. The power of the local field factor used in these studies from literature is most probably quadratic, although this is indicated explicitly only in the work of Wahid, but assumed to be the case also in the other references due to the common practice at that time and due to the agreement with the values of Wahid. Hence, through the comparison of experimental anisotropy parameters of 136 molecules (including the one shown later in figure 4.3) with DFT calculations, it got clear that $m = 2$ and $R_{\text{CIS}}^{\text{VH}} = 0$ should be used when calculating β -values from depolarized scattering intensities with equation 4.8.

Of course, most molecules are not rigid, i.e., they have one or more rotatable bonds, especially the cations of the ILs under investigation in this work are highly flexible. Therefore, it should be checked whether it is also possible to obtain calculated β -values in accordance with experimental values for non-rigid molecules. These molecules will exist as different conformers, whose population p_i is related to their respective difference in energy ΔE_i to the lowest energy conformer via [202, 232]

$$p_i = \frac{\exp(-\Delta E_i/(RT))}{\sum_{j=1}^{n_{\text{CE}}} \exp(-\Delta E_j/(RT))} \quad (4.11)$$

where n_{CE} is the number of different conformers in the ensemble. Thus, the intensity of the

depolarized scattered light might be considered as stemming from a mixture of different conformers with different number densities and β values, or, equivalently, a mean anisotropy factor for the ensemble could be defined via

$$\langle \beta \rangle = \sum_i^{n_{CE}} p_i \beta_i \quad (4.12)$$

The difficulty in calculating the $\langle \beta \rangle$ value is twofold: At first, one has to identify the lowest energy conformer, and then, the relative energies ΔE_i of the other conformers have to be determined. Especially the first point is crucial, and erroneous identification of one conformer as the lowest in energy can lead to a completely different $\langle \beta \rangle$ value. Therefore, great efforts must be made to determine a correct conformer ensemble. This is done, for example, in great detail in reference [233] for the case of phenyloctane, which is one of the non-ionic molecules considered below. Because it is impossible to do such a detailed analysis for all molecules of this work, the automatic conformer search tool CREST is used as mentioned in section 3.4. This means that full reliance is placed on CREST for the accuracy of the conformer ensemble, i.e., the correct determination of the lowest energy conformer and the correct relative energies of the other conformers in respect to it. Anisotropy parameters $\langle \beta \rangle$ for 52 non-rigid molecules calculated using equations 4.11 and 4.12 are compared to experimental values obtained in solution in figure 4.3, where again the solid black line represents the equality of experimental and calculated values. Alkanes or substituted alkanes are explicitly excluded from this comparison for reasons detailed later.

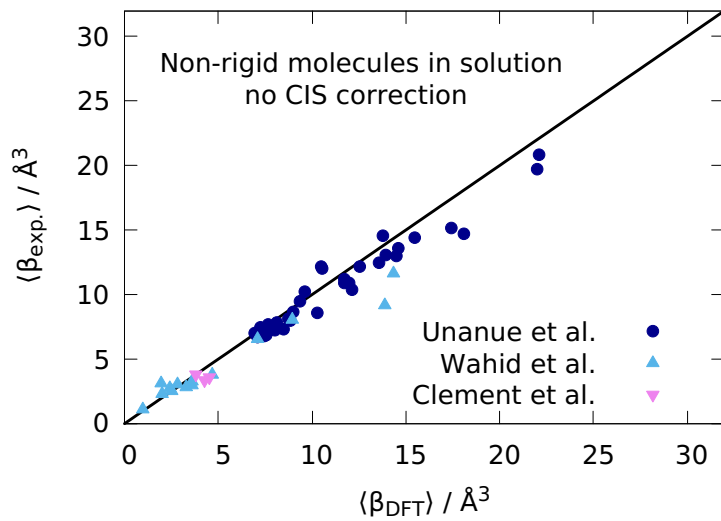


Figure 4.3.: Experimental anisotropy parameters from the literature [225, 234, 226, 228, 229, 230, 227] compared to calculated ones for flexible molecules in solution where no measures were taken in the experiments to exclude CIS.

One can see that the agreement between experiment and calculation is quite good, however not as good as for rigid molecules, as is easily seen by comparing Figures 4.2 and 4.3. This means

that this procedure is, in principle, suited for calculating the anisotropy parameters of non-rigid molecules. However, the molecules contained in figure 4.3 have not too many rotational bonds with a maximum of 9. Therefore, it could be expected that the accuracy of the calculated $\langle \beta \rangle$ worsens further upon increasing the complexity of the molecules. Additionally, for some flexible molecules, the calculated and the experimental anisotropy values can not be brought into accordance at all. This holds for the family of linear n-alkanes, which are discussed in appendix B to show that not only some caution has to be paid when comparing calculated and experimental anisotropies, but also that for these molecules, the scattering mechanism seems to be different than for other molecules. Nevertheless, for most of the molecules in solution, the agreement between the experiment and DFT calculations is quite good.

Until now, only molecules in solutions have been considered, and thus, as a next step, the experimental β -values from the test set of 13 non-ionic neat liquids should be compared to the calculated values in the following. The measurements on those neat liquids were performed in two different ways: On the one hand, the total scattering intensity in VH geometry was measured with a PCS setup, similar to the one described in section 3.1.1, but with an index matching bath and a laser operating at 633 nm. The intensity was measured three times for 100 s, and between each measurement, the cuvette was rotated. In this way it was assured that no scratch on the cuvette surface might be located in the laser beam and thus influence the measured intensity. In rare cases where a peak in the intensity was observed, indicating a dust particle going through the scattering volume, the measurement was discarded and repeated. The intensity was averaged over the three runs, and the mean dark count rate was subtracted to yield the final scattering intensity, from which the anisotropy parameters were calculated. On the other hand, the intensity was measured by combining the TFPI and the Raman setup, i.e., this is the first step towards connecting the scattering intensity with the dynamic information. In order to be able to obtain correct relative intensities, measurements with a single mirror spacing of the TFPI were performed for several liquids directly in a row, without any change of the setup, especially with the very same stabilization of the TFPI. If the measurements were continued the other day, a substance from the day before was measured again to ensure the connection of the new measurements to the old ones. This procedure was repeated for all mirror spacings. Additionally, low-frequency Raman measurements were performed on each sample. In this way, spectra for all substances were obtained, for which the correct relative intensity among each other is known by the TFPI measuring procedure. To obtain a value for the total intensity of the spectrum, the low-frequency flank of the α -relaxation was first extrapolated by an ω^1 -law to 1×10^7 Hz in order to ensure that error made by the limited frequency window of the TFPI is minimal. Then, the whole spectrum was interpolated and integrated numerically on a logarithmic grid up to frequencies where the quasi-elastic region ends, and the Raman lines start (see figure 3.1). That the so obtained total area of the susceptibility spectrum $\Delta\chi$ (which can be regarded as the light scattering pendant to the dielectric strength $\Delta\epsilon$) is proportional to the scattering intensity I_{VH} divided by temperature, can be directly seen by considering equation 3.13 in the classical limit, from which one obtains

$$k_B T \int_0^\infty \frac{\chi''(\omega)}{\omega} d\omega = k_B T \int_0^\infty \chi''(\omega) d\ln\omega = k_B T \Delta\chi = \int_0^\infty I_{\text{VH}}(\omega) d\omega = I_{\text{VH}} \quad (4.13)$$

The intensity values from the PCS and the TFPI/Raman measurements were then transferred to Rayleigh ratios by comparison to reference Rayleigh ratios from the literature for toluene, one for green light obtained with high accuracy for VV scattering geometry [235], and for red light with vertical incident polarization and scattered light of vertical and horizontal polarizations [236]. From these values, VH Rayleigh ratios were calculated using the measured depolarization ratio of toluene ($\rho_{\text{VH}} = 0.357$) resulting in $R_{\text{VH}^{532}}^{\text{Tol}} = 8.35 \times 10^{-4} \text{ m}^{-1}$ and $R_{\text{VH}^{633}}^{\text{Tol}} = 3.58 \times 10^{-4} \text{ m}^{-1}$.¹ The anisotropy parameters calculated from the Rayleigh ratios of the 13 neat van der Waals liquids are shown in Figure 4.4, where the green symbols are the values from measurements with the TFPI/Raman setup (green laser) and the red points utilizing the PCS setup (red laser).² The difference between these two data sets is probably either due to an imperfect compatibility of the two reference Rayleigh ratios or due to the usage of the refractive index measured at 589 nm for the 633 nm measurements or due to the uncertainties of the measurement. Thus, this difference could be regarded as an estimate of the size of the experimental error bars.

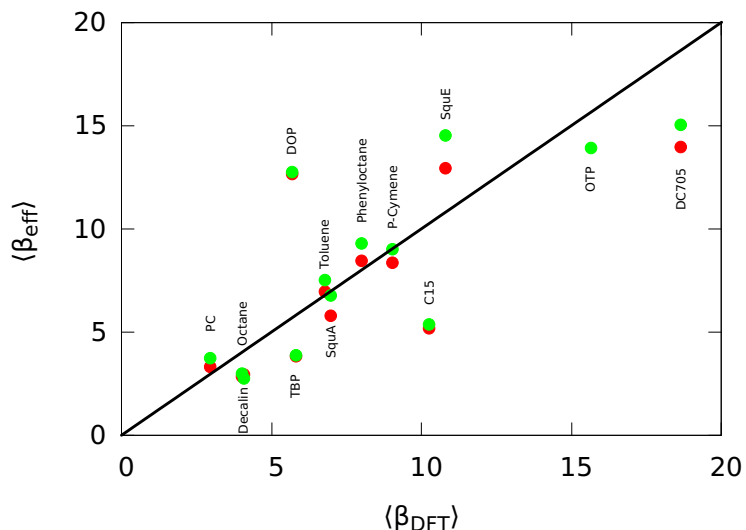


Figure 4.4.: Anisotropy parameters from TFPI/Raman (green circles) and PCS (red circles) measurements compared to calculated values. Abbreviations of the substances can be found in appendix A. The differences between the red and green points may be regarded as the size of the experimental error bars. The black solid line marks the equality $\langle \beta_{\text{eff}} \rangle = \langle \beta_{\text{DFT}} \rangle$.

It is clear that a rough correlation is visible; however, many outliers are present, and the correlation is by far worse than those seen in Figures 4.2 and 4.3. This is due to two main reasons: First, neat liquids are considered here, in contrast to the measurements in solution as in those figures. This means that orientational correlations might exist, which will shift the

¹ $R_{\text{VH}} = \rho_{\text{VH}} R_{\text{VV}}$ and $R_{\text{VH}} = \rho_{\text{VH}} / (1 + \rho_{\text{VH}}) R_{\text{V,V+H}}$

² The densities of the liquids necessary for these calculations are taken from the literature. The references are given in appendix A. Refractive indexes are necessary as well, which were measured during this work and are also compiled together with the measuring procedure in appendix B.

experimental value away from the DFT calculation ones due to the correlation parameter g_2 present in the experiment. Second, a wide variety of rigid and highly flexible molecules are among these 13 liquids. Thus, inaccuracies in the calculated conformer ensemble of flexible molecules might lead to a large deviation from the experiment. Therefore, a detailed look will be taken at these points in the following:

Four molecules are rigid or considered fairly rigid: PC, trans-decalin, p-cymene, and toluene. Except for decalin, the experimental anisotropy parameters of these substances are similar to those from DFT calculations, thus implying no pronounced orientational order in these neat liquids. The low experimental value of β_{eff} in the case of trans-decalin could be explained by a correlation factor g_2 less than one. The g_2 value can be simply extracted by comparing the experimental and calculated anisotropy parameter via $\beta_{\text{eff}}^2 = g_2 \beta_{\text{DFT}}^2$. Since two values are obtained from the experiment, one from the depolarized scattering intensity and one measured with the TFPI/Raman setup, the mean value is $g_2 = 0.55 \pm 0.05$. When comparing this value, which is below unity, with equation 4.9, a preferred perpendicular ordering of the molecules could be extracted. It should be noted that a pronounced correlation between neighboring decalin molecules was shown to exist by neutron diffraction measurements [237]. On the other hand, in cumene, a molecule structurally similar to p-cymene, studied here, the correlation was found to be much weaker. Although no information about the orientation of the molecules can be extracted from those neutron diffraction data, these findings are in line with the results here, as trans-decalin exhibits orientational correlations between neighboring molecules, where p-cymene does not. It is important to note that no information of the g_1 correlation factor can be obtained by dielectric spectroscopy on trans-decalin due to its vanishing small dipole moment.

It is possible for TBP to calculate the g_2 factor in the same way as done above for trans-decalin. A value of $g_2 = 0.41 \pm 0.06$ is obtained here. TBP is not a rigid molecule, thus the deviation of β_{eff} from β_{DFT} could stem from an incorrect conformer ensemble, which would render the obtained g_2 value meaningless. To check whether indeed an orientational correlation exists, the temperature dependence of the depolarized scattered light intensity is exploited. This could reveal an orientation correlation based on the following reasoning: At high temperatures, i.e., low densities, such correlation must diminish due to the reduced interactions of the molecules. Therefore, a temperature dependence of the scattering intensity must be present in cases of orientational correlations. This fact was used, for example, in reference [238] to check the orientational correlations for a large set of liquids. For the case of TBP, where the g_2 factor is below unity, this means that the scattered intensity must increase with increasing temperature to support this value. To test if this is the case, measurements were performed with the TFPI setup between 300 K and 400 K and the results are shown in Figure 4.5, where the temperature-dependent $g_2 \langle \beta \rangle^2$ value is depicted. The temperature dependence of g_2 can be directly seen since $\langle \beta \rangle$ is temperature independent to a good approximation. This is because although the conformer ensemble changes with temperature according to equation 4.11, for the case of the calculated conformer ensemble, this affects the $\langle \beta_{\text{DFT}} \rangle$ value only marginal ($\langle \beta_{\text{DFT}} \rangle = 5.804 \text{ \AA}^3$ at 300 K and 5.808 \AA^3 at 400 K) and is thus neglected.

It gets clear from figure 4.5 that g_2 decreases with decreasing temperature. Thus, orientational correlations intensify on lowering the temperature, leading to a more perpendicular ordering

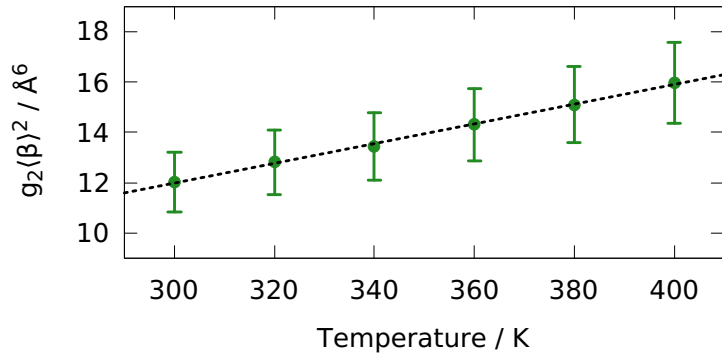


Figure 4.5.: Temperature dependence of the effective anisotropy parameter for the case of TBP, obtained by the TFPI setup.

of the TBP molecules. Thus, although the absolute value of g_2 as calculated above might be slightly in error due to an inaccurate conformer ensemble used in calculating $\langle \beta_{\text{DFT}} \rangle$, the fact that its value is less than unity is confirmed by the temperature-dependent measurements. It should be noted that TBP has a permanent dipole moment, which allows dielectric studies on the Kirkwood correlation factor g_1 . This was done very recently, and with the aid of a new theory, very detailed information about the ordering of the molecules was obtained [50]. Especially, it was found that neighboring dipoles align in angles between 0° and 97° and the increasing g_1 with decreasing temperature indicates an increasing orientational ordering. So, a pronounced ordering is found in both experiments, intensifying with decreasing temperatures, giving a congruent picture of the orientational correlations of the TBP molecules.

Now, the remaining outliers in figure 4.4 are addressed more briefly: For the highly flexible alkanes, especially for pentadecane (C15), a marked discrepancy between the experimental and calculated anisotropy parameters can be seen. A detailed discussion of the n-alkanes, which seem to behave very special in regard to light scattering, as mentioned above, can be found in appendix B.

The three remaining outlier DOP, DC705 and Squalene, deserve attention: While for Squalene a, orientational ordering as well as an incorrect conformer ensemble could explain the discrepancy, in the case of DOP and DC705, it is plausible that at least most of the discrepancy is caused by an erroneous conformer ordering: The minimal and maximal β values within the energy window of 1 kcal/mol for DC705 are 7.08 \AA^3 and 20.61 \AA^3 , respectively. Thus, an incorrect conformer ordering can easily explain the discrepancy to the experimental anisotropy parameter. For DOP, only three conformers are within the energy window of 1 kcal/mol, which possess similar β values. For these conformers, one of the octyl chains is bent above and one under the phenyl ring, leading to a low β value of 4.15 \AA^3 . In contrast, the β value of the all-trans conformer is as high as 22.15 \AA^3 . Thus, the experimental value could be explained by a prevalence of conformers with a structure intermediate between the completely stretched all-trans conformer and the highly curled one.

In summary, it can be stated from the discussion of the results of the neat liquids shown in figure 4.4 that it is possible to obtain scattering intensities from the spectra measured by TFPI/Raman in accordance with the one measured with a PCS setup. From these intensities, it

is possible to obtain anisotropy parameters via

$$R_{\text{VH}} = \frac{1}{15} \left(\frac{2\pi}{\lambda} \right)^4 \left(\frac{n^2 + 2}{3} \right)^2 N g_2 \langle \beta \rangle^2 \quad (4.14)$$

by setting $g_2 = 1$. These values can then be compared to DFT-calculated ones. These two values agree very well for rigid molecules without orientational ordering, i.e., $g_2 = 1$. In the case of rigid molecules with orientational order, the correlation factor g_2 can be directly obtained by comparing the calculated and the experimental β -value. In the case of non-rigid molecules, the g_2 value obtained in this way should be checked by inspecting the temperature dependence of g_2 , as shown for TBP, to exclude an incorrect conformer ensemble to be the reason for an apparent $g_2 \neq 1$ value. For highly flexible molecules, where the different conformers differ greatly in their β -values, the significance of the DFT-calculated mean anisotropy parameter is reduced, since errors in constructing the conformer ensemble may lead easily to an unreliable $\langle \beta_{\text{DFT}} \rangle$ value. In such cases, a more thorough determination of the conformer ensemble would be highly desirable.

4.1.2. Mixtures of non-ionic liquids

It has been shown in the preceding subsection that from the total intensity of the spectra obtained with a combination of the TFPI and Raman setup, an anisotropy factor for neat liquids can be determined, which is in good accordance with the DFT-calculated one for not too flexible molecules. In this subsection, equimolar mixtures of van der Waals liquids are addressed that can be considered as pre-stage to ionic liquids, which are mixtures of two ion species. The aim is to see whether the contribution of the two molecular species can be separated by comparing their relaxation strength with the DFT-calculated anisotropy parameter. Therefore, however, it is necessary to check whether not only the total intensity of the light scattering spectrum can be related to the optical anisotropy of a single molecular species, but also if a part of the spectrum, i.e., the α -relaxation strength, is proportional to the β -value of the molecules under consideration. In order to determine the contribution of the α -relaxation to the spectrum, a fit is employed consisting of a Cole-Davidson (CD) function describing the α -relaxation and two Brownian oscillators (BO) modeling the high-frequency part, i.e., the microscopic dynamics. The high-frequency flank of the CD function is cut off at the frequency of the second oscillator, following the procedure detailed in reference [239]. The fit function thus reads

$$\chi''_{\text{LS}}(\omega) = \frac{A_{\text{CD}}}{(1 + i\omega\tau)^{\gamma}} - \frac{A_{\text{CD}}}{(1 + i\omega\tau + \Omega_1\tau)^{\gamma}} + \sum_{j=1}^2 \frac{A_j \Omega_j^2}{\Omega_j^2 - \omega(\omega + i\zeta_j)} \quad (4.15)$$

where Ω_j are the oscillator frequencies and ζ_j the damping rates, such a fit describes the data of the 13 neat van der Waals liquids rather well, which is shown later in figure 4.7 for the example of TBP.

The area of the alpha process $\Delta\chi_\alpha$ is calculated by integrating over the first two terms in equation 4.15, i.e., over the CD function with the high-frequency cutoff. This area is shown in dependency of the total area of the susceptibility spectrum $\Delta\chi$ in figure 4.6.

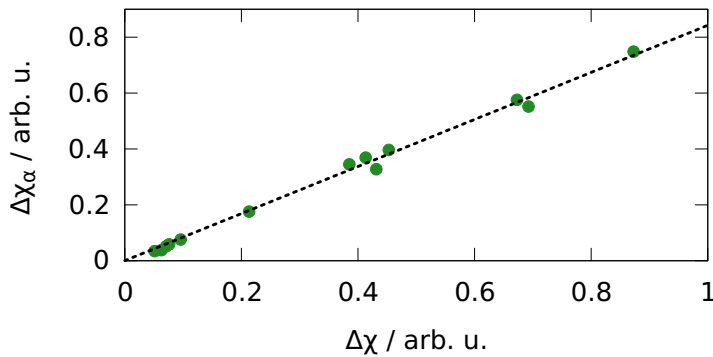


Figure 4.6.: Comparison of the area of the α -peak to the whole area of the spectrum.

As indicated by the dashed line, these two values are proportional to each other in good approximation. This means that it is indeed possible to calculate the Rayleigh ratios for each

substance by considering only the area of the α -relaxation and from that calculate the β -value.³ Thus, it should be possible to determine the contribution of the two molecular species in a binary mixture by comparing the area of the respective α -process to the optical anisotropy. In order to test this notion, three different equimolar mixtures were prepared, namely TBP+PC, squalane+toluene, and squalane+C15. The spectra of the mixture of TBP and PC are shown in figure 4.7 together with the spectra of the two neat components. It can be seen that the α -relaxation in the spectrum of the mixture is markedly broader than that of the single components. The reason for this gets immediately clear when considering the difference in size between the TBP and the PC molecules, which causes the larger TBP molecules to rotate slower than the smaller PC molecules. This can also be seen by the fact that the peak position is almost identical for the two neat liquids, where the TBP spectrum is, however, measured 85 K above the one of PC.

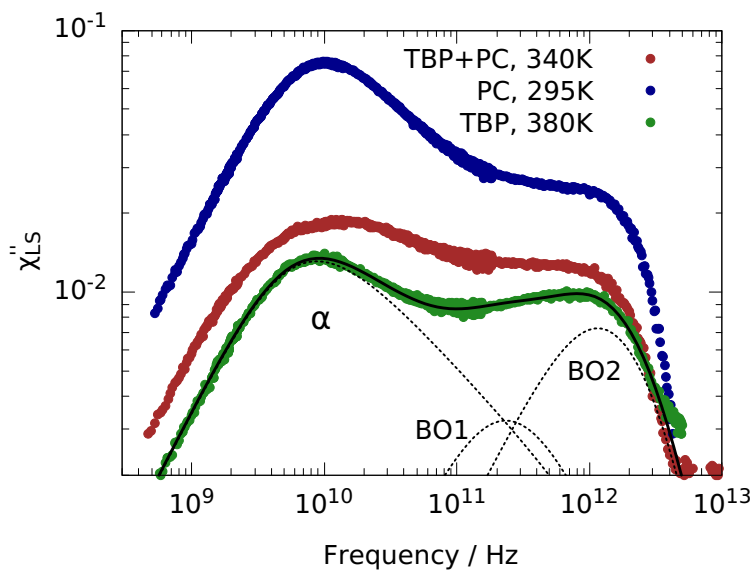


Figure 4.7.: A small difference in size of the molecules in the mixture leads to a single, broadened peak in the spectrum measured by the TFPI/Raman setup. Solid line is a fit with equation 4.15. Dashed lines are the components of the fits as indicated.

The difference in the size of the two molecules is yet not enough to produce a bimodal spectrum. This is achieved in the case of the mixture of squalane+toluene, as can be seen in figure 4.8. A slow process is distinctly separated from a very broad peak at high frequencies. From the measurements of the neat liquids, it is clear that at this temperature, the dynamics of squalane is located somewhere near the low-frequency limit of the TFPI, whereas the dynamics of toluene is very fast due to the closeness to the boiling point. Thus, the slow process is attributed to squalane, and the fast broad peak must consist of the toluene α -process at intermediate frequencies and the microscopic dynamics at the highest frequencies.

³It should be noted that this finding is not trivial and using a different part of the spectrum representing the α -relaxation, like for example the central Lorentzian, as done in older literature, leads to a poorer proportionality. This indicates once more that the reorientational dynamics of the molecules is not mono-exponential, even at that high temperatures.

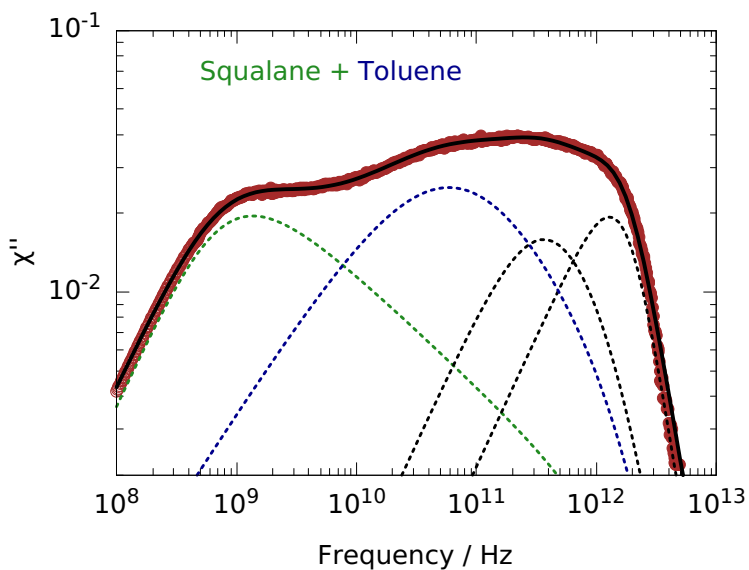


Figure 4.8.: A Large difference in size of the molecules in the mixture leads to a bimodal spectrum. Dashed lines are components of the fit, as detailed in the text.

It can be seen that the region between the structural relaxation of squalane and toluene is very broad. When trying to fit the spectrum, it is possible to identify two ways to account for this broad region: First, one could use two CD functions for the two α -processes. Then, the shape parameter of the slower process, i.e., the structural relaxation of squalane, becomes very small. Thus, the slope of the high-frequency flank is rather flat. This results in a small contribution of the toluene α -process, sitting on this broad high-frequency flank. Thus, the intensity $\Delta\chi_\alpha T$ of squalane is markedly larger than that of toluene. When comparing this to the intensities calculated from the anisotropy parameters with equation 4.14, one sees that it should be the other way round. This means that unless something strange happens in the mixture, like a pronounced ordering of the squalane molecules or if a distinctly different conformer ensemble of squalane is present in the mixture than in the neat liquid, this way of modeling the spectrum is incorrect. Therefore, a second way is tried: The structural relaxation of squalane is again described by a CD function, but the one of toluene is modeled by a Havriliak-Negami (HN) function, which is able to produce a broadening on the low-frequency flank. This way of modeling is shown in figure 4.8. One can see that the broad region between the two structural relaxations is now captured by the low-frequency flank of the toluene HN function instead of by the high-frequency flank of the squalane CD function, as was the case in the first model. Now, the intensity of toluene obtained by this fitting procedure is larger than that of squalane, in accordance with equation 4.14. A broadening on the low-frequency flank of the faster relaxation process in a mixture is often observed in dielectric spectroscopy [52, 240, 241, 58], however, there is a debate regarding the question of whether the smaller molecules might take part in the structural relaxation of the larger molecules [242, 243]. Here, based on the intensity argument, it can be checked whether the qualitative argument used above to assign the portion of the spectrum which is due to the small and large molecules, respectively, holds also quantitatively. This is done by comparing the intensity of the α -relaxation $\Delta\chi_\alpha T$ for the different neat liquids

and mixtures to $L^2 N \langle \beta_{\text{eff}} \rangle^2$ in Figure 4.9, where L^2 is the quadratic Lorentz local field factor. According to equation 4.14, a linear dependency is expected. Besides the combined value for the squalane + toluene mixture, the values for squalane and toluene from their respective peaks in the mixture are shown as open symbols. For the C15 + squalane mixture, like for TBP + PC, no separated α -processes could be observed; thus, only one merged peak is evaluated. The values of $\langle \beta_{\text{eff}} \rangle$ of the neat components are taken from the measurements with the PCS setup and a mean anisotropy parameter for the mixture is calculated via equation 4.12 with $p_{1,2} = 0.5$.

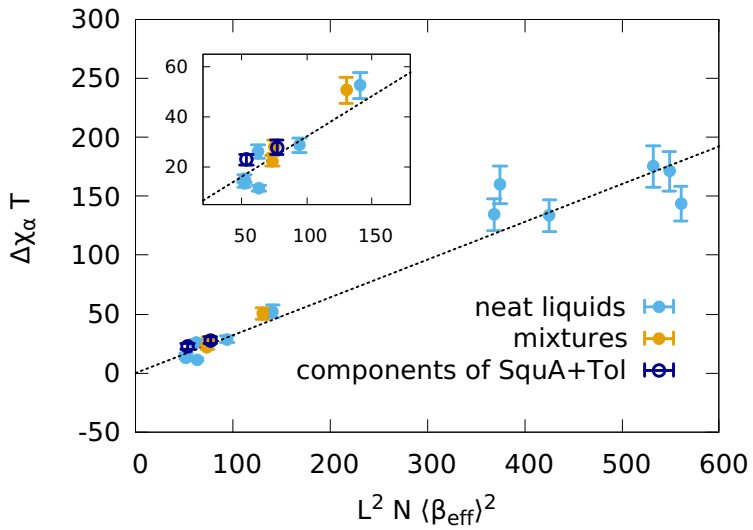


Figure 4.9.: Peak areas of the α -relaxation multiplied with temperatures from TFPI/Raman measurements, i.e. α -peak intensities, in dependence of intensity calculated from the optical anisotropy parameters determined by the PCS intensity measurements of neat liquids and mixtures. The black dashed line is a linear fit to the neat liquids.

It is clear that the mixtures and the single components follow this linear relationship very closely. This shows that the intensity of the α -relaxations in mixtures can be obtained quantitatively by knowing the $\langle \beta_{\text{eff}} \rangle$ -value of the neat components, either from an independent experiment or from DFT calculations. It should be stressed with regard to ionic liquids, discussed later, that it is crucial that this works by only considering the intensity of the α -relaxations since due to the fluorescence in most of these substances, the frequency range starting from the region of the microscopic dynamics is not accessible. Thus a measurement of the total intensity would lead to incorrect results. However, since in ionic liquids, the $\langle \beta_{\text{eff}} \rangle$ -value of the two ion species is not accessible experimentally, it has to be obtained by DFT calculations.

It got clear from this section which version of the equations should be used when comparing experimental depolarized scattering intensities with optical anisotropy parameters. The methods used in the literature, which try to exclude the CIS contribution, do not yield β values in accordance with DFT calculations. Contrary, experimental β -values obtained with equations neglecting CIS agree favorably well with DFT calculated values. Moreover, it has been shown

that intensity information can be deduced from dynamical measurements. Also, the intensity of the α -relaxation of the individual molecule can be connected to its optical anisotropy. This puts depolarized light scattering measurements on the same level as dielectric spectroscopy, as it is now possible to identify relaxation features in mixtures based on their intensity. Furthermore, it is now possible to obtain orientational correlation factors g_2 from dynamic depolarized light scattering measurements.

4.2. The shape of the structural relaxation

As mentioned above, the non-exponentiality of the structural, or α -relaxation, is one of the hallmarks of glassy dynamics, but its origin is still not understood. In this respect, the most experimental data are probably obtained by dielectric spectroscopy since these measurements are easily performed over the whole temperature and frequency range [14]. When describing the dielectric loss peak with a model curve, like the KWW or the CD function, it is found that the stretching parameter varies largely depending on the molecule under study. Consequently, in the attempt to understand the origin of this different stretching, correlations to other features of glassy dynamics were investigated. For example, it has been found that the fragility of a liquid, i.e., the slope of the VFT-equation describing its correlation times at the glass transition temperature, is inversely proportional to the value of the stretching exponent [244]. This view is controversial and not shared by other authors [245, 246]. Also, the stretching exponent was related to the time scale of the β -relaxation by the coupling-model, where the secondary relaxation is predicted to be located in proximity to the α -relaxation for high values of the stretching exponent, while it is well separated in the case of low values [247]. Some studies relate the stretching of the α -relaxation to the anharmonicity of the intermolecular potential [248, 203]. One of these is the work of Paluch and coworkers, where a set of 88 substances is compiled, for which it was shown that an anti-correlation exists between the dielectric strength and the stretching parameter of the α -relaxation. The explanation for this behavior was the dipole-dipole interaction, which leads in the case of high polar molecules to a more harmonic interaction potential and thus to a narrower α -relaxation peak. From this, it might be suspected that the light scattering spectrum should be influenced similarly. Hence, the work of Paluch *et al.* was the inspiration for studying van der Waals liquids like tributyl phosphate (TBP) and the vacuum pump oil DC704 by light scattering, the results of which are discussed below. These two liquids were chosen for the following reasons: TBP is a dipolar molecule with a dipole moment of 2.6 D [249], for which it was shown in the literature that the dielectric loss peak exhibits a markedly higher value of the stretching parameter than the one deduced from DSC measurements [189]. This can be understood as a first hint in the direction that the findings of Paluch *et al.* are not directly transferable to other experimental techniques. DC704, on the other hand, is an apolar oil, which is regarded as a "simple" liquid, i.e., a substance for which intermolecular interactions within the first coordination shell determine all properties of the liquid [250], and for which an identical shape of the dielectric loss and the shear modulus was found in the literature [251]. Therefore, in the next subsection, dielectric and light scattering spectra of these two and several other substances are compared. The spectra of these liquids were measured by different people in the workgroup over the last several years and are published in reference [252], where the names of all contributors can be found. An explanation of the differences found is proposed and then tested on dilution experiments of TBP below, which are published in reference [253].

In figure 4.10, dielectric data for a wide variety of liquids is shown, scaled in such a way that their peak maxima superimpose. Among them are polar and apolar substances, hydrogen bonding liquids, and ionic systems. The latter ones and a monohydroxy alcohol are shown as gray symbols since, for ionic systems, it is known that the dielectric loss peak may be influenced

by conductivity relaxation and thus does not reflect pure dipolar reorientations. In the case of monohydroxy alcohols, it is well known that the most prominent dielectric peak is the Debye peak and thus should not be compared to α -relaxation peaks. As expected, the shape of the spectra differs largely among the various liquids. However, one can already see that polar substances, like, for example, TBP, exhibit a markedly steeper slope of their high-frequency flank than apolar substances like DC704, in accordance with the findings by Paluch.

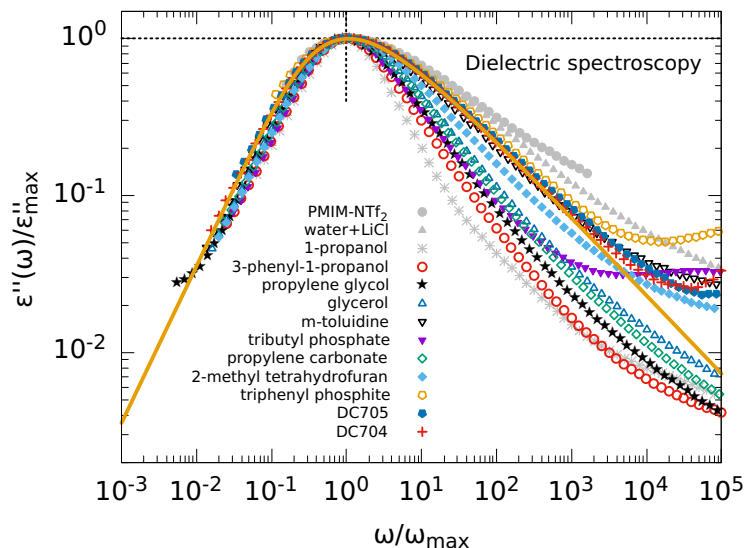


Figure 4.10.: Spectra from dielectric spectroscopy. Orange line is a model function with a high frequency slope of $\omega^{-1/2}$.

Additionally, it seems that the different apolar substances have similar shapes, which can be seen by the fact that they are located near the orange line. This orange line is a fit to the DC704 data based on the generalized gamma distribution of relaxation times. Details about this model can be found in references [254, 20]. Here, it suffices to say that in this way, a peak is produced, which has a high-frequency slope of $\omega^{-1/2}$ and a width that is intermediate between that of the KWW and the CD function when choosing the stretching exponent to be 0.5 in both cases.

As a next step, the spectra from light scattering measurements are shown in figure 4.11 for the same substances as above and additionally for some monohydroxy alcohols, where it is known that the Debye process does not show up in the light scattering spectrum. There, a completely different picture shows up than in the case of the dielectric spectra. It can be seen that the spectra almost perfectly superimpose from the lowest frequencies up to frequencies where secondary relaxations start to contribute in some cases. Most importantly, the high-frequency slope follows a $\omega^{-1/2}$ law to a good approximation for all substances. This can be seen from the orange line, which is the same as above.

Thus, a rather generic behavior for the light scattering spectrum of various liquids has been found, which is in marked contrast to the substance-dependent spectra observed in dielectric spectroscopy. Therefore, a reason for this discrepancy has to be found. It should be noted in

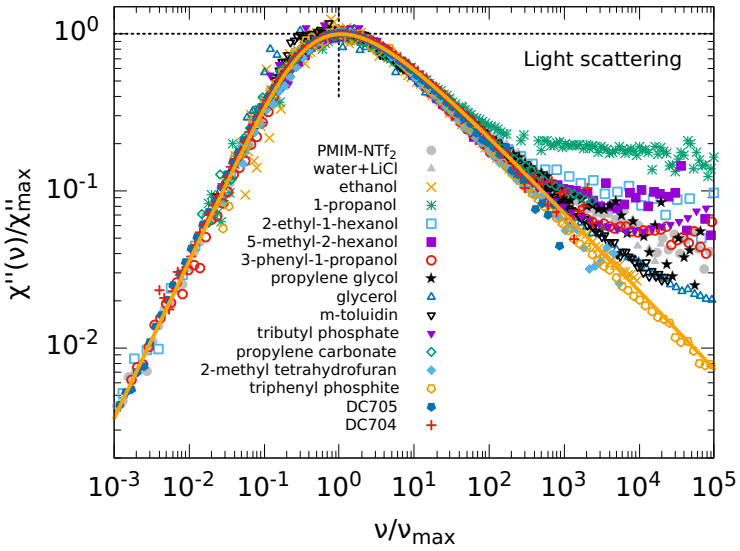


Figure 4.11.: Spectra from depolarized dynamic light scattering. Orange line is a model function with high frequency slope of $\omega^{-1/2}$.

this respect that theoretical models from the literature indeed predict a high-frequency slope of $\omega^{-1/2}$ for the α -relaxation [255, 256, 257]. Furthermore, there exist indications that also the high frequency slope of dielectric spectra tends to a $\omega^{-1/2}$ behavior at low temperatures [258]. However, the theory on which the rationalization of the difference in the spectra is based here is a different one. It is well known that the dielectric Debye process found in monohydroxy alcohols is usually not, or only very weakly, seen in light scattering measurements [44, 45]. As mentioned above, the model of transient chains of H-bonded molecules explains the Debye-process with the movement of these supramolecular structures by attaching and detaching of molecules at the ends of the chains. This movement is seen in the dielectric spectra due to the large end-to-end dipole vector of such chains. Thus, one might speculate that light scattering is not sensitive to such supramolecular structures because it probes more locally the anisotropy of single molecules. A different view than that put forward in the transient-chain model comes from the theory of Pierre-Michel Déjardin [50]. With this theory, it is possible to reproduce quantitatively the static permittivity of linear monohydroxy alcohols in dependence of the temperature by calculating the Kirkwood correlation factor from the physical properties of the liquid and one independent temperature parameter which is related to induction/dispersion forces and which has to be determined by comparing the theoretical and experimental ϵ_s -values. This means that the Déjardin theory is able to rationalize the Debye-process – which is responsible for most of the static permittivity – just by considering dipolar cross-correlations between neighboring molecules, thus without the need of invoking some special H-bonded structures. But it is also clear that the two models are not contradictory since H-bonding between two neighboring molecules directly implies an orientational correlation. However, it is also clear that the Déjardin theory is more universal in that sense that it can also describe polar liquids, where no H-bonds are possible, but orientation correlation arises due to dipole-dipole interactions. Thus all kinds of liquids are described based on the same footing, and no

discrimination is made into H-bonding or non-H-bonding substances.

Moreover, the dynamic part of the Déjardin theory predicts that in addition to the relaxation of single molecules, an additional relaxation shows up for cases where the Kirkwood factor exceeds unity, which is attributed to collective dynamics [259]. Thus, when identifying the experimental Debye- and α -relaxation with the single molecular and collective relaxation from the Déjardin theory, respectively, one could rationalize the experimental findings in monohydroxy alcohols. But most importantly, this would imply that a Debye-process is also expected for substances in which no H-bonding occurs but with a Kirkwood correlation factor larger than one. If this would be indeed true, it could rationalize the apparent narrower peak in the dielectric spectra since an additional Debye peak, not too far separated from the α -relaxation, would render the combined relaxation process narrower than the actual α -relaxation.

This idea is tested in the following on the example of TBP, where a Kirkwood factor of around $g_K = 2$ was found [50]. Therefore, the dielectric and the light scattering spectra, both measured at 147 K, are shown in figure 4.12. The light scattering spectrum is shifted only vertically in such a way that it is superimposed in the frequency range of the β -relaxation with the dielectric spectrum. Both techniques nearly identically probe this secondary relaxation. However, the differences of the spectra are well pronounced when considering the main peaks. There, it can be seen that the dielectric peak is markedly more intense and narrower than the one measured by light scattering.

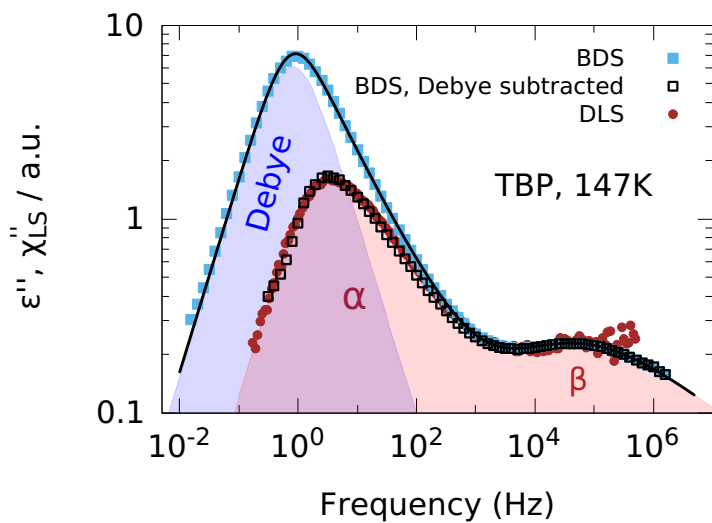


Figure 4.12.: DLS and BDS data of neat TBP at 147 K. In addition to the α and β process present in the DDLS data, a Debye process is visible in the BDS spectra. BDS data are also shown with this Debye process subtracted.

It should be noted that this finding cannot be explained by a different vertical shifting of the data. For example, one could argue that the light scattering α -process is faster than the one from dielectric spectroscopy due to probing the P_2 and P_1 correlation function, respectively. Then, by matching the intensities of the main peaks, the secondary relaxation in the light scattering spectrum is more intense, which could be rationalized by small-angle rotations, as

described in section 3.1. However, this explanation can account for a maximal factor of three between the time constants and the intensity of the secondary relaxation. Since factors of up to 13 and 7.5 between the time constants and the intensities are observed in the experiment, this reasoning must be discarded.

Instead, when a Debye-process is fitted to the low-frequency part of the dielectric spectrum and subtracted afterward from the data, one ends up with the black open squares in figure 4.12. It is clear that they almost perfectly resemble the light scattering spectrum, i.e., the dielectric data is compatible with the idea of a Debye process being present in addition to the α -relaxation, the latter being probed by light scattering. Thus, if this additional Debye-process in the dielectric spectrum arises indeed due to orientational cross-correlations, as implied by the Déjardin theory, it should be possible to reduce these cross-correlations by diluting TBP by an apolar solvent. Then, the TBP molecules will be further separated from each other, and the Debye process should vanish at some degree of dilution. In order to test this idea, mixtures with the apolar solvent n-pentane were prepared, which is miscible over the whole concentration range with TBP and does not show any sign of a dielectric relaxation when measured as neat substance. The dielectric spectra were found to broaden upon increasing the n-pentane concentration, until at concentrations below 29 mol% no further change in the spectral shape could be seen. Thus, dielectric data for this concentration together with the spectra for a concentration of 11 mol% and neat TBP are shown as a master plot in figure 4.13.

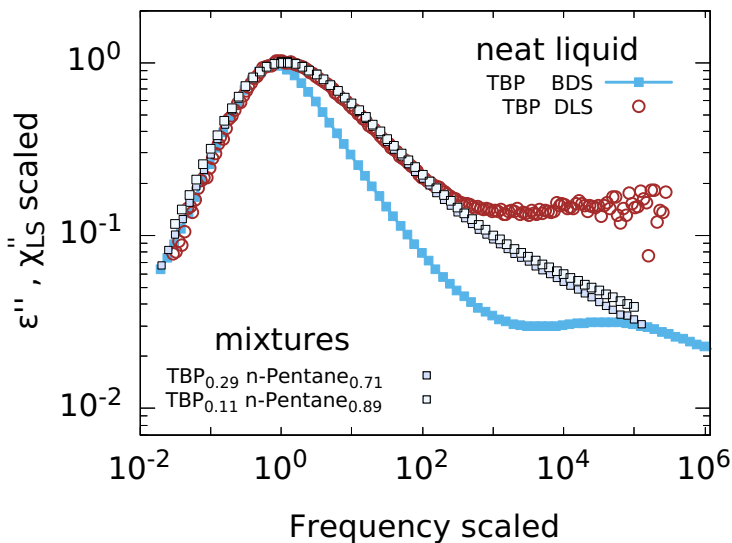


Figure 4.13.: Data of neat (BDS+DLS) and mixed TBP (BDS). Spectra were chosen with the main peak located around 1 Hz, and were scaled to overlap in peak height and on the low frequency flank. The α -process of the two low-TBP-concentration mixtures measured by BDS and neat TBP measured by DLS have the same spectral shape. Temperatures (from top to bottom) of the data sets are 147 K, 147 K, 132 K and 130 K.

It can be seen that the spectral shapes of the mixtures with 29 mol% and 11 mol% are identical, while that of neat TBP is markedly narrower. This indicates indeed that the contribution from

the cross-correlation is absent below 29 mol%, leading to a broader peak, which in addition resembles the one of neat TBP measured by light scattering. Together that means that a Debye-process is present in the dielectric spectrum of neat TBP, which is due to orientational cross-correlations and therefore diminishes upon dilution with an apolar solvent until it eventually vanishes around a concentration of 29 mol% TBP. The shape of the dielectric spectrum without the influence of cross-correlations is then the same as found in light scattering, and since TBP is among the substances complied in figure 4.11, it is the generic shape.

It follows from these considerations that an apolar substance, which is just polar enough to give a weak dielectric signal, should exhibit a dielectric loss shape, which is identical to the light scattering one. Additionally, the light scattering peak frequency should be a factor of three higher, at most. To test this notion, DC704 is chosen, as mentioned above, which has a small, but non-zero dielectric strength of $\Delta\epsilon = 0.2$. Measurements were performed at the same temperature in dielectric spectroscopy and light scattering, and the spectra are shown in figure 4.14. The light scattering spectra, shown as open black circles, are only shifted vertically to superimpose on the dielectric ones, shown in different colors.

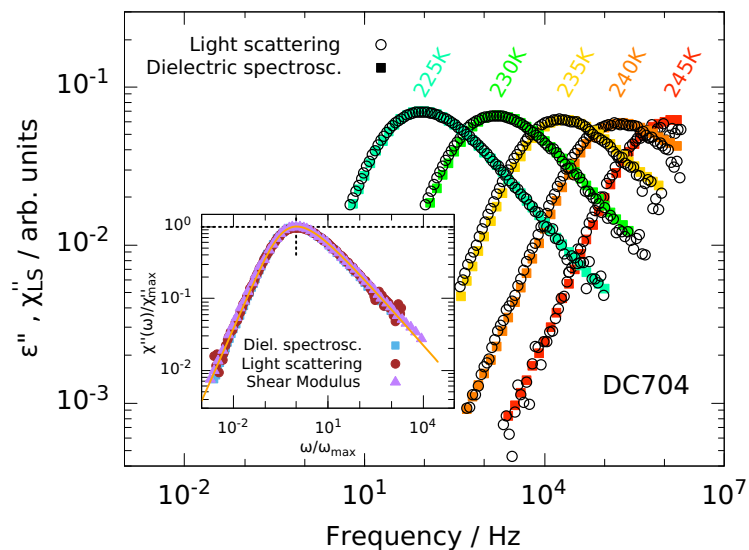


Figure 4.14.: Comparison of the light scattering and dielectric susceptibilities of the silicon oil DC704 with respective spectra obtained at the same temperatures. Only the absolute intensity of the light scattering spectra is scaled, i.e., both methods reveal the same dynamics due to lack of cross-correlations. Inset: Dielectric and light scattering spectra together with shear modulus data from reference [260] scaled to the peak maximum reveal the same spectral shape in all three methods. The solid line is the same as that in figure 4.10 and 4.11.

It can be seen that the spectra perfectly superimpose, i.e., not only the shape is exactly the same, but also the relaxation time. In the inset, a dielectric and a light scattering spectrum is shown together with the imaginary part of the shear modulus from the literature as a master plot [260]. The orange line is again the generic shape from above. It can be seen that the shape measured by the three experimental techniques is the same as the generic one.

Together, this means that a generic shape of the α -relaxation seems to exist in the supercooled regime, which is probed by light scattering. In the dielectric spectra, this generic shape is often masked by a dynamic contribution from the cross-correlation, which appears on lower frequencies than the α -peak as a Debye-like process, rendering the combined peak narrower than the generic shape. The generic shape can also be recovered in dielectric spectra, either by diluting the polar substance with an apolar liquid, thus destroying the cross-correlations or for the case of liquids with a tiny polarity. It should be noted that also in triplet state solvation dynamics measurements, which can be regarded as a local dielectric experiment, the generic shape was found in polar substances [252]. However, it should be kept in mind that the generic shape seems to be special to the supercooled regime since a wide variety of shapes of the DLS spectra is observed in the high-temperature regime, as discussed in section 2.1.

Since the above results were published previously, several reactions have appeared in the meantime. Some of them support the above findings [261, 262, 263] and some are contradictory [264, 265]. One of the latter is the pre-print study of Moch *et al.*, which raises an interesting point and should therefore shortly be discussed in the following: Therein, the authors report on rheological measurements and dielectric aging experiments of TBP. Both data sets are found to be in better accordance with the dielectric relaxation time than with the light scattering relaxation time. From that, they concluded that the glass transition is governed by the collective dynamics, i.e., by the Debye-relaxation, rather than by the α -relaxation, as probed by light scattering. The question of which dynamics really freeze at the glass transition is very interesting. To answer this question, however, it seems most appropriate to compare dielectric and light scattering time constants to those obtained by DSC measurements, where in the latter method indeed the freezing of dynamical degrees of freedom is monitored.

Several liquids already contained in figure 4.11, for which the glass transition temperature is within the accessible temperature range of the DSC apparatus, are therefore considered in the following. The procedure is explained for the example of TBP.

Relaxation times from light scattering, dielectric spectroscopy, and DSC measurements are shown in figure 4.15.⁴ Included is the dielectric aging time from reference [264] and ^{31}P -NMR data from reference [266]. It is underscored by the excellent agreement of NMR and light scattering data that light scattering monitors the self-correlation contribution of the TBP molecules. Also, the calorimetric time constants agree perfectly with those from light scattering. On the other hand, the dielectric relaxation times are larger for all temperatures. In the range of the DSC measurements, of about a factor of 10, as can be best seen in the inset. From such data, ratios of the correlation times, namely $\tau_{\text{BDS}}/\tau_{\text{DSC}}$ and $\tau_{\text{DLS}}/\tau_{\text{DSC}}$, are calculated in the following way: The dielectric and light scattering relaxation times are fitted by a VFT-function, where the peak position of the dominant peak in the dielectric spectrum is used. Then, at each temperature where DSC data exist, the above mentioned ratios are calculated by using the VFT values at the temperature of the DSC time constants. The geometrical mean of these five values is used with error bars denoting the minimal and the maximal value. The ratios are shown for several substances in figure 4.16, which are subdivided into classes by different colors. The $\tau_{\text{BDS}}/\tau_{\text{DSC}}$ and $\tau_{\text{DLS}}/\tau_{\text{DSC}}$ values which fall in the range $1/3 < \tau_i/\tau_{\text{DSC}} < 3$ within the limits of

⁴ Dielectric data at frequencies higher than 1×10^7 Hz were obtained during the master thesis of Andreas Helbling, supervised by the present author, with two different high-frequency dielectric setups.

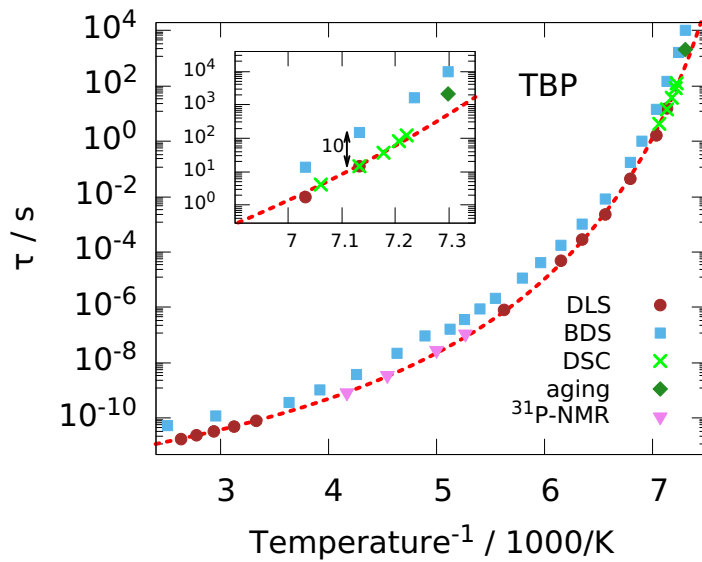


Figure 4.15.: Arrhenius plot of the time constant of TBP measured by different experimental techniques. The inset highlights the temperature range around the glass transition, where it can be clearly seen that the DSC time constants agree with those from DLS, while the dielectric time constants are a factor of 10 higher. Aging data is from [264] and NMR data from [266].

uncertainty (indicated by the black shaded area), are excluded from further discussion, since it is unclear whether calorimetric time constants should compare to a P_1 or P_2 correlation time and since experimental uncertainties preclude a discussion of such small differences in time constants.

It can be seen that only a few ratios lie outside the black shaded area. Of course the ratio $\tau_{\text{BDS}}/\tau_{\text{DSC}}$ for TBP, as already seen in figure 4.15, but also the one for two monohydroxy alcohols, 2E1H and 5M2H. However, this is not surprising since it is well known that the Debye-process in monohydroxy alcohols has no signature in DSC measurements [41, 42, 43]. Instead, the α -relaxation as probed by light scattering is in accordance with the calorimetric relaxation times. This shows once more that the cross-correlation of H-bonding substances, like monohydroxy alcohols, should be treated on an equal footing as the one in non-H-bonding polar substances, like TBP. However, it is also seen that three $\tau_{\text{DLS}}/\tau_{\text{DSC}}$ ratios are located outside the black shaded area. This is the case for network-forming liquids. The discrepancy is largest for the water-LiCl mixture, where the $\tau_{\text{BDS}}/\tau_{\text{DSC}}$ ratio is identical to the one from light scattering. Regarding the dielectric time constant, however, it is most likely that not the reorientation of the water molecules is monitored, but the conductivity relaxation as discussed in section 5.1. For propylene glycol and glycerol, on the other hand, the ratio $\tau_{\text{BDS}}/\tau_{\text{DSC}}$ is within the black shaded area. This might indicate in these cases that the glass transition is indeed governed by the collective dynamics as probed by dielectric spectroscopy, while the α -process probed by light scattering is faster. This means that it has to be checked individually for each substance, which dynamics freeze at the glass transition. More work is needed in this direction to understand the reason for this different behavior.

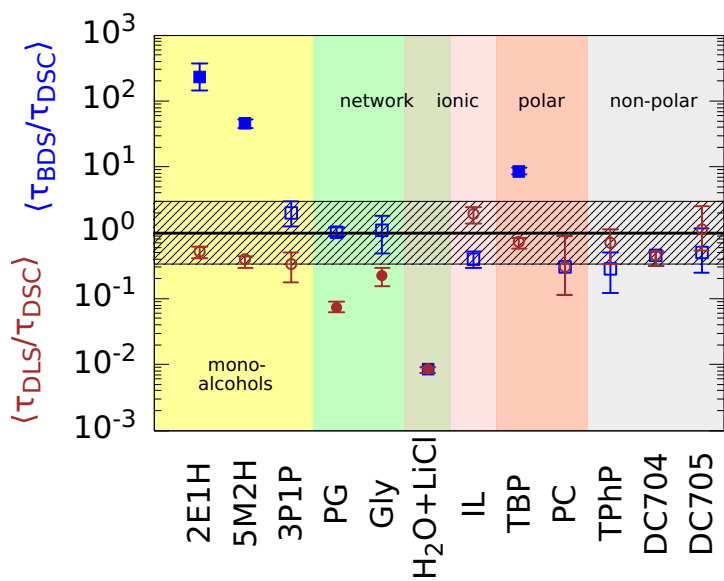


Figure 4.16.: Ratios of DLS (red) and BDS (blue) time constants to the calorimetric time constants.

5. Molecular dynamics in neat ionic liquids

This chapter aims to extract from DLS, BDS, and DSC measurements the microscopic nature of the ion dynamics in neat ionic liquids. Although those experiments increasingly attracted attention already around 15 years ago, when ILs became commercially available and their ability to form nanoscale structures was discovered, the interpretation of the results is still not straightforward and debated in the literature. This is on the one hand because DLS measurements on ILs are scarce, and DSC measurements usually only focus on the determination of glass transition or melting temperatures. BDS is used routinely on ILs, but there, the evaluation of the spectra is considerably complicated due to the charge transport, resulting in controversies in the literature. On the other hand, this is because a multitude of relaxational processes might be present in the spectra of ILs because not only the dynamics of two different molecular species but also motions of aggregates may contribute. Moreover, rotational and translational dynamics can be measured by dielectric spectroscopy in the case of ILs, while in non-ionic liquids, only reorientational motions of permanent dipole moments are monitored. Thus, it is crucial to disentangle the microscopic origin of the various dynamic processes in neat ionic liquids first, before addressing mixtures of ILs with non-ionic additives in chapter 6. Therefore, as the first step in this chapter, the appearance of translational motions of ions in the dielectric spectrum should be discussed in the next section, most of which is published in reference [267]. After that, the separation of cation and anion dynamics will be considered in cases where the cation is markedly larger than the anion. Following this, the dynamic signatures of nanoscale aggregates are addressed. In the last section, it will be shown that the reorientation of ions equipped with a permanent dipole moment can be identified in some cases in the dielectric spectrum in addition to the translational dynamics of the ions.

5.1. Modeling of translational dynamics

The dielectric spectra of non-ionic polar substances are almost always evaluated in the permittivity representation, most often in its imaginary part $\epsilon''(\omega)$. There, a peak shows up due to the reorientation of the permanent dipole moments, which can easily be fitted, for example, by a Cole-Davidson equation, directly providing the relaxation time constant, the dielectric strength, and the stretching parameter. In the case of ionic liquids, however, the imaginary part of the permittivity is rather featureless since the DC-conductivity contribution overshadows all relaxational processes which might be present underneath. Therefore, a different representation is usually chosen, for example, the imaginary part of the dielectric modulus $M''(\omega)$, where a peak in the case of conducting materials can be observed reminiscent of the peak in $\epsilon''(\omega)$ for dipolar liquids. Accordingly, this peak can be fitted by common empirical functions

as it is done for dipolar liquids. However, the practice of evaluating data in the modulus representation is sometimes criticized [268, 269], since contributions from translational and rotational dynamics, as well as electronic polarization, are convoluted reciprocally, as can be seen from equation 3.20, making it difficult to assign a microscopic origin to the peak. Another possibility is using the real part of the conductivity representation $\sigma'(\omega)$, which is especially useful for directly reading off the DC-conductivity from the plateau appearing at low frequencies. At frequencies higher than the plateau, a transition to AC-conductivity is observed, leading to an increasing flank. The frequency of the transition point is also often identified with the ion hopping time scale, and there are models constructed to fit such conductivity spectra. Two of them will be discussed below. The real part of the permittivity $\epsilon'(\omega)$ seems to get less attention when evaluating the dielectric spectra of ILs, except for room temperature measurements, where it is common to look at the real and imaginary part of the permittivity simultaneously. Advantageously, the DC-conductivity does not contribute to $\epsilon'(\omega)$, while dipolar relaxation and conductivity relaxation do. The latter can be rationalized when considering the empirical Barton–Namikawa–Nakajima (BNN) relation [270, 271]

$$\Delta\epsilon = \frac{\sigma_0\tau_\sigma}{p\epsilon_0}, \quad (5.1)$$

which relates the dielectric relaxation strength $\Delta\epsilon$ of the ion-conducting process to the DC-conductivity σ_0 and the ion relaxation time τ_σ where p is a parameter on the order of 1. Thus, the BNN relation implies that a clearly visible step appears in $\epsilon'(\omega)$, whenever the product $\sigma_0\tau_\sigma$ is notably larger than the vacuum permittivity ϵ_0 . This is why these conductivity relaxation steps might easily be confused with dipolar relaxation, as their appearances are very similar. Additionally, the $\epsilon'(\omega)$ representation can be used to calculate the so-called conductivity free representation of $\epsilon''(\omega)$ [272] via

$$\epsilon''(\omega) \approx \epsilon''_{\text{der}}(\omega) = -\frac{\pi}{2} \frac{d\epsilon'(\omega)}{d \ln \omega}. \quad (5.2)$$

This approximation of the Kramers-Kronig relation employs that a DC-conductivity does not contribute to the real part of the permittivity. Hence, a peak is observed in $\epsilon''_{\text{der}}(\omega)$, the shape of which is slightly distorted due to the approximate character of equation 5.2, but the peak position can be evaluated. Even more importantly, this representation is most useful in identifying by eye if only one relaxational process is present in the dielectric spectrum or if there are two, which is demonstrated in section 5.4. Here in this section, only ILs are considered for which just one relaxation peak can be observed in $\epsilon''_{\text{der}}(\omega)$. In this case, the microscopic origin of this peak has to be conductivity relaxation since, in highly conducting materials, its appearance is mandatory, while the existence of dipolar relaxation or aggregates dynamics depends on the molecular peculiarities. Nevertheless, for example in ILs mixed with a non-ionic substance, as in section 6.2, the step in $\epsilon'(\omega)$ and consequently the peak in $\epsilon''_{\text{der}}(\omega)$ due to conductivity relaxation might be hardly resolved. Thus, it is important to check whether the BNN relation holds to ensure that conductivity relaxation is the molecular origin of the step or the peak, respectively. Such a check is shown in figure 5.1 for the IL $[N_{8,8,8,1}][NTf_2]$. There, the dielectric strength $\Delta\epsilon$ as well as the DC-conductivity σ_0 , which can both be read off the spectra in good approximation without any fitting procedure, are used to calculate the crossover frequency $\omega_c = 1/\tau_\sigma$ via

equation 5.1. It can be seen that ω_c is indeed located at the point where the DC-conductivity plateau transitions into the AC regime. Thus, the BNN-relation holds, indicating that the origin of the step in $\epsilon'(\omega)$ and then also the peak in $\epsilon''_{\text{der}}(\omega)$ is the conductivity relaxation.

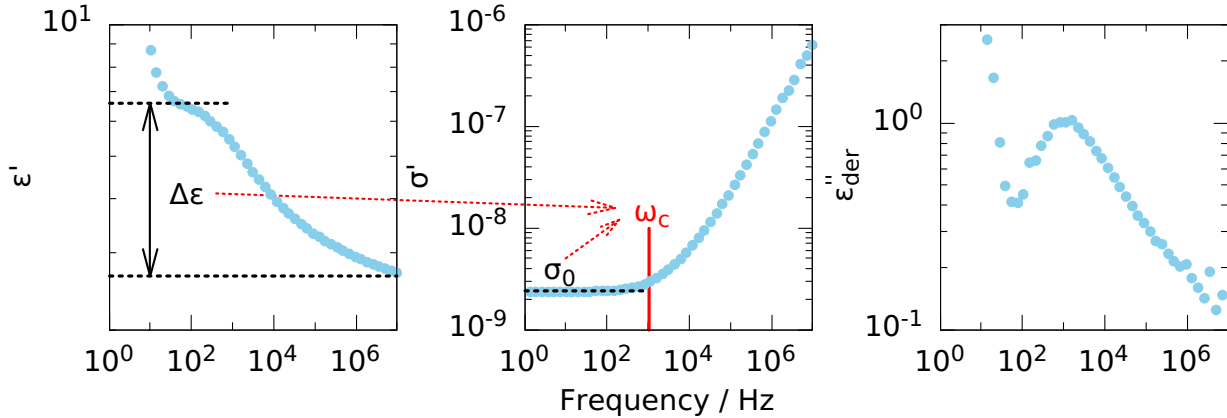


Figure 5.1.: Dielectric spectrum of $[\text{N}_{8,8,8,1}][\text{NTf}_2]$ at 220 K in three different representations. The model free determination of $\Delta\epsilon$ and σ_0 allows to calculate ω_c via the BNN relation (equation 5.1), which is shown to be located at the transition from DC- to AC-conductivity, indicating that the relaxational process is due to ion hopping.

Having assured that no other relaxational process than the conductivity relaxation is present in the dielectric spectrum, the modeling of this process can be addressed: A model which is often used to describe dielectric spectra of ILs is the random barrier model (RBM) developed by Jeppe Dyre and coworkers originally for glassy ion conducting materials. Two basic models were proposed by them, as detailed in reference [273] and references therein, a macroscopic and a microscopic one, in order to describe AC-conductivity. Both models are based on the idea of extreme disorder, which means that local mobilities cover many orders of magnitude. Both models have been solved in different approximations leading to different expressions for the conductivity spectrum. The equation probably used most frequently is

$$\sigma(\omega) = \frac{\sigma_0 i\omega\tau_\sigma}{\ln(1 + i\omega\tau_\sigma)}, \quad (5.3)$$

which was first derived in 1985 from the microscopic model and is named RBM85 in the following [274]. Later, it was also derived from the macroscopic model in percolation path approximation [273]. The microscopic idea underlying the RBM85 is to consider a disordered material as a lattice with randomly varying jump frequencies, i.e., the ions hop between sites, described by a hopping-time distribution, introduced in continuous time random walk approximation.

Two other expressions have been combined in what seems to be the most recent work in this area by Dyre and coworkers in 2008 (RBM08). Both expressions on their own could either not describe the conductivity data at high frequencies or low frequencies, respectively. However, in combination, a good description of simulation data was obtained [275]. The resulting equation is

$$\ln \left(\frac{\sigma^*}{\sigma_0} \right) = \frac{i\omega\sigma_0\tau_\sigma}{\sigma^*} \left(1 + 2.66 \frac{i\omega\sigma_0\tau_\sigma}{\sigma^*} \right)^{-1/3} \quad (5.4)$$

It can be seen that equation 5.4 has to be solved numerically, while equation 5.3 can be directly fitted to data. Thus, the RBM08 is only used rarely to describe experimental data. However, inconsistencies have been reported when using the RBM85 [91, 69]. These are manifested when converting the fit obtained in the $\sigma(\omega)$ representation to the $\epsilon'(\omega)$ representation. Although the conductivity data might be well described by the RBM85, the real part of the permittivity is not captured by the transformed fit in such a way that the dielectric strength is underestimated [91, 106, 69, 276]. The RBM08 is reported to overcome this inconsistency, and it was used to model dielectric spectra of a polymerized IL [69], of the archetypal glassy ion conductor CKN [63] and a lithium-chloride solution [277]. However, it should be emphasized that both the RBM85 and the RBM08 predict a universal shape of the conductivity relaxation process, irrespective of the temperature and substance under investigation. Although the conductivity spectra of different materials are indeed qualitatively very similar – even for the case of electronically conducting materials – it was already mentioned in Dyre's 1985 work that a universal shape is not observed in experiments. Therefore, it is necessary to have a model that incorporates a shape parameter, thus allowing for deviation from a universal shape.

To this end, the MIGRATION model, developed by Funke and coworkers, is discussed in the following based on references [278, 279, 280]. The acronym stands for MIsmatch Generated Relaxation for the Accommodation and Transport of IONs. The underlying physical picture is quite simple and illustrated in figure 5.2.

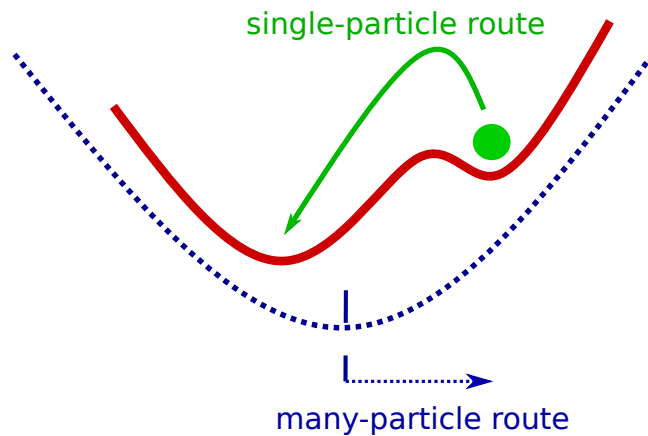


Figure 5.2.: Illustration of the single- and many-particle route of the MIGRATION model. Adapted from reference [280].

When an ion hops from its previous position to a new site, a mismatch is created between the new position of the ion and the ionic neighborhood. This mismatch can be reduced via two different hopping routes of the ions. On the single-particle route, the ion might hop backward to its original site, restoring the starting configuration, where no mismatch was present. This can be regarded as a correlated forward-backward movement. It implies that the ion has moved, but no charge has been transferred. The second route to reduce the mismatch is the

many-particle route, where the neighboring ions rearrange so that the mismatch created by the ion's hop is relaxed. The mathematical formulation of these model ideas is performed by introducing a rate equation for the correlation factor $W(t)$, which can be considered as the normalized time derivative of the mean square displacement or the normalized integral of the velocity autocorrelation function due to the ion hopping [279], as

$$-\frac{\dot{W}(t)}{W(t)} = -B\dot{g}(t) \quad (5.5)$$

where B is given by $W(\infty) = \exp(-B)$ and $g(t)$ is a normalized mismatch function for which the rate equation

$$-\frac{\dot{g}(t)}{g(t)} = \Gamma_0 W(t) N(t) \quad (5.6)$$

is introduced. In equation 5.6, Γ_0 is the elementary hopping rate. An empirical equation for the number of mobile ions available on the many-particle route $N(t)$ is given by

$$N(t) = N(\infty) + [Bg(t)]^\lambda. \quad (5.7)$$

The time-dependent correlation factor $W(t)$ can be considered the probability of finding the respective ion at time t in the position it jumped to at time $t = 0$. Hence, $W(\infty)$ is the small but not vanishing probability of a successful jump, i.e., a hopping process contributing to the DC-conductivity. Consequently, $W(t)$ decays from 1 at $t = 0$ to $W(\infty)$ at long times. The normalized mismatch function $g(t)$ can be regarded as the distance between the present position of the ion and the potential minimum at that time. Thus, due to the rearrangement of the neighboring ions, $g(t)$ decays from $g(0) = 1$ to $g(\infty) = 0$. As the time precedes, the number of neighboring molecules which are available for rearrangements on the many-particle route decreases due to the decreasing driving force $g(t)$ until at long times only the next neighbors $N(\infty)$ remain.

By combining equations 5.5, 5.6 and 5.7, a differential equation for $W(t)$ is obtained:

$$-\dot{W}(t) = \Gamma_0 W^2(t) \ln W(t) (N(\infty) + (\ln W(t))^\lambda) \quad (5.8)$$

The complex conductivity spectrum can be calculated by numerically solving equation 5.8 and inserting into equation 5.9 [278].

$$\frac{\sigma^*(\omega)}{\sigma_0} = 1 + i\omega \int_0^\infty \left[\frac{W(t)}{W_\infty} - 1 \right] \exp(-i\omega t) dt \quad (5.9)$$

Thereby, the elementary hopping rate Γ_0 is replaced by the rate of successful hops $\omega_0 = \Gamma_0 W_\infty$. This equation can then be directly fitted to experimental conductivity data, but of course also in other data representations, as indicated by equation 3.20. Besides the high-frequency permittivity ϵ_∞ , which has to be considered in some representations, and the DC-conductivity σ_0 , i.e., the plateau value in $\sigma'(\omega)$, three fitting parameters are inherent to the MIGRATION model. The hopping rate ω_0 is located at the crossover from DC- to AC-conductivity, similar, but not equal, to ω_c from the RBM. Therefore, in this work the time constants from the MIGRATION

model are not taken as $1/\omega_0$, but – for better comparability – are taken from the peak maximum in $\epsilon''_{\text{der}}(\omega)$ as $\tau_\sigma = 1/\omega_{\max}$ or calculated via the BNN relation (equation 5.1), both usually giving identical results in the limits of the fitting errors. The other two parameters, λ and $N(\infty)$, influence the shape of spectra, which is shown in figure 5.3. Dielectric model spectra are shown where the shape parameter λ is varied between 0.25 and 1.25 in the left and the middle column. In the left column this is shown for a fixed value of $N_\infty = 0$ and in the middle column for $N_\infty = 0.01$. In the right column the influence of N_∞ is shown for a fixed value of $\lambda = 1.00$.

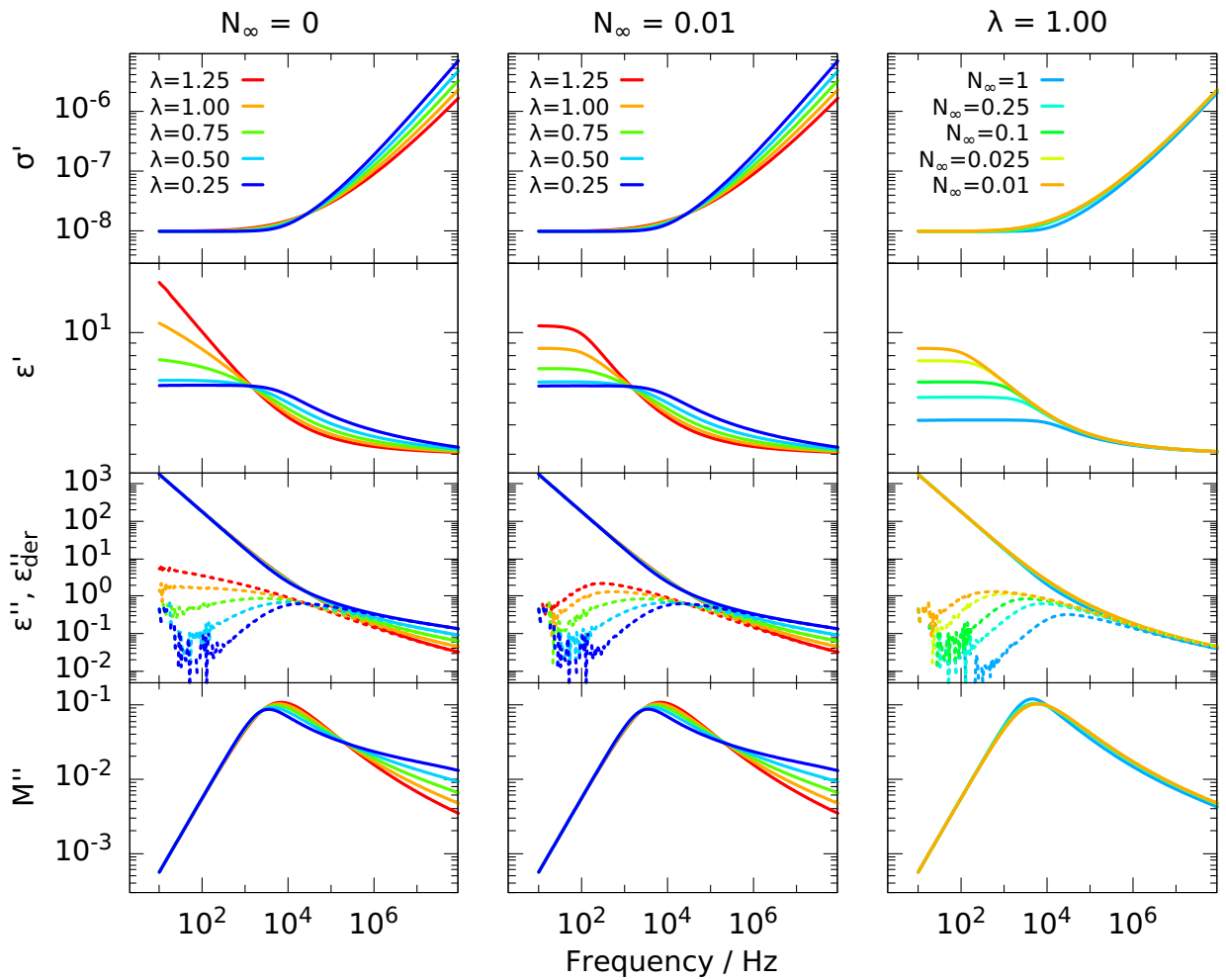


Figure 5.3.: Illustration of the changes in the spectra of the MIGRATION model upon variation of the parameters.

It can be seen that the differences between these two columns are limited to the real part of the permittivity and thus naturally also to $\epsilon''_{\text{der}}(\omega)$. Thus, the influence of changes in λ should be addressed. The slope of the AC-conductivity decreases with increasing λ . This also influences the region of the transition from DC- to AC-conductivity in such a way that it is ascending steeper in the case of lower λ -values. At the same time, the broadening of the relaxational step

in $\epsilon'(\omega)$ and thus also the broadening of the relaxation peak in $\epsilon''_{\text{der}}(\omega)$ increases with decreasing λ . This behavior is reminiscent of fitting models like the CD function, where a decreasing shape parameter β_{CD} also leads to a broadening of the relaxation peak. Additionally, the slope of the high-frequency flank in $M''(\omega)$ increases with increasing λ .

The parameter $N_\infty \neq 0$ was introduced in reference [278] because it was found that the predecessor of the MIGRATION model, the so-called concept of mismatch and relaxation (CMR), was not able to describe the low-frequency behavior of the permittivity $\epsilon'(\omega)$. However, it described the data in conductivity representation rather well. Unlike the case of the RBM85, where the real part of the permittivity is underestimated at low frequencies concerning experimental spectra, in the case of the CMR $\epsilon'(\omega)$ diverges at low frequencies for λ values around unity and above. This is rectified by introducing $N_\infty \neq 0$, and a low-frequency plateau is obtained, irrespective of the λ value. However, for the λ -values lower than unity in figure 5.3, it is clear that the plateau is readily obtained also for $N_\infty = 0$ and these spectra hardly change upon introducing a non-zero N_∞ .

The spectral changes under variation of N_∞ are shown in the right column of figure 5.3. It can be seen that the changes in $\sigma'(\omega)$ and $M''(\omega)$ are only marginal, while the low frequency plateau in $\epsilon'(\omega)$ decreases with increasing N_∞ accompanied by a shift of the peak frequency in $\epsilon''_{\text{der}}(\omega)$ to higher frequencies. It should be emphasized that although an increasing λ -value with constant N_∞ leads to similar behavior of the permittivity plateau as a decreasing N_∞ -value with constant λ , the shape of the spectrum is otherwise hardly changed by varying N_∞ , while it changes markedly by varying λ . Thus, it is possible to discriminate between the two scenarios by fitting them to experimental data. Moreover, the number of nearest neighbors N_∞ is expected to be material-dependent but not temperature-dependent, which is not always observed experimentally [279].

To find out which of the three models described above is best suited to describe the conductivity relaxation of the ILs in this work, $[\text{N}_{8,8,8,1}][\text{NTf}_2]$ is chosen, where the only relaxational process present in the dielectric spectrum is the conductivity relaxation as shown in figure 5.1. It should be noted that the MIGRATION model and the RBM are based on very different theoretical grounds, but it is not clear *a priori* which one should be used to describe the experimental data. As mentioned above, the RBM85 is the easiest to use, while the MIGRATION model has a shape parameter, allowing to fit experimental data with a shape different than the universal RBM shape. Thus, the spectrum of $[\text{N}_{8,8,8,1}][\text{NTf}_2]$ is shown in six different representations in figure 5.4 at 215 K together with fitting curves of the three models as indicated. Of course, the values of the fit parameters are the same in all representations for the respective model.

The solid black line denotes the MIGRATION model, where a power law was added to describe the low-frequency increase in the permittivity representation due to electrode polarization. The data is described perfectly in all six representations. The parameter N_∞ was set to zero since the λ parameter is markedly lower than one in this IL, which means that no divergence is obtained in $\epsilon'(\omega)$. Thus there is no need for introducing a N_∞ different from zero. The RBM85, as indicated by the green dashed line, is able to describe the data in $\sigma'(\omega)$ and $M^*(\omega)$ as good as the MIGRATION model. However, it fails to simultaneously describe the data in the $\sigma''(\omega)$ and the permittivity representation. The inaccuracy is such as already mentioned above, namely the plateau in $\epsilon'(\omega)$ is underestimated, consequently the peak in $\epsilon''_{\text{der}}(\omega)$ is not captured by the model. The RBM08, on the other hand, does not underestimate the dielectric strength, as can

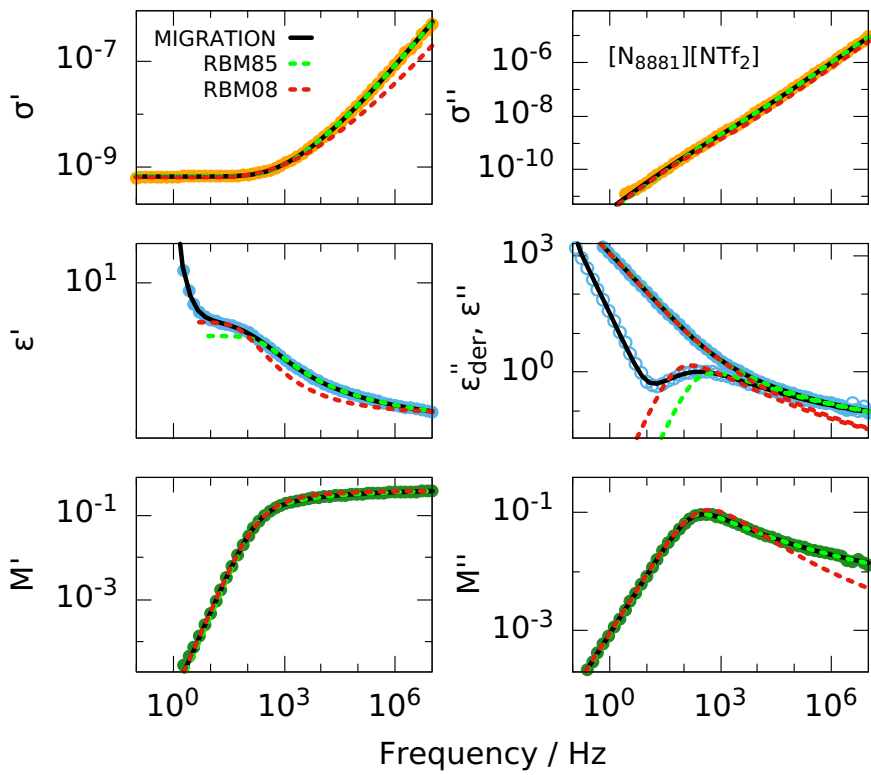


Figure 5.4.: Dielectric spectra of $[N_{8,8,8,1}][NTf_2]$ in six different representations. Black lines are fits with the MIGRATION model (equations 5.9 and 5.8). Green dashed lines are fits with the RBM85 model (equation 5.3) and red dashed lines are fits with the RBM08 model (equation 5.4), each fit with the same values for all parameters in all representations.

be seen by the red dashed line. However, its shape does not fit the data, leading to unacceptable descriptions in all representations. Hence, as a result of this comparison, the MIGRATION model seems to be the most suitable to describe the conductivity relaxation, primarily because of its flexibility to adopt different shapes through the shape parameter λ . In order to show that this holds not only for the one temperature shown in figure 5.4, data from 255 K to 200 K are shown in 5 K steps in figure 5.5 with MIGRATION fitting curves as black lines.

It can be seen that the description of the data by the model is excellent for all temperatures and in all six data representations. Just at the lowest temperature, a slight deviation between the model and the data is observed at high frequencies in the $\epsilon''_{\text{der}}(\omega)$ and $M''(\omega)$ representation, which is most probably due to a small contribution of a secondary relaxation, not included in the fit. As a consequence of the success of the MIGRATION model to describe the conductivity relaxation, it is used in this work for this purpose. It should be noted that the model is mainly used by the authors who were involved in its development, a fact which might be due to the difficulty of implementing the model. On the other hand, there seems to be criticism about the theoretical foundations of the model, which, however, are not published to the best of the author's knowledge. Therefore, the criticism can not be reconstructed here, and the model is

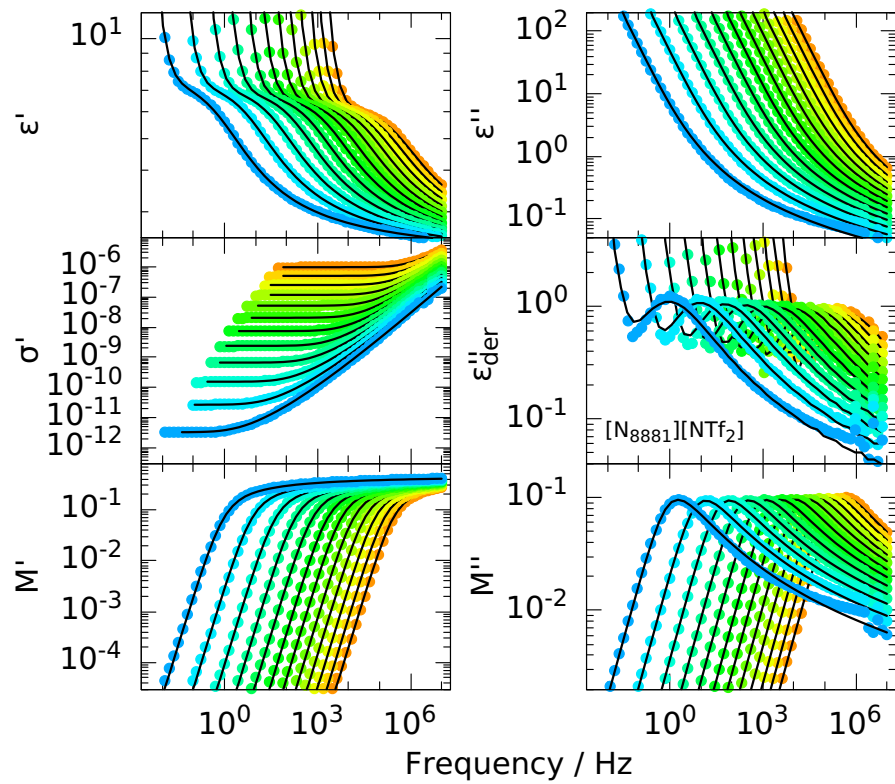


Figure 5.5.: Temperature dependent dielectric spectra of $[N_{8,8,8,1}][NTf_2]$ in six different representations from 255 K to 200 K in 5 K steps. Black lines are fits with the MI-GRATION model (equations 5.9 and 5.8) and an additional electrode polarization contribution in $\epsilon^*(\omega)$.

used with the justification that it describes the conductivity relaxation very well.

5.2. Chain length dependent separation of ion dynamics

In this section, the possibility is explored of whether or not the dynamic contributions of cations and anions might show up as separated peaks in the BDS or DLS spectra. In the case of non-ionic binary mixtures, this happens when the dynamic contrast between the two constituents is large enough. An example of such a DLS spectrum is seen above in figure 4.8, where the small toluene molecules are mixed with large squalane molecules. Thus, separated anion and cation dynamics might be expected to appear when their size difference becomes large enough. Therefore, evidence for separately visible cation and anion dynamics is carefully collected in this section, starting with DLS measurements. After that, the influence on the BDS spectrum and the calorimetric glass transition step is addressed.

5.2.1. Light scattering

Homologous series of ILs, where the anion is kept fixed, and the length of one or more alkyl chains of the cation is altered, were used in the literature to explore the minimal length of the alkyl chains needed for structural or dynamical evidence of nanoscale aggregates to show up [73, 107, 281, 282, 283]. For the case of imidazolium-based ILs, although they are certainly one of the most investigated families of ILs and were the first ones where experimental evidence for nanostructurization was found [73], a systematic dynamic study with light scattering or dielectric spectroscopy lacks. This is also because these ILs are prone to crystallization from chain lengths starting from around nine carbon atoms, depending on the anion. However, as light scattering studies can be performed above the melting point utilizing the Tandem-Fabry-Pérot interferometer (TFPI), this is done here for the series of imidazolium cations $[C_n C_1 Im]$ combined with the $[NTf_2]$ anion, using chain lengths of $n = 3, 6, 8, 10, 12$ carbon atoms. Some of the results of this section are published in reference [188].

It should be noted that in order to shift the rotational dynamics of the highly viscous long-chained ILs into the frequency window of the TFPI, temperatures far above room temperature have to be chosen. One has to keep in mind that the X-ray scattering intensity of the pre-peak is found to decrease with increasing temperature up to room temperature in a study where temperature-dependent X-ray measurements of imidazolium-based ILs are reported [73]. This might indicate that the structurization diminishes at high temperatures and may not be detectable in TFPI measurements for this reason. However, for other ILs, X-ray data was reported at temperatures comparable to the one used here for the imidazolium ILs, and it was shown that the pre-peak is still visible, i.e., the nanostructures are still present at such high temperatures [281, 284]. Thus, although the nanostructurization might be less pronounced at high temperatures, it could still exist in the case of the imidazolium-based ILs studied in this section.

In figure 5.6 a master plot is shown, where the spectra of the ILs with alkyl chain lengths as indicated are scaled in such a way that they superimpose on the low-frequency flank. In this way, it is seen most clearly that the spectrum broadens upon lengthening the alkyl chain or even gets bimodal, as can be seen by eye for the case of $n = 12$.

Thus, one might think of two different interpretations of this finding: Either two relaxational processes exist in each IL, which separate more and more with increasing chain length, or a

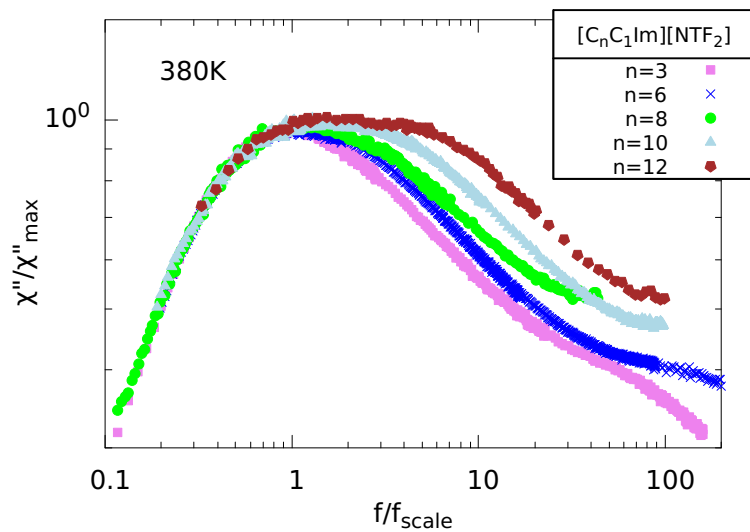


Figure 5.6.: Shifted TFPI spectra for different alkyl chain lengths, showing broadening of the spectrum with increasing number of carbon atoms in the chain. At $n = 12$, a clear bimodal spectrum can be seen.

second process appears for chain length $n > 3$, which gets more intense and more separated for higher n . It is clear that regarding the latter scenario, an appearance of an additional process on the high-frequency side is suggested by the scaling performed in figure 5.6. However, a scaling such that the high-frequency flanks superimpose would suggest an appearance on the low-frequency side. Such an additional process appearing on frequencies lower than the α -relaxation for chain length $n > 4$ perfectly matches the expectation one has for a dynamical contribution stemming from nanoscale aggregates, which are naturally larger and thus slower than a single molecule. Also, in view of previous interpretations in the literature, where a second process appearing in light scattering or dielectric spectra was almost always attributed to dynamics of aggregates (except for secondary relaxations, of course), as detailed in section 2.2, these findings fit in the overall picture.

Nonetheless, this assignment must not be made too hastily. One should first check whether the features of the slow dynamic process match with those of the pre-peak as found by X-ray scattering, as the latter is the most direct method to probe the nanostructurizaton. As mentioned above, the pre-peak gets more intense upon decreasing temperature and shifts to lower scattering vectors, indicating an increasing size of the aggregates. This implies that for the shape of the light scattering spectrum, if indeed the slow dynamic process can be ascribed to aggregates, it should be temperature-dependent so that the low-frequency process increases in intensity and separates more from the α -process with decreasing temperature. The latter can be rationalized because the aggregates increase in size in relation to a single molecule responsible for the α -process, which should lead via equation 2.2 to a relative slowing down of the aggregate process. Although this picture might be oversimplified, a trend in this direction should be observable when examining the temperature-dependent spectra. However, the temperature range accessible with the TFPI might not be enough to see any effect. Therefore,

low-temperature measurements with the PCS setup are needed, which – as mentioned above – is difficult or impossible for the two ILs with chain lengths $n = 10, 12$, respectively, due to crystallization. Hence, a masterplot of the spectra for $[C_8C_1Im][NTf_2]$ is shown for a temperature range of nearly 200 K in figure 5.7, along with a superposition of the spectrum at 400 K and at 210 K for the case of $[C_{10}C_1Im][NTf_2]$. There, 210 K was the only temperature at which the dynamics was well located in the PCS time window while a sufficient long measuring time was feasible before crystallization set in.

It can be seen that for $n = 8$, the spectrum slightly narrows upon decreasing temperature. This behavior disagrees with the expectation put forward above that the spectrum should rather broaden on cooling due to the increasing separation of the dynamics of the aggregate from the α -process if this picture is not too simplistic. In the case of $n = 10$, it is evident that the shape of the main peak hardly changes between the two temperatures, which are separated by 190 K. Instead, it seems that on the low-frequency flank of the 210 K spectrum, a weak additional process has appeared, which is absent in the 400 K spectrum. Although it can not be excluded that this slow process is a kind of dynamical sign of the emerging crystallization, in light of the observations discussed in section 5.3, it might be attributed to dynamics of the aggregates, getting visible only at low temperatures. Together, these results point into the direction that the broadening or emerging bimodality of the main peak with increasing chain length as seen in figure 5.6 is not due to aggregates dynamics arising and separating from the α -relaxation in the case of longer alkyl chains.

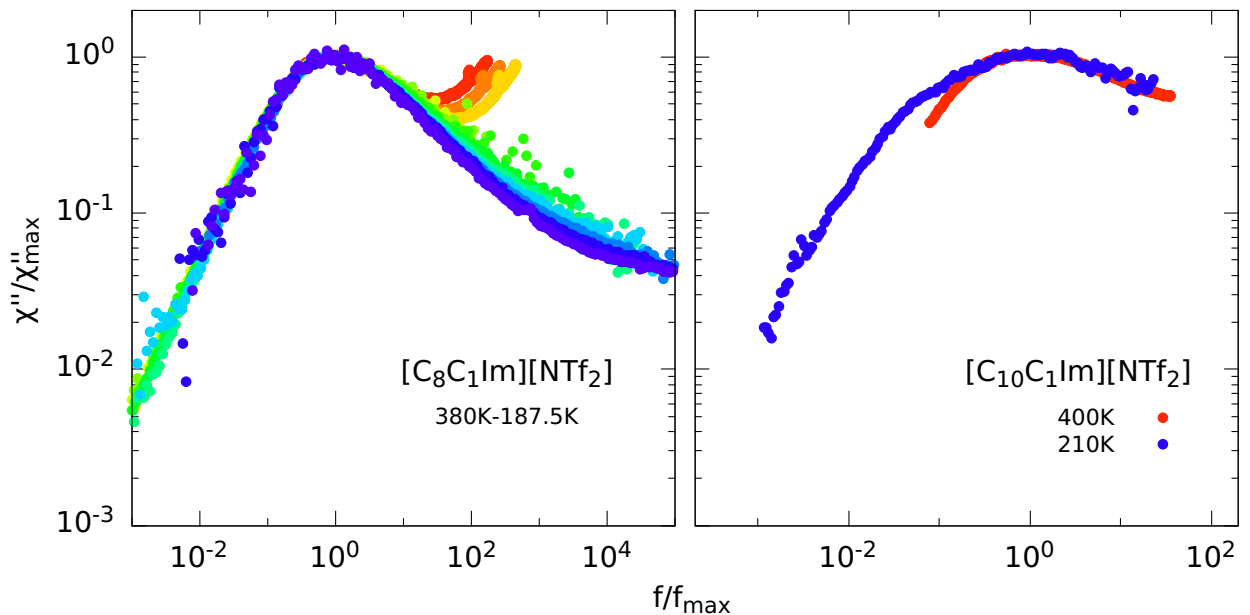


Figure 5.7.: A master plot of $[C_8C_1Im][NTf_2]$ is shown for a temperature range of nearly 200 K on the left hand side. A slight narrowing with decreasing temperature can be seen. On the right hand side, two spectra of $[C_{10}C_1Im][NTf_2]$ are shown for temperatures 190 K apart. At 210 K, an additional contribution on the low frequency flank appears.

Thus, an alternative explanation for this observation has to be found. Therefore, it is instructive to come back to the second interpretation of the spectra as mentioned above, namely that two dynamical processes are already present in the case of $n = 3$ and get separated for increasing chain length. This interpretation might be rationalized by considering that ILs are naturally a mixture of two kinds of molecules. As it was shown in figure 4.8, a mixture of a large and a small molecule can exhibit a bimodal spectrum, where the two relaxational processes reflect the dynamics of the two sorts of molecules, or in the case of two molecules with only slightly different sizes, a broadening of the spectrum of the mixture with respect to the spectra of the components can be observed as seen in figure 4.7. So why should this not be possible in the case of ILs, when the difference in size between the cation and anion gets large enough? To the best of the author's knowledge, such an interpretation of light scattering spectra of ILs was not reported in the literature so far. Hence, evidence will be carefully collected to support this interpretation in the following.

At first, nuclear magnetic resonance (NMR) measurements from the literature should be briefly considered, as NMR is a versatile experimental technique where the rotational dynamics of molecules can be monitored. The main advantage is that the dynamics of different nuclei can be accessed separately, which is especially useful in the case of ILs to probe the dynamics of cations and anions selectively. This is done by choosing ^1H and ^2H NMR for the $[\text{C}_n\text{C}_1\text{Im}]$ cations and ^{19}F NMR for the $[\text{NTf}_2]$ anion in reference [8]. There, the time constants of the $[\text{C}_8\text{C}_1\text{Im}]$ cation are slightly larger than those of the anion at high temperatures in the range of the TFPI data and merge at lower temperatures. Moreover, at temperatures near the glass transition temperature, not only the time constant but also the shape of the PCS and ^2H -NMR measurements are virtually identical, as can be seen, by plotting the respective correlation decays of both measurements on top of each other as done in reference [8]. Thus, at least qualitatively, the NMR results are in line with interpreting the light scattering spectra of $[\text{C}_8\text{C}_1\text{Im}][\text{NTf}_2]$ shown in figure 5.7 as being due to cation and anion dynamics separated at high temperatures, which merge at low temperatures, resulting in a narrowing of the spectrum. A quantitative comparison of the light scattering and NMR time constants is difficult because the dynamics of the anions and cations are so little separated that for fitting the light scattering spectrum of $[\text{C}_8\text{C}_1\text{Im}][\text{NTf}_2]$ with two processes, their shapes or relaxation strengths have to be fixed to more or less arbitrary values, which greatly influences the obtained time constants. In the case of $[\text{C}_{12}\text{C}_1\text{Im}][\text{NTf}_2]$, where a more robust fitting procedure is possible due to the visibly separated processes, no rotational time constants from NMR measurements for cations and anions are reported.

Scattering intensity

Thus, more information about the strength and shape of the two processes should be obtained to confirm their origin due to cations and anions. From knowing the optical anisotropies of cations and anions, the strengths of the two light scattering processes are directly accessible, as seen in section 4.1. As mentioned above, this whole section about light scattering intensities was inspired by the quest for obtaining the correct scattering intensities of cations and anions. Here, the ILs with alkyl chain lengths of $n = 3, 8, 10, 12$ and additionally $[\text{C}_8\text{C}_1\text{Im}][\text{BF}_4]$ were measured in comparison to toluene. The reason for including $[\text{C}_8\text{C}_1\text{Im}][\text{BF}_4]$ is that the $[\text{BF}_4]$

anion is optically isotropic. Thus, no contribution to the light scattering spectrum from this anion is expected in contrast to the optical anisotropic $[\text{NTf}_2]$ anion. To be able to connect the peak strengths, i.e. the pre-factor of the CD function $\Delta\chi_\alpha$, to the optical anisotropy parameter $\langle\beta_{\text{eff}}\rangle$, the following procedure was performed: At first, the linear relationship between $\Delta\chi_\alpha T$ and $L^2 N \langle\beta_{\text{eff}}\rangle^2$ found for the 13 van-der-Waals liquids in figure 4.9 was used in connection with the $\langle\beta_{\text{eff}}\rangle$ values calculated for the conformer ensemble of each cation and the $[\text{NTf}_2]$ anion found by CREST to calculate $\Delta\chi_\alpha$ for each ion. Then, a fit to the spectrum of each IL was performed using these strength parameters. It was necessary to introduce a correction parameter c to the strengths of the cations in order to obtain satisfactory fits so that the strength of the cations is given by $c \Delta\chi_\alpha^{\text{cation}}$. The introduction of the additional parameter could be rationalized by the fact that the optical anisotropy parameters of the different conformers of the respective cation differ significantly so that an erroneous identification of the lowest energy conformer by CREST leads to a $\langle\beta_{\text{eff}}\rangle$ value which is not in accordance with experiment. This issue was already discussed in detail in section 4.1. For the case of the $[\text{NTf}_2]$ anion, the different conformers have very similar optical anisotropy parameter, thus $\langle\beta_{\text{eff}}^{\text{anion}}\rangle$ was fixed. The resulting fits can be seen in figure 5.8, where the solid line is the total fit comprised of a CD function for each cation and anion and a power-law accounting for the fluorescence contribution or two harmonic oscillators for the microscopic dynamics in the case of $[\text{C}_3\text{C}_1\text{Im}][\text{NTf}_2]$. The dashed lines are the cation and anion contributions. The spectra are plotted on an absolute y-scale with respect to toluene and shifted on the x-axes for better visibility.

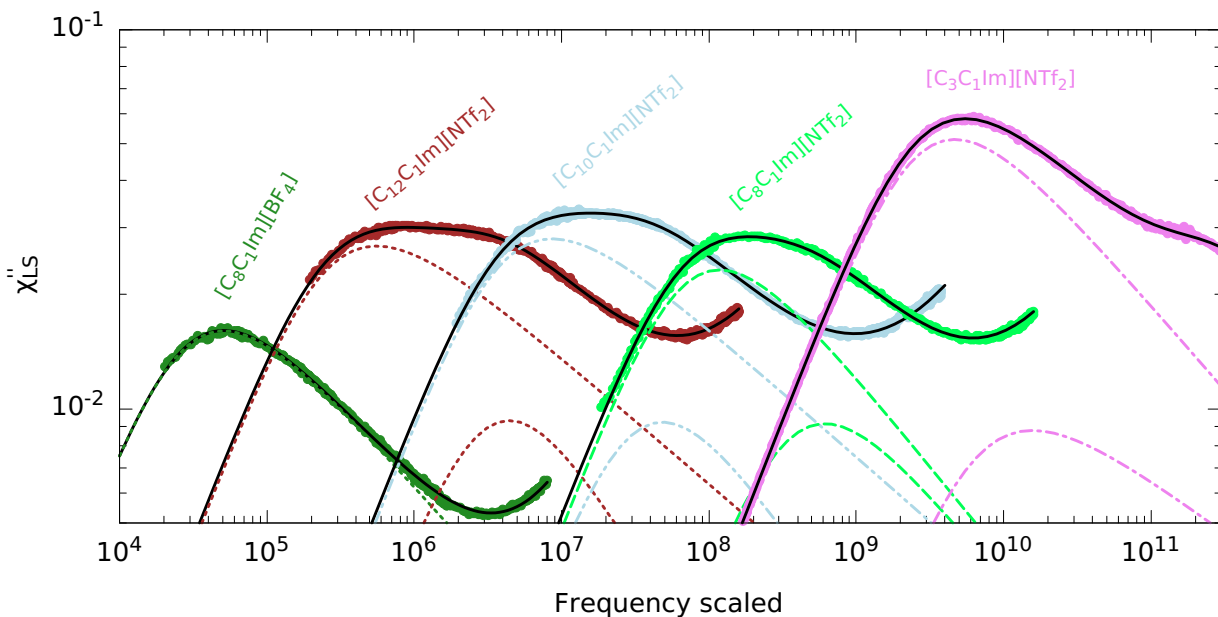


Figure 5.8.: Comparison of the intensity of several ILs. The spectra are plotted on an absolute y-scale with respect to toluene and shifted on the x-axes for better visibility. Solid and dashed lines show the total or the components of the fits, respectively.

It can be seen that the fits are able to reproduce the experimental data excellently. The shape parameter of the CD function was left as free fitting parameters, as no information is available

a priori, which could be used to fix the shape.¹ Nevertheless, all shape parameters were found to be in a reasonable range, i.e., between approximately 0.3 and 0.65. From the correction parameter c obtained by the fit, the experimental optical anisotropies were calculated. These are compared to the calculated values in figure 5.9, where the error bars of these values are taken as the minimal and maximal value of the optical anisotropy found in the conformer ensemble within an energy of $\Delta E = 1 \text{ kcal/mol}$. The black solid line marks the equality $\langle \beta_{\text{eff}}^{\text{exp}} \rangle = \langle \beta_{\text{eff}}^{\text{DFT}} \rangle$.

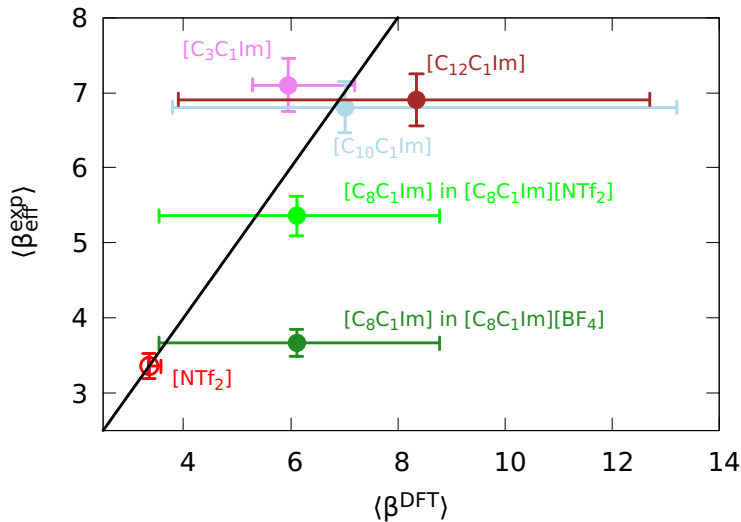


Figure 5.9.: Comparison of the calculated and experimental anisotropy parameters for the ILs shown in figure 5.8. The error bars on the x-axis denote the minimal and maximal β^{DFT} parameter of the respective conformer ensemble.

It can be seen that the correlation between the calculated and the experimental values is only moderate. However, within the – admittedly very large – uncertainties regarding the calculated optical anisotropies, the experimental values agree with calculated ones. The largest discrepancy is found for the [C₈C₁Im] cation in the IL [C₈C₁Im][BF₄], while in [C₈C₁Im][NTf₂] the deviation is markedly smaller. A reason for this might be that it is easier in the case of [C₈C₁Im][BF₄] to bend the alkyl-chain of the cation over the imidazolium-ring, resulting in a scorpion-like conformer, while the [NTf₂] anion seems to prevent such a bending. This behavior was found under high pressure by X-ray scattering and MD-simulations [285, 286, 287, 288], thus, it is unclear if this tendency is already present at ambient pressure. However, if this is the case, than it could explain the difference in the $\langle \beta_{\text{eff}}^{\text{exp}} \rangle$ value of the [C₈C₁Im] cation between the IL with [BF₄] and [NTf₂] anion since the curled conformer naturally has a lower optical anisotropy than the extended one. This is, of course, not reflected in the single-molecule DFT calculation, where no influence of the anion is involved.

The second-largest deviation of the experimental β value from the calculated one is found for

¹Please note that these measurements were performed at temperatures much higher than the glass transition temperature; thus, a generic shape, as discussed in section 4.2, can not be expected here.

$[C_3C_1Im][NTf_2]$. There, a detailed look at the conformer ensemble is possible due to the short alkyl chain, and it can be examined whether indeed an inaccurate weighting of the different conformers is responsible for the deviation. Three conformers can be identified: The all-trans conformer with extended alkyl-chain and two conformers with bended alkyl-chain, gauche+ and gauche-. The g+ conformer was identified as the one with the lowest Gibbs free energy. This resulted in a population of 47% : 30% : 23% for g+ : trans : g-. In contrast, a study from the literature found the all-trans conformer as the most stable one with a resulting population of the conformers of 17% : 43% : 40% [289]. From this, one obtains a mean β -value higher than that shown in figure 5.9, highlighting the importance of the correct conformer ensemble again. Nevertheless, it was found by comparing experimental Raman spectra with DFT-calculated Raman frequencies that the two gauche conformers are present, while a "large concentration" of the all-trans conformer is also detected [289]. A quantitative population analysis of the experimental spectrum was not given. Thus, when assuming a higher trans-population than obtained by DFT-calculations of the present study, the calculated β -value could be brought into accordance with the experimental one in the limits of the intensity uncertainty.

Additionally, a correlation factor $g_2 \neq 1$ might be present in the experiment, through which the effective optical anisotropy might differ from the calculated one. However, in the rare cases where correlation factors of ILs are reported in the literature, these are Kirkwood factors g_1 , which were found to be slightly below one for imidazolium-based cations with a chain length of $n = 4$, indicating anti-parallel ordering of the dipole moments [290]. As the dipole moment of an imidazolium-based cation lies in the plane of the ring, just as the main axis of the polarizability tensor does in cases of a short alkyl chain, this means for the g_2 correlation factor that it should be above one when $g_1 < 1$, simply speaking. Thus, for the case of $[C_3C_1Im][NTf_2]$, an orientation correlation is reasonable, which might be responsible for a larger effective anisotropy parameter than the one found by DFT calculations. For longer alkyl-chains, it is likely that the influence of the imidazolium ring on the ordering of the molecule reduces, and effects like π -stacking play a less important role due to the increasing influence of the alkyl chain.

As discussed in section 4.1, information about the correlation factor g_2 can be easily obtained also for highly flexible molecules, where the exact value of the anisotropy parameter can not be well determined from DFT calculations by considering the temperature dependence of the scattering intensity. Therefore, temperature-dependent light scattering data for $[C_3C_1Im][NTf_2]$ are shown in figure 5.10, where the TFPI data are recorded in the intensity consistent way, and the PCS data are shifted vertically such that they extrapolate smoothly to the TFPI data, as indicated by the dashed lines between the two data sets. It is clear that the heights of the α -peaks decrease with decreasing temperature. It was also tried to perform the shifting according to the Curie law, i.e., to fix the height of the PCS spectra according to $\Delta\chi T = const.$, as it was done in reference [179] for 1-phenyl-1-propanol. However, this led to unphysical kinks between the TFPI and PCS data. Therefore, albeit there is, of course, some degree of freedom when shifting the PCS data, the general trend of decreasing relaxation strength is inherent to this data set.

That there is no prominent β -process in the spectra as it is the case for 1-phenyl-1-propanol, which would render the linear interpolation erroneous, can be seen by the fact that a very weak secondary peak shows up only below the glass transition temperature, i.e., when the strong

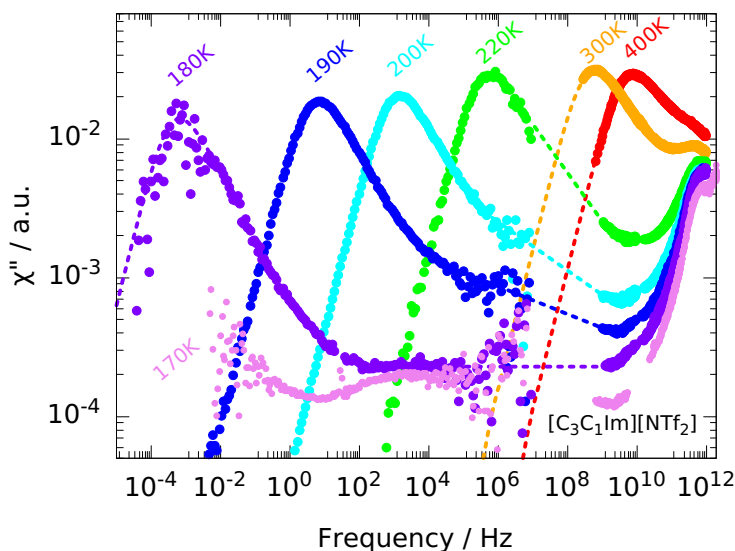


Figure 5.10.: Temperature dependent DLS spectra of $[C_3C_1\text{Im}][\text{NTf}_2]$. The TFPI data are measured with correct relative intensities and the PCS data are shifted vertically in such way that they extrapolate smoothly to the TFPI data, as shown by the dashed lines.

α -relaxation has shifted outside the frequency window, as seen in the 170 K spectrum. Its frequency position and strength render it unlikely that a noteworthy β -relaxation contribution is present in the frequency range of the interpolation. From these spectra, the peak areas are calculated and plotted as $\Delta\chi T$, which is proportional to the scattering intensity as seen in equation 4.13, in dependency of the temperature in figure 5.11. Around room temperature, TFPI measurements were performed in small temperature steps, as the peak intensity already started to decrease in this range. It can be seen that above room temperature, the $\Delta\chi T$ values are constant within the limits of uncertainty, while they decrease markedly on lowering the temperature. The error bars indicate the uncertainty of the absolute intensities due to the TFPI measuring procedure.

These results indicate no orientational correlations above room temperature since the $\Delta\chi T$ values do not change upon increasing the temperature, as would be expected when orientational correlations diminish at high temperatures. Moreover, below room temperature, there is a tendency of perpendicular ordering of the molecules – in the simple picture – as can be seen by the decreasing intensity with decreasing temperature. This means that a correlation factor $g_2 > 1$ can be excluded to be the origin of the difference of the anisotropy factor β found by experiment and DFT calculation for the case of $[C_3C_1\text{Im}][\text{NTf}_2]$.

Together, this means – at least – that from the point of the intensities, the light scattering spectra are not in conflict with the idea that the two relaxational processes can be ascribed to the cations and anions. Unfortunately, no stronger statement can be made in this regard since the differences in the optical anisotropies of the various conformers are quite large, and thus the mean β value is highly sensitive to the population of the different conformer.

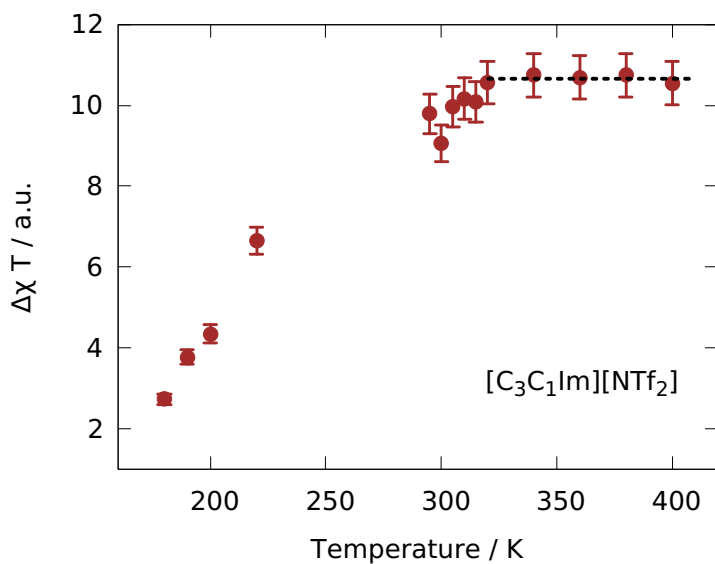


Figure 5.11.: Intensity $\Delta\chi T$ of the DLS data as a function of temperature. Dashed line is a fit with a constant to the values of the five highest temperatures.

Influence of the anion

As a further test, a closer look at the shape of the light scattering spectra of samples without the optical anisotropic $[\text{NTf}_2]$ anion should be taken in the following. When replacing this anion with the optical isotropic $[\text{BF}_4]$, the anion contribution in the light scattering spectrum should vanish, and just the cation contribution should remain. Additionally, it is possible to choose a non-ionic molecule similar to the respective cation and see if its shape resembles the IL with the optical isotropic anion, which is done in the following. The spectra of the ILs with $n = 8, 12$, each with $[\text{BF}_4]$ and $[\text{NTf}_2]$ anion, are compared to the one of octylimidazole (C_8Im) and dodecylimidazole (C_{12}Im), i.e., the non-ionic counterparts of the respective cations. The spectra of the imidazoles were measured during the master thesis of Rolf Zeißler, supervised by the present author. In figure 5.12, the structures of C_8Im and $[\text{C}_8\text{C}_1\text{Im}]$ are shown for a visualization of the differences.



Figure 5.12.: 1-Octylimidazole (C_8Im) on the left and 1-octyl-3-methylimidazolium $[\text{C}_8\text{C}_1\text{Im}]$ on the right.

It can be seen that the only difference is the methyl-group on the second nitrogen atom present for $[\text{C}_8\text{C}_1\text{Im}]$, which is absent in the case of C_8Im . Therefore, it can be expected that the spectral shapes of the two molecules should be very similar. The same holds for the pendants

with $n = 12$. The spectra of the six substances are shown in figure 5.13, where in the top row, a masterplot is shown, highlighting the differences in the spectral shapes best. In the lower row, the spectra are shown separately with corresponding fits. The substances with alkyl chain lengths of $n = 8$ are shown in the left column. It can be seen that the spectra of $[C_8C_1Im][BF_4]$ and C_8Im almost perfectly superimpose and then naturally, the shape parameter from the fit with a CD function are virtually identical. In marked contrast, the spectrum of $[C_8C_1Im][NTf_2]$ is broader, indicating that a contribution is present in this IL, absent in the other two substances. This is the most substantial evidence that indeed the optical anisotropic $[NTf_2]$ anion is responsible for the additional relaxation process since the $[BF_4]$ anion is not visible in the light scattering spectrum due to its optical isotropy, and no second component is present in C_8Im at all.

However, another feature of molecules comprised of a ring structure as a head group and a long alkyl tail has to be considered additionally: It was observed for phenyloctane, as one of the non-ionic liquids considered in section 4.1, that a bimodal spectrum shows up even in this neat liquid, which can be seen in figure B.1 in appendix B. As a first guess, when considering the molecular structure, one could imagine that one of the two processes might be due to the rotation of the phenyl-ring, while the other one is due to the relaxation of the whole molecule. If this simple picture is applicable, one could expect a similar contribution in the case of the imidazolium cations. Therefore, the master thesis by Rolf Zeißler was devoted, i.a., to elucidate the origin of the bimodal spectrum in the case of phenyl-alkanes and molecules with similar structures. It could be shown by systematically varying the length of the alkyl chain as well as by suitable mixing experiments that the faster process is due to the reorientation of the (phenyl)-ring. When taking a closer look at the spectrum of C_8Im in the left column of figure 5.13, one can see that there is a very tiny hump on the high-frequency flank, which can be ascribed to the rotation of the imidazole ring. The reason why this fast contribution is so weak in comparison to the fast contribution in phenyloctane can be rationalized by the fact that the ratio of the squared anisotropy parameter β of a phenyl-ring and an imidazole-ring is approximately 2.8 as obtained from DFT calculations, i.e., the light scattered by a phenyl-ring is almost three times more intense than that scattered by an imidazole-ring. The β^2 -value of an 1-methylimidazole ring as present in the imidazolium cations is only 1.5 times higher than that of the imidazole ring, which might explain the slightly broader peak of $[C_8C_1Im][BF_4]$ in comparison to C_8Im . It should be mentioned that the width of the phenyloctane spectrum is between that of $[C_8C_1Im][BF_4]$ and $[C_8C_1Im][NTf_2]$. Thus, although a dynamic contribution from the imidazolium ring might be present in the octylimidazolium ILs, it can not be responsible for the spectral differences of $[C_8C_1Im][BF_4]$ and $[C_8C_1Im][NTf_2]$.

When turning to the right column of figure 5.13, where the same comparison of the different substances is performed like in the left column, just for alkyl chain lengths of $n = 12$, one can see that the situation here is more complex. Now, a bimodal spectrum is clearly seen by eye for $[C_{12}C_1Im][NTf_2]$ as discussed above, but also for $C_{12}Im$, where the contribution of the faster process is weaker than for the IL. In the case of $[C_{12}C_1Im][BF_4]$, only one peak is observed, however, with a distinct broadening on the low-frequency flank. It can be modeled with an HN-function as shown in the lower panel. The other two spectra are fit with two CD functions to account for the two relaxational processes. The vertical dashed line marks the positions of these processes, and it can be seen that the separation of the peak maxima is almost identical

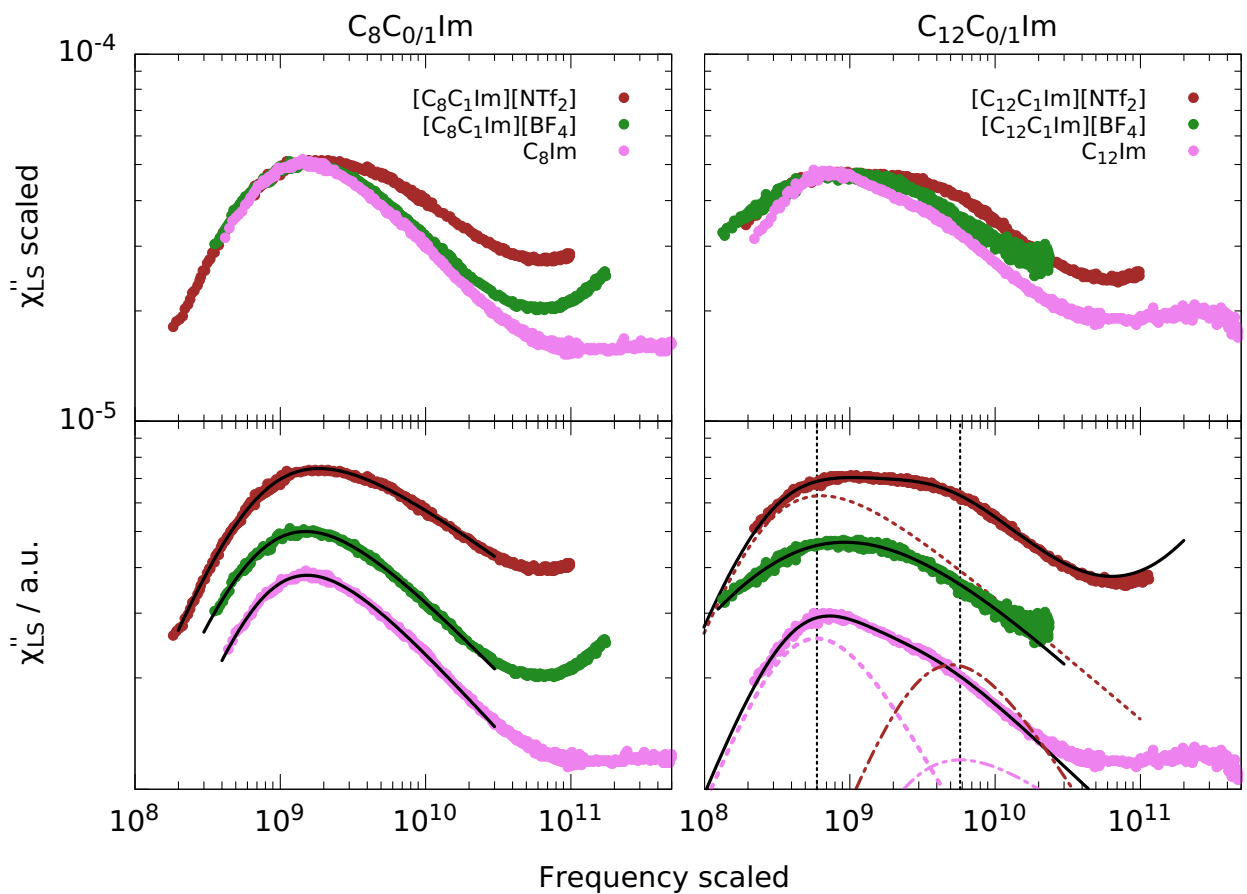


Figure 5.13.: Comparison of the spectra with $[\text{NTf}_2]$ and $[\text{BF}_4]$ anion to the alkyl-imidazole spectra. On the left hand side for octyl-chains and on the right hand side for dodecyl-chains. In the upper row the data is shown as a master plot to visualize the difference in shape, while in the lower row the data is shown with the components of the fits.

for C_{12}Im and $[\text{C}_{12}\text{C}_1\text{Im}][\text{NTf}_2]$. From the above discussion, it is clear that the fast, weak process in the spectrum of C_{12}Im is due to the rotation of the imidazole ring. In the IL $[\text{C}_{12}\text{C}_1\text{Im}][\text{NTf}_2]$, the fast process should then be considered as a superposition of the weak rotation of the imidazolium ring and the reorientation of the anion, which seem to take place on a very similar time scale. However, the contribution of the anion is strong, and the intensity of the high-frequency process can not be explained with the ring rotation alone, as the comparison with the C_{12}Im spectrum clearly shows. Thus, it seems that the $[\text{NTf}_2]$ anion and the imidazolium ring relax on very similar time scales, which is reasonable due to the Coulomb interaction between the ring and anion. The long, non-polar alkyl-chains are excluded from these polar regions and relax on slower time scales. In the case of $[\text{C}_{12}\text{C}_1\text{Im}][\text{BF}_4]$, the ring rotation seems to be too weak to be resolved and the isotropic anion does not contribute to the spectrum either. The broadening of the low frequency flank is reminiscent of that in $[\text{C}_{10}\text{C}_1\text{Im}][\text{NTf}_2]$ at

low temperatures shown in figure 5.7 and is similarly observed for $[C_8C_1Im][BF_4]$ as discussed in detail in section 5.3. Thus, its origin might be due to the dynamics of aggregates.

In conclusion, it has been shown in this subsection that the bimodality in the light scattering spectra found for the ILs with long alkyl chains in the series of $[C_nC_1Im][NTf_2]$ is mainly due to the dynamic contribution of the optical anisotropic cations and anions being separated in frequency. The strongest argument in favor of this is that the second relaxational process vanishes or markedly weakens when the $[NTf_2]$ is replaced by the optical isotropic anion $[BF_4]$ or when the spectrum of imidazole molecules are considered, respectively, which are structurally very similar to the cations. However, it also got obvious that light scattering can separately resolve motions from the ring, which appear on faster time scales than the dynamics of the whole molecule. The results of the intensity considerations and the NMR measurements from the literature are also in accordance with this picture. Therefore, as a next step, it should be investigated if the separation of the dynamics of cations and anions is also reflected in the spectra measured by dielectric spectroscopy and in the width of the glass transition step as measured by differential scanning calorimetry.

5.2.2. Dielectric spectroscopy and differential scanning calorimetry

It is known from the literature that in binary mixtures of non-ionic molecules, the dynamics of the two species might separate. This can lead to a broadened or bimodal dielectric spectrum and a broadening or splitting of the glass transition step measured by DSC [240]. Therefore, it is instructive to see if such behavior can also be found in ILs, with the knowledge from the preceding section that at least in light scattering spectra the separation is visible when the size of the cation is considerably larger than that of the anion. However, since the imidazolium-based ILs with long alkyl chains, where the separation of the ion dynamics is largest, are hardly supercoolable, other ILs with a marked difference in size of cations and anions have to be chosen for dielectric and DSC measurements. Additionally, some remarks concerning the dynamics, which are active in dielectric or DSC measurements and thus can broaden or separate, are in order: As detailed later in section 5.4.2, the rotational dynamics of anions are not resolved in the dielectric spectra, most probably due to their low dipole moment. Thus, only the reorientation of the cations can be detected in the dielectric spectra, at most. This means, of course, that no separation of rotational dynamics can be expected in the dielectric spectra. Therefore, only the translational motions, i.e., the ion hopping process as described by the MIGRATION model, is considered here in the case of dielectric spectroscopy. The glass transition step measured by DSC represents the freezing of dynamic degrees of freedom as they get slower than the time scale defined by the cooling rate. In principle, the glass transition step involves rotational and translational degrees of freedom. This is best seen by considering measurements on a system that can form a plastic crystal, such as ethanol [291, 292, 293]. There, it has been shown that the glass transition of the plastic crystal, i.e., the freezing of only rotational motions, is accompanied by a smaller change in the specific heat than the glass transition from the liquid state, where rotational and translational motion freeze jointly. Thus, a separation of the ion dynamics, regardless of whether rotational or translational, may be expected to show up as a broadening of the glass transition step since the degrees of freedom of the slower ions will freeze at higher temperatures than those of the faster ions.

To test these considerations, in a first step two ammonium-based ILs are chosen, one with short chains and one with long alkyl-chains, namely $[N_{2,2,1,201}][NTf_2]$ and $[N_{8,8,8,1}][NTf_2]$. The cations are shown for visualization of the differences in figure 5.14.

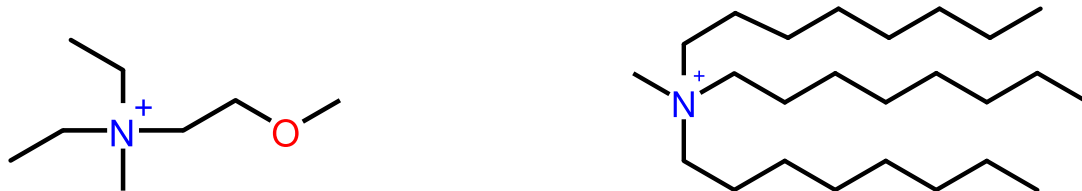


Figure 5.14.: Diethylmethyl(2-methoxyethyl)ammonium $[N_{2,2,1,201}]$ on the left and Methyl-trioctylammonium $[N_{8,8,8,1}]$ on the right.

Both ILs lack a rotational contribution in their dielectric spectrum and are thus well suited for a direct visual comparison of the shape of their ion hopping process. Such comparison can be made by inspecting the left-hand side of figure 5.15, where the conductivity free representation $\epsilon''_{der}(\omega)$ is shown as a master plot for temperatures where the relaxation time of the two ILs are similar.

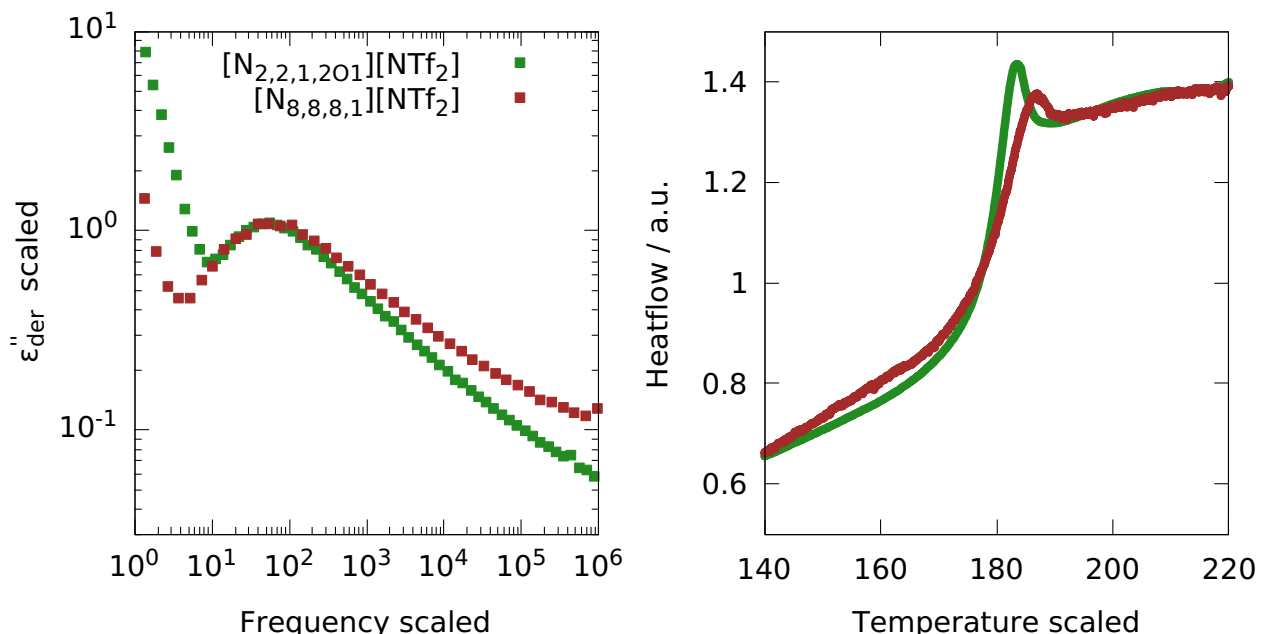


Figure 5.15.: Comparison of the dielectric (left-hand side) and DSC data for $[N_{2,2,1,201}][NTf_2]$ and $[N_{8,8,8,1}][NTf_2]$. Both spectra are broader in the latter case.

It can be clearly seen that the peak in the case of $[N_{8,8,8,1}][NTf_2]$ is broader than the one of the IL with the short chains. Additionally, the glass transition steps as measured by DSC are shown on the right-hand side of figure 5.15. In analogy to the dielectric spectra, the glass transition step is broader in the case of the cation with the long alkyl-chains. Together, this

example shows that the translational dynamics as measured by dielectric spectroscopy and the dynamic degrees of freedom involved in the glass transition are more heterogeneous in the case of the larger size difference of cation and anion. This is in full accordance with the results obtained by light scattering measurements in the preceding section, where, however, rotational dynamics is probed. For a more quantitative assessment of the broadening of the ion hopping process and the glass transition step, fit parameters are compared in the following. To this end, the DSC data obtained at a heating rate of 80 K/min are fitted with the TNMH model (see section 3.3), which is shown on the left-hand side of figure 5.16 for a variety of ILs.

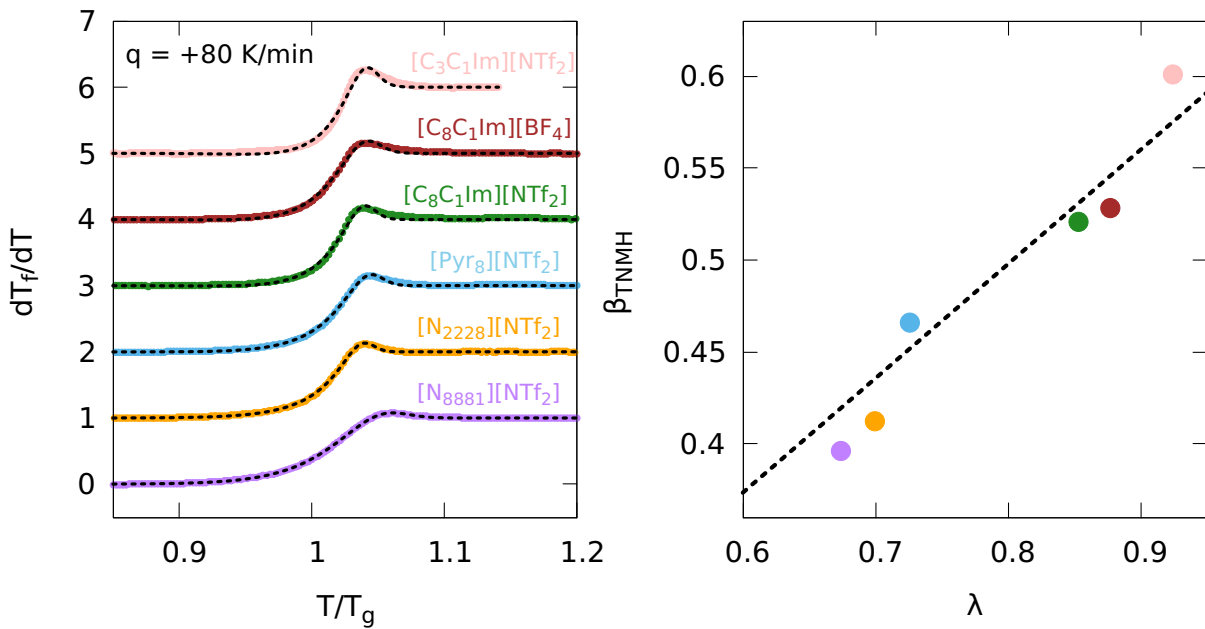


Figure 5.16.: On the left-hand side, glass transition steps for several ILs are shown. The broadening of the step increases from top to bottom. On the right-hand side, the TNMH stretching parameter β_{TNMH} is correlated to the stretching parameter λ obtained by fitting the dielectric data with the MIGRATION model.

The reason for choosing the heating rate of 80 K/min is that there the signal to noise ratio is largest, and usually, the least artifacts appear, and thus best comparability is given at this heating rate. The stretching parameter β_{TNMH} obtained by the fit is used as a measure of the broadening of the glass transition step. β_{TNMH} is directly related to the slope of the increasing flank and to the actual width of the glass transition step as determined by the onset and end temperatures. This can be seen in reference [294], where the shape of the glass transition step is shown in dependency of the TNMH fit parameters. The width is sometimes used in the literature for a measure of the broadening [295]. However, since it also depends on the activation energy, β_{TNMH} , as obtained by the fit, seems to be a more suitable measure for the stretching of the glass transition step. It should be noted that the β_{TNMH} parameters are dependent on the heating rate, which, however, does not impact the comparison with the dielectric stretching parameters as performed below, as a similar correlation can be found for other cooling rates in the limits of uncertainty. The dielectric stretching parameter, as

obtained by fitting with the MIGRATION model, is found to be temperature-dependent but leveling off to a constant value at low temperatures near the glass transition, as detailed later in section 5.4.1. Therefore, this constant low-temperature value is compared with the glass transition step stretching from DSC measurements. This comparison is made on the right-hand side of figure 5.16.

It can be clearly seen that a strong correlation between the TNMH and MIGRATION stretching parameters is present for the various ILs. In addition, there is a tendency for the broadening to be more pronounced in ILs where the size difference between the cation and anion is larger. This implies, on the one hand, that the separation of the dynamics of cations and anions with an increasing difference of their sizes, as observed by light scattering in the preceding section, is also reflected in the translational motions of the ions as probed by dielectric spectroscopy. This also highlights the fact that both ions are taking part in this ion hopping process, i.e., the separation is not as large as, for example, in the case of CKN or polymerized ILs, where only one species is responsible for the ion hopping process, while the other is already immobilized. On the other hand, the correlation of the dielectric stretching parameter with the one obtained by DSC measurements shows that either the glass transition step is dominated by the translational motions or that translational and rotational degrees of freedom, which should both contribute to the glass transition step, are highly coupled. In order to test this, it is instructive to compare not only the stretching parameters but also the time constants from dielectric and DSC measurements. Together with the reorientational relaxation times from PCS measurements, this should give a conclusive picture.

Therefore, in figure 5.17 the time constant of five ILs with at least one octyl-chain are compared, where a separation of the cation and anion dynamics is expected from the results of the preceding section due to the size difference between cation and anion.

The dielectric time constants, which are obtained from the MIGRATION model as detailed in section 5.1, are shown as solid squares, while the calorimetric time constants τ_g extracted via the TNMH model for five cooling/heating rates and five different definitions of the glass transition temperature, as described in section 3.3, are shown as crosses. The solid lines are fits with a VFT equation (equation 2.7) jointly to the dielectric and calorimetric time constants of each IL. It is clear that the fit describes the data quite well, indicating that the translational motions as probed by dielectric spectroscopy are closely connected to the freezing of the degrees of freedom as measured by DSC, not only by the stretching parameter but also by the time constants.

It is now interesting to see how the rotational time constants fit into this picture. Therefore, the two ammonium-based ILs, one with short and one with long chains, as already compared above and shown in figure 5.14, are chosen again. In the case of $[N_{8,8,8,1}][NTf_2]$ a bimodal PCS spectrum is reported in the literature [106], while only one relaxational process is observed for $[N_{2,2,1,201}][NTf_2]$ in this work. The two insets of figure 5.17 compare the dielectric and light scattering time constants for these two liquids. It can be seen that the dielectric time constants are located right between the light scattering relaxation times from the literature in the case of $[N_{8,8,8,1}][NTf_2]$. For the IL with short chains, the light scattering time constants closely follow the dielectric spectroscopy pattern, with slight separation at high temperatures and an almost perfect agreement at lower temperatures. The light scattering and dielectric spectra of the two ILs are directly compared in figure 5.18 for a selected temperature. $[N_{8,8,8,1}][NTf_2]$ could

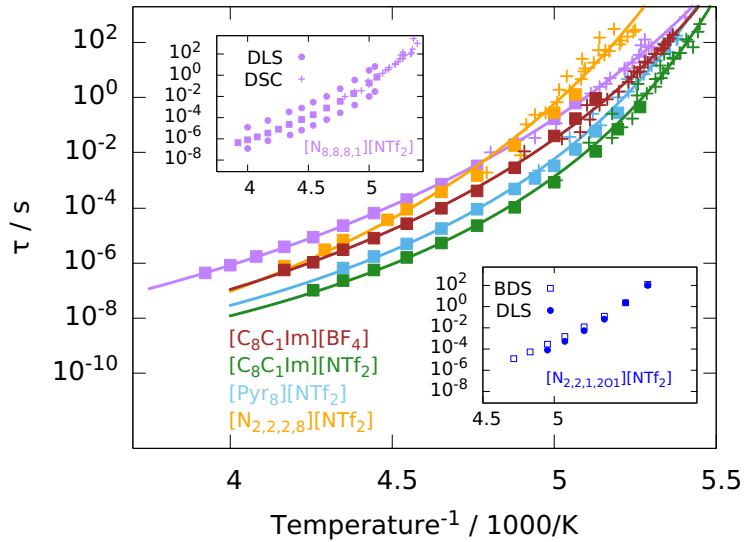


Figure 5.17.: Ion hopping correlation times from the MIGRATION model (solid squares) and calorimetric correlation times from the TNMH model (crosses) for ILs with octyl-chains. Solid lines are VFT-fits to dielectric and calorimetric time constants combined. Insets: Comparison with correlation times from depolarized dynamic light scattering. DLS data of $[N_{8,8,8,1}][NTf_2]$ adapted from [107].

only be measured for three temperatures during this work in the PCS setup due to interfering crystallization, which is why the time constants from the literature are used above. However, the data are in agreement with the literature. It can be seen that a single peak is present in the light scattering spectrum of $[N_{2,2,1,201}][NTf_2]$, like it is the case for the dielectric spectrum, while the light scattering spectrum of $[N_{8,8,8,1}][NTf_2]$ is clearly bimodal. The single peak in the dielectric spectrum is located right between the two light scattering processes, already implied by the time constants in figure 5.17.

Together, a possible interpretation of these findings may be as follows: For the IL with a cation equipped with short chains, the rotational and translational dynamics of cations and anions are similar and highly coupled, resulting in a single peak spectrum in light scattering and dielectric spectroscopy with similar relaxation times. In the case of $[N_{8,8,8,1}][NTf_2]$, the bimodal light scattering spectrum arises due to the separation of the cation and anion dynamics as a consequence of their difference in size. The dielectric spectrum may be regarded as an average over the translational dynamics of the two ion species, resulting in a broadened process located between the two reorientational processes.

Although this picture looks pretty conclusive, it must be noted that the slow process of $[N_{8,8,8,1}][NTf_2]$ observed by PCS was attributed in the work by Griffin *et al.* to the reorientational motions of long-lived alkyl aggregates and not to cations, while the faster process was assigned to the structural α -relaxation [106]. This was done based on rheology measurements, where the Maxwell relaxation times were found to coincide with the fast light scattering process and the hydrodynamic radius calculated using the viscosity and the Debye-Stokes-Einstein equation (equation 2.2) for the slow process agreed with the length scale obtained from

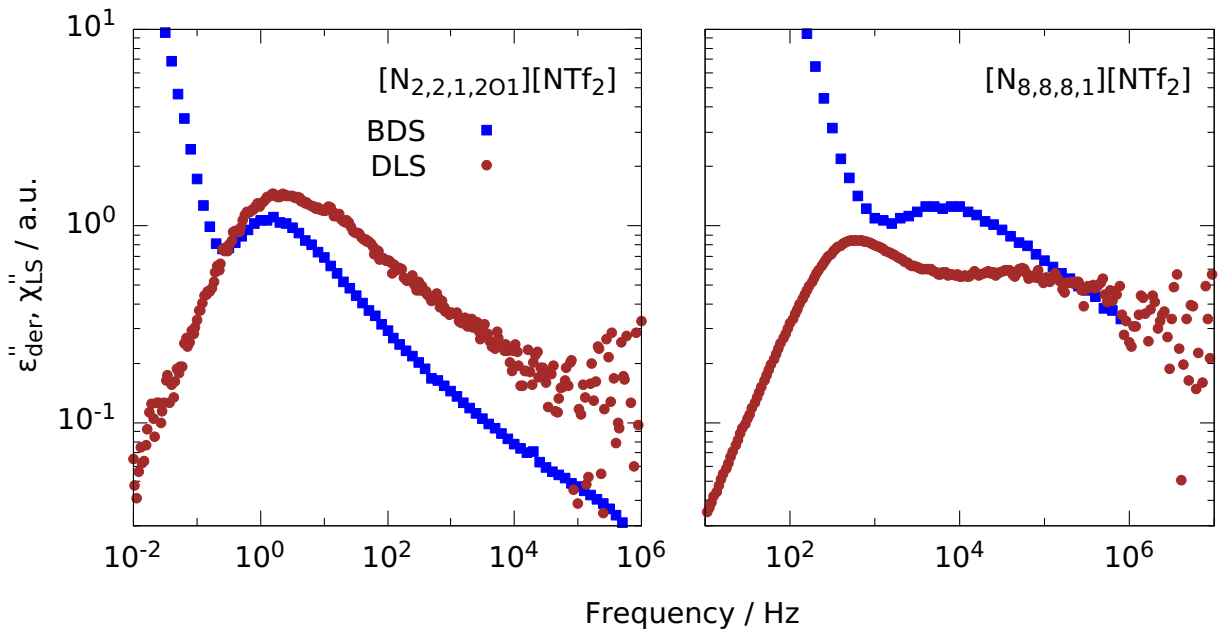


Figure 5.18.: Comparison of dielectric and light scattering spectra for the two ILs $[N_{2,2,1,201}][NTf_2]$ and $[N_{8,8,8,1}][NTf_2]$.

the pre-peak in X-ray measurements. The fact that the ion hopping process is notably slower than the α -relaxation was tentatively explained by the presence of the hydrophobic aggregates, which slow down the ion translational dynamics. Thus, the interpretation of the spectra of $[N_{8,8,8,1}][NTf_2]$ in the literature is different from the one performed in this work. Therefore, another IL will be discussed in the following subsection, namely $[P_{14,6,6,6}][Cl]$, where it is hoped that discrimination between cation and aggregates dynamics might be more straightforward.

5.2.3. The special case $[P_{14,6,6,6}][Cl]$

The IL trihexyl(tetradecyl)phosphonium chloride ($[P_{14,6,6,6}][Cl]$) was chosen for several reasons. On the one hand, it comprises the cation with the largest alkyl chain in this study, where at the same time, the chloride anion is the smallest anion of this study. With the results of the two previous subsections in mind, this is supposed to lead to a large dynamical separation of the dynamics of the two ion species. On the other hand, the chloride anion is not visible in light scattering spectra due to its optical symmetry. Thus, the occurrence of two dynamical processes might directly indicate the presence of a dynamical contribution of the aggregates and no confusion with the separated dynamics of cations and ions is possible as discussed in the preceding subsection for $[N_{8,8,8,1}][NTf_2]$. Moreover, the existence of a pre-peak in the structure factor indicates the presence of supramolecular aggregates and dielectric studies on supercooled $[P_{14,6,6,6}][Cl]$ exhibited no interfering crystallization [296, 297, 298, 299, 300]. Thus, this IL seems to be a good candidate for studying a large dynamical separation of cation and anion that should be easily discriminated from aggregate contributions.

At first, the light scattering spectra for selected temperatures are shown in figure 5.19. It can be seen that at 550 K the main peak is highly broadened and merged with the microscopic dynamics. Thus, the shape of the main relaxation can be obtained only very approximate by fitting the data. On lowering the temperature, the spectra stay very broad at first, and only at temperatures near the glass transition does the main peak separate from a secondary peak.

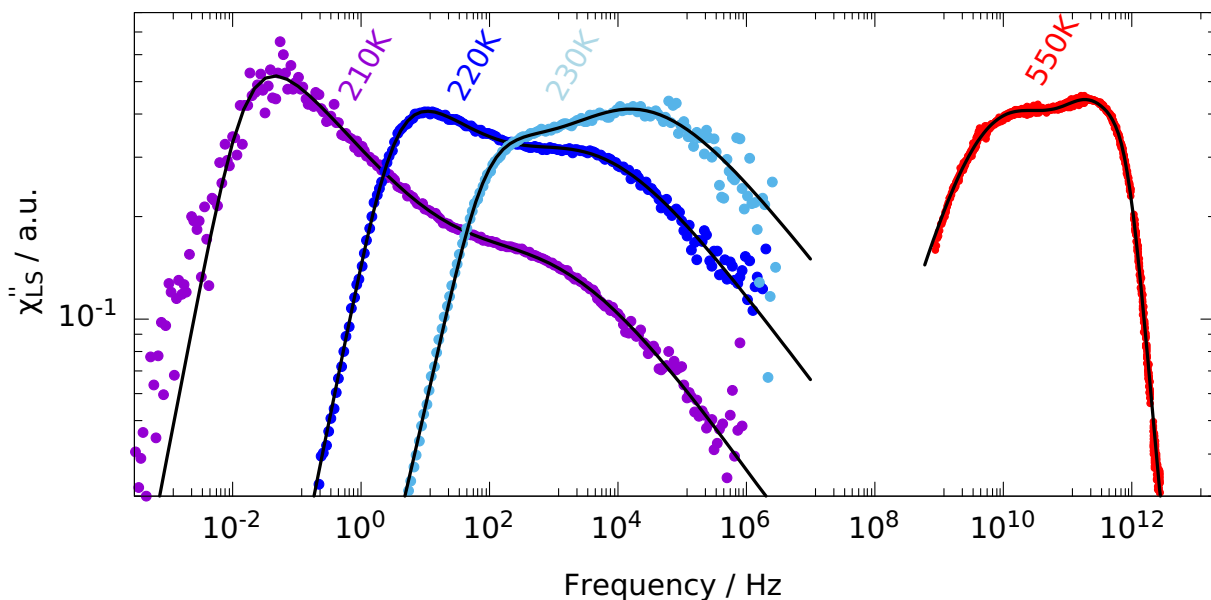


Figure 5.19.: Light scattering spectra of $[P_{14,6,6,6}][Cl]$ at selected temperatures.

The black lines are fits with a sum of a CD and a HN function accounting for the α - and β -process in the case of the PCS data, respectively. The TFPI spectrum is fitted with a HN function and two Brownian oscillators. However, since the data quality is poor due to the low scattering intensity and the highly merged dynamical processes, this fit should be considered

cautiously. The huge β -relaxation is unusual, and it is reminiscent to some extent of the dielectric spectra of sorbitol or the light scattering spectrum of 3-methyl-2-butanol [301, 45], both being hydrogen bonding liquids. Nevertheless, the temperature-dependent intensity, as well as the Arrhenius behavior of the relaxation times (shown in figure 5.23), clearly identifies this process as a β -relaxation. A comparison with dielectric data shows that only an extremely weak sign of an additional process in the dielectric data is present at those frequencies where the secondary relaxation is visible in the light scattering spectra. However, another secondary relaxation shows up in the dielectric spectra only at lower temperatures and higher frequencies, as was already observed in the literature [299, 300]. This indicates that the motions involved in the light scattering β -relaxation result in a pronounced change of the anisotropic part of the polarizability tensor while almost not affecting the orientation of the dipole moment. Such a scenario could be rationalized with motions of the non-polar alkyl chains independent of the polar core of the cation. In order to better visualize the evolution of the light scattering shape with temperature, a masterplot is shown in figure 5.20 for selected temperatures.

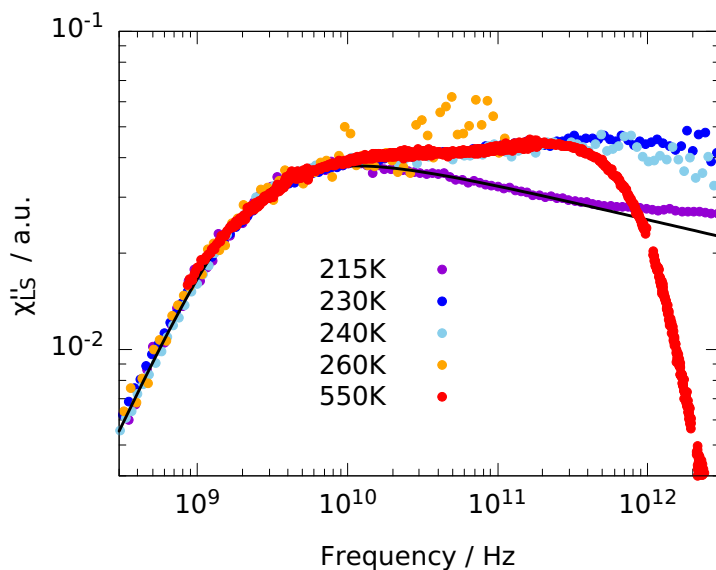


Figure 5.20.: Master plot of the light scattering spectra of $[P_{14,6,6,6}][Cl]$.

One can clearly see that the shape of the primary relaxation changes little from 550 K down to 230 K although the spectrum is dominated at high frequencies by the microscopic dynamics or the β -relaxation for the high and the low temperatures, respectively. Starting around 215 K and below, the secondary relaxation is separated enough from the main relaxation that high-frequency flank of the latter gets visible. Most importantly, no additional slow process appears at any temperature, which could be connected to the dynamics of aggregates. Only at 550 K a slight broadening of the low-frequency flank might indicate an additional contribution. However, the data quality is not sufficient to state this with certainty, and higher temperatures could not be measured due to the limiting temperature of the oven and the decomposition temperature of $[P_{14,6,6,6}][Cl]$ [302]. Nevertheless, it should be mentioned that it was found in the literature that the pre-peak intensifies with increasing temperature [296], i.e., just the opposite trend as for other ILs. Therefore, it might indeed be possible to see an aggregate contribution only at

high temperatures. The light scattering results indicate a tiny aggregate contribution at the highest temperature at most, while the main α -process is due to the reorientation of cations. The separation of the anion dynamics from this process should be addressed in the following, using dielectric and calorimetric results, since the chloride anion is not visible in the light scattering spectrum.

The dielectric spectra for three selected temperatures are shown in figure 5.21. The conductivity free representation $\epsilon''_{\text{der}}(\omega)$ exhibits a clear single peak, indicating that only the conductivity relaxation is visible in these spectra. Accordingly, the black lines are fits with the MIGRATION model without an additional process. The quality of the fits is quite good, however, not as good as in the case of the other ILs where only the conductivity relaxation is visible, as shown above, even though N_∞ was left here as a free fitting parameter. The deviations are best seen in the $\epsilon''_{\text{der}}(\omega)$ representation.

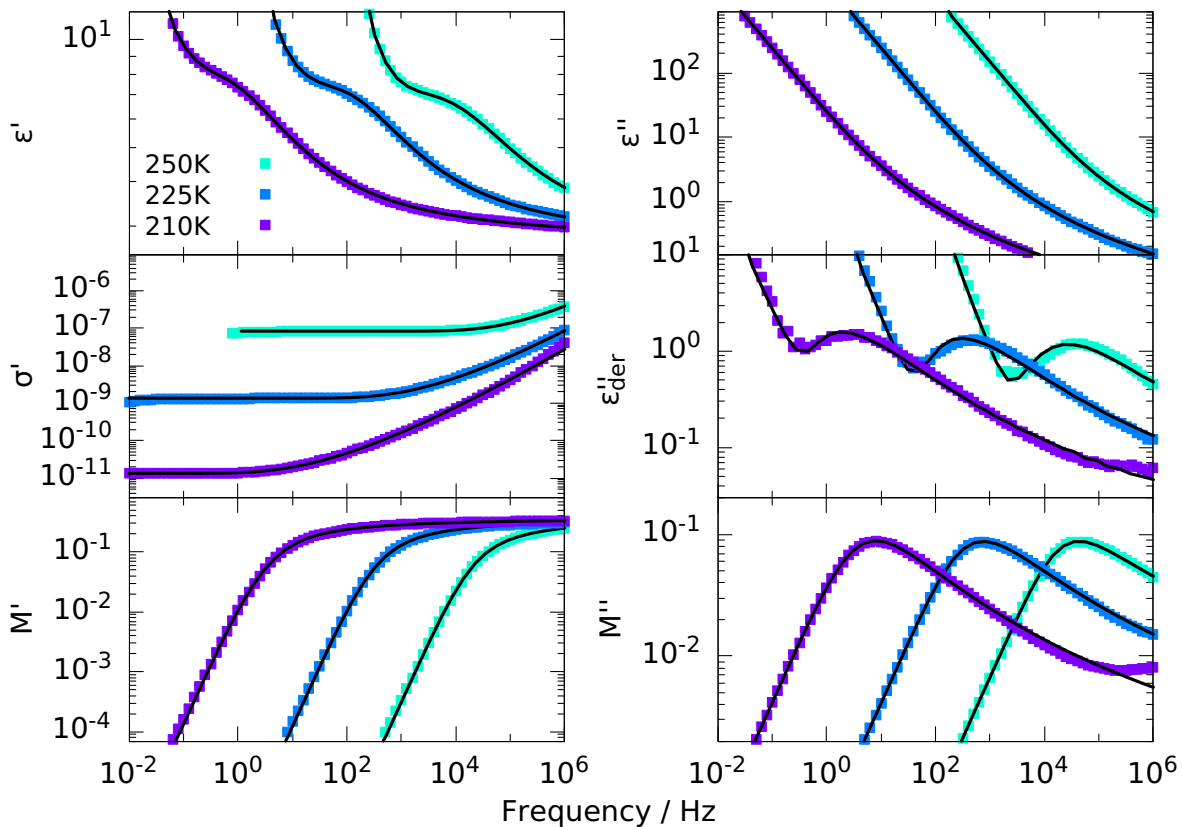


Figure 5.21.: Dielectric spectra of $[\text{P}_{14,6,6,6}][\text{Cl}]$ in six representations at three selected temperatures. Black lines are fits with the MIGRATION model.

The attempt to fit the data with an additional CD function resulted in a marginally better description of the data, but the time constants from this CD match perfectly those from the MIGRATION model at all temperatures, indicating that indeed only one relaxational process is present in the spectra, which, however, is not captured perfectly by the MIGRATION model for unknown reasons. In this respect, it is important that at high temperatures, also only conductivity relaxation was reported in the literature without a sign of dipolar relaxation [85].

The trends of the fit parameters of the MIGRATION model are in agreement with the one for the other ILs, i.e., the stretching parameter λ as well as the dielectric strength $\Delta\epsilon$ increase with decreasing temperature. Thus, $[P_{14,6,6,6}][Cl]$ is another example for an IL without an additional slow relaxation process, despite its long alkyl chains and the presence of a pre-peak in the structure factor [296]. The relaxation times of the conductivity relaxation will be compared to those from light scattering after addressing the calorimetric data.

A heating curve measured at 20 K/min is shown in figure 5.22 in the dT_f/dT representation. For comparison, shifted data for $[N_{8,8,8,1}][NTf_2]$ obtained at the same heating rate is also shown as black squares. The by far most eye-catching feature in the $[P_{14,6,6,6}][Cl]$ data is the massive enthalpic overshoot at the glass transition step. This leads to a very broad glass transition region. No other substance measured in this work shows a comparable overshoot. When modeling this glass transition step with the TNMH-model, a slightly higher stretching parameter $\beta_{TNMH} \approx 0.64$ and a slightly lower non-linearity factor $x \approx 0.25$ compared to the other ILs contained in figure 5.17 is found, which account for the substantial overshoot. When determining the fictive temperature of this data set by the area matching method, as indicated by the shaded areas in figure 5.22, it can be seen that T_f is located at the lower end of the glass transition step due to the fact that the blue area must match the area of the overshoot plus the small area on lower temperatures than T_f .

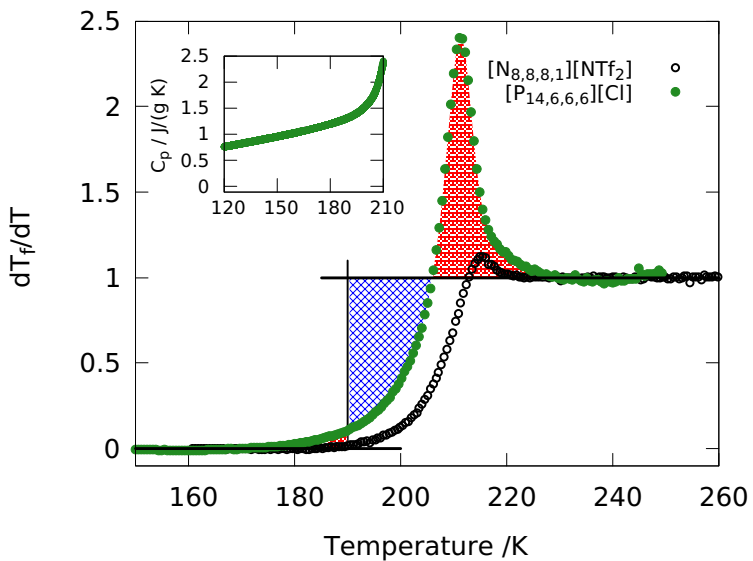


Figure 5.22.: Glas transition step of $[P_{14,6,6,6}][Cl]$ compared to the one of $[N_{8,8,8,1}][NTf_2]$, highlighting the enormous enthalpy overshoot in the former case. The shaded areas indicate the determination of the fictive temperature. The inset shows the DSC trace below the glass transition step, where no hint of a second step can be found.

Thus, the significant overshoot is directly connected to a low fictive temperature, indicating that a notable enthalpy relaxation has occurred during the cooling below the glass transition step. This phenomenon is known to take place in cases when the material is aged below the glass transition temperature, i.e., when an out of equilibrium glass is allowed to relax for a

certain amount of time towards the equilibrium [193, 303]. The enthalpy lost during this aging is recovered upon heating which leads to a larger overshoot for longer aging times. This behavior is demonstrated in figure B.2 in the appendix, where a huge increase of the overshoot can be seen with increasing aging time for the example of 1-phenyl-1-propanol. Thus, now the question is, which molecular motions might be responsible for the enthalpy relaxation in the case of $[P_{14,6,6,6}][Cl]$ during the usual cooling run, where no additional aging time was allowed. To this end, all relaxation times of the light scattering, dielectric and calorimetric measurements are shown in figure 5.23. The red dashed line is a VFT fit to the light scattering α -relaxation or an Arrhenius fit to the β -relaxation, respectively.

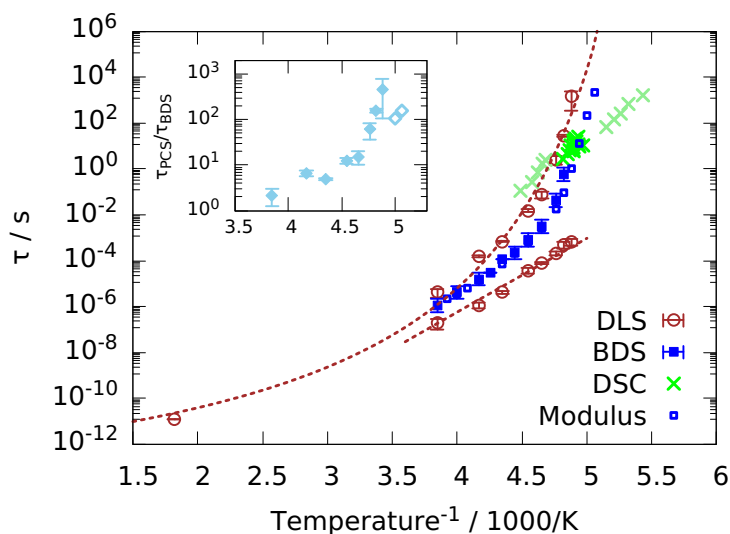


Figure 5.23.: Arrhenius plot of the time constants of $[P_{14,6,6,6}][Cl]$ from different experimental techniques. Inset shows the ratio of the light scattering and the conductivity relaxation times.

It can be seen that the light scattering time constants merge with the one of the conductivity relaxation near the temperature where the α - and β -relaxation start to separate. At lower temperatures, the dielectric relaxation times, separate from the α -relaxation, although also following a VFT slope rather than an Arrhenius one. The separation between the light scattering and dielectric relaxation times is shown in the inset as τ_{PCS}/τ_{BDS} . In the case of the calorimetric data, the five different sets of time constants are shown for the different definitions of the glass transition temperature. The calorimetric time constants for the top, half, and onset temperature are clustered near the dielectric relaxation times. The one for the high-end temperature of the glass transition step and the one for the fictive temperature, which is located at the lower end of the glass transition step, as shown in figure 5.22, have to be considered with great care since they are both dominated by the influence of the enthalpic overshoot. The calorimetric relaxation times at the fictive temperature display a markedly weaker temperature dependence than those at the other temperatures, leading to an overall slope of the calorimetric time constants reminiscent of a fragile to strong transition. Such a transition has been observed in the literature for the conductivity relaxation times of several ion conductors [63, 90, 304,

305]. To test whether this change of slope is also followed here by the conductivity relaxation times, the dielectric data obtained by the Alpha-Analyzer setup does not extend to sufficiently low frequencies. Therefore, modulus measurements with the time domain setup have been performed, which is described in detail in reference [20], and the modulus time constants are shown as open squares in figure 5.23, where Alpha-Analyzer and time domain measurements are combined. It is directly clear that these data do not follow the low-temperature DSC slope but continue in a VFT-like manner. From that, it must be concluded that the fictive temperatures are highly influenced by the large enthalpic overshoot and thus do not reflect the real dynamics. The open question remains, which dynamics is responsible for this enthalpy overshoot, i.e., which relaxations take place at temperatures below the glass transition step to drive the glassy system towards equilibrium. The two possibilities are the conductivity relaxation on the one hand, which is notably separated from the cationic relaxation times, as measured by light scattering, and the secondary relaxation on the other hand, which has been attributed above to movements of the alkyl chains.

Since the conductivity relaxation is most probably strongly influenced by the dynamics of the anions being faster than the cations, this leads to a very similar picture as in the case of $[N_{8,8,8,1}][NTf_2]$, discussed in the preceding section. The difference for the case of $[P_{14,6,6,6}][Cl]$ is that the dynamics of the anion is not visible in the light scattering spectra. Thus, the reorientation of the large cations is slower than the conductivity relaxation, which agrees to good approximation with the DSC time constants, and the reorientation of the anions would most probably appear on even shorter timescales, if visible in the spectra. Of course, the separation of the cationic and the conductivity relaxation is larger in the case of $[P_{14,6,6,6}][Cl]$ than it was for $[N_{8,8,8,1}][NTf_2]$. However, it seems unlikely that the separation is large enough to cause the large enthalpic aging. Instead, it seems more likely that the strong secondary relaxation, which is still active far below the glass transition temperature, is responsible for the enthalpic overshoot. There are hints in the literature that β -processes indeed contribute to the physical aging of glassy substances [303, 306, 307].

Thus, it has been shown that $[P_{14,6,6,6}][Cl]$ shows some peculiarities not seen in other ILs of this study, like the huge β -relaxation in the light scattering spectrum and the accompanied enthalpic overshoot in the DSC trace. Also, the increasing separation of the cation dynamics from the conductivity relaxation with decreasing temperature was not observed in other ILs and is probably caused by the large difference in size between the cation and the anion. However, although $[P_{14,6,6,6}]$ is the largest cation in this study, no dynamic signatures of an aggregate relaxation could be found in any of the experimental methods. Furthermore, due to the similarity of the appearances of the various relaxation processes to $[N_{8,8,8,1}][NTf_2]$, it supports the assignments to the microscopic origins made in the previous section.

5.3. Dynamics of nanoscale aggregates

As discussed in detail in section 2.2, many studies in the literature were devoted to the search for dynamic signatures of aggregates formed by cations equipped with long alkyl chains after their discovery by X-ray scattering experiments [73]. Spectral features were indeed found for several ILs using different experimental techniques, which were assigned to the dynamics of aggregates. In table 5.1, ILs are listed for which nanostructurization was found in at least one experimental technique. Most of these ILs are also addressed in this work or are structurally similar to those treated here. The ✓ symbol means that a spectral feature was found in the literature indicated, which was assigned to the presence of aggregates. The ✗ symbol means that a contribution of aggregates to the respective spectrum was either explicitly excluded or that the observed spectral features were assigned to different origins without necessarily mentioning aggregates. The question marks denote that there seems to be no study with that respective technique for the particular IL. Where no references are given after the symbols, the findings are from this work, some in anticipation of subsequent discussions. Furthermore, it should be noted that some of the assignments made in the literature are not confirmed in the present work, as shown below.

IL	X-ray ²	BDS	DDLS	Rheo.
[C ₈ C ₁ Im][BF ₄]	✓	[73]	✓	[98] ✓ ? [98]
[C ₈ C ₁ Im][NTf ₂]	✓	[73]	✓	[98] ✗ ?
[N _{2,2,2,8}][NTf ₂]	?		✓	[95] ✗ [95] ?
[N _{8,8,8,1}][NTf ₂]	✓	[74]	✗	[106] ✓ [107] ✗ [106]
[P _{2,2,2,8}][NTf ₂]	✓	[105]	✓	[105] ✗ [95] ✗ [105]
[P _{4,4,4,8}][NTf ₂]	✗	[105]	✗	[105] ? ✗ [105]
[P _{14,6,6,6}][Cl]	✓	[298]	✗	✗ ?

Table 5.1.: Table of several ILs where aggregates were found using different experimental techniques as indicated.

As can be seen, the picture is rather inhomogeneous in that sense that the identification of aggregates with a particular experimental technique does seemingly not imply that a signature of those nanostructures is also observed necessarily with other techniques. Also, the fact that a certain experimental method seems to be capable of detecting a dynamic signature of aggregates in principle does not mean that it is able to detect it in all ILs.

In respect thereof, it should be emphasized that the presence of aggregates is often declared based on the mere appearance of an additional spectral feature. However, as has been shown in detail in section 5.2, the separation of cation and anion dynamics can also lead to a bimodal spectrum in dynamic measurements, unrelated to the presence of nanostructures. Likewise, the appearance of a pre-peak in X-ray scattering measurements does not inevitably signal the existence of aggregates. It was, for example, highlighted in reference [76] that spacing of polar regions by the cationic alkyl-tails might lead to a pre-peak without the existence of

²Either experimental or simulated

aggregates. In this respect, a method was proposed by Cosby *et al.* [105], to determine whether the pre-peak can be explained without invoking aggregation: They used the Tanford equation

$$l_{\max} = 1.5 \text{ \AA} + 1.265 \text{ \AA}/\text{CH}_2 n_c, \quad (5.10)$$

where n_c is the number of carbon atoms in the alkyl-chain [308], to obtain the maximal length of a fully extended alkyl chain. In cases where l_{\max} was found to be larger than the spatial correlation length determined by the q -value of the X-ray scattering pre-peak as $L = 2\pi/q_{\text{pre}}$, the occurrence of the pre-peak was no longer connected to aggregation. Together, this means that all spectral features have to be checked very carefully before assigning them to nanostructurization. Such a detailed treatment is performed below for the IL $[\text{C}_8\text{C}_1\text{Im}][\text{BF}_4]$, which – in anticipation of the result – is the only IL of this study where the slow relaxational process found in light scattering measurements can be safely assigned to the dynamics of aggregates, taking into account all data from the different experiments listed in table 5.1. As mentioned in section 5.2.1, in the light scattering spectra of $[\text{C}_{12}\text{C}_1\text{Im}][\text{BF}_4]$ and $[\text{C}_{10}\text{C}_1\text{Im}][\text{NTf}_2]$, a broadening of the low frequency flank or a additional relaxational contribution at low frequencies and low temperatures were observed, respectively. These features were tentatively ascribed to aggregates dynamics, however, they could not be measured in a significant temperature range due to interfering crystallization. Thus, the assignment remains questionable.

In the case of $[\text{C}_8\text{C}_1\text{Im}][\text{BF}_4]$, crystallization is not observed, and the IL can be measured in the whole temperature range. As indicated in table 5.1, this was done in the literature and bimodal spectra were observed in dielectric and shear mechanical spectra, where the slower of the two relaxational processes was identified with the dynamics of aggregates in both cases [98]. Additionally, a pre-peak was observed in X-ray scattering measurements, from which the spatial correlation length $L \approx 22 \text{ \AA}$ was deduced [73]. When comparing to the length of a fully extended octyl-chain of 11.6 \AA , calculated by equation 5.10, it is clear that the experimental correlation length is almost twice the size of the all-trans octyl chain, implying that indeed aggregates are responsible for the occurrence of the pre-peak, following the above reasoning of Cosby *et al.* In light of the discussion in section 5.2 about the conformers of the cation, it is even more likely that the octyl-chains are curled instead of being fully extended. Moreover, the experimental pre-peak shift to even lower q -values, i.e., the size of the structures increases with decreasing temperatures. Thus, $[\text{C}_8\text{C}_1\text{Im}][\text{BF}_4]$ seems to be the ideal candidate for the search of aggregate dynamics in the light scattering spectrum. As a first step, data is shown at 400 K obtained by TFPI measurements together with data at 205 K as a master-plot on the left-hand side of figure 5.25. For comparison, two spectra of $[\text{C}_8\text{C}_1\text{Im}][\text{NTf}_2]$ with a similar temperature difference are shown on the right.

In the latter case, the spectrum narrows slightly with decreasing temperature, as already seen before in figure 5.7. In contrast, the spectrum of $[\text{C}_8\text{C}_1\text{Im}][\text{BF}_4]$ broadens at frequencies slightly lower than the peak frequency at low temperatures. At even lower frequencies, the reason for this is visible, as a weak additional relaxational contribution appears, leading to the apparent broadening of the low-frequency flank of the main peak. As discussed earlier, the main peak is due to the reorientation of the cation in this IL since the optically isotropic anion does not contribute to the spectrum. Thus, it seems plausible that the additional slow process appearing at low temperature might indeed be a signature of aggregate dynamics. However, in order to confirm this assignment, a detailed comparison with other experimental techniques should be

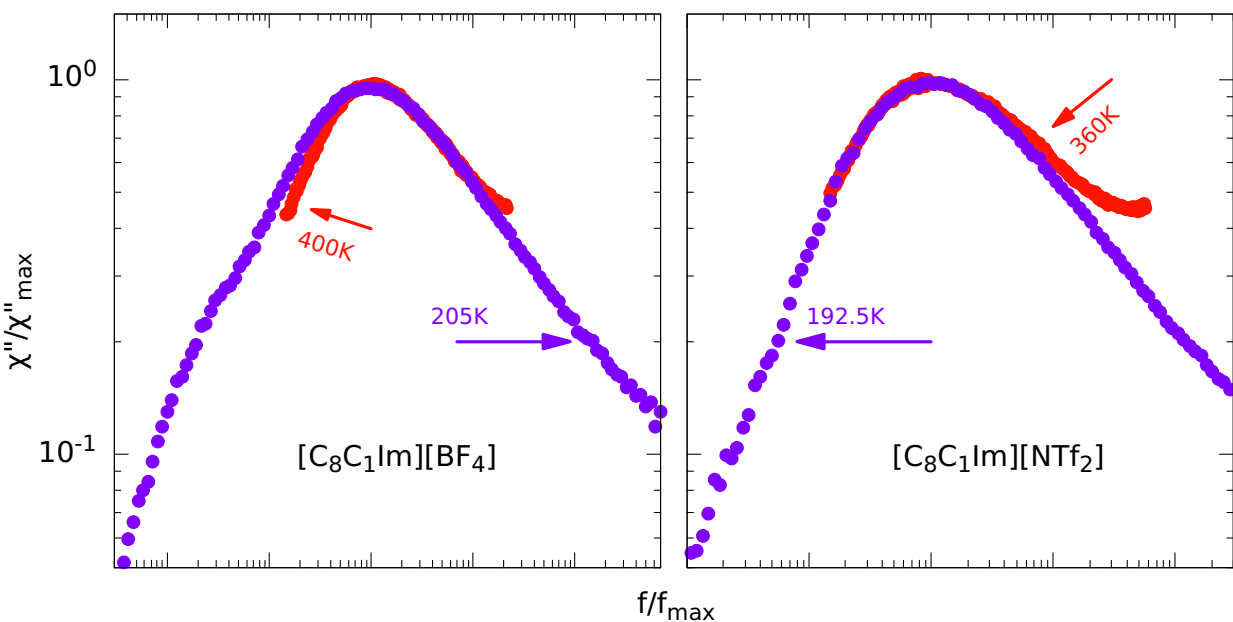


Figure 5.24.: Light scattering spectra at a high and a low temperature superimposed for $[C_8C_1Im][BF_4]$ on the left-hand side and for $[C_8C_1Im][NTf_2]$ on the right-hand side.

performed in the following to support this idea. As a first step, temperature-dependent PCS data is compared to the features of the X-ray scattering pre-peak. As mentioned above, the pre-peak intensity was found to increase with decreasing temperature, indicating that more aggregates are present at lower temperatures. Additionally, the size of the aggregates increases, as seen by the position of the pre-peak [73]. Thus, the question is, how these features are expected to influence the appearance of the slow relaxation process in the light scattering spectrum if it has the same microscopic origin as the pre-peak. An increasing number of aggregates should lead to an increasing relaxation strength of the associated peak in the light scattering spectrum, as can be seen by equations 4.14. At the same time, the intensity of the cation peak should decrease as more and more cations take part in the aggregate process. Thus, it is irrelevant that the absolute scattering intensity is not known from the PCS measurements alone, as the intensity of the aggregate process is expected to increase relative to the cation contribution. And since the PCS data is normalized, an increasing relaxation strength of the low-frequency process could be directly associated with an increasing number of aggregates. The increasing size of the aggregates can be rationalized to appear in the light scattering spectrum as follows: Assuming rotational diffusion for both the single cations and the aggregates, one can see by using the Debye-Stokes-Einstein equation (equation 2.2) that the relaxation time of the aggregates in comparison to that of the cations should increase for increasing aggregate size, i.e., increasing hydrodynamic radius r . Hence, the ratio $\tau_{\text{agg}}/\tau_{\alpha}$ is expected to increase with decreasing temperature. In figure 5.25, the PCS data are shown from 225 K down to 192.5 K on the left hand side. Fits are indicated as solid lines, where a superposition of a CD function for the weak, slow process a HN function for the α -process are used. An additional CC-function

for the secondary relaxation for temperatures below 215 K is used.

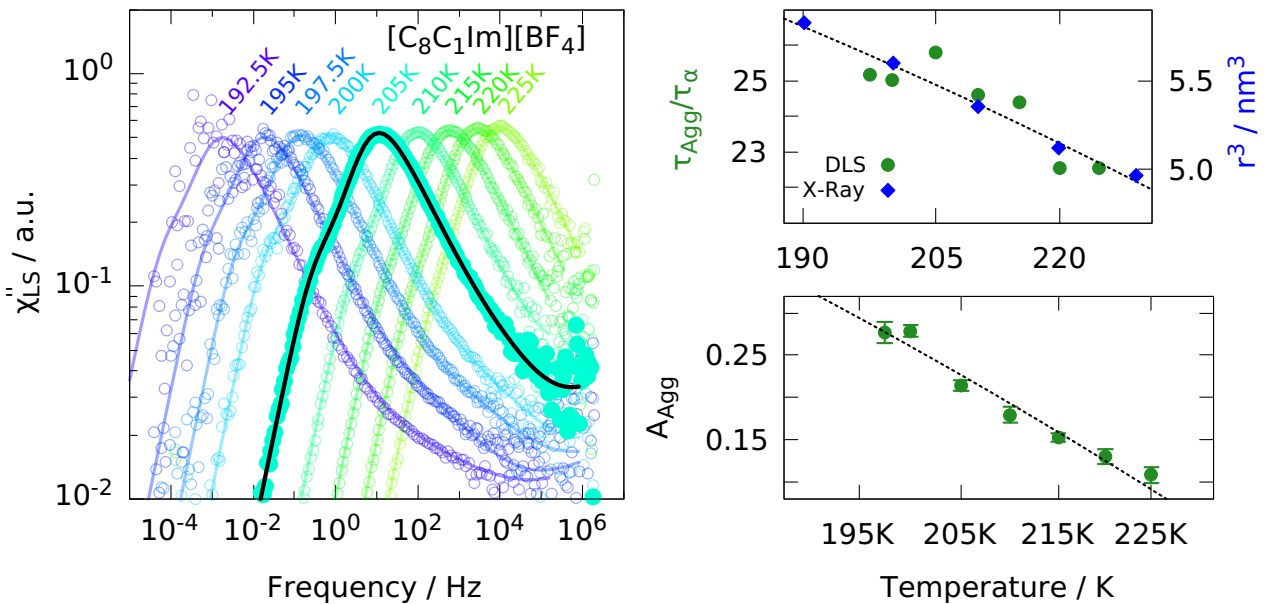


Figure 5.25.: Temperature dependent light scattering spectra of $[\text{C}_8\text{C}_1\text{Im}][\text{BF}_4]$ on the left-hand side including fits with a CD plus a HN and a CC function, accounting for the slow, the main and the secondary relaxation, respectively. On the right-hand side, the ratio of the time constants of the slow and the main relaxation are shown together with the size of the aggregates obtained by X-ray measurements from the literature [73]. Below that, the strength of the slow light scattering process is shown in dependency of the temperature.

The reason for using a HN function for the cation reorientation is that the broadening between this peak and the low-frequency process could not be described otherwise. The fits describe the data very well, and the fit parameter A_{agg} , i.e., the relaxation strength of the aggregate process, as well as the ratio of the relaxation times $\tau_{\text{agg}}/\tau_\alpha$ are shown on the right-hand side dependent on temperature. There, also the temperature-dependent size of the aggregates as obtained from the pre-peak position in reference [73] is shown. It can be seen that the temperature dependence of these two values is identical in good approximation. Additionally, the size of the aggregates can be calculated from the PCS measurement using the relaxation time of the slow process and the viscosity in the DSE equation. The viscosity of $\eta = 2.4 \times 10^6 \text{ Pa s}$ is taken at 200 K from a master plot of the real part of the mechanical shear data from reference [98], which are courtesy of Taylor Cosby and are shown again later. Employing the DSE, this gives a hydrodynamic diameter of $d \approx 22 \text{ \AA}$, which is in favorable accordance with the value of the correlation length deduced from the pre-peak at 200 K of 23 \AA .

The relaxation strength A_{agg} can not be compared quantitatively to the intensity of the pre-peak because it is not given in absolute measures in reference [73]. However, the quantitative behavior, namely the increasing intensity with decreasing temperature, is identical in the PCS and the X-ray scattering spectra. Together, this means that the slow additional process

found in the PCS spectra has not only the same temperature-dependent properties as the X-ray scattering pre-peak, but also the actual size of the aggregates performing rotational diffusion compares excellently with the X-ray scattering results. This is a strong indication of a common microscopic origin, reflected in the rotational diffusion of nanoscale aggregates in the PCS measurements and in a structural low q -peak in X-ray scattering.

As a next step, the light scattering data should be compared to the other dynamic measurements, i.e., dielectric spectroscopy and rheology from the literature. Since in both methods, two relaxational processes were detected, the slower of which was assigned to aggregate dynamics, it can now be expected that the time scale of the slow process coincides with the slow process in the PCS spectra. To directly compare the data, the $\epsilon''_{\text{der}}(\omega)$ representation of the dielectric data was chosen, and the rheology data from the literature is presented as a master plot in the imaginary part of the viscosity $\eta''(\omega)$ in figure 5.26. This representation has two advantages over the commonly used shear modulus $G''(\omega)$, as demonstrated by Arrese-Igor *et al.* [309]: At first, multimodal behavior is strongly highlighted in this representation, which is often only seen as a very weak shoulder in $G''(\omega)$. Second, the peak position was shown to be directly comparable to the one from dielectric spectroscopy, thus also to the one from light scattering, unlike the modulus peak, which is naturally located at higher frequencies. The comparison of the spectra at 200 K is shown in figure 5.26.

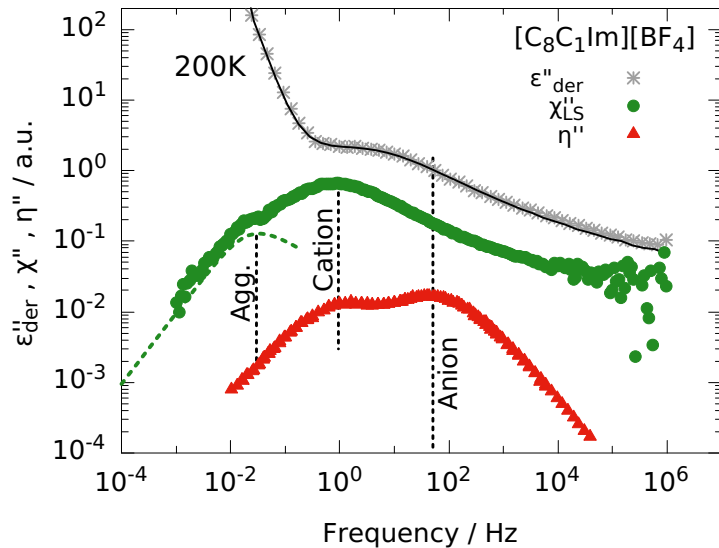


Figure 5.26.: Comparsion of the spectra obtained by different experimental methods for $[C_8C_1\text{Im}][\text{BF}_4]$ at 200 K. Black dashed lines are guides to the eye. Shear-mechanical data are courtesy of the authors of [98].

The fit of the dielectric data is also shown to highlight the bimodality already observed in the literature [98]. Details of the dielectric fits are given later in section 5.4.2. The shear mechanical data $\eta''(\omega)$ displays a pronounced bimodality. The low-frequency peak corresponds to a shoulder in the low-frequency flank of $G''(\omega)$ as shown by the original authors, which they assigned to the dynamics of the aggregates as they did for the slow dielectric process [98]. By comparison with the light scattering data, however, it is obvious that the slow shear mechanical

as well as the slow dielectric process almost perfectly coincide with the α -relaxation of the light scattering spectrum, which was identified with the reorientation of the cation. The dynamics of the aggregates, i.e., the slow process in the light scattering spectrum, are located at notably lower frequencies. At those frequencies, the electrode polarization overshadows all relaxational contributions which might be present in the dielectric spectra. Thus it is not possible to resolve the aggregate relaxation in the dielectric spectrum. In the shear mechanical spectrum, on the other hand, it can be observed that the slope of the low-frequency flank is not proportional to ω^1 , as would be expected for pure viscous flow. This might indicate that a small contribution from aggregates is present in this frequency range in accordance with the light scattering data. In fact, it has been shown in monohydroxy alcohols that the ω^1 behavior is restored on time scales of the Debye relaxation, which is also sometimes assigned to supramolecular dynamics. However, more detailed measurements are needed to adequately cover those low frequencies in order to observe the crossover to ω^1 behavior. Additionally, it should be noted that recent MD simulations have shown that nanoscale structures hardly contribute to the shear stress [310]. Thus, they might be hard to resolve.

The high-frequency peak of the rheology data has no counterpart in the light scattering data, but it coincides with good approximation with the conductivity relaxation in the dielectric spectrum. Thus, when assuming that the conductivity is dominated by the small $[\text{BF}_4^-]$ anions, it seems plausible that the fast shear mechanical process is due to the anions, i.e., the cation and anion dynamics are separated because of their size difference and are therefore visible as two relaxational processes in the viscosity spectrum. This reasoning is perfectly in line with the results from section 5.2.1, where the bimodality in the light scattering spectrum was explained by separated cation and anion dynamics. Here, however, the anion is not visible in the light scattering spectrum due to its optical isotropy, but its contribution is seen separated from the cation dynamics in the rheology spectra, similar to the bimodal spectra found for binary mixtures [57]. This means that neither the slow dielectric process nor the slow shear mechanical process can be identified with the dynamics of the aggregate, which are located at even lower frequencies in the light scattering spectrum. Instead, these processes seem to be due to the cation dynamics.

In order to compare the time constants from the different experimental techniques, also in dependency of the temperature, Arrhenius-plots are shown in figure 5.27. On the left-hand side, the entire temperature range is shown, including high-temperature measurements using the TFPI setup, while on the right-hand side, zoom to the low-temperature range is shown, where the time constants from rheology are included. The latter are obtained by using the peak positions of the master-plot of $\eta''(\omega)$, as shown in figure 5.26, and the shift factors of the respective temperature.

It can be seen that the aggregate process as identified in the PCS spectra is the slowest at all temperatures. The calorimetric time constants agree very well with conductivity relaxation times, as already seen in figure 5.17. The blue dashed line is a VFT-fit combining these time constants. The slow dielectric relaxation is similar or slightly slower than the cationic process from light scattering. The slow shear mechanical time constants agree at low temperatures with the cation time constants. The fast rheological process agrees at low temperatures with the conductivity relaxation and the calorimetric time constants. At higher temperatures, however, they deviate markedly from those relaxation times. Assuming that the two shear mechanical

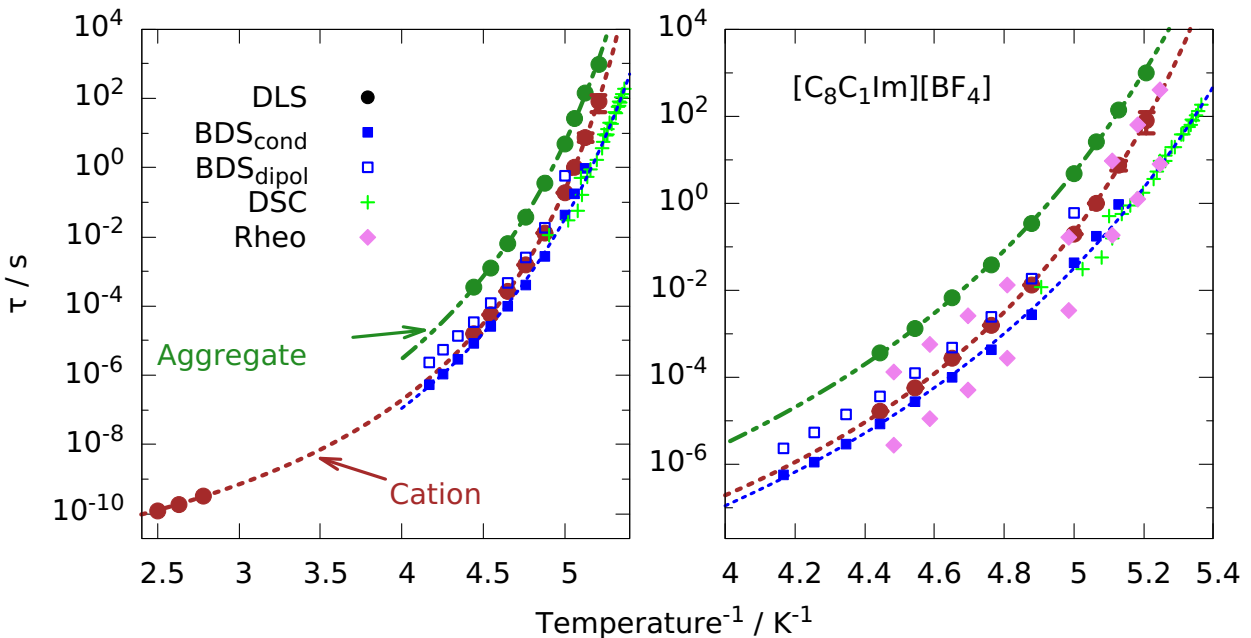


Figure 5.27.: Arrhenius plot of the time constants of $[C_8C_1\text{Im}][\text{BF}_4]$. On the left hand side, the whole temperature range is shown and on the right hand side only the low temperature range is depicted. There, also rheological time constants are included.

relaxations are indeed due to cation and anion dynamics, the reason for this deviation is probably the non-validity of time-temperature superposition. As can be seen, the conductivity relaxation times and the cationic time constants approach each other by increasing the temperature. Thus, assuming time-temperature superposition for these two processes in the rheology spectrum must fail. This is supported by the fact that the time constants obtained from a master-plot in the modulus representation, as done in the original publication [98], leads to slightly different relaxation times at high temperatures.

However, it is surprising that the correlation times obtained in $G^*(\omega)$ and $\eta''(\omega)$ are virtually identical at least at low temperatures since usually, modulus relaxation times are faster. As there seems to be no consensus in the literature about the question of which relaxation times from rheology measurements should be compared to the one from other experimental techniques [98, 311, 309], some uncertainty might be present in the comparison. However, irrespective of which representation is chosen, be it the modulus, the viscosity, or the compliance, in no case does the slow rheological process coincide with the aggregate process observed in light scattering, but its time scale is always similar to the cation reorientation.

Thus, from all the above discussion, it has to be concluded that in the case of $[C_8C_1\text{Im}][\text{BF}_4]$, the dynamic signature of aggregates is observed as a slow contribution in the light scattering spectra. Its temperature dependence matches those of the X-ray scattering pre-peak, and also, the hydrodynamic radius obtained from light scattering is in accordance with the correlation length deduced from the pre-peak. However, the slow process found in the dielectric and shear mechanical spectrum can not be connected to the aggregate dynamics, as they appear on the

time scale of the cation dynamics as determined by light scattering measurements. This is in contrast to a previous interpretation in the literature [98]. Here, the bimodality in the rheology spectra is tentatively ascribed to the separation of cation and anion dynamic, as has been found to appear in light scattering spectra for ILs where both ions are optically anisotropic, which is also known to appear in shear mechanical spectra of binary mixtures [57]. The aggregate dynamics might be active in rheological measurements as well. However, to confirm this, measurements at lower frequencies are needed, ideally with a setup covering several orders of magnitude in frequency, to circumvent the problem of failing time-temperature superposition. In the case of dielectric spectroscopy, the conductivity relaxation appears on similar time scales as the fast shear mechanical relaxation, which might indicate that the conductivity is dominated by the anion dynamics, at least at those low temperatures. The slow dielectric relaxation, which was formerly ascribed to aggregate dynamics [98], coincides with the cation reorientation as observed by light scattering. Thus, it seems natural to identify this slow dielectric relaxation with the reorientational motion of the dipolar cation. However, since a slow dielectric process has been identified with aggregate dynamics in several studies and for various ILs, this assignment should not be made too hasty. Therefore, the next section is devoted to this slow dielectric relaxation, where the discrimination between aggregate dynamics and cation reorientation is performed by comparison with light scattering and high-pressure dielectric measurements.

5.4. Origin of the low-frequency relaxation in dielectric spectra

As discussed in detail in section 2.2, a second process observed in dielectric spectra for several ILs was ascribed to the dynamic signature of aggregates in the literature. However, as seen in the previous section for the case of $[C_8C_1Im][BF_4]$, the time scale of the slow dielectric process did not coincide with those of the dynamics of the aggregate as identified by combining light scattering and X-ray data. Therefore, the aim of this section is to evaluate whether $[C_8C_1Im][BF_4]$ is an exception or if the slow dielectric process cannot be identified with motions of aggregates also for other ILs.

In order to decide whether a second dynamic contribution is present in the dielectric spectra at all, the conductivity free $\epsilon''_{der}(\omega)$ representation is chosen since it is best suited for distinguishing different relaxation processes by the naked eye. This is illustrated in figure 5.28, where the real part of the permittivity and its derivative is shown for two different ILs, namely $[N_{8,8,8,1}][NTf_2]$ and $[C_8C_1Im][BF_4]$. As can be seen, both spectra show a step-like behavior in $\epsilon'(\omega)$ before electrode polarisation sets in at lower frequencies. No bimodality can be observed in this representation. The only difference between the two ILs is that the plateau, denoting the static permittivity, is well established for $[N_{8,8,8,1}][NTf_2]$, while this is not the case for $[C_8C_1Im][BF_4]$ where the step directly transitions into the electrode polarization without a notable plateau.

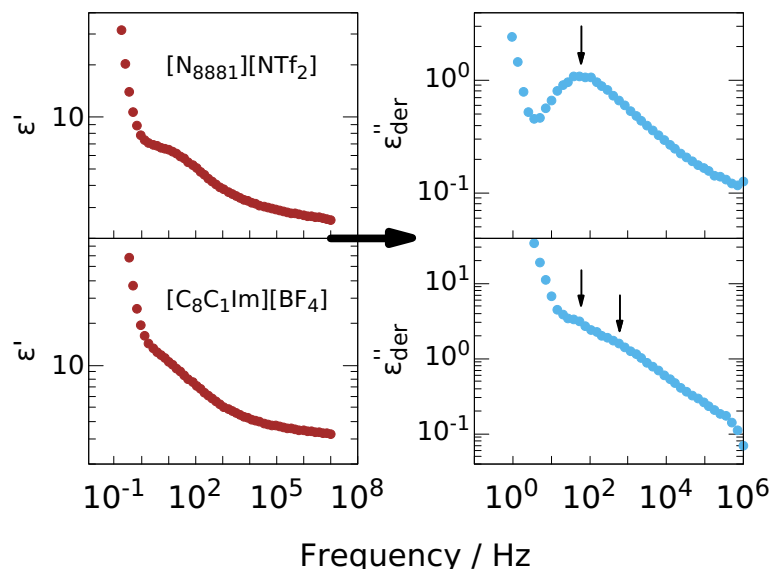


Figure 5.28.: In the left panels data are shown in $\epsilon'(\omega)$ representation and in the right panels in $\epsilon''_{der}(\omega)$ representation for $[N_{8,8,8,1}][NTf_2]$ (top) and $[C_8C_1Im][BF_4]$ (bottom). In the former case, only one peak is visible and in the latter case two peaks can be distinguished as shown by the arrows.

In the $\epsilon''_{der}(\omega)$ representation, however, the differences are seen more pronounced. While in the case of $[N_{8,8,8,1}][NTf_2]$ a clear single peak is observed, two peaks are discernible for $[C_8C_1Im][BF_4]$, as indicated by the arrows. The slower one is highly merged with the electrode polarization, as already seen for the step in $\epsilon'(\omega)$, and thus the low-frequency flank of the peak is not visible. In the following, the temperature and pressure-dependent behavior of the slow

relaxation process is investigated, and from that conclusions about its molecular origin will be drawn.

5.4.1. High pressure measurements

In order to determine whether the slow dielectric relaxation is due to the dynamics of the aggregate, as proposed in the literature, a comparison with the X-ray scattering pre-peak is desirable since this has been proven extremely useful in ascribing the slow light scattering process to aggregates motions in the previous section. In this subsection, the pressure responsiveness of the slow dielectric relaxation is the focus, since it was found in the literature that nanoscale structures in ILs depend on the pressure. More precisely, it was found for some ILs by X-ray measurements or simulations that the aggregates are present at ambient pressure as indicated by the pre-peak but vanish at elevated pressure, as seen by the reduction and eventually vanishing of the pre-peak [286, 312]. This was attributed to the bending of the octyl-chain in the case of $[C_8C_1Im][BF_4]$ under high pressure, thus preventing the formation of aggregates of extended alkyl-chains [285]. By replacing the $[BF_4]$ anion with the $[NTf_2]$ anion, this bending of the octyl-chain was prevented, leading to an unchanged pre-peak intensity at elevated pressures [288, 287]. Thus, high-pressure dielectric measurements on these ILs should reveal whether the slow dynamic process can be connected to the pre-peak, i.e., to aggregates, based on the pressure dependence of its appearance. Therefore, those measurements were performed in the laboratory of Marian Paluch at the University of Katowice by the present author assisted by Zaneta Wojnarowska with the equipment described in section 3.2. The results were previously published in reference [267].

At first, the IL $[C_8C_1Im][BF_4]$ is considered, where it is known from section 5.3 that the time scale of the slow dielectric process does not coincide with the dynamics of the aggregate as identified by combining light scattering and X-ray data. Since the intensity of the pre-peak is found to decrease with increasing pressure, due to the inability of the cations to form aggregates at high pressure [286, 285], it is expected that the slow dielectric process should diminish or vanish at elevated pressure if it can be assigned to the dynamic contribution of the aggregates. Thus, a master-plot of the dielectric data at 253 K is shown in the $\epsilon''_{der}(\omega)$ representation for pressures between ambient condition and 500 MPa in figure 5.29.

In the inset, the X-ray scattering data in the scattering vector range of the pre-peak is reproduced from reference [286]. There, it can be seen that the pre-peak, which is clearly visible at ambient pressure, has a markedly reduced intensity at 300 MPa and is almost vanished at 1000 MPa. In contrast, the shape of the dielectric spectrum does not change at all up to a pressure of 500 MPa. Most importantly, the intensity of the slow peak does not decrease. The temperature dependence of its intensity will be discussed later, but it can be already stated that the slow dielectric relaxation in $[C_8C_1Im][BF_4]$ does neither agree in time scale nor in pressure responsiveness with that of the aggregates.

In order to check whether this behavior is special to $[C_8C_1Im][BF_4]$, or if the slow dielectric process can not be assigned to aggregate dynamics in general, other ILs are considered in the following. Like before, the comparison of the dielectric master-plot with the pre-peak intensity is shown in figure 5.30, this time for the pyrrolidinium based IL $[Pyrr_8][NTf_2]$.

The data in the inset is the simulated pressure-dependent structure factor at room temperature

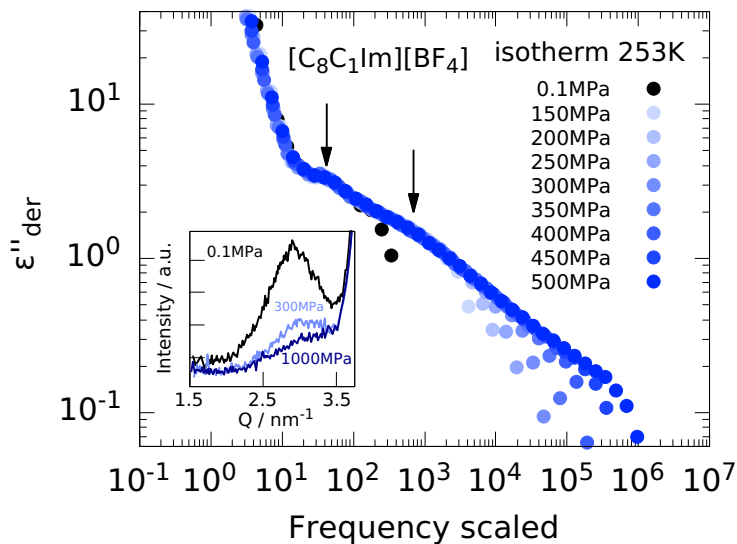


Figure 5.29.: Pressure dependent conductivity free representation $\epsilon''_{\text{der}}(\omega)$ of $[\text{C}_8\text{C}_1\text{Im}][\text{BF}_4]$ at 253 K. Data is shifted horizontally to superimpose on the 500 MPa data set. Two distinct processes are marked by arrows. Neither the shape nor the intensity of the spectra changes with increasing pressure.

Inset: Pressure dependent, room temperature X-ray scattering data adapted from reference [286]. The pre-peak intensity decreases markedly by increasing the pressure.

in the q -range of the pre-peak adapted from reference [312]. Again, the decreasing intensity of the pre-peak with increasing pressure can be seen, which is again not reflected in the dielectric spectrum, where the overall shape stays constant up to a pressure of 550 MPa.³ Thus, also in this case, the pressure dependence of the pre-peak does not agree with that of the slow dielectric relaxation, implying a different microscopic origin.

Three more ILs with at least one octyl chain were investigated by high pressure dielectric spectroscopy: $[\text{C}_8\text{C}_1\text{Im}][\text{NTf}_2]$, $[\text{N}_{2,2,2,8}][\text{NTf}_2]$ and $[\text{N}_{8,8,8,1}][\text{NTf}_2]$. As discussed before, only one dielectric relaxation process was found in the latter case, which is the conductivity relaxation, although a pre-peak in the X-ray scattering data was found [74]. Therefore, the measurements on this IL can provide information about the pressure dependence of the conductivity relaxation without complicating the data evaluation by the presence of an additional process. This is discussed below. In the case of $[\text{C}_8\text{C}_1\text{Im}][\text{NTf}_2]$, the weak pressure dependence of the X-ray scattering pre-peak, found by experiment and simulation [288, 287], was explained by the role played by the anion in preventing the bending of the alkyl chain, which was found for $[\text{C}_8\text{C}_1\text{Im}][\text{BF}_4]$. Thus, the formation of aggregates takes place even at high pressures in $[\text{C}_8\text{C}_1\text{Im}][\text{NTf}_2]$. The slow dielectric process also does not change upon pressurization, which would, in principle, match the X-ray results. However, this finding loses its significance in the

³The total intensity of the dielectric spectra slightly decreases with increasing pressure, which is accounted for by shifting the spectra vertically to superimpose. This does not influence the statement, as the intensity of the slow relaxational process stays constant compared to the intensity of the fast process.

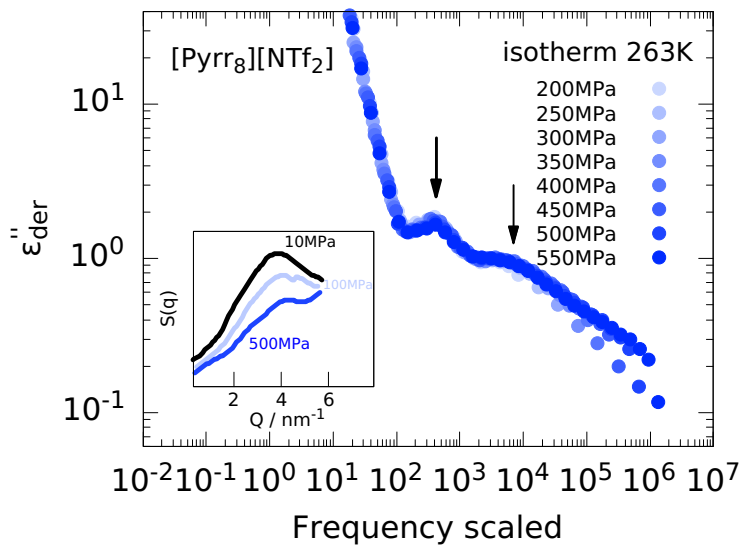


Figure 5.30.: Pressure dependent conductivity free representation $\epsilon''_{\text{der}}(\omega)$ of $[\text{Pyrr}_9][\text{NTf}_2]$ at 263 K. Data is shifted horizontally to superimpose on the 550 MPa data set and slightly adjusted vertically due to the onset of crystallization (see text for details). Two distinct processes are marked by arrows. The shape does not change with increasing pressure.

Inset: Pressure dependent simulated structure factor at 295 K adapted from reference [312]. The pre-peak intensity decreases markedly by increasing the pressure.

light of the other two ILs, where the same pressure insensitivity was found but combined with decreasing intensity of the pre-peak. Also, in the case of $[\text{N}_{2,2,2,8}][\text{NTf}_2]$, the slow dielectric relaxation is insensitive to increasing pressure. However, to the best of the author's knowledge, no pressure-dependent X-ray scattering measurements exist in the literature for this IL, thus preventing a direct comparison.

It should be noted that all the above comparisons of the dielectric and X-ray scattering data are performed at the highest isotherm recorded in dielectric measurements because the X-ray scattering measurements were carried out around room temperature. The temperature dependence of the slow dielectric relaxation is discussed in the following, including isobaric measurements at atmospheric pressure and isothermal measurements at three different temperatures with pressures up to the limit determined by the crystallization of the pressurization oil. All data was evaluated by combining the MIGRATION model, describing the conductivity relaxation, with a CD function for the slow relaxation. The shape parameter β_{CD} was fixed to 0.5 in all cases, i.e., the value which was found to be generic for dipolar reorientations where dipole-dipole interactions are small. If this is justified for the case of ILs is unclear. However, a very good description of the dielectric data is obtained utilizing this value, as seen below. In cases where a secondary relaxation was observed, i.e. for $[\text{Pyrr}_8][\text{NTf}_2]$ and $[\text{N}_{2,2,2,8}][\text{NTf}_2]$ at low temperatures, an additionally CC-function was employed. This β -relaxation is not discussed further. As always, a power law is added in the $\epsilon^*(\omega)$ representations to account for

the electrode polarization. As an example of those fits, the temperature-dependent spectra at ambient pressure of $[C_8C_1Im][NTf_2]$ are shown in figure 5.31 in six different representations, where the black lines are fits as described right before. The spectra and the fits are qualitatively similar to the other ILs.

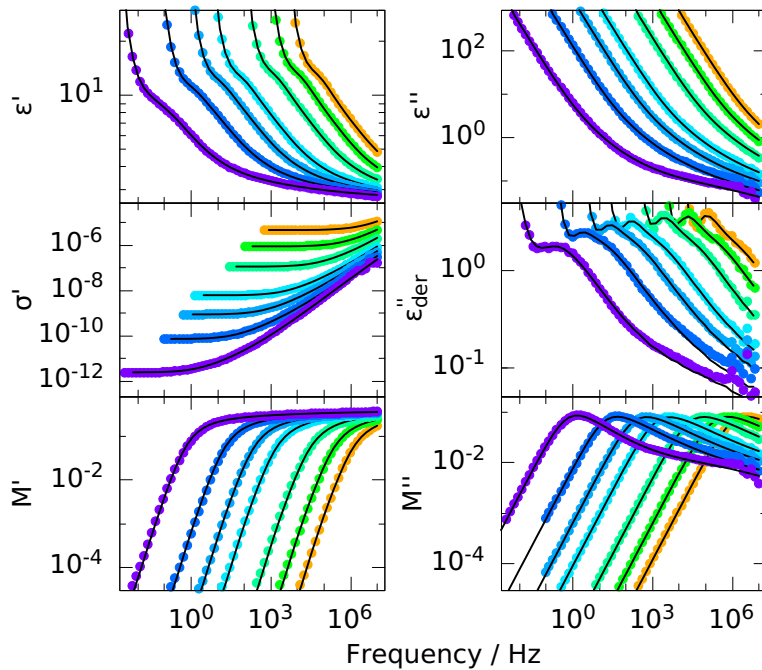


Figure 5.31.: Data of $[C_8C_1Im][NTf_2]$ at ambient pressure in 10 K steps from 235 K to 205 K and further on in 5 K steps from 200 K to 190 K. Black solid lines are fits with a sum of the MIGRATION model and a Cole-Davidson function.

It can be seen on the one hand that the model can describe the dielectric data in all representations and for all temperatures very well. On the other hand, as discussed before, the slow process is only seen by eye in the conductivity free representation $\epsilon''_{\text{der}}(\omega)$ as a sharp peak at frequencies lower than the conductivity relaxation peak. However, the attempt to fit the data with the MIGRATION model without an additional CD function naturally not only fails in this representation but also in the other ones. Additionally, it can be directly seen that the intensity of the slow process decreases at low temperatures, where its presence at 190 K is only noticeable by the fact that the rising low-frequency flank of the conductivity relaxation is not visible.

The shape parameter of the MIGRATION model λ , as well as the dielectric strength of the slow and the conductivity relaxation, are shown in figure 5.32 as a function of the conductivity relaxation time τ_σ . This is done in this way in order to be able to compare the isothermal and isobaric measurements. Red diamonds denote ambient pressure measurements while the other colors/symbols show isothermal measurements with temperatures as indicated for each IL. Since the measurements under ambient and elevated pressure are performed in different sample cells, slight variations can occur in $\epsilon'(\omega)$ due to imperfect calibrations, which are accounted for by scaling $\epsilon'(\omega)$ of the high-pressure cell in such way that ϵ_∞ matches the one

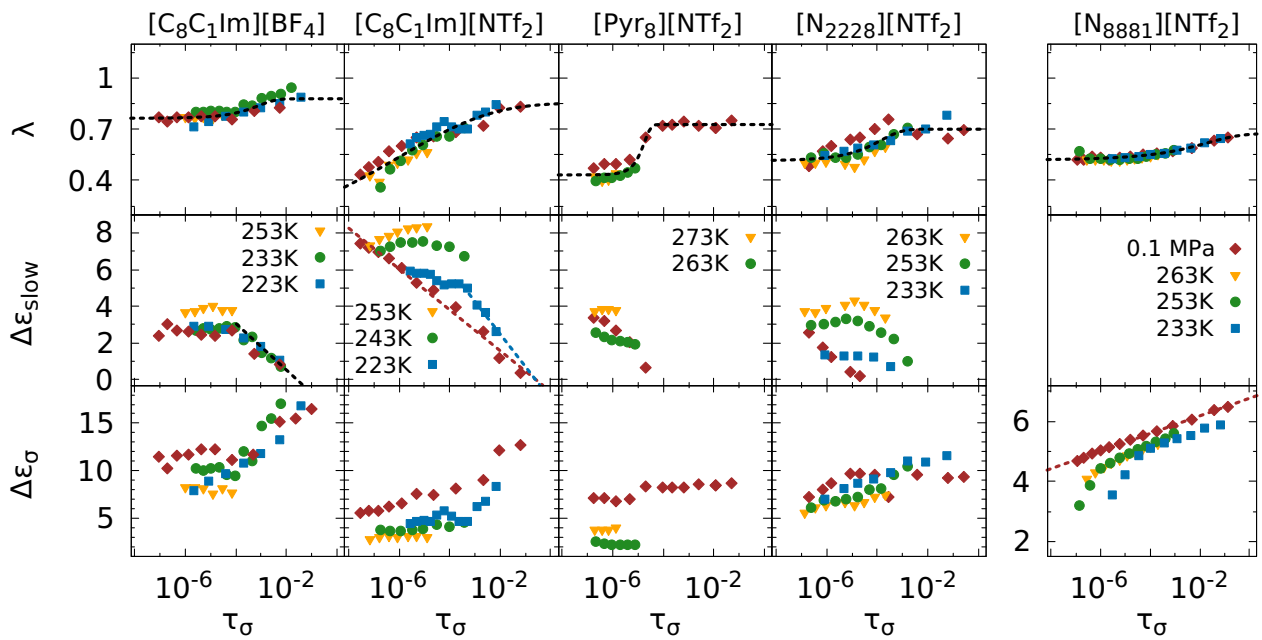


Figure 5.32.: From top to bottom: Shape parameter λ of the MIGRATION model, dielectric strength of the slow and fast relaxation process, respectively, for all five ILs studied under high pressure, represented as a function of the ion hopping time τ_σ . The different isothermal and the isobaric measurements are distinguished by different symbols and colors as indicated. Dashed lines are guides to the eye.

from the ambient pressure cell. In this way, comparability of the dielectric strengths is ensured. It can be seen that the shape parameter of the MIGRATION model λ shows a sigmoidal behavior as a function of the ion hopping time τ_σ , i.e., for all isotherms and the isobar for all ILs. In the case of [C₈C₁Im][NTf₂], however, the assumed plateau at short τ_σ is not within the accessible relaxation time range. This means that the distribution of relaxation times gets narrower near the glass transition, indicating that the dynamics of anions and cations get more coupled since the broadening of the conductivity relaxation was connected to the separation of these two motions in section 5.2.2. There, the plateau value of λ at long τ_σ was used to show the correlation with the shape of the glass transition step from DSC measurements.

In the case of $\Delta\epsilon_{\text{slow}}$ of [C₈C₁Im][BF₄], the isobar and the isotherm data follow the same trend, namely an approximately constant value of the dielectric strength at short τ_σ followed by its decrease until this process vanishes at low temperatures or high pressures, respectively. For [C₈C₁Im][NTf₂] and [N₂₂₂₈][NTf₂] a similar decreasing $\Delta\epsilon_{\text{slow}}$ is observed, but with a different behavior for the isobar in comparison to the isotherms: The dielectric strength decreases starting already from the shortest τ_σ with decreasing temperature. In contrast, when increasing the pressure, $\Delta\epsilon_{\text{slow}}$ starts at the value predefined by the isobaric trend at this respective τ_σ , but then stays constant or even slightly increases with increasing pressure before it starts to decrease at higher values of τ_σ . The situation for [Pyr₈][NTf₂] seems to be like for the two ILs discussed right before, with the difference that [Pyr₈][NTf₂] is prone to crystallization, which makes this statement less clear: Only two isotherms could be measured, where it is already

seen from the decreasing intensity of the whole spectrum that crystallization sets in. Thus, for all four ILs where a slow dielectric process is observed, neither the temperature nor the pressure alone seems to be the decisive parameter for the decreasing dielectric strength $\Delta\epsilon_{\text{slow}}$. Instead, it seems connected to the relaxation timescale since the relaxation process vanishes at long relaxation times induced by high pressure or low temperatures. This means that the behavior of the slow dielectric process is not in accordance with that of the X-ray scattering pre-peak, neither for the pressure dependence as discussed above nor for the temperature dependence, since usually, the pre-peak intensity increases with decreasing temperature [73], in contrast to the decreasing intensity of the slow dielectric relaxation. Although only for one of the investigated ILs temperature-dependent X-ray measurements are reported, it is, however, also intuitively plausible that supramolecular structures will be more stable at low temperatures since less thermal energy is available for the molecules to break them. This can be seen, for instance, in the case of many monohydroxy alcohols, where the nanostructurization increases with decreasing temperature, as seen by the increasing Kirkwood correlation factor [175]. Together, this means that a different microscopic origin for the slow dielectric relaxation has to be found. As seen in section 5.3, its time scale coincides with the cation reorientation as measured by light scattering in the case of $[\text{C}_8\text{C}_1\text{Im}][\text{BF}_4]$. Thus, in the next subsection, a comparison between dielectric and light scattering data for other ILs will be performed to check whether the rotational motions of the cationic dipole moment might indeed be responsible for the slow dielectric relaxation. There, the decreasing dielectric strength of this process will also be discussed. Before, however, a comment about the pressure and temperature-dependent dielectric strength of the conductivity relaxation $\Delta\epsilon_\sigma$ is in order:

As already seen above, the slow process is absent in $[\text{N}_{8,8,8,1}][\text{NTf}_2]$, and only the conductivity relaxation is observed. It can be seen in figure 5.32 that $\Delta\epsilon_\sigma$ increases with increasing τ_σ , i.e., for increasing pressure and decreasing temperature. Similar behavior of $\Delta\epsilon_\sigma$ is found for the other ILs, however, with more scatter in the data, which is due to the correlation of the fit parameter from the slow and the ion hopping process. The size of the error bars obtained from the fits is similar to the symbol size and is thus omitted for clarity. So, although the parameters from the slow and fast process are correlated, the general trends, i.e. decreasing $\Delta\epsilon_{\text{slow}}$ and increasing $\Delta\epsilon_\sigma$ and λ with increasing τ_σ , are significant. The decreasing $\Delta\epsilon_{\text{slow}}$ for example is seen directly by eye in the $\epsilon''_{\text{der}}(\omega)$ representation of figure 5.31, as mentioned above, and similarly for the other ILs. The increasing $\Delta\epsilon_\sigma$ is reminiscent of the increasing dielectric strength with decreasing temperature of usual dipolar systems, the so-called Curie-law. In ion-conducting network glasses, an increasing dielectric strength with decreasing temperature is also often observed [313, 271, 278]. For $[\text{N}_{8,8,8,1}][\text{NTf}_2]$, where the dielectric strength of the conductivity relaxation can be determined with the highest accuracy, indeed a $\Delta\epsilon_\sigma \propto 1/T$ behavior is found. However, since $\Delta\epsilon_\sigma$ also increases with increasing pressure, there must be another origin of this behavior. Because the BNN relation (equation 5.1) connects only empirical the dielectric strength with τ_σ and σ_0 , no more can be deduced from it other than the fact that the product $\tau_\sigma\sigma_0$ increases with increasing pressure or decreasing temperature. However, this increment is so small that it is not visible in a plot as shown in reference [101], where τ_σ is shown in dependency of σ_0 in a double-logarithmic plot for various ILs and temperatures, from which a universal coupling of these two parameters was deduced. Considering the Nernst-Einstein equation, an increase in the DC-conductivity could be rationalized by an increasing

number of mobile ions. This, however, seems rather unlikely for decreasing temperatures. Thus, this question has to be left open for further studies.

5.4.2. Dipolar relaxation

An alternative microscopic origin has to be found since the slow dielectric process can not be explained to arise due to aggregates, as shown in the preceding subsection. A first hint was already given in section 5.3, where it was seen in figure 5.26 that the timescale of the slow dielectric process coincides with the reorientation time scale of the cation for the case of $[C_8C_1Im][BF_4]$. Thus, in this subsection, it should be checked whether the reorientation of the cationic permanent dipole moment might be responsible for the relaxational process found in dielectric spectra in addition to the conductivity relaxation. As mentioned already in section 2.2, the reorientation of dipoles was assumed to be the only relaxational process contributing to the dielectric spectra of ILs in several studies [79, 80, 81, 82]. It seems that a joint contribution of dipolar and conductivity relaxation was only reported in computer simulation studies [78, 86]. Therefore, as a first step, the dielectric spectra of several ILs should be compared to those from light scattering, where it was shown in section 4.1 that the cation reorientation dominates the latter. Thus, the coincidence of the slow dielectric peak with the light scattering peak for more ILs than the one already discussed in section 5.3 would indicate that indeed dipolar reorientations are responsible for the slow dielectric process. In figure 5.33, four different ILs with imidazolium-based cations equipped with alkyl-chains of different lengths and with three different anions are shown. It can be seen that the dielectric spectra, shown in the conductivity free representation $\epsilon''_{der}(\omega)$, are qualitatively similar, in the sense that no clear single peak is observed. However, a slow contribution seems to be present, which, together with the electrode polarization, renders the low-frequency flank of the conductivity relaxation invisible. At higher temperatures than the one shown here, this slow contribution develops into a clear additional peak for $[C_8C_1Im][BF_4]$, as shown above, and also for $[C_6C_1Im][NTf_2]$ as previously reported in the literature [98]. In the case of the cations with propyl and butyl chains, the separation between the slow and the conductivity relaxation and/or the relaxation strength of the slow process is too small to observe two distinct peaks. Since the appearance of the slow contribution is irrespective of the anion and the alkyl-chain length, the slow process is absent in some ammonium or phosphonium bases ILs, as seen above, it seems to be closely connected to the detailed structure of the cation.

Notably, the time scale of the slow dielectric contribution is similar in good approximation to the time scale of the reorientational process as observed in light scattering for all four ILs. This can be seen in figure 5.33 by the fact that the light scattering peak is located at frequencies slightly above the insetting electrode polarization and thereby in the frequency range of the slow dielectric contribution. Thus, it is slower than the conductivity relaxation, which can be seen by the fact that the dashed lines, indicating the DLS peak position, are located at frequencies lower than the DC- to AC-transition. In the case of the ILs with $[C_6C_1Im]$ and $[C_8C_1Im]$ cations, the CD time scale was left as a free fitting-parameter, while it was fixed to the time scale obtained from the light scattering data for $[C_3C_1Im][NTf_2]$ and $[C_4C_1Im][DCA]$. This was done due to an unstable fitting procedure for these two ILs when the CD time scale was left as a free fitting parameter since the two relaxational processes are hardly distinguishable. Thus,

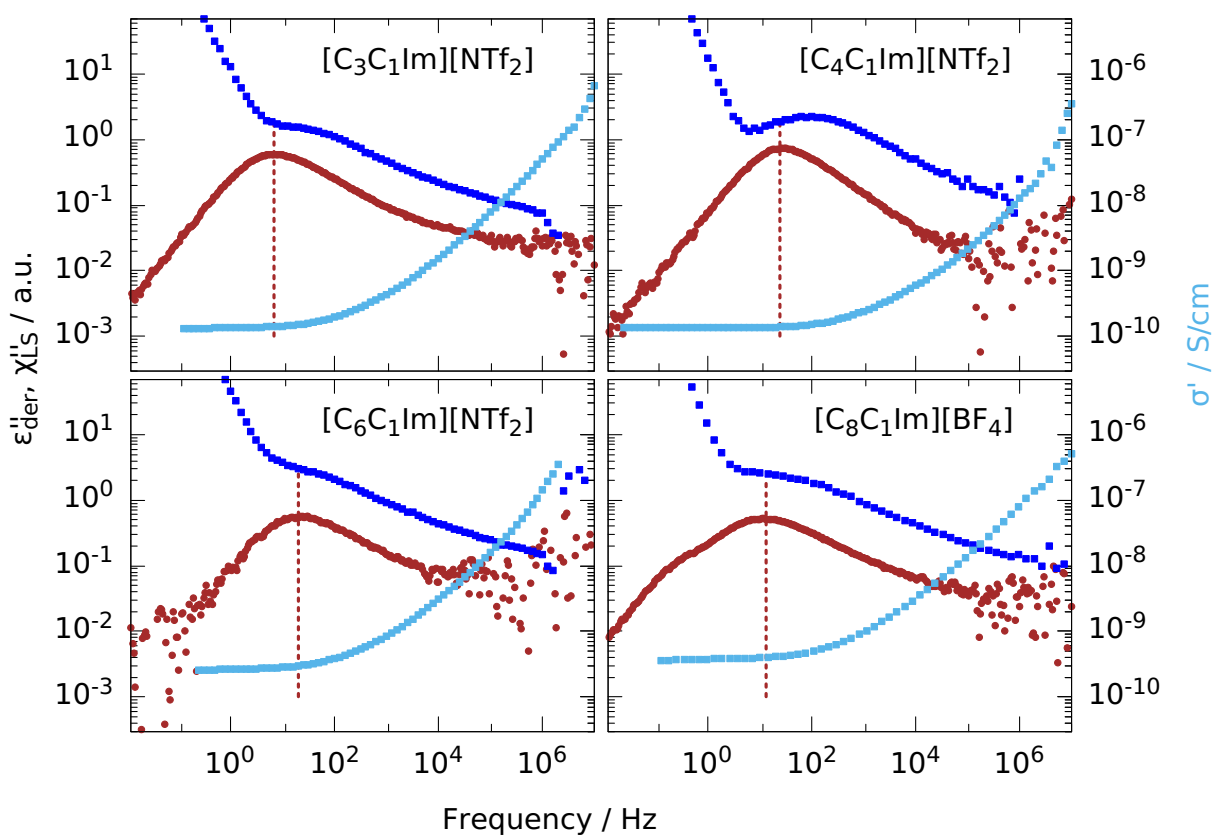


Figure 5.33.: Dielectric and light scattering spectra of imidazolium based ILs with different alkyl-chain lengths. In each case, the light scattering peak is located near the slow dielectric process, while the conductivity relaxation takes place at higher frequencies.

this kind of fitting tests the coincidence of the light scattering and the slow dielectric time scale. In either case, the fitting works well at all temperatures measured. The Arrhenius-plots are shown for $[C_3C_1Im][NTf_2]$ and $[C_6C_1Im][NTf_2]$ in figure 5.34, for $[C_8C_1Im][BF_4]$ in figure 5.27 and for $[C_4C_1Im][DCA]$ later in figure 6.7. In all cases the relation $1 < \frac{\tau_{slow}}{\tau_{DLS}} < 3$ holds to good approximation in the limit of experimental uncertainties. In the cases where $\tau_{slow} = \tau_{DLS}$ was fixed, the successful dielectric fits indicate the coincidence of these two relaxation times. Thus, for all ILs where a slow dielectric process is observed and for which light scattering data were obtained, the agreement of their relaxation times indicate a common origin, which is the reorientation of the cation, observed via the reorientation of its permanent dipole moment or its polarizability tensor in dielectric spectroscopy and light scattering, respectively.

The question which then naturally arises is why the slow dielectric process is not visible in dielectric spectra of all ILs. Concerning dipolar reorientation, the decisive point is, of course, the magnitude of the permanent dipole moment μ of the molecule. The dielectric strength $\Delta\epsilon_{slow}$ of the dipolar relaxation is coupled via equation 3.18 to the square of the permanent dipole moment. Thus, for ions with a too low μ -value, no dipolar relaxation process is expected to be visible beside the conductivity relaxation. Therefore, it should be checked in the following

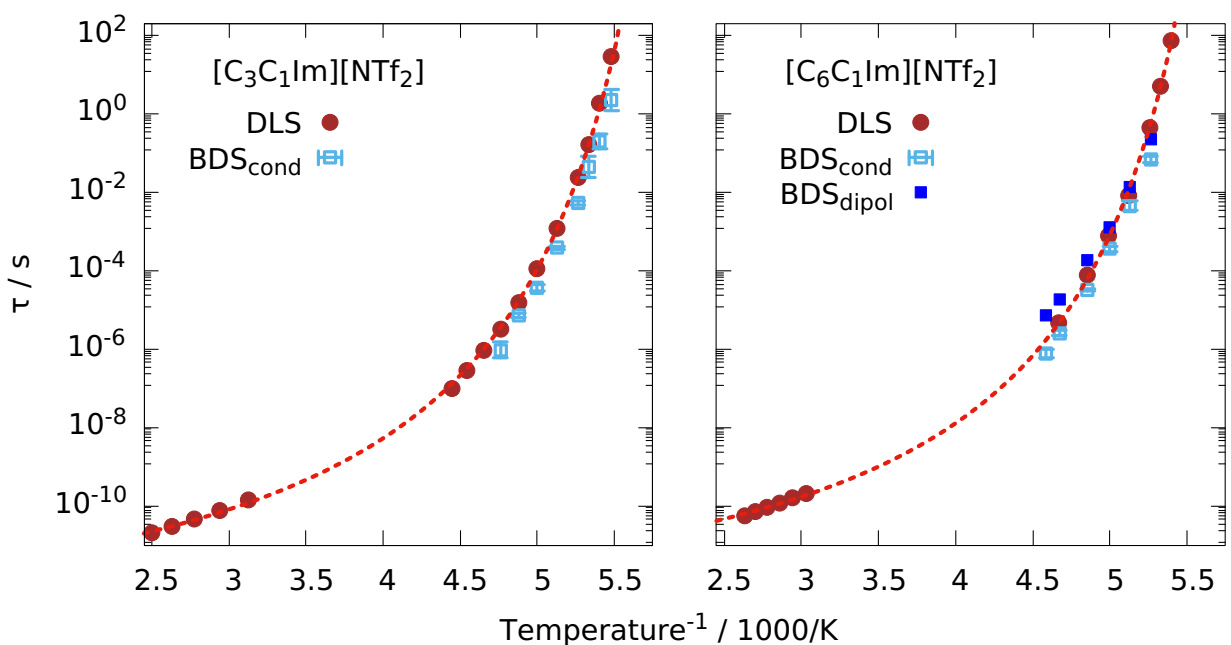


Figure 5.34.: Arrhenius plots for $[C_3C_1\text{Im}][\text{NTf}_2]$ and $[C_6C_1\text{Im}][\text{NTf}_2]$.

whether the appearance of the slow dielectric process is connected to the magnitude of the dipole moment of the cation. The anions are neglected in this discussion for the following reason: The $[\text{BF}_4^-]$ anion does not bear a permanent dipole moment due to its symmetry. The most stable conformer of the $[\text{NTf}_2^-]$ anion has a small dipole moment of 0.3 D, while averaging over the two conformer found in reference [314] with the experimental energy difference of 3.5 kJ/mol leads to a dipole moment of $\langle \mu \rangle = 1.1$ D. This value is similar to the DFT calculated value of [DCA], where $\mu = 1$ D and both are thus markedly lower than the smallest dipole moment of the cations, which is 2.5 D in the case of $[\text{N}_{2,2,1,201}][\text{NTf}_2^-]$. Since the dielectric strength depends on the quadratic dipole moment, the contribution of the anion is small compared to that of the cation and thus neglected in the following considerations. In table 5.1, the dipole moments of the cations are listed, where in the first column the values for the all-trans conformer is shown as calculated by DFT calculations. For cations equipped with long alkyl-chains the values are tremendous, which would lead to a huge dipolar contribution in the dielectric spectrum. However, it is known from the discussion in section 4.1 that the all-trans conformer is usually not the most stable one for long chain molecules. Therefore, the mean dipole moment for the conformer ensemble determined with CREST is shown in the second column. Although these values are also fraught with considerable uncertainty, due to the size of the conformer ensemble, they are more reasonable. In the third column, the dielectric strength $\Delta\epsilon_{\text{slow}}$ of the slow process is shown, which is taken at the highest temperature at which fitting was possible, thus at similar relaxation times for the different ILs. This is done to assure at least some degree of comparability of the values of the various ILs since it was found (see figure 5.32) that $\Delta\epsilon_{\text{slow}}$ decreases with increasing correlation time. It can be seen that for the homologous series of imidazolium-based ILs with the $[\text{NTf}_2^-]$ anion, the dielectric strength increases with increasing dipole moment. The lower value of $\Delta\epsilon_{\text{slow}}$ for $[C_8\text{C}_1\text{Im}][\text{BF}_4^-]$

in comparison to $[C_8C_1Im][NTf_2]$ indicates the presence of more curled conformers in the former case, in accordance with the findings from light scattering measurements detailed in section 5.2.1.

Cation	μ_{trans}	$\langle \mu \rangle$	$\Delta\epsilon_{slow}$	Cation	μ_{trans}	$\langle \mu \rangle$	$\Delta\epsilon_{slow}$
$[C_3C_1Im]$	3.3 D	2.8 D	1.6	$[N_{2,2,1,201}]$	4.1 D	2.5 D ^a	0
$[C_4C_1Im]$	5.2 D	4.2 D	1.2 ^[DCA]	$[N_{8,8,8,1}]$	6.0 D	10.9 D	0
$[C_6C_1Im]$	9.8 D	7.0 D	2.8	$[N_{2,2,2,8}]$	10.5 D	7.1 D	2.6
$[C_8C_1Im]$	14.9 D	7.3 D	1.7 ^[BF₄] , 8.3	$[P_{14,6,6,6}]$	14.5 D	5.7 D	0
$[Pyrr_{8,1}]$	12.6 D	7.5 D	3.4				

Table 5.2.: Permanent dipole moments of various cations calculated by DFT and experimental dielectric strengths. Dipole moments of the all-trans conformers are shown as well as conformer averaged values. $\Delta\epsilon$ values are taken at the highest temperature at which fitting was possible, i.e., at similar relaxation times for each IL. a) Calculated using the conformer ensemble from reference [315].

However, no slow dielectric process is visible for the two ammonium-based cations and the phosphonium-based cation, although the magnitude of their dipole moments is similar to the imidazolium-based cations. This means that although some correlation between the dielectric strength of the process and the magnitude of the dipole moment exists, a notable dipole moment seems not to suffice for a dipolar relaxation to show up. Two cations are especially suited for direct comparison: $[C_3C_1Im]$ and $[N_{2,2,1,201}]$. Both are small enough to consider their conformers explicitly in order to determine the mean dipole moment. This was done for $[N_{2,2,1,201}]$ in great detail in reference [315] and from the energetically most stable eight conformers the mean dipole moment was calculated here to be $\langle \mu \rangle = 2.5$ D. In the case of $[C_3C_1Im]$, only three conformers are possible, namely the all-trans, gauche+ and gauche-. The considerable population of all three conformers found in DFT calculations agrees with the Raman measurements performed in reference [289]. Thus, the value of the mean dipole moment is $\langle \mu \rangle = 2.8$ D, i.e. very similar to the value of $[N_{2,2,1,201}]$, and both values can be considered to be quite accurate. Nevertheless, no slow dielectric process is seen in $[N_{2,2,1,201}][NTf_2]$, while it is seen in $[C_3C_1Im][NTf_2]$. It should be noted that the number density, which could influence the dielectric strength additionally according to equation 3.18, is also almost identical for both ILs. Hence, there must be a reason besides the magnitude of the dipole moment for the slow dielectric process to be visible or not. A possible hint might have been already given in figure 5.18. There, a comparison of the dielectric and the light scattering spectra of the two ammonium-based ILs, for which no slow dielectric relaxation is observed, was performed. It can be seen that the light scattering peak agrees very well with the dielectric peak in the case of $[N_{2,2,1,201}][NTf_2]$, whereas the slow light scattering peak, associated with the cation, is markedly slower than the dielectric peak in the case of $[N_{8,8,8,1}][NTf_2]$, where it is located in the frequency range which is dominated by electrode polarization in the dielectric spectrum. From that, the idea arises that a dipolar contribution might also be present in those dielectric spectra, which, however, is hidden either under the conductivity relaxation or under the electrode polarization, depending on the time scale of

the dipolar reorientation. As this idea is very hard to prove using actual data, model spectra are considered to check this conjecture. Therefore, in figure 5.35 spectra are shown in $\sigma'(\omega)$, $\epsilon'(\omega)$ and $\epsilon''_{\text{der}}(\omega)$ representation obtained by a superposition of the MIGRATION model, a CD function and electrode polarization. Three columns are shown, where the only difference between them is the change in the CD relaxation time τ_{CD} , which is chosen in such a way that the CD and the conductivity relaxation peak coincide in the first column, while they are slightly separated in the second and markedly separated in the third column.

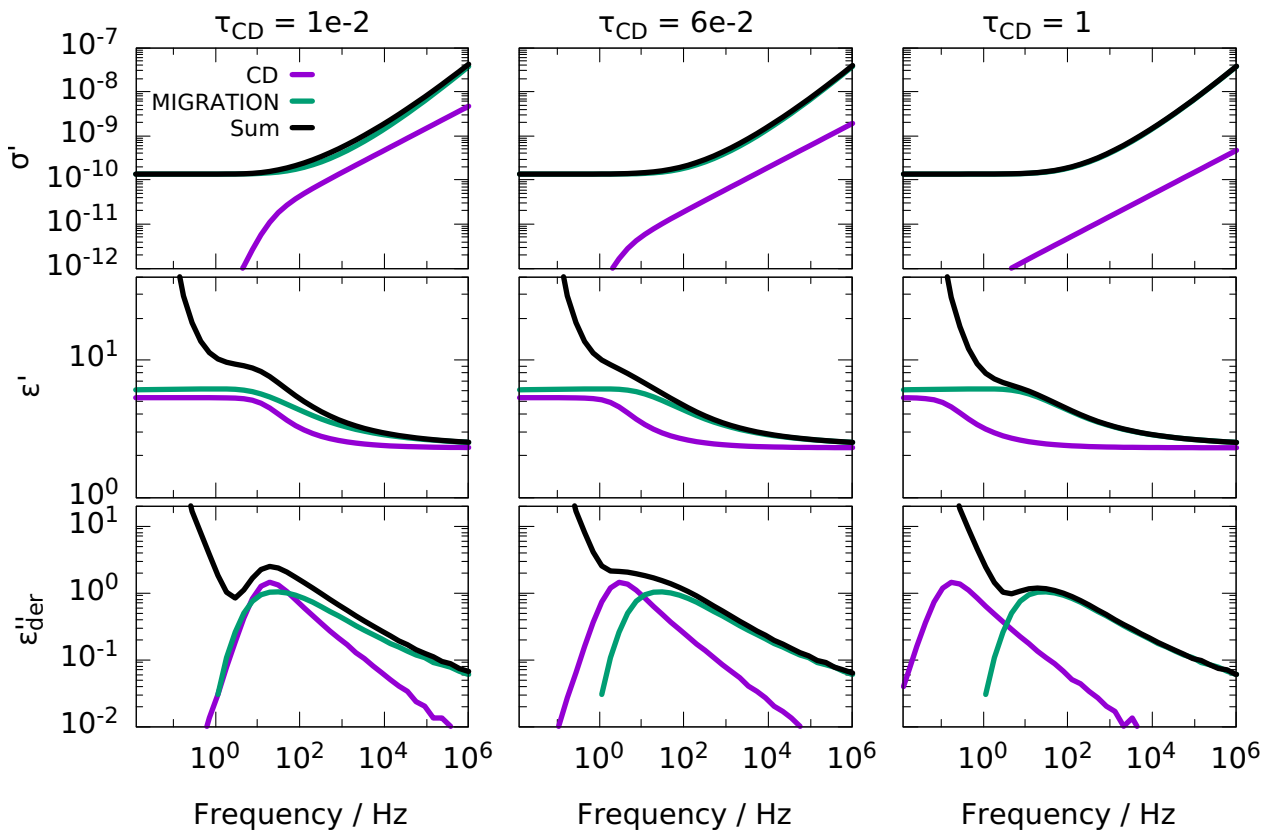


Figure 5.35.: Visualization of model spectra for different time constants of the CD function, while all other parameters are fixed. A single peak can be observed in the case of similar peak positions of the CD function and the MIGRATION model (left column) or in the case of a peak position of the CD function notably lower in frequency (right column).

As can be seen, the changes in the conductivity representations are only marginal, with the strongest influence of the CD function on the spectrum in the case where its peak frequency is similar to the MIGRATION peak frequency. This means that if a fit were performed to such data with a conductivity relaxation model in this representation, the fit parameter would hardly change between these three scenarios. Thus, the subtlety of the dipolar relaxation is easily overlooked. In the real part of the permittivity, the relaxation strength depends on the separation of the two processes, and the low-frequency plateau is best established in the left column. The most evident difference is seen in the conductivity-free representation. A

clear single peak is observed in the left column, i.e., when the peak position of dipolar and conductivity relaxation is similar. In the case where the CD peak frequency is slightly lower than the conductivity relaxation, as seen in the middle column, a broad bimodal spectrum appears, where no transition to the low-frequency flank can be observed before the electrode polarization sets in. In the right column, where the CD relaxation time is markedly slower than the conductivity relaxation time, a single broad peak is observed with only a slight portion of the low-frequency flank visible. It should be noted that the strength of the CD relaxation is chosen rather high in this comparison in order to emphasize its contribution thus the effects might even be more subtle in real spectra.

Together, the situations in the three columns of figure 5.35 can rationalize the findings for different ILs: The scenario in the left column could be connected to $[N_{2,2,1,201}][NTf_2]$, where the light scattering peak is located at the same or slightly higher frequencies than the dielectric peak, thus indicating that the reorientation of the cation takes place on nearly identical time scales as the conductivity relaxation, leading to a single dielectric peak. It should be noted that in an early publication of the present author [90], the origin of the dielectric process was entirely ascribed to dipolar reorientation due to the accordance with the light scattering time scale. However, in light of the present work results, the contribution of the conductivity relaxation has to be taken into account, resulting in the interpretation that the dielectric spectrum can most probably be ascribed to a sum of conductivity and dipolar relaxation appearing on a very similar time scale. The appearance of the peak in $\epsilon''_{der}(\omega)$ in the middle column is reminiscent of the imidazolium-based ILs shown in figure 5.33, indicating a slight time scale separation between the slower dipolar relaxation and the faster conductivity relaxation. This separation increases with the increasing length of the alkyl-chain like it was the case for the separation of cation and anion rotation in the light scattering spectra detailed in section 5.2.1. The scenario in the right column could explain the dielectric spectra of $[N_{8,8,8,1}][NTf_2]$, where it was seen in figure 5.18 that the reorientation of the cation, as measured by light scattering, appears on frequencies where the electrode polarization overshadows the possibly present dipolar relaxation in the dielectric spectrum. It should be noted that in cases where a dipolar relaxation appears on higher frequencies than the conductivity relaxation, this contribution is also clearly visible in $\sigma'(\omega)$. This can already be anticipated by the trend of the CD contribution in the upper row of figure 5.35. Such a scenario was not observed in any neat IL in this study but will be seen in chapter 6, where mixtures of an IL with dipolar solvents are considered. Thus, from the above findings of this subsection, it must be concluded that the origin of the slow dielectric process is most probably due to the reorientation of the permanent dipole moments of the cations. The strength and time scale greatly impact its visibility, competing with the omnipresent conductivity relaxation and electrode polarization. However, one feature of the dipolar relaxation in ILs is opposite from what is usually observed in non-ionic liquids, namely the decreasing relaxation strength upon decreasing temperature as seen in figure 5.32. Therefore, possible reasons for this should be discussed in the following.

At first, it is crucial to discriminate decreasing dielectric strengths from the literature in ion-conducting materials from the one in this work. For example, a decreasing dielectric strength was found in CKN, where no permanent dipole moments are present [59]. This means that in this case, the strength of the conductivity relaxation decreases, unlike what is found in this work, i.e., a decreasing strength of the dipolar relaxation. Thus, in CKN, this feature can be

rationalized by the fact that the potassium cations are still mobile below the glass transition, while the calcium cations and nitrate anions are immobile [63, 316]. Thus, only about one-fourth of all mobile ions in the liquid state remain mobile in the glassy state. Considering the Nernst–Einstein equation, this gives a decrease in the DC-conductivity of more than a factor of 4 in the glass transition region, which is directly reflected in the dielectric strength according to the BNN relation (equation 5.1) [316]. Above and below the glass transition region, the number of mobile ions is constant and so is the dielectric strength. This behavior was also reported for a polymerized IL below the glass transition, where only the lithium anion remains mobile [102].

In the case of the decreasing strength of the dipolar relaxation, a different explanation has thus to be found. Commonly, in non-ionic dipolar liquids, the relaxation strength increases with decreasing temperature according to the Curie law with $\Delta\epsilon \propto 1/T$ [175]. A tendency of the dipole moments to orient parallel can amplify this increase through an increasing Kirkwood correlation factor g_K . However, a decreasing dielectric strength is also reported for some alcohols, and carboxylic acids [175]. This behavior is associated with a more anti-parallel ordering of the dipoles, leading to a decreasing g_K . Thus, it might be possible that the decreasing dielectric strength found for the ILs of this study is caused by a decreasing Kirkwood correlation factor, which in turn might be due to a loss of preferred parallel ordering or an increasing anti-parallel ordering. Since it was found in section 5.2.1 that also the light scattering strength decreases in the case of $[C_3C_1Im][NTf_2]$ with decreasing temperature, it is instructive to compare the strengths and correlation factors from dielectric spectroscopy with those obtained by light scattering. This is done in figure 5.36. There, it can be seen in the upper panel that the values of $T\Delta\epsilon$ decrease similarly, but slightly steeper, than the $T\Delta\chi$ values at low temperatures. The correlation factors g_1 , i.e., the dielectric Kirkwood factor and g_2 , calculated from light scattering data, are compared in the lower panel.

For the calculation of g_1 a mean dipole moment of $\langle\mu\rangle = 1.96$ D and a mean optical anisotropy $\beta = 4.62 \text{ \AA}^3$ for $[C_3C_1Im][NTf_2]$ is used, obtained from DFT calculations. The black dashed line is a fit to the g_2 values, the slope of which is then taken for a fit of the g_1 values. It can be seen that it describes the data quite well thus the temperature dependence of the g_1 and g_2 values are identical. This is a rather surprising finding and does not match the expectation one has when comparing these values. This is because the correlation factors are dependent on the cosine of the angle between the molecules, as seen in equations 3.19 and 4.9, but proportional to the first or second Legendre polynomial in the case of the dielectric g_1 and the light scattering g_2 factor, respectively. Thus, when the average angle between the neighboring molecules changes depending on the temperature, the change in g_1 and g_2 should be markedly different. This means that it is rather unlikely that indeed a change in the correlation factor is responsible for the decreasing relaxation strengths.

Instead, an explanation has to be found, which takes into account the concomitantly decreasing relaxation strength found in dielectric spectroscopy and light scattering. One possibility would be that the population of the all-trans conformer diminishes with decreasing temperatures, and the more curled conformer are thus preferred. This would lead to a decreasing mean effective optical anisotropy parameter $\langle\beta\rangle$ and a decreasing mean dipole moment $\langle\mu\rangle$ and consequently to a decreasing relaxation strength. While this scenario seems more realistic for cations with longer alkyl chains, where the difference of these values is large between the stretched and

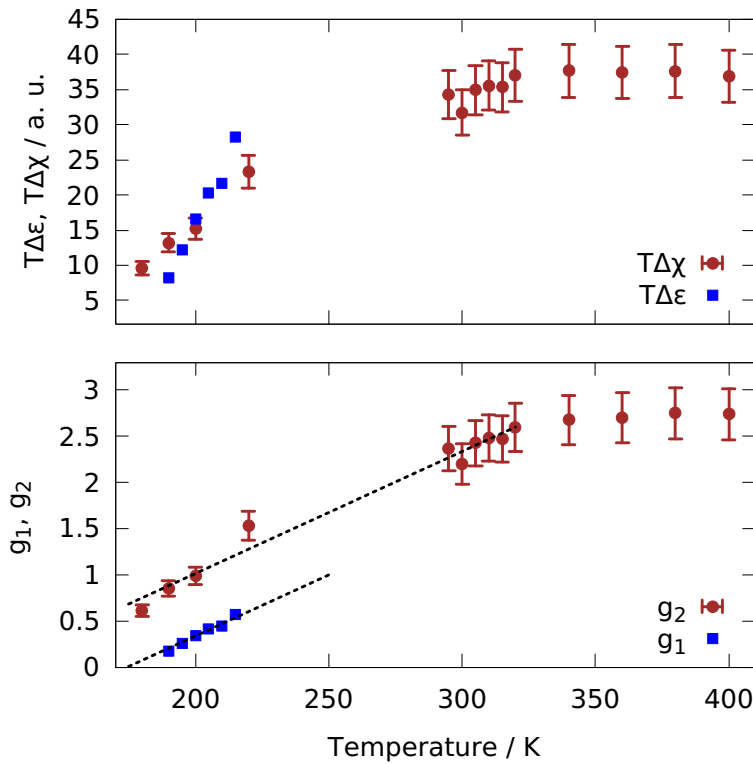


Figure 5.36.: Relaxation strength of $[C_3C_1Im][NTf_2]$ from dielectric and light scattering measurements multiplied with temperature in the upper panel. In the lower panel, the correlation factors g_1 and g_2 are shown, calculated from the relaxation strengths.

curled conformers, it cannot explain the amount of decrement of the relaxation strength in $[C_3C_1Im][NTf_2]$, where these values do not differ enough between the conformers. Moreover, a identical percentage decrease in $\langle\beta\rangle$ and $\langle\mu\rangle$ with temperature is required, which seems rather unlikely.

A scenario that would naturally lead to a simultaneous decrease in the scattering intensity and the dielectric strength is the immobilization of some cations. One could imagine that at lowering the temperature, aggregates form due to the clustering of non-polar alkyl-chains. Those cations incorporated in such an aggregate are hindered in free rotational motion and thus do not contribute to the α -relaxation. Instead, the aggregates, which necessarily need to have a low optical anisotropy to be invisible in the light scattering spectrum, perform slow rotational diffusion, which is also not observed in the dielectric spectra due to the overlying electrode polarization. This idea could explain the markedly lower scattering intensity of the $[C_8C_1Im]$ cation in the IL $[C_8C_1Im][BF_4]$ than in $[C_8C_1Im][NTf_2]$ with a markedly higher degree of aggregation in the former IL as seen by the additional slow process appearing in the light scattering spectrum. However, some questions remain, as usually no aggregates are expected for such short chain length as in $[C_3C_1Im][NTf_2]$. Also, regarding the light scattering intensity, only one-fourth of the cations contributing to the spectrum at high temperatures seem to contribute near the glass transition temperature. Thus, most cations are within aggregates, and

their dynamics are still not detectable. Together, this scenario could explain the experimental findings best, but some implications are questionable. Thus, it is still speculative, and more work is needed in this direction to confirm this picture.

Concluding this subsection, it became clear that the slow dielectric process originates in the reorientation of the permanent dipole moment of the cation. This assignment was made for various ILs by comparison with light scattering data, where it was found that the timescale of the cation reorientation from light scattering agrees with that of the slow dielectric process. This is contradictory to some works in the literature, where the dielectric low frequency process is often ascribed to dynamics of aggregates. The fact that in some ILs, the slow relaxation is not seen in the dielectric spectra was explained by a too small or too large separation from the conductivity relaxation. Also, the temperature dependence of the dielectric strength of the slow process is in agreement with the light scattering intensity. The reason for this decreasing strength is not resolved conclusively. It has been speculated that some cations may be prevented from performing free rotational motions because they are bound in aggregates.

6. Molecular dynamics in ionic liquids with admixtures

As detailed in section 2.2, mixtures of ionic liquids with gelling agents might be highly interesting for several applications since, in this way, the high ionic conductivity of the IL can be combined with the mechanical rigidity of the sample, thus preventing leakage, which is desirable e.g. for electrolyte applications. However, to tailor such gels for specific needs, it is crucial to understand the molecular dynamics of the ions. Therefore, this chapter considers mixtures of the IL $[C_4C_1Im][DCA]$ with three different admixtures, namely water, 1-propanol, and gelatin. This is done for the following reasons: If an ionic gel should be produced with gelatin as a gelling agent, it is usually necessary to add water since gelatin is not soluble in most ILs, but in water. Thus, it is important as a first step to understand the dynamics in an IL-water mixture and to have the dynamics of this mixture as a reference to compare to the ionic gel, which is composed of IL, water and gelatin. However, as will be seen, a thorough understanding of the dynamics of the IL-water mixture is hampered by the fact that such a mixture can only be investigated up to a certain concentration of water due to insetting crystallization in the case of higher concentrations. This amount of water does not suffice to unequivocally separate the dynamics of water and ions, which is why 1-propanol is chosen as a second admixture, where mixtures over the whole concentration range can be investigated, allowing to address the dynamics separately in the 1-propanol rich mixtures. With this knowledge, the dynamics of the Ion Jelly is finally addressed in the last section of this chapter.

6.1. Mixtures with water

The mixtures of $[C_4C_1Im][DCA]$ with water were mainly investigated during the master thesis of Jennifer Kraus, supervised by the present author. There, the focus was to find evidence for the presence of so-called water pockets, i.e., nanoscale water clusters in the ionic liquid matrix. This was achieved by combining Raman spectroscopy in the OH-stretching region with small-angle neutron scattering and molecular dynamics simulations. These results were published in reference [317] and are not repeated here. Instead, this section focuses on how the added water impacts the spectra of dielectric, light scattering, and DSC measurements. In principle, one could imagine a broadened spectrum compared to the neat IL due to more heterogeneous dynamics imposed by the water, which has a lower glass transition temperature than the IL [318]. Also, even an additional relaxational feature in the dielectric spectra due to the reorientation of water molecules might appear. This is because neat water has a high dielectric strength of around 80 at room temperature [319]. However, the microscopic origin

of the strong dielectric relaxation process is debated in the literature [320, 321, 322, 323], where one interpretation is that its appearance is connected to the cross-correlations imposed by the hydrogen bonds, while the α -relaxation has a markedly lower dielectric strength and is located at higher frequencies, coinciding with the light scattering α -relaxation [320]. This interpretation is just like the one for monohydroxy alcohols. And indeed, mixtures with salt show that the dielectric strength of water dramatically decreases with increasing salt concentration. This is accompanied by a shift of the peak to higher frequencies [321], albeit the viscosity of the mixture increases with increasing salt concentration [324]. From the increasing viscosity, one would expect a decreasing peak frequency instead. This indicates that due to the breaking of the hydrogen-bonded network by the salt molecules, the Debye process diminishes, and only the weaker and faster α -relaxation remains at sufficient high salt concentrations. Thus, a similar scenario may be expected for the IL-water mixture, and it is not *a priori* clear whether the reorientation of water molecules will show up in the dielectric spectrum, where it would have to be discriminated from the conductivity relaxation and the reorientation of the cations. The optical anisotropy parameter β of water, on the other hand, is a factor of approximately 38 lower than the one of the $[C_4C_1Im]$ cation,¹ thus, the water relaxation is not expected to be visible in the light scattering spectra since the anisotropy parameter enters quadratic in the calculation of the scattering intensity.

Therefore, in what follows in this section, the mixture of $[C_4C_1Im][DCA]$ with 72 mol% water is considered, which was determined as the highest concentration of water for which no crystallization occurred in any experimental setup. A comparison of calorimetric, light scattering, and dielectric spectra of this mixture with neat $[C_4C_1Im][DCA]$ is shown in figure 6.1, where the spectra of the neat IL are shifted in such a way that they superimpose with one of the mixtures.

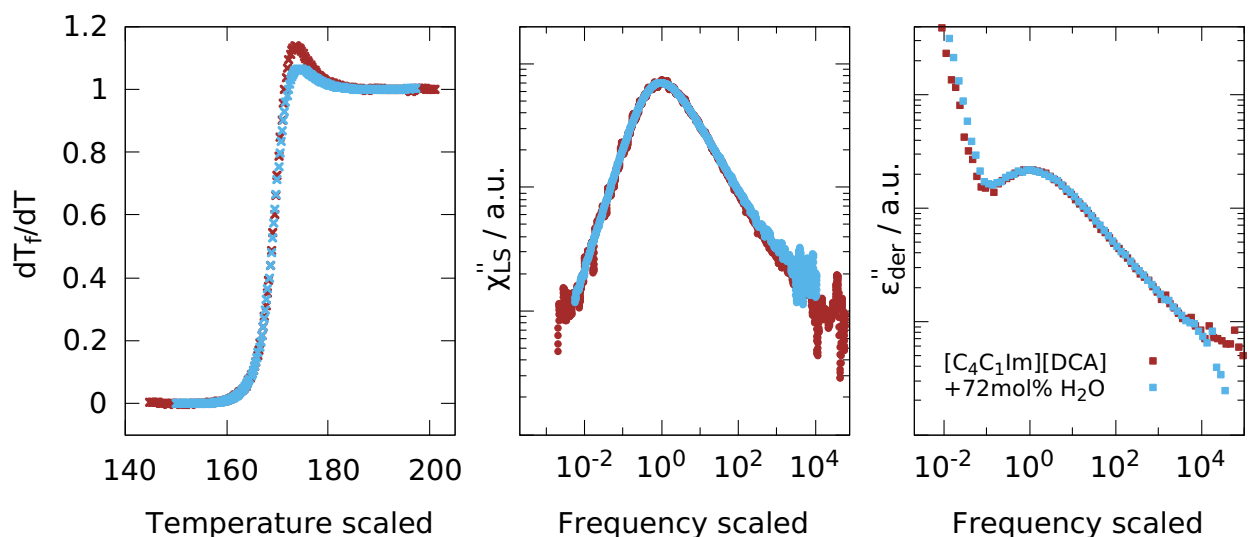


Figure 6.1.: DSC, light scattering and dielectric spectra of neat $[C_4C_1Im][DCA]$ and of the mixture with 72 mol% water. The shape of the spectra is almost identical for all experimental techniques.

¹For $[C_4C_1Im]$ the value of $\langle \beta \rangle = 6.0 \text{ \AA}^3$ is determined by DFT via the standard procedure, while the value for water is determined with the B3LYP functional and the aug-cc-pVTZ basis set ($\beta = 0.16 \text{ \AA}^3$).

It can be seen that the shape of the spectra is almost identical for the neat IL and the mixture for all experimental methods. Especially, neither a broadening nor the appearance of an additional relaxational process is seen for the case of the mixture. Thus, it seems at first glance that the only influence of the water is that the glass transition temperature is lowered compared to the neat IL, and consequently, the relaxation peaks are located at higher frequencies in the case of the mixture for identical temperatures. Since the shape and the dielectric strength of an aqueous salt solution was found to be temperature-dependent [321], it should be checked whether this finding is just a coincidence due to the chosen temperatures. Therefore, the light scattering spectra of the 72 mol% mixture are shown for a temperature range of more than 200 K in figure 6.2.

There, fits with a CD function are shown as black dashed lines, where the shape parameter β_{CD} was fixed to 0.5 for all temperatures, leading to a good description of the main peak. Thus, the shape of the light scattering spectrum stays constant from temperatures above the boiling point of water down to slightly above the glass transition temperature. Together, this means for the light scattering spectra that the water reorientation is either too weak to be visible and/or takes place on a very similar time scale as the ion reorientation. The latter is supported by the fact that if the water molecules would reorient at notably different timescales than the ions, they might also influence the dynamics of the ions in such a way that the ion relaxation peak broadens like it was observed for the mixture of toluene and squalane in figure 4.8, which is not seen here.

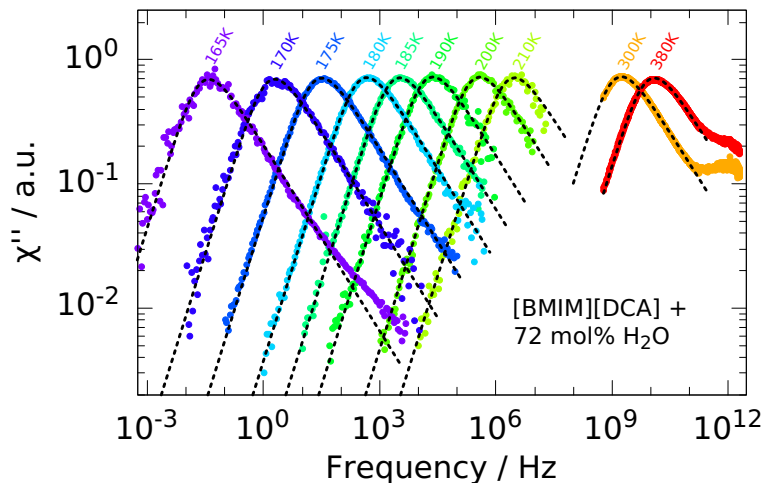


Figure 6.2.: Temperature dependent light scattering spectra of $[C_4C_1Im][DCA]$ with 72 mol% water. The dashed lines are fits with a CD function using a fixed stretching parameter $\beta_{CD} = 0.5$ at all temperatures.

As a next step, a closer look should be taken at the dielectric spectra to see whether there is any difference between the neat IL and the mixture at all temperatures. Master plots containing all temperatures measured are shown in figure 6.3, where on the left-hand side, the spectra of the neat IL, and on the right-hand side, the spectra of the mixture with 72 mol% water are shown. The data is presented in the conductivity free representation in the upper row and

in the modulus representation in the lower row. Indeed slight differences in the temperature dependence between the neat IL and the mixture can be observed: In the case of the neat IL, the intensity in the $\epsilon''_{\text{der}}(\omega)$ representation between the electrode polarization and the peak maximum decreases with decreasing temperature. This was attributed in section 5.4.2 to the decreasing contribution of the dipolar relaxation of the cation. However, this contribution is so weak in the case of $[\text{C}_4\text{C}_1\text{Im}][\text{DCA}]$, even at the highest accessible temperature, that no clear bimodality can be observed like it was the case for other ILs. In contrast, in the case of the mixture, a bimodal spectrum can be seen at high temperatures, and on lowering the temperature, the strength of the *faster* process slightly decreases, while that of the slower rather slightly increases. Such behavior was not found in any of the neat ILs in this study.

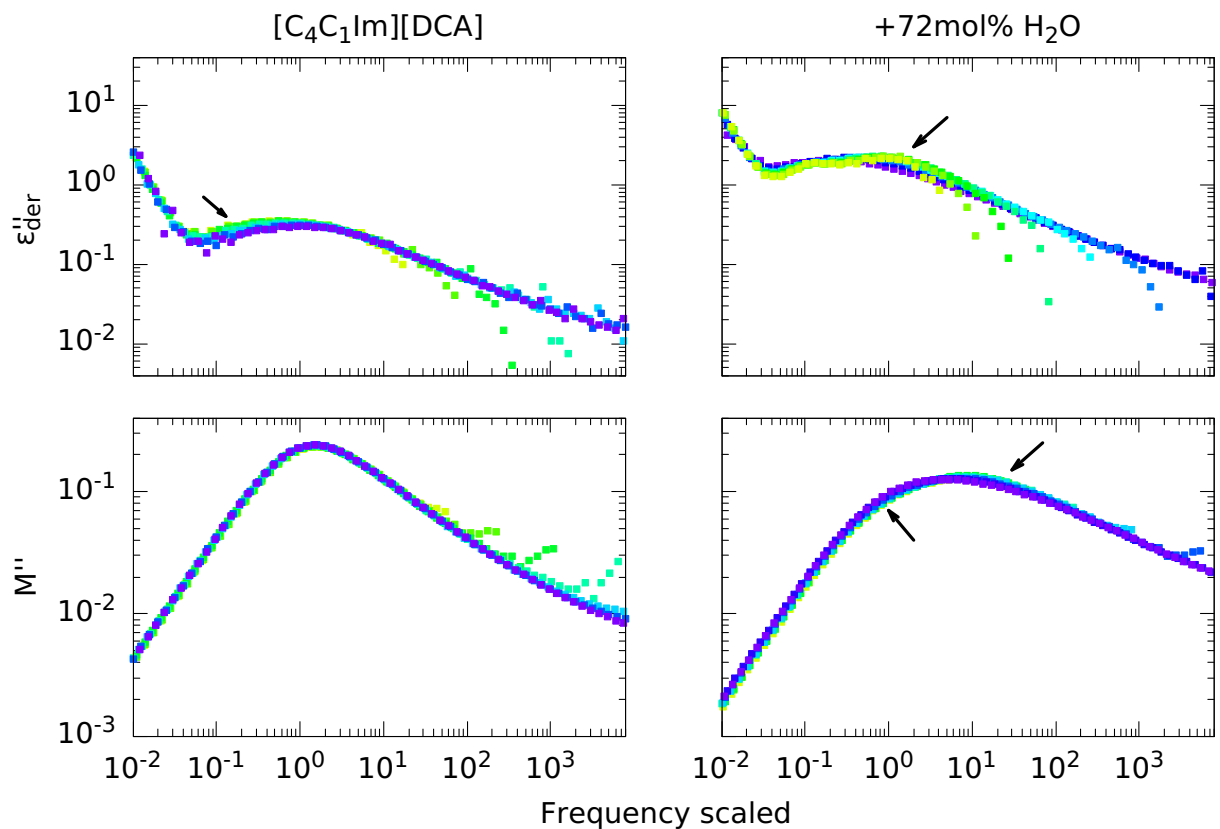


Figure 6.3.: Comparison of the temperature dependent dielectric spectra of neat $[\text{C}_4\text{C}_1\text{Im}][\text{DCA}]$ one the left-hand side to those of the mixture with 72 mol% water on the right-hand side, shown as master plots. Subtle differences can be seen in the $\epsilon''_{\text{der}}(\omega)$ representation as well as in the modulus representation. Please note that the temperatures in the upper right panel are plotted in reversed order to make the bimodality, present at high temperatures, visible.

When taking a look at the modulus representation, differences between the neat IL and the mixture can be seen as well. At first, the peak is markedly broader in the mixture, which can be ascribed at least in parts to the higher relaxation strength $\Delta\epsilon$ of the mixture, which results in a broader spectrum in the modulus. Despite this, another difference can be seen: The

modulus spectra of the neat IL perfectly superimpose for all temperatures, while a temperature-dependent shape can be seen in the case of the mixture, where the low-frequency flank and the peak position shift slightly to higher frequencies, while the high-frequency flank stays constant. This is rather surprising since the shape of the modulus and especially the low-frequency flank is dominated by conductivity relaxation in cases where the dipolar relaxation is slower. This can be seen in the spectrum of the neat $[C_4C_1Im][DCA]$, where the decreasing dipolar relaxation strength is observed in the $\epsilon''_{der}(\omega)$ representation, while the imaginary part of the modulus is entirely unaffected. The variation in $\epsilon''_{der}(\omega)$ of the mixture with temperature is not significantly more pronounced than in the neat IL. However, the modulus is visibly affected in this case. Thus, a reason for this different behavior has to be found. An idea for a possible explanation comes from the model spectra considered in figure 5.35. There, it was seen that the impact of the dipolar reorientation on the conductivity spectrum increases when its time scale approaches the one of the conductivity relaxation coming from low frequencies. But what happens if the dipolar relaxation time further decreases, eventually being faster than the conductivity relaxation? Is this possibly what happens in the mixture? Model spectra are constructed in figure 6.4 to test this idea.

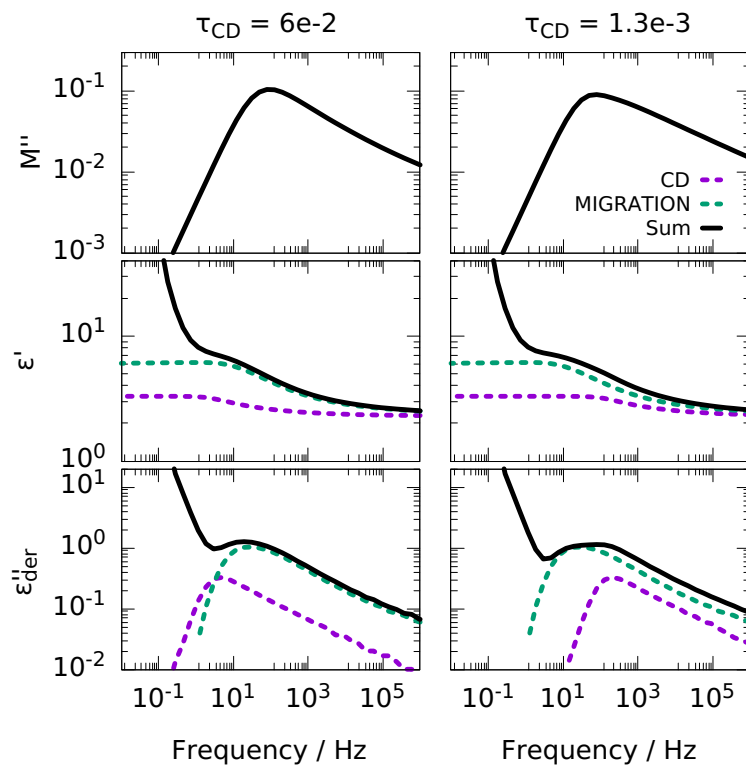


Figure 6.4.: Comparison of model spectra in three representations. The only difference between the two columns is the time constant of the CD function. On the left-hand side, the CD peak position is located at lower frequencies than the one of the conductivity relaxation, while the opposite ordering is shown on the right-hand side.

In the left column, spectra are shown, which resemble the one of the neat IL, i.e., a weak

CD function is added to the MIGRATION model, where the CD function is located at lower frequencies. In the right column, the values of all model parameters are the same, except the time constant τ_{CD} , which is chosen such that the CD peak is located at higher frequencies than the one of the MIGRATION model. It can be seen that now a bimodality in the $\epsilon''_{\text{der}}(\omega)$ representation appears, although the relaxation strength of the CD function is so low that no bimodality is visible as long as the CD peak is located at lower frequencies than the MIGRATION peak. Additionally, the peak shape in the modulus representation is markedly altered so that the high-frequency flank appears broader than in the left column. Thus, these model spectra seem to be able to rationalize the differences in spectra of the neat IL and the mixture with 72 mol% water. Therefore, a fit of the mixture's dielectric data is performed to test whether the data can indeed be described with a CD function located at higher peak frequencies than the MIGRATION model. This is in fact satisfactorily possible for all temperatures. As an example, the spectrum at 190 K is shown in figure 6.5 in six different representations with the related fit.

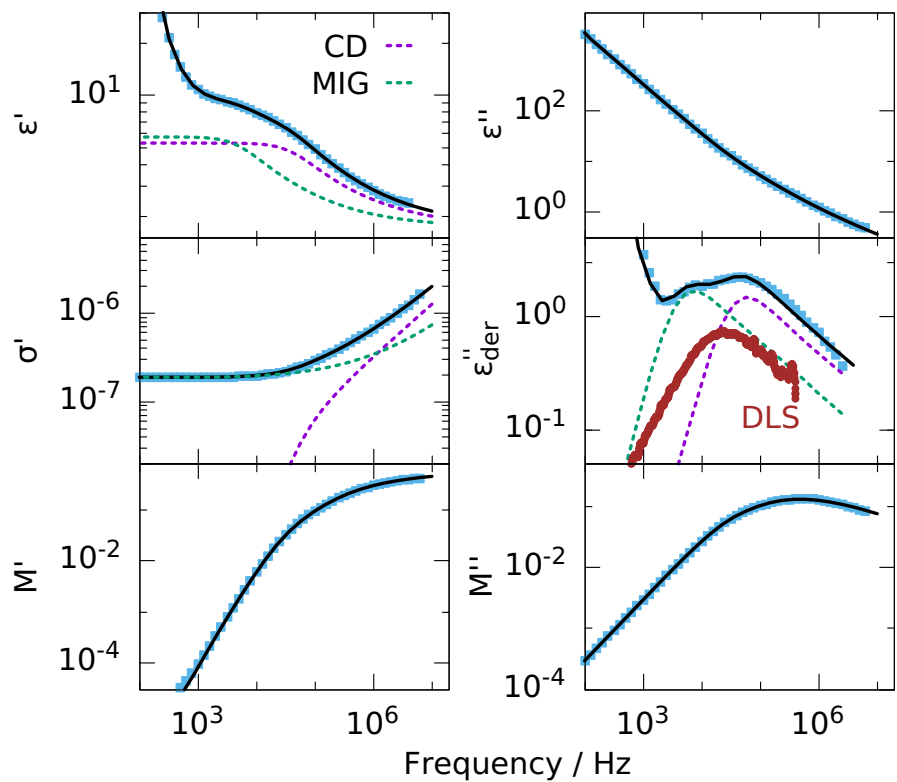


Figure 6.5.: Dielectric spectrum of $[\text{C}_4\text{C}_1\text{Im}][\text{DCA}]$ with 72 mol% water at 190 K in six representations. Solid lines are a fit with the MIGRATION model plus a CD function, which are both shown as dashed lines. Additionally, a light scattering spectrum recorded at the same temperature is shown in the $\epsilon''_{\text{der}}(\omega)$ panel.

It should be noted that the fit is also able to describe the data with the inverted ordering of the relaxational processes, which is the procedure published before [317]. There, however, N_∞ of the MIGRATION model has to be left as a temperature-dependent free fit parameter to achieve satisfactory fits. The authors of the MIGRATION model consider N_∞ as a temperature-

independent parameter, which depends on the substance under study. Nevertheless, the fit is able to describe the data with both orderings of the relaxation processes, in principle. Due to the discussion related to the model spectra in figure 6.4, the version with the CD function located at higher frequencies than the MIGRATION peak seems more realistic.

In figure 6.5 the light scattering spectrum is also included in the panel of the conductivity free representation. It can be seen that the light scattering peak is located in between the two dielectric peaks. Since the slow process was tentatively assigned to the conductivity relaxation, the reorientational relaxation is faster in dielectric spectroscopy than in light scattering. If both processes are due to the same molecular dynamics, this can not be brought into an agreement based on the different ranks of the correlation functions. Therefore, an explanation would be that the fast dielectric relaxation is due to the reorientation of water molecules, which is not visible in the light scattering spectra, where only the reorientations of the ions – mainly the cations – is observed. The water dynamics being faster than that of the IL can be rationalized by the fact that the glass transition temperature of water is commonly estimated to be around 136 K [318], whereas T_g of the IL is around 40 K higher. Although this scenario seems plausible, a test of this idea would involve mixtures with higher water concentrations, which, unfortunately, is not possible due to crystallization. Therefore, in the next section mixtures with 1-propanol will be considered where no crystallization interferes.

Before that, polarized light scattering measurement of the mixture of $[C_4C_1Im][DCA]$ with 72 mol% water are considered here. These measurements were performed to test whether a diffusive motion of the water pockets could be observed by light scattering. Indeed, a very weak signal showed up in the VV-measurements, with a small intercept of only around 0.05. Angle-dependent measurements were performed to test the scattering vector dependency of this relaxation. Such data at 250 K is shown in figure 6.6.

Angles between 50° and 130° are shown in steps of 10°. Each curve was measured for twelve hours. Still, strong scatter in the data at short times can be observed, highlighting the weak scattering intensity of this relaxation. Clear angle dependence of the correlation time can be seen. The correlation decays are fitted with a mono-exponential function, and the time constants obtained by this fit are plotted inversely in dependency of the squared scattering vector in the inset. Thereby, the refractive index $n = 1.48$ was approximated by assuming ideal mixing [325] between water ($n = 1.33$) and $[C_4C_1Im][DCA]$ ($n = 1.51$) [326] for an IL-water mixture with a water concentration of 72 mol% $\cong 19.16$ vol%. The solid black line is a linear fit, indicating diffusive behavior, and from which the diffusion constant is directly obtained via $Dq^2 = 1/\tau$, and its value is $D = 7.15 \times 10^{-11} \text{ m}^2/\text{s}$. This diffusion constant is used together with the viscosity of the mixture² in the Stokes-Einstein equation (equation 2.1) to obtain the hydrodynamic radius $r_{\text{hyd}} = 0.48 \text{ \AA}$. This is about a factor of 20 smaller than the radius of the water pockets obtained by small-angle neutron scattering [317]. However, such a direct comparison might not be justified. This is because it is not the self-diffusion coefficient measured in the light scattering experiment since the water pockets can not be assumed to be highly diluted in the ionic liquid matrix due to the high water concentration. Instead, the collective diffusion coefficient is measured, incorporating the contribution from

²Measured during the master thesis of Jennifer Kraus by Sebastian Stock, TU Darmstadt, with a rheometer. At 253 K the viscosity is $\eta = 53.91 \text{ mPa s}$

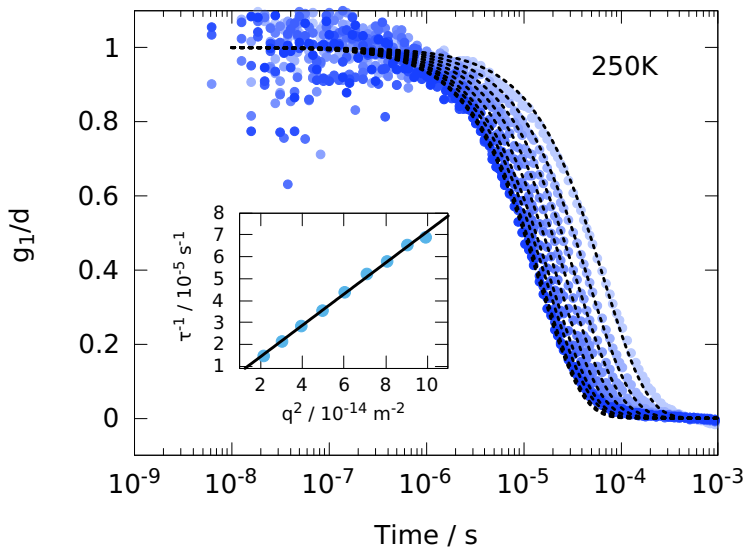


Figure 6.6.: Polarized PCS measurements at 250 K for angles between 50° and 130°, in steps of 10°. A mono-exponential, angle dependent relaxation can be observed. The inset shows that the inverse time constants follow a q^2 law, indicating diffusive behavior.

particle interactions [327]. These interactions can render the apparent hydrodynamic radius as measured by light scattering either larger or smaller than the actual one, in cases of attractive or repulsive interactions, respectively [327]. Thus, in order to rationalize the observed diffusive process with the diffusion of water pockets, a strong repulsive interaction of the water pockets has to be assumed. Since such a high decrease in the apparent hydrodynamic radius due to repulsive forces seems questionable on the one hand, and since it is completely unclear whether water pockets indeed diffuse through the ionic liquid as a connected entity, on the other hand, an alternative explanation should be discussed in the following:

The van der Waals radius of a single water molecule is around 1.4 Å [328]. The hydrodynamic radius obtained by the angle-dependent light scattering measurements is still almost a factor of three lower. Thus, the first question, which has to be addressed, is whether it is theoretically possible to see the diffusion of water molecules in the light scattering experiment. If this would be possible, the second question is why the apparent hydrodynamic radius is notably lower than the actual radius of a water molecule. During the discussion of these two questions, it is assumed for the moment that what is measured is the self-diffusion coefficient of water and that the SE equation is applicable. Of course, a volume concentration of nearly 20% water can not be regarded as a dilute solution. In order to answer the first question, it is instructive to consider equation 3.5, where it can be seen that in the polarized field-correlation function, only the distance over which the diffusion takes place enters, but not the size of the diffusing particle. Thus, in principle, there is no lower limit of the size of the diffusing particle to be detectable. In fact, light scattering measurements of the sub-nanometer diameter of sucrose molecules in water have been reported, which were performed with a commercial apparatus utilizing a red laser with a power of only 4 mW [329]. However, in order for such diffusion to be visible in the

light scattering spectrum, a scattering contrast between the diffusing particle and the solvent is necessary. It has to be preserved over the distance corresponding to the scattering vector, thus in the order of the wavelength. According to Einstein's theory for isotropically scattered light (see section 3.1), fluctuations in the refractive index are responsible for the scattered intensity. Here, the difference in refractive index between water and $[C_4C_1Im][DCA]$ is high, making it plausible that these refractive index fluctuations might be detected, if preserved over a sufficiently large distance.

Still, an explanation for the low hydrodynamic radius has to be found if the diffusion can be really connected to water molecules. As above, repulsive forces might be responsible for an apparent small hydrodynamic radius, but the literature also reported that the diffusion of water or other non-ionic tracers in ionic liquids is markedly faster than expected by the Stokes-Einstein (SE) equation [330, 331, 332]. To be more precise, the diffusion constant D_{obs} of highly diluted tracers as measured by pulsed-field gradient 1H NMR and compared to the one calculated via the SE equation using the van der Waals radius of the respective solute. A correlation of the ratio D_{obs}/D_{SE} and the ratio of solute-to-solvent van der Waals volumes was found [330, 331]. This means the smaller the neutral solute in comparison to the ions, the larger the deviation of its measured diffusion constant from the one predicted by the SE equation. This behavior was explained by Arque *et al.* [331] by the fact that a neutral tracer molecule experiences locally stiff (i.e., charged) and locally soft (i.e., apolar) regions of the IL. Its diffusion is slowed down in the former, while it is sped up in the latter regions. On larger length scales, this leads to a random walk, the step size of which is strongly influenced by the fast diffusion in the apolar regions.

In another study by Bayles *et al.* [332], microfluidic Fabry-Pérot interferometry measurements were performed to obtain concentration-dependent water diffusivities in different ILs. It was also found that the diffusion of water is notably faster in the ILs than predicted by the SE equation. This was explained by activated hops of the water molecules between polar regions of the IL matrix, which are considered immobile over the time of a hop. With this model, the authors were able to describe the water diffusivities dependent on the water concentration and the electronegativity of the anion of the respective IL. Qualitatively, this model seems similar to the one of Araque *et al.*, discussed right before, in that sense that the diffusing solutes probe the different environments of the IL matrix, whereby they are located at polar sites for longer times than at apolar sites. This behavior gives rise to the fast diffusion of the water molecules and is also in accordance with own Raman spectroscopy measurements [317] and those from the literature [119], where it was found that the water molecules are mainly located near the anions.

Moreover, the diffusion constant of infinitely diluted water in $[C_4C_1Im][DCA]$ was measured by the Taylor dispersion method in the literature [333]. The hydrodynamic radius calculated from that via the SE equation amounts to 0.38 Å and is thus similar to the value obtained here by polarized light scattering for the mixture with 72 mol% water. In the light of the work by Bayles *et al.*, discussed before, this is surprising since there a strong dependence of the failure of the SE equation with concentration was found, with a larger deviation from the measured values for smaller concentrations. Also from the correlation between the ratio D_{obs}/D_{SE} and

the ratio of solute-to-solvent van der Waals volume [330, 331], one could calculate³ a factor of approximately 120 between the measured and the SE value of the diffusion coefficient for water in $[C_4C_1Im][DCA]$ at infinitely dilution. This shows that measurements from different experimental methods and different water concentrations may be hard to bring into accordance. As mentioned above, it is probably not justified to regard the measured diffusion as self-diffusion, as it can not be regarded as a dilute solution. It seems thus more appropriate to consider the experimentally determined diffusion coefficient as a mutual diffusion coefficient D_m . This concept considers that not only the solute but also the solvent is mobile, affecting each other. Such mutual diffusivities have been obtained in the literature for IL-water mixtures with a heterodyne light scattering experiment, which are comparable to the one found here [335]. Assuming ideal mixing and a vanishing cross-diffusion constant,⁴ one can relate the mutual diffusion coefficient of the mixture to the self-diffusion coefficients D_i of the constituents by $D_m = x_1 D_1 + x_2 D_2$, where x_i are the molar fractions [336]. This means that the mutual diffusion coefficient is dominated by water, contributing with 72 mol%. Furthermore, the self-diffusion coefficient of neat ILs was found to be in good accordance or even slightly below the value predicted by the SE equation using the van der Waals radius, see reference [337] and references therein. This implies that indeed the self-diffusion coefficient of water is unusually high.

Together, the above discussion shows that it might indeed be possible – although it seemed unrealistic at first glance – that the diffusional process observed in the polarized light scattering data is dominated by fast water molecules diffusing in the heterogeneous IL matrix. Mainly two observations are in strong favor of this interpretation: The extremely low scattering intensity of this relaxation and the hydrodynamic radius, which is below that of a single water molecule, which was explained in several studies in the literature with the abnormal diffusive mechanism of small neutral solutes in ILs. In fact, it was speculated in reference [335] that the low scattering intensity in the IL-water mixtures – in comparison to IL mixtures with other solvents – originates from water clusters, where the mobility of water molecules is lower than that of free water molecules. However, no sign of diffusing water clusters was found in this study either. This might indicate that the water pockets do not diffuse as a whole, but only single water molecules exchange between the water-rich sites. More evidence for this interpretation is needed, though, for example, by concentration-dependent measurements or supporting pulsed field gradient NMR measurements.

The temperature-dependent time constants of the diffusive light scattering relaxation are shown on the right-hand side in figure 6.7 together with all other time constants measured by different experimental methods for the case of the mixture with 72 mol% water. It can be seen that its temperature dependence does not follow an Arrhenius law, as it was found for concentration fluctuations in binary mixtures measured by polarized PCS or X-ray PCS [338], or like it is discussed for the mixture with gelatin in section 6.3. Instead, a VFT-behavior is found as indicated by the dashed line.

This is similar to the case of the diffusion data from NMR measurements contained in this

³Thereby, the van der Waals radius of the ions was determined by the method of Zhao *et al.* [334], giving a mean value of 103.28 \AA^3

⁴The error made by these assumptions seem to be in the order of some ten percent according to [336], contrasted by the factor of three between the measured hydrodynamic radius of a water molecule and the actual one.

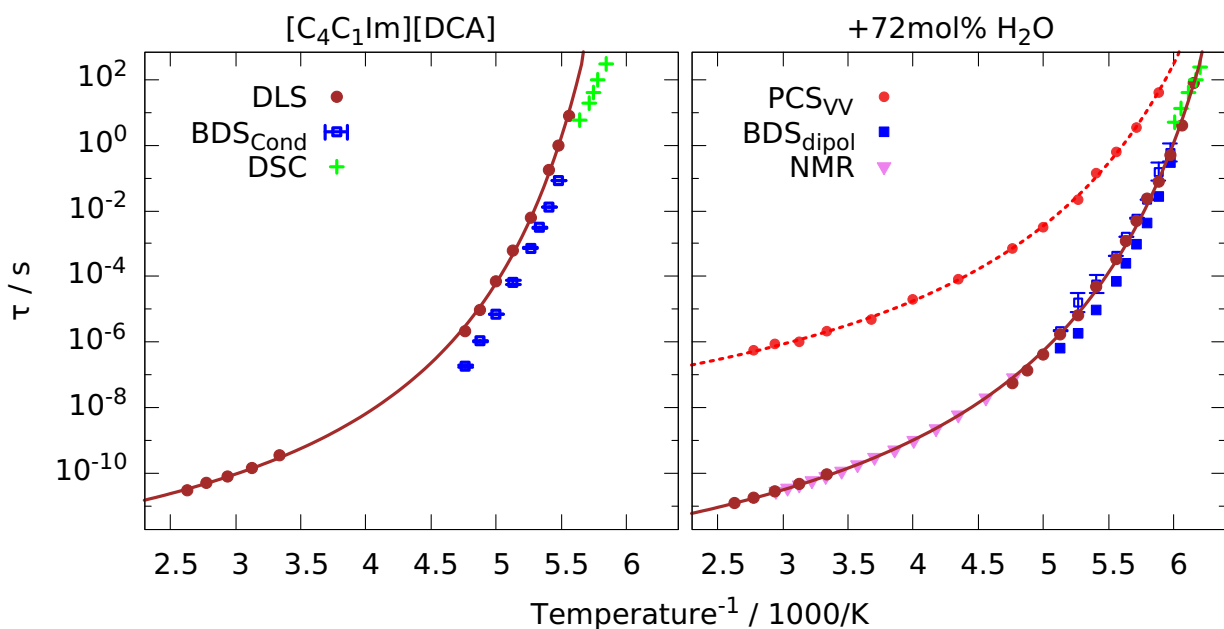


Figure 6.7.: Arrhenius plot of neat $[\text{C}_4\text{C}_1\text{Im}][\text{DCA}]$ (left) and of the mixture with 72 mol% water (right). Correlation times were obtained by different experimental methods as indicated.

figure. These NMR data were obtained by Elisa Steinrücken, TU Darmstadt, using a static field gradient setup to measure the ^1H diffusion constant of the cations in a mixture with D_2O . From these diffusion constants, rotational time constants are calculated via the SED relation, where the hydrodynamic radius of a cation was chosen so that the resulting time constants superimpose to the one from depolarized light scattering. It can be seen that the temperature dependence of the so obtained NMR time constants is in perfect agreement with that of the light scattering data. Also, the conductivity and dipolar relaxation times follow this VFT-law closely. Interestingly, the DSC time constants are in good accordance with the conductivity relaxation times, just like in the case of the neat IL as seen on the left-hand side of figure 6.7 and which was observed for a wide variety of ILs above. This might be seen as a confirmation of the assignment of the slow relaxation process to the conductivity relaxation in the case of the mixture, while it is the fast process in the neat IL. However, since the conductivity and the dipolar relaxation are only slightly separated and seem even to merge near the glass transition, this argument is not very strong. Therefore, in the next section, mixtures of $[\text{C}_4\text{C}_1\text{Im}][\text{DCA}]$ with 1-propanol are addressed. It is hoped that due to the possibility of measuring very low IL concentrations in 1-propanol, more insight into the question if it is realistic that the conductivity relaxation is slower than dipolar relaxation in the IL-water mixture, which should be assigned to water reorientation, might be gained.

6.2. Mixtures with alcohol

In this section, mixtures of $[C_4C_1Im][DCA]$ with 1-propanol are considered, whereby the focus is on mixtures with a low concentration of IL, which could not be measured in the case of admixed water in the preceding section due to crystallization. 1-propanol is chosen because it is easily supercooled, and due to the OH-group, it is miscible in all concentrations with $[C_4C_1Im][DCA]$, just like water. Furthermore, neat 1-propanol is well studied by dielectric spectroscopy and also by PCS [339, 159, 44, 340]. This means that in both experimental techniques, a contribution from 1-propanol is expected to occur, which should make it possible to disentangle the rotational relaxation of the ions and 1-propanol from the conductivity relaxation. This could also help to better understand the IL-water mixture's dielectric spectra from the preceding section. However, there is also a complication: From the above-mentioned literature, it is well known that in the dielectric spectra of 1-propanol, a strong Debye-process is present in addition to the α -relaxation. This was most clearly demonstrated by a combination of dielectric spectroscopy and PCS measurements, where in the latter, no sign of the Debye-process could be detected, and only the α -relaxation and a secondary relaxation is seen [44]. It is known that by the addition of salt to monohydroxy alcohols, the Debye-process is weakened because the ions interact with the OH-group: Thus, the ability of the alcohol molecules to form supramolecular H-bonded structures is reduced [341]. Since $[C_4C_1Im][DCA]$ is miscible with 1-propanol in all concentrations, unlike salts like LiCl, the influence of the IL on the Debye-process can be monitored over the whole concentration range. Together, the dielectric spectra will be highly complex due to the possible contribution of a multitude of relaxational processes: The Debye process, the dipolar reorientation of 1-propanol and the ions, and the additional conductivity relaxation. Thus, the comparison with light scattering data will be useful, where only the reorientation of the different molecules is expected to show up.

From the results of the proceeding section it is known that the shape of the light scattering spectrum of $[C_4C_1Im][DCA]$ was not altered at all by the addition of 72 mol% water. Therefore, it should be tested as a first step how adding 1-propanol affects the light scattering spectrum. From preliminary considerations, it gets clear that the influence of 1-propanol on the spectrum will be markedly larger than that of water. First, 1-propanol has a lower glass transition temperature of around 98 K [342], which is almost 40 K below that of water. Therefore, the dynamical contrast to $[C_4C_1Im][DCA]$ is expected to be higher. Furthermore, the optical anisotropy of water is extremely small, leading to a very weak scattering intensity of water. A quantitative comparison shows that the intensity of the depolarized scattered light by 1-propanol is approximately a factor of 11 more intense than that of water. This value is obtained via equation 4.14, where the density and refractive index of both substances at room temperature is used and the optical anisotropy parameters β as obtained by DFT calculations.⁵ In comparison, the mean anisotropy of $[C_4C_1Im][DCA]$ is $\langle \beta \rangle = 7.5 \text{ \AA}^3$, together with the density and refractive index, this gives a factor between the scattering intensity of $[C_4C_1Im][DCA]$ and water of 260 and between $[C_4C_1Im][DCA]$ and 1-propanol of only 23. Therefore, based on the lower glass transition temperature and higher scattering intensity of 1-propanol, it can be expected to

⁵The DFT calculations were performed with the B3LYP functional and the aug-cc-pVTZ basis set. The value of the optical anisotropy parameter β is 0.16 \AA^3 for water and $\langle \beta \rangle = 1.68 \text{ \AA}^3$ for 1-propanol

see its rotational contribution in the spectrum of the mixture with even larger concentration of $[C_4C_1Im][DCA]$. That this assumption holds is shown in figure 6.8, where the spectra of neat 1-propanol and neat $[C_4C_1Im][DCA]$ are shown together with four different mixtures as a master plot. The temperatures of each data set are chosen so that the peak maximum is located at similar frequencies. Please note that the concentrations are denoted with x being the molar concentration of the IL.

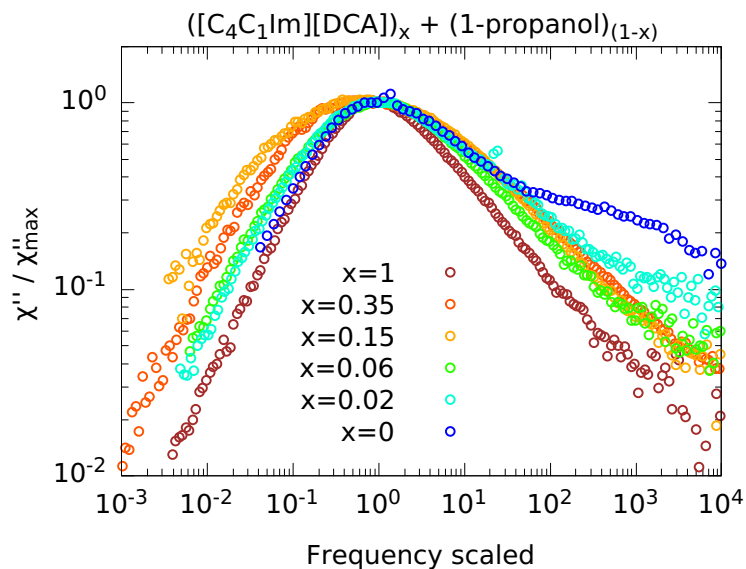


Figure 6.8.: Master plot of light scattering spectra of mixtures of 1-propanol with $[C_4C_1Im][DCA]$ with different concentrations as indicated. The broadening of the spectrum has a non-trivial concentration dependence, with the 15 mol% mixture exhibiting the broadest peak.

A strong influence of the concentration on the shape of the spectra can be seen, unlike the case for water seen in the foregoing section. Starting from neat 1-propanol, the amplitude of the secondary relaxation decreases, but more importantly, the low-frequency flank broadens upon increasing the IL concentration. The latter can be rationalized by the fact that the reorientation of the ions takes place at lower frequencies than that of 1-propanol, due to the lower glass transition temperature of the latter. However, the broadening of the low-frequency flank seems to have a maximum at a concentration of 15 mol% IL – at least for the concentrations under investigation here – although the influence of the IL should, of course, be more prominent in the case of the 35 mol% mixture. This points to the direction that the separation of the rotational dynamics of the 1-propanol molecules and the ions depends on the concentration. That this holds not only in dependence on the concentration but also in dependence on the temperature can be seen in figure 6.9, where the spectra of the mixture with 15 mol% IL are shown for selected temperatures. Starting at high temperatures with a relatively narrow peak, the spectrum broadens with decreasing temperatures. It can be seen that the relaxational process, which dominates the low-frequency flank, separates from the one dominating the high-frequency flank. This means that the slower reorientation of the ions has a stronger temperature dependence than the reorientation of the 1-propanol molecules.

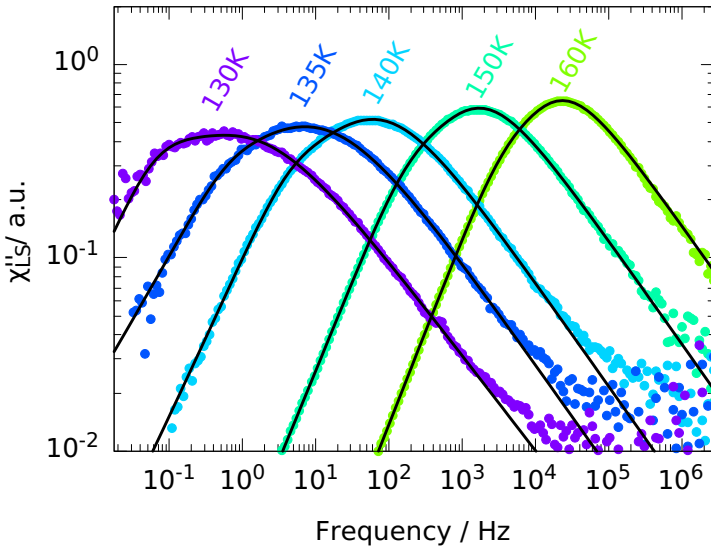


Figure 6.9.: Temperature dependent light scattering spectra of the mixture with 15 mol% $[C_4C_1\text{Im}][\text{DCA}]$. The solid line is a fit with two CD functions for the reorientational dynamics of 1-propanol and $[C_4C_1\text{Im}][\text{DCA}]$.

Therefore, the trend in shape seen before in figure 6.8 might be influenced by the particular temperatures which were chosen for the master plot. Nevertheless, it got clear from the light scattering spectra of the 1-propanol IL mixtures that the reorientation of 1-propanol can be separated from that of the ions. Thus it is now instructive to discuss the dielectric spectrum of the mixtures in detail.

Due to the markedly lower measuring time, dielectric spectra were recorded for more concentrations than for light scattering. These spectra are compiled in the $\epsilon''_{\text{der}}(\omega)$ representation for all concentrations measured at 180 K in figure 6.10. It immediately stands out that the prominent peak observed at low IL concentrations does not change its position in frequency up to an IL concentration of 10 mol%. This is rather surprising since with the addition of IL, the viscosity of the mixture increases, which is expected to lead to a slowing down of the dynamics. However, this reasoning holds for the α -relaxation, but as mentioned above, the prominent peak in the dielectric spectrum of 1-propanol is the Debye-process. In fact, when assuming that the Debye process arises due to a movement of the supramolecular structures as described by the transient chain model like it was done for n-butanol [47], one could even rationalize an acceleration of the transient chain dynamics with increasing IL concentration. This is because some H-bonds between the 1-propanol molecules will be destroyed by the presence of the IL, thus shortening the average length of the chains, which will render their orientation relaxation faster. Indeed, it was found for a mixture of water and LiCl that the peak position of the dielectric loss peak shift to higher frequencies with higher salt concentration, although the viscosity increases as mentioned above [321]. Concomitantly, the strength of the Debye-process decreases with increasing salt or IL concentration in the case of the water-salt mixture reported in the literature or the present case, respectively, as can be seen in figure 6.10. This indicates that the cross-correlations, mediated through the H-bonding of the water or

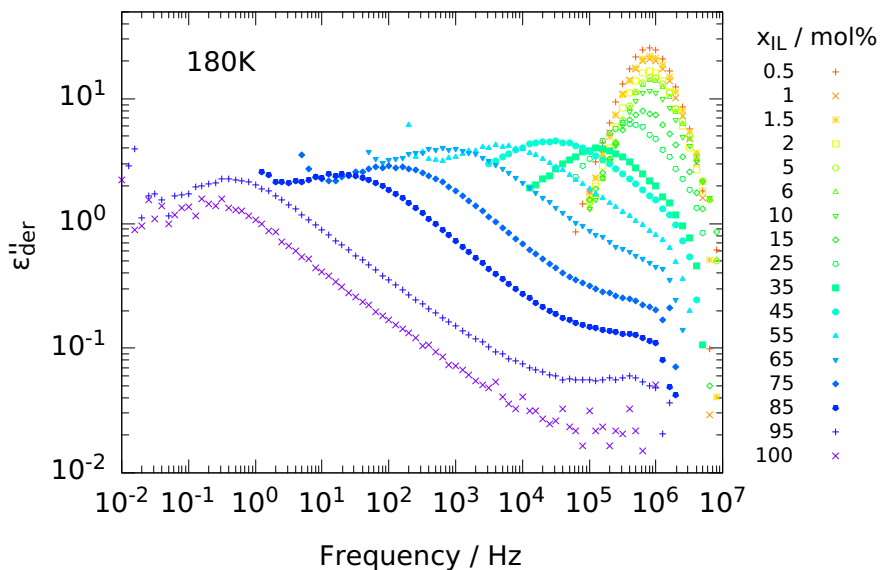


Figure 6.10.: Dielectric spectra at 180 K for different concentrations of $[C_4C_1\text{Im}][\text{DCA}]$ in 1-propanol as indicated.

1-propanol molecules, decrease upon addition of salt or IL. Thus, in the light of the transient chain model, a constant Debye-relaxation time together with a decreasing amount of H-bonding would suggest that the average length of the chains stays constant while the number of chains decreases.⁶ However, it should be stressed again that the theory of Pierre-Michel Déjardin, as discussed in section 4.2, is able to reproduce the dielectric strength of 1-propanol without invoking any kind of H-bonding, just by calculating the Kirkwood correlation factor from physical properties of the liquid and one free parameter, which is related to induction/dispersion forces. Both the transient chain model and the Déjardin theory do not make predictions about the absolute time scale of the Debye process but about the separation of the Debye- from the α -relaxation. In the transient chain model, the ratio τ_D/τ_α is correlated with the length of the transient chain, while in the Déjardin theory, the additional collective process, which arises for Kirkwood factors larger than unity, shifts to lower frequencies in respect to the single-molecule process for stronger intermolecular interactions. Also, the dielectric strength of the Debye process should decrease when the transient chains get shorter or when the intermolecular interactions decrease, respectively.

Thus, it is necessary to fit the dielectric spectra of the mixture in order to determine the dielectric strength and time constants of the α - and Debye-process in dependency of the IL concentration. This is done by combining the MIGRATION model with a Debye-function, a CD function for the α -relaxation and a CC-function for the secondary relaxation. Fits with this model are shown in figure 6.11 for four different IL concentrations in four different representations. The temperature of each data set is chosen so that the relaxational processes are clearly visible within the frequency window. When visually inspecting the spectra, some

⁶However, it can not be excluded that the influence of the increasing viscosity and the decreasing chain length may coincidentally cancel each other out.

peculiarities can be observed: In the conductivity representation, a knee is visible at frequencies above the DC-conductivity plateau, which diminishes upon addition of IL until it eventually disappears at a concentration of 35 mol% IL. The real part of the permittivity shows the typical step-like behavior and the onset of the electrode polarization, thus no peculiarities. From that, only the decreasing dielectric strength with increasing IL concentration can be directly seen. In the $\epsilon''_{\text{der}}(\omega)$ representation, several relaxation processes can be identified at a concentration of 2 mol%. At low frequencies, the prominent Debye-process is apparent, and at higher frequencies, the α -relaxation, which is notably weaker than the Debye-process, is observable. At even higher frequencies, a broad secondary relaxation can be seen. This overall picture changes notably upon increasing IL concentration.

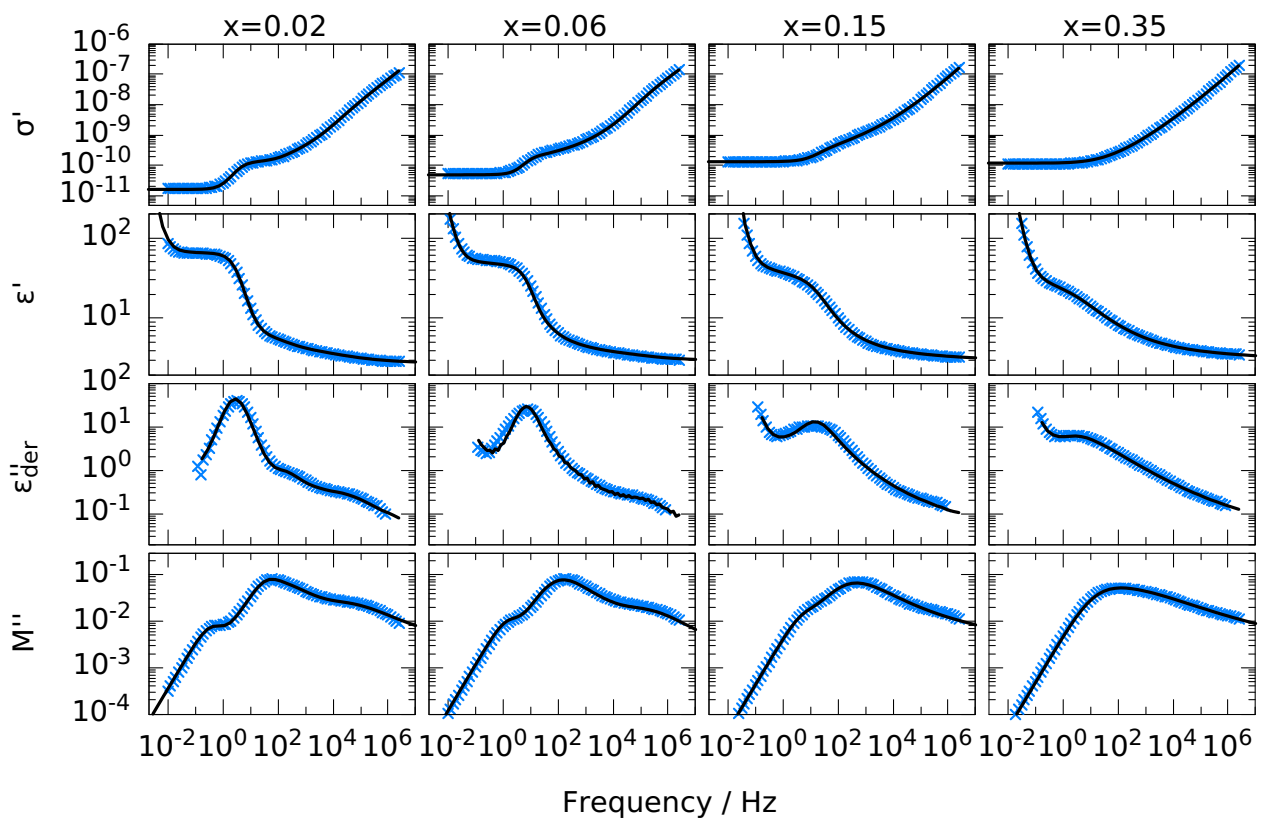


Figure 6.11.: Dielectric spectra of four different mixtures of $(1\text{-propanol})_{(1-x)}$ with $([\text{C}_4\text{C}_1\text{Im}]\text{[DCA]})_x$ at 180 K in four different representations. The solid lines are fits with a sum of a MIGRATION model, a Debye and a CD function and a CC function for the secondary relaxation.

At 6 mol%, the Debye-process is still dominating the spectrum, while the α -relaxation is no longer seen as a clear peak but only as a wing-like contribution at the high-frequency flank of the Debye-peak. The β -relaxation, on the other hand, is still visible. At 15 mol%, the Debye- and α -process have merged, and the conductivity relaxation has intensified, leading to a highly convoluted spectrum without a clear low-frequency flank of the peak. Finally, at 35 mol% even no clear peak structure can be identified any longer. The appearance of the

modulus representation is also interesting since such kind of $M''(\omega)$ spectra were not seen in the case of neat ILs or in the mixture with water. At low IL concentrations, a pronounced low-frequency peak is observed, which is less intense than the peak located at higher frequencies, but markedly separated in frequency. This slow process is located at even lower frequencies than the prominent Debye-process in the $\epsilon''_{\text{der}}(\omega)$ representation. While relaxation processes appear in the modulus representation at similar frequencies as in the permittivity representation for weak, broad processes, they are located at higher frequencies in the modulus representation in the case of strong, small relaxation processes [177]. Therefore, the main peak in $M''(\omega)$ at low IL concentrations can be attributed to the Debye-Process or the combination of Debye- and α -process, respectively, while the low-frequency peak is due to the conductivity relaxation. This is also clear from the fact that the frequency position of the latter is similar to the transition to the DC-conductivity plateau in $\sigma'(\omega)$. By increasing the IL concentration, the slow modulus peak intensifies and merges with the main peak until at 35 mol% only a single process is seen. From these considerations, it gets clear that the dielectric spectra of the mixtures of 1-propanol with $[\text{C}_4\text{C}_1\text{Im}][\text{DCA}]$ transform from dipolar dominated spectra to spectra which closely resemble the one of neat ILs, already at an IL concentration of 35 mol%. Due to the multitude of relaxational processes, which additionally merge with increasing IL concentration, the description of these spectra with model curves is non-trivial. It results in fits that might slightly deviate from the data, as seen best – as usual – in the $\epsilon''_{\text{der}}(\omega)$ representation. Nevertheless, important insights can be gained from these spectra in the low IL concentration range, which was prohibited in the IL-water mixtures due to the crystallization of water. Especially, it can be seen that the dipolar dynamics of 1-propanol, may it be single molecule or cross-correlation dynamics, can be very well separated from the conductivity relaxation for small IL concentrations. However, the strength of the prominent Debye-process decreases very quickly upon addition of IL, so that already at IL concentrations of 10 mol% the Debye- and α -process can no longer be separated either by eye or by a fit, leading to a single dipolar relaxation. But still at 15 mol%, one can distinguish the contribution of the dipolar and conductivity relaxation by eye when inspecting the $\sigma'(\omega)$ or $M''(\omega)$ representation.

It is now interesting to consider a mixture of 1-propanol similar in concentration to the mixture with water discussed in section 6.1 to see whether, in this case, dipolar and conductivity relaxation can be better distinguished than for the IL-water mixture. If this is the case, it could be possible to infer from the appearance of these spectra the correct assignment of the relaxation processes in the mixture of the IL with 72 mol% water, which was not conclusively possible in section 6.1. Therefore, dielectric data of the mixture of 1-propanol with 25 mol% $[\text{C}_4\text{C}_1\text{Im}][\text{DCA}]$ is shown in figure 6.12 in the $\epsilon''_{\text{der}}(\omega)$ and $M''(\omega)$ representation. A dramatic change of spectral shape with temperature can be directly seen in both representations. While at high temperatures, a peak with a clear low-frequency flank can be seen in the conductivity-free representation, upon lowering the temperature, a slower relaxational process seems to intensify, pushing up this low-frequency flank. This behavior is even more clearly seen in the modulus representation, where at high temperatures, a prominent peak is visible, where an additional weak hump can be detected on its low-frequency flank. At lower temperatures, however, this hump intensifies until it evolves to a dominating peak at the lowest temperature, whereas the peak at higher frequencies is lower in amplitude and located at the high-frequency flank of the slower process. Moreover, it can be seen that the separation of the two processes increases

with decreasing temperature. From the discussion of the concentration-dependent dielectric spectra, which were shown in figure 6.11, it is immediately clear that the slow process can be assigned to the conductivity relaxation, while the faster one is due to dipolar reorientation.

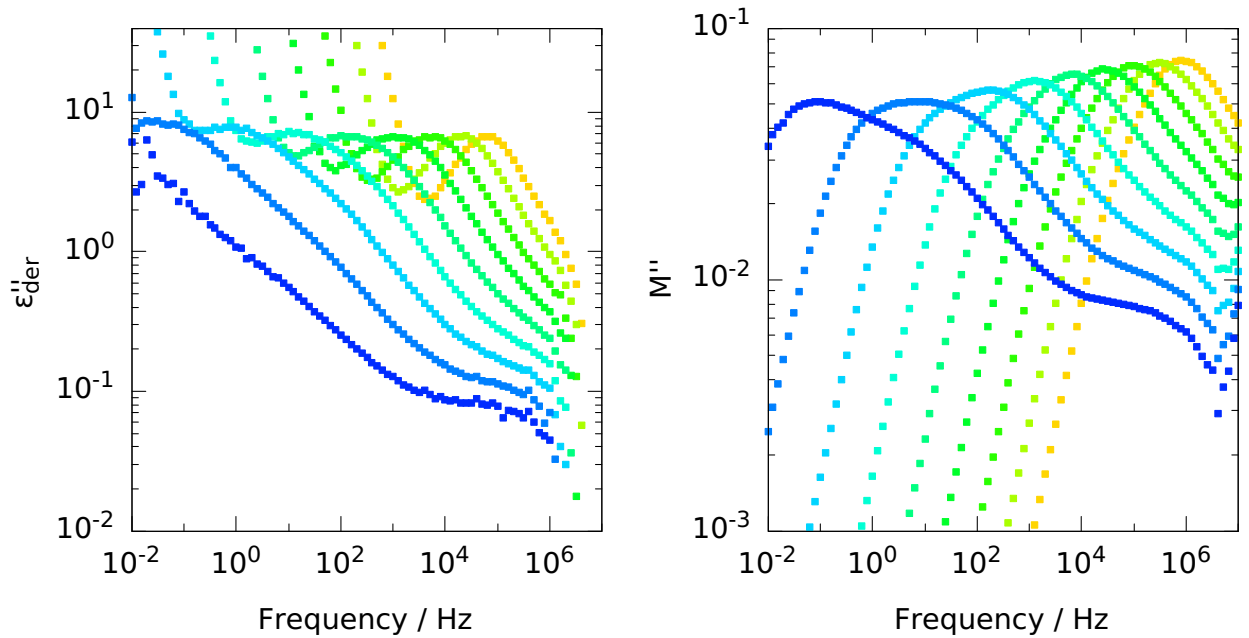


Figure 6.12.: Dielectric spectra of the mixture of 1-propanol with 25 mol% $[C_4C_1IM][DCA]$ for temperatures from 170 K to 130 K in 5 K steps in two different representations.

Although the change of the spectra with temperature is by far more pronounced in the case of this mixture with 1-propanol than it was in the case of the mixture with water, it nevertheless clearly demonstrates that the low-frequency part of the $\epsilon''_{\text{der}}(\omega)$, right above the electrode polarization, can be influenced by the conductivity relaxation. The dipolar relaxation is located at higher frequencies, leading to a similar spectral appearance as in the case of neat ILs, where, however, the ordering of these two processes is reversed. Moreover, it can be seen that a change of the intensity ratio of the two processes does not only lead to a change in the $\epsilon''_{\text{der}}(\omega)$ spectrum, as it was the case in the neat ILs but also to a marked change in the modulus representation. The latter is not observed in neat ILs, which is shown exemplified for the case of $[C_8C_1Im][NTf_2]$ in figure B.3 in the appendix, while a distinct change in the conductivity free representation can be observed for this IL. This was shown in figure 5.31 and assigned to the decreasing dipolar intensity. The same behavior, i.e. a change of the shape in $\epsilon''_{\text{der}}(\omega)$ together with an unchanged shape in the modulus representation was also found for neat $[C_4C_1Im][DCA]$ as seen in figure 6.3. There, however, the spectral change in the conductivity free representation was not as pronounced as in the case of $[C_8C_1Im][NTf_2]$.

Thus, it is possible to determine the ordering of dipolar and conductivity relaxation based on observing temperature-dependent changes in the modulus representation in cases where spectral changes in the conductivity free representation occur. In order to further test this notion, two sets of model spectra are shown in figure 6.13. There, the $\epsilon''_{\text{der}}(\omega)$ representation is shown in the upper row and the imaginary part of the modulus in the lower row. In the

left column, the relaxation time of the CD function, representing dipolar reorientation, is chosen in such a way that its peak is located at lower frequencies than that of the conductivity relaxation, modeled with the MIGRATION model using $\tau_\sigma = 5 \times 10^{-3}$ s. In the right column, τ_{CD} is chosen such that the CD peak is located at higher frequencies than the MIGRATION peak. Three different values of the strength parameter d of the CD function are shown in each case. It can be seen in the left column that with increasing dielectric strength, the dipolar relaxation gets visible as a separate peak at frequencies below those of the conductivity relaxation in the $\epsilon''_{\text{der}}(\omega)$ representation. However, in the $M''(\omega)$ spectra, hardly any change is seen.

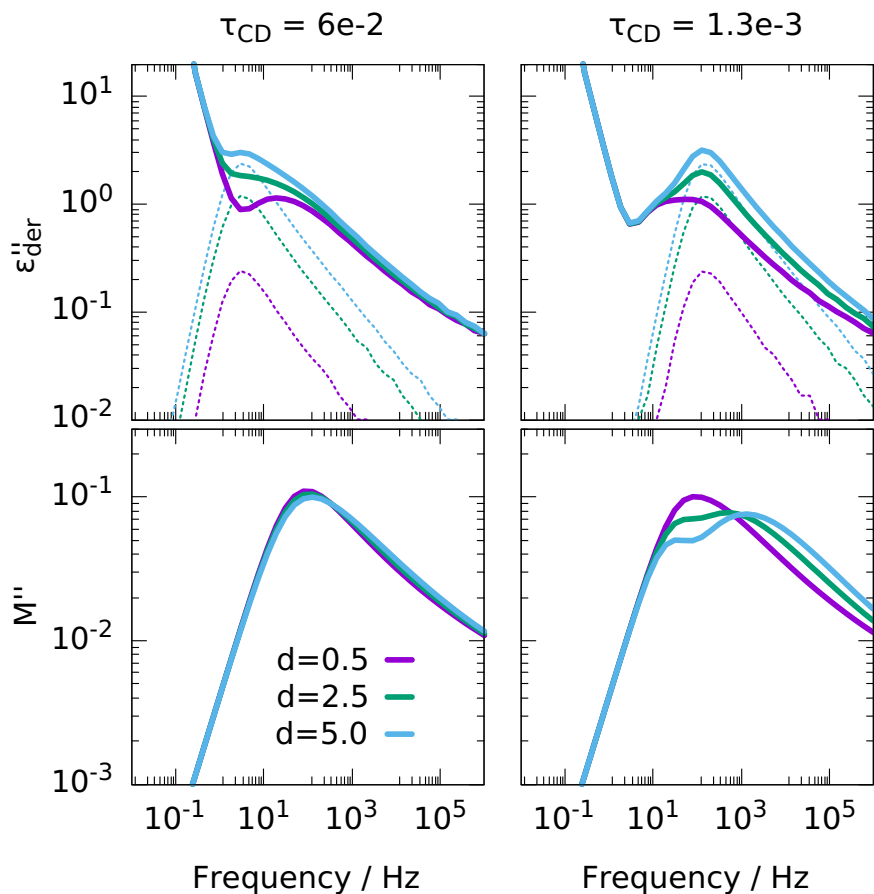


Figure 6.13.: Comparison of model spectra in two representations. The only difference between the two columns is the time constant of the CD function (shown as dashed lines). On the left-hand side, the CD peak position is located at lower frequencies than the one of the conductivity relaxation, while the opposite ordering is shown on the right hand side. Three different values of the dielectric strengths of the CD function are shown in each case, as indicated.

The situation is markedly different in the right column, where the CD peak is located at higher frequencies than the conductivity relaxation peak. Again, the CD peak naturally increases in intensity with increasing d -value in the $\epsilon''_{\text{der}}(\omega)$ representation, but a bimodal spectrum is already observed at the lowest d -value, in contrast to the case in the left column. In the

imaginary part of the modulus, a dramatic change of the spectral shape can be seen upon increasing dielectric strength. While the $M''(\omega)$ spectrum is dominated by the conductivity relaxation at $d = 0.5$, exhibiting a single peak, the contribution of the CD function increases with increasing d , which leads to a bimodal spectrum, dominated by the dipolar relaxation at $d = 5$. Together, this discussion indeed shows that the ordering of dipolar and conductivity relaxation can be identified in cases where temperature- (or pressure-) dependent changes in the $\epsilon''_{\text{der}}(\omega)$ occur, by inspecting the $M''(\omega)$ representation. When conductivity relaxation is the fastest process, the modulus spectrum remains almost unchanged upon altering the dipolar relaxation. In cases where the conductivity relaxation is slower, a distinct change in the modulus spectra can be observed when the dipolar relaxation strength changes. Thus, this supports the assignment of the slow relaxation process as being due to the conductivity relaxation in the case of the IL-water mixture in the foregoing section, since there a change in the $M''(\omega)$ spectra was found in contrast to the neat IL, although in both cases the spectral shape of $\epsilon''_{\text{der}}(\omega)$ changed.

After these qualitative considerations of the dielectric spectra, it is now instructive to look at the parameters obtained by the fits of the data. Some of these fits were already shown in figure 6.11 and discussed above. Especially the static permittivity, the Kirkwood factor, and the ratio of the time constant of Debye- and α -process dependent on concentration at a fixed temperature of 140 K are considered in order to compare it to the predictions of the transient chain model and the Déjardin theory, as discussed above. Therefore, ϵ_s and τ_D/τ_α is shown on the left hand side in the top and bottom row of figure 6.14, respectively. It can be seen that both quantities strongly decrease with increasing IL concentration up to around 6 mol%, which is emphasized by the solid black lines. The decrease in ϵ_s is smaller at higher concentrations, highlighted by the dashed black line. The ratio τ_D/τ_α is unity at concentrations larger than 6 mol% since the fitting procedure can no longer separate both processes, and only one combined dipolar process is fit to the data. Thus, the strong decrease in the dielectric strength with increasing IL concentration is directly accompanied by the Debye- and α -process shifting towards each other and the eventual merging of both processes.

In the upper left panel, the ϵ_s -values expected for an ideal mixture are shown as a red dashed line, calculated via $\epsilon_s = \varphi_1\epsilon_1 + \varphi_2\epsilon_2$, where φ_i is the volume concentrations of the components and ϵ_i are the static permittivities of the neat components, i.e., the plateau value in $\epsilon'(\omega)$ disregarding the microscopic origin of the permittivity step. Since ϵ_s of neat [C₄C₁Im][DCA] could not be measured at 140 K, the value at a temperature slightly above the glass transition is used. It can be seen, especially at low concentrations, that the measured ϵ_s -values decrease markedly faster with increasing IL concentration than predicted by the ideal mixing law. This might already indicate that some cross-correlations, which are present in 1-propanol, reduce upon addition of IL. However, it should be kept in mind that the dielectric strength of neat [C₄C₁Im][DCA] is dominated by the conductivity relaxation, which means that the mixing rule can not be directly applied, since the latter assumes that the ϵ_s is due to dipolar reorientations. Therefore, in the upper right panel of figure 6.14, only the dipolar contribution of the dielectric strength is shown, calculated by subtracting the conductivity relaxation contribution from the total dielectric strength. Additionally, the mixing rule proposed by Kraszewski *et al.* is shown as a dashed line [343], which was found in the literature to describe the static permittivity of mixtures of 1-propanol with pyridine very well and which is given by $\epsilon_s^{0.5} = \varphi_1\epsilon_1^{0.5} + \varphi_2\epsilon_2^{0.5}$ [344].

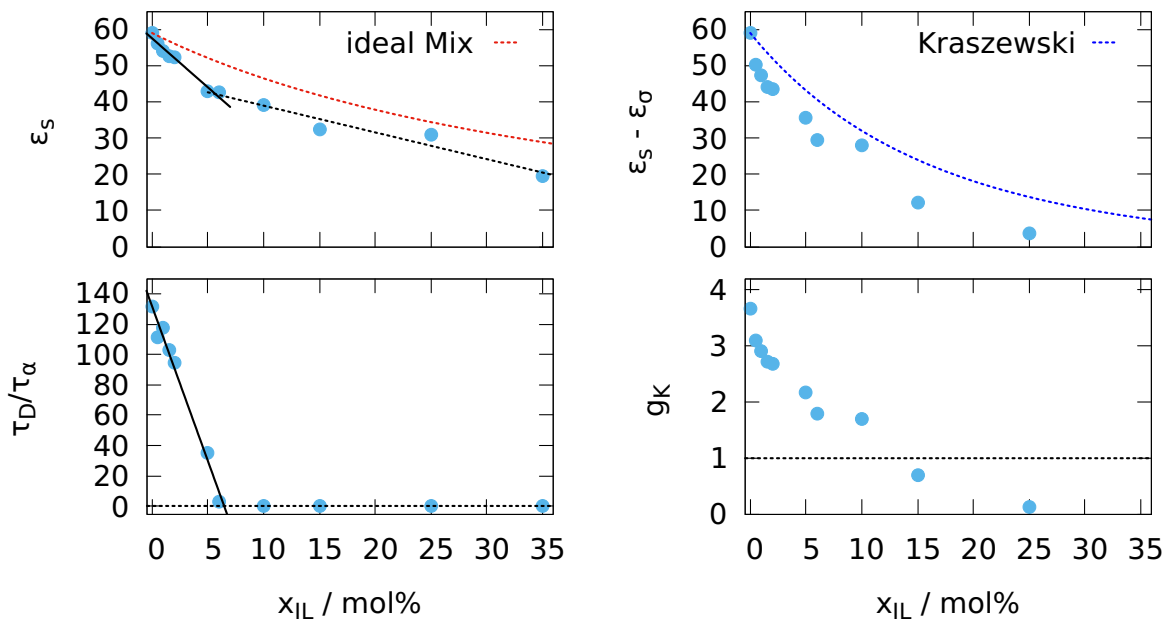


Figure 6.14.: Parameters obtained from the fit to the dielectric data of the mixtures of 1-propanol and [C₄C₁Im][DCA].

There, the dipolar relaxation strength of the neat IL is chosen to be zero since it was found in section 5.4.2 that the dipolar contribution disappears for all ILs under study at temperatures near the glass transition. Still, the measured values are lower than predicted by the mixing rule. It should be noted that various mixing rules have been proposed in the literature (see for example references [344, 345]), which yield results not too different from each other [344], so that it seems that the results here can not be captured by any of them. Thus, more insights might be obtained by considering the Kirkwood factors of the mixtures. These are calculated by equation 3.18, using only the dipolar part of the dielectric strength. Densities and refractive indices were extrapolated to 140 K from the literature [346, 347, 348, 349, 350], and the dipole moment of the IL is the mean value of the cation, listed in table 5.2, and the anion, both calculated by DFT, which together gives 2.6 D. For 1-propanol, the value of 1.68 D is used, which can be commonly found in the literature [351]. The resulting Kirkwood factors are shown in the lower right panel of figure 6.14. A strong decrease can be seen with increasing IL concentration, indicating a dramatic reduction of the cross-correlations. The transition from values higher than one, i.e., preferred parallel alignment in the simple picture, to values below one happens somewhere in the concentration range between 10 mol% and 15 mol%. This is similar to the concentration range where the merging of Debye- and α -process occurs. However, it should be noted that these g_K values should be considered with some caution, since the dipolar contribution disappears in neat ILs at low temperatures, as discussed in detail in section 5.4.2, which inevitably leads to an unphysical g_K value of zero. Nevertheless, the parameter compiled in figure 6.14 can now be compared to the predictions of the transient chain model and the Déjardin theory.

The number of molecules N contained in a transient chain can be estimated from the ratio of the

dielectric strength of the Debye process ε_D to the one of the α -relaxation ε_α via $\varepsilon_D/\varepsilon_\alpha \approx 4N$ [47]. Here, ε_α can be determined only with large uncertainty, due to its small value in comparison to ε_D for small IL concentration and due to the additional conductivity relaxation complicating the fitting. However, it has been found for n-butanol that ε_α increases upon decreasing ε_D [47], so assuming here either the same behavior or an approximately constant value of ε_α leads with a marked decrease of ε_D to the conclusion that the number of molecules in a chain decrease upon addition of IL. The same conclusion can be drawn more directly from the decreasing ratio of the time constants τ_D/τ_α , which also indicates the shortening of the end-to-end distance of the transient chains. Since it is necessary for 1-propanol molecules, which are integrated into such a linear chain, to form two hydrogen bonds, except for the first and the last molecule of the chain, the number of molecules which form two hydrogen bonds must decrease upon the addition of the IL, if the chains indeed shorten. This has been tested by Raman measurements in the Master thesis of Hannah Kirchhof. The OH-stretching region of the Raman spectrum was decomposed into the contributions from differently bound molecules by comparison with DFT calculated spectra, and the decrease of the intensity of the OH-bands associated with twofold bound molecules was found with increasing IL concentration. Thus, it seems that the dielectric results of the 1-propanol-[C₄C₁Im][DCA] mixture could be rationalized by the model of transient chains, which are comprised of a larger number of 1-propanol molecules at low IL concentration but shorten upon addition of IL due to the tendency of the 1-propanol molecules to associate with the ions. Intuitively, one would assume shorter relaxation times for shorter chains, leading to a shift of the Debye peak to higher frequencies for increasing IL concentration. This, however, is not observed as seen in figure 6.10, where the peak position stays constant, i.e., for the ratio τ_D/τ_α to decrease, the α -relaxation shifts to lower frequencies for higher IL concentrations. Thus, although most of the findings are in accordance with the transient chain model, some questions remain open, and it has to be emphasized that through the reduction of H-bonds between 1-propanol molecules, the orientational correlation naturally decreases. Thus a comparison with the Déjardin theory is in order.

However, since the Déjardin theory is unable to deal with mixtures at the present stage, only qualitative considerations can be performed. As was already discussed in section 4.2 for the case of the non-associating liquid TBP, the dynamic part of the Déjardin theory predicts a dynamic contribution in addition to the single molecular motion for cases where the Kirkwood factor is larger than unity. This additional peak is ascribed to collective motions of strongly coupled dipoles [259]. The separation of the single-molecule and the collective mode increases with increasing interaction parameter λ , which is given by $\lambda = 4\pi\rho_0\mu^2/(3k_BT)$, where ρ_0 is the particle density. Thus, when identifying the Debye process with the collective mode and the α -process with the single molecular motion of the Déjardin theory, the decreasing separation of the Debye- and α -relaxation, as seen in figure 6.14 could be caused by the decreasing λ value due to the decreasing number density of 1-propanol molecules. In addition, the Kirkwood factor of the mixtures falls below unity in the concentration range between 10 and 15 mol%, which means that from that concentration on, no additional relaxational process due to collective modes is expected by the Déjardin theory at all. This is in the limits of uncertainty in accordance with the experimental finding, where, starting at a similar concentration (10 mol%), no separation between the Debye- and α -relaxation could be resolved any longer by the fitting procedure. Thus, it can be summarized that the dielectric measurements of the 1-propanol-[C₄C₁Im][DCA]

mixtures presented in figure 6.14 could be qualitatively be rationalized by both the transient chain model and the Déjardin theory. However, while in the light of the former, the constant Debye-relaxation time upon addition of IL and thus upon shortening of the transient chains is hard to imagine as discussed above, the Déjardin theory is not directly applicable to mixtures in its present form. Therefore, the interpretation of the data with these models has to be done with some caution. Nevertheless, it should be mentioned that the improved version of the Déjardin theory is able to reproduce very well the temperature-dependent static permittivity of neat 1-propanol [50], where only one free parameter exists, which has to be determined by comparison with experimental values and which is related to induction/dispersion forces. Its value increases for longer alkyl-chains in the homologous series of the n-alcohols, as expected, since the polarizability of the molecules increases with increasing molecular volume. Thus, the Déjardin theory is well suited for describing at least the data of neat 1-propanol invoking dipolar cross-correlations, which lead to a Kirkwood factor markedly larger than one, and it seems natural that these orientational cross-correlations between neighboring 1-propanol molecules diminish upon addition of IL, since the ions interact with the 1-propanol molecules. Furthermore, the results of a recent study on ethanol seem also to be more easily rationalized by the Déjardin theory than by the transient chain model. It has been found that a Debye process is present in the plastic crystalline phase of ethanol, i.e., where translational degrees of freedom are frozen, and the molecules are only free to rotate [352]. While it is hard to imagine how the movement of a transient chain could possibly take place in the plastic crystalline phase, an orientational correlation between neighboring molecules is easy to imagine.

Up till now, the discrimination of relaxation processes in the mixtures was made into conductivity relaxation, Debye-relaxation, and dipolar reorientation. However, it had been silently assumed – at least for low IL concentrations – that only the dipolar relaxation of the 1-propanol molecules is seen in the spectra. No statement was made about the reorientation of the ions, which could be expected to become visible for higher IL concentrations. Hence, it should be checked where the ion reorientation may show in the dielectric spectra and if it should be considered in the fitting routine. Therefore, comparison with the light scattering data is useful since it was shown above that both 1-propanol and ion reorientations could be seen separately in the light scattering spectra. Hence, dielectric spectra of neat 1-propanol and neat $[C_4C_1Im][DCA]$ and four different mixtures are shown in the $\epsilon''_{der}(\omega)$ representation together with the light scattering spectra obtained at the same temperature. The temperatures for each data set are chosen such that all relaxational processes are visible in the frequency window. The data of neat 1-propanol were measured previously in the course of the works [159], and [44].⁷ It can be seen that the light scattering α -process, which is due to the reorientation of 1-propanol molecules, coincides with the dielectric α -relaxation, while the Debye-process is located at around two orders of magnitude lower frequencies. For the concentration of 2 mol% IL, the α -relaxation is still clearly visible in the dielectric spectrum. However, the peak frequency from light scattering is lower than that and located between the dielectric Debye- and α -relaxation. This is surprising, as the light scattering spectrum should still be dominated by the reorienta-

⁷Since the light scattering spectrum was recorded at a slightly higher temperature than the dielectric spectrum, it was shifted by a factor of 0.8 in frequency to resemble a data set at the same temperature as in dielectric spectroscopy. This factor was determined via the VFT-fit to the light scattering time constants.

tion of the 1-propanol molecules, which is also seen as the dielectric α -relaxation. A repeated measurement with a new sample leads to similar results. Thus, the reason for the discrepancy needs further research. It should be noted in this respect that an intermediate relaxational process has been found in several monohydroxy alcohols by dielectric spectroscopy, NMR, and rheology [309, 341, 47], which was assigned to the breaking of individual H-bonds and thus the reorientation of the hydroxy group. Thus, it could be speculated that such an intermediate process is also present in 1-propanol, which is probed by light scattering. However, it is unclear why this should be the case in the 2 mol% mixture and not in neat 1-propanol. Furthermore, it has been found recently for other monohydroxy alcohols that the light scattering relaxation is faster than the intermediate process and coincides with the dielectric α -relaxation [353]. Therefore, it seems highly unlikely that the intermediate process is probed by light scattering in the case of 1-propanol, and another explanation has to be found in the future.

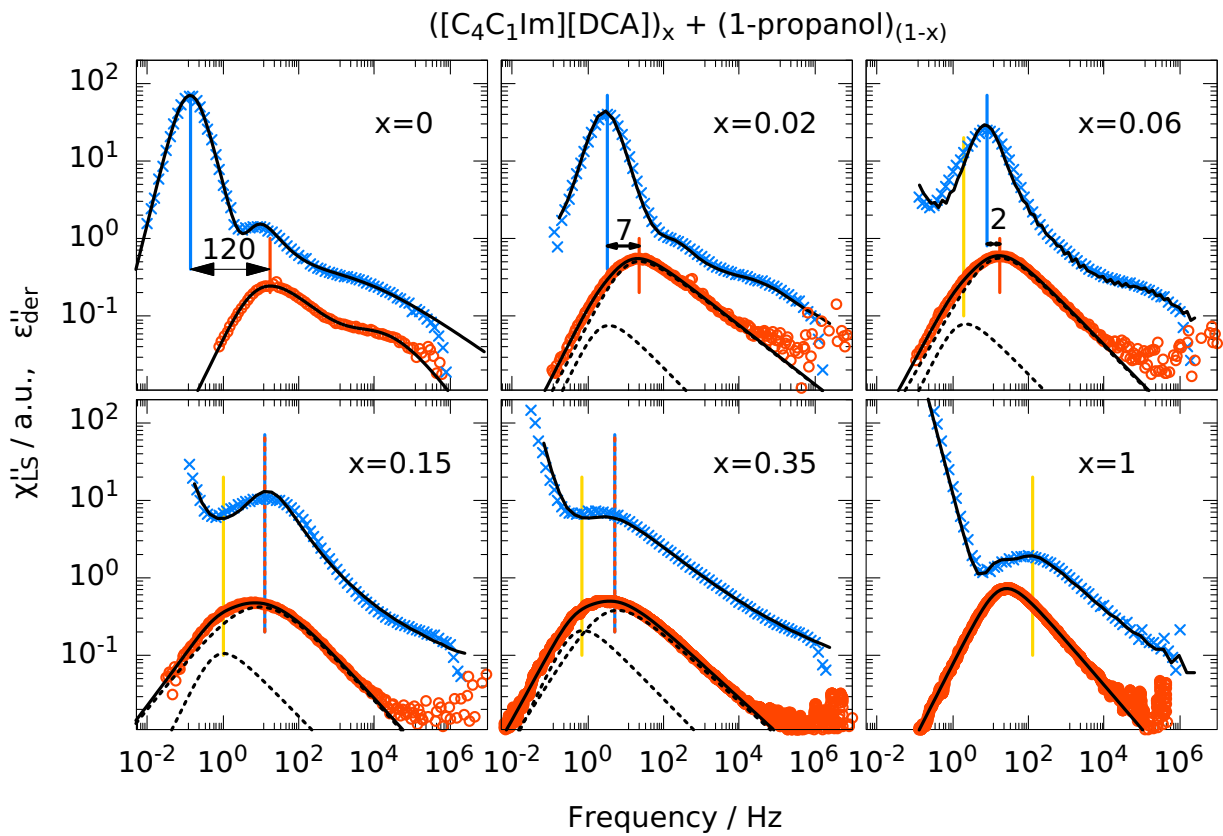


Figure 6.15.: Comparsion of the dielectric and the light scattering spectra of neat 1-propanol and neat $[C_4C_1\text{Im}][\text{DCA}]$ as well as for the case of four different mixtures of these two liquids. The dielectric data is shown in the conductivity free representation. Solid lines are the total fits to the spectrum and dashed lines are the components of the fits to the main peak of the light scattering data. Blue, orange and yellow vertical lines mark the position of the main BDS, the DLS- α (1-propanol) and the conductivity relaxation, respectively.

The contribution of the ion reorientation can be seen in the light scattering spectrum appearing

on the low-frequency flank of the 1-propanol reorientational process, which is both shown as dashed lines. It can be seen that the peak position of the ionic contribution is located at almost the same frequency as the dielectric Debye-process in the case of the 2 mol% mixture, which means that it can not be resolved in the dielectric spectrum beneath the overwhelming Debye-intensity. At a concentration of 6 mol% IL, the position of the dielectric Debye-peak and the light scattering 1-propanol peak have approached each other further. This is in accordance with the dielectric α -process approaching the Debye process for increasing IL concentration as seen in figure 6.14. When considering the fit of the dielectric data, one can see that the data is not described perfectly at the low-frequency flank of the peak, although the conductivity relaxation, which is located in this frequency range, is very well described in the modulus representation, as can be seen in figure 6.11. This might indicate that a weak additional contribution is present in this frequency range, which is hardly visible in the modulus representation, but can be seen in $\epsilon''_{\text{der}}(\omega)$. Such characteristics bears a dipolar relaxation with a slower relaxation time than the conductivity relaxation, as seen above. Additionally, the ion reorientation contribution in the light scattering spectrum is located in this same frequency range, as indicated by the vertical gold line. Together, this might indicate that indeed a weak signature of the ion reorientation is visible in the dielectric spectrum. A similar picture emerges for the two higher IL concentrations, supporting this interpretation. However, the attempt to include an additional CD function for this contribution would result in overfitting of the data.

For the concentrations of 15 and 35 mol%, the Debye- and α -process have merged, or the Debye-process has vanished in the dielectric spectrum. This leads to a single dipolar relaxation in addition to the conductivity relaxation, which is located at similar frequencies as the 1-propanol reorientation in the light scattering spectra. Thus, the assignment of the dielectric relaxation processes to their microscopic origins as well as the merging of Debye- and α -process could be confirmed by the light scattering measurements.

Concerning the IL-water mixture from section 6.1, the results from the 1-propanol-IL mixture suggest that it is indeed likely that also there the conductivity relaxation is slower than the dipolar relaxation and that this dipolar reorientational process might indeed be due to water molecules. In order to take this IL-water system a step further, in the next section, measurements are discussed for an IL-water-gelatin mixture.

6.3. Mixtures with water and gelatin

This section considers a mixture of water, $[C_4C_1Im][DCA]$ and gelatin. Due to the presence of a gelling agent and an ionic liquid, this mixture forms an ionic gel, often called Ion Jelly in the literature [133]. First proof of concept measurements on these gels were performed during the bachelor thesis of Jennifer Kraus, and most of the data shown here were obtained during her master thesis, both supervised by the present author. The Ion Jelly (IJ) was prepared by mixing 73.7 wt% IL, 17.1 wt% water and 9.2 wt% gelatin, yielding a mole ratio of IL–water of approximately 72 mol%, which is the same concentration ratio as for the IL–water mixture discussed in section 6.1. Thus, by comparing the measurements with the IL–water mixture, direct conclusions can be drawn on the impact of the gelatin on the dynamics. The resulting Ion Jelly has the consistency of jello to eat. The color is slightly yellow due to both the IL and the gelatin being yellowish. To directly demonstrate the ability of the Ion Jelly to mediate charge transfer, two teaspoons of the gel are used, which are connected to a battery and a LED, as shown in figure 6.16. As soon as the current circuit is closed, the LED lights up, demonstrating good charge transfer of the Ion Jelly.



Figure 6.16.: Demonstration of the Ion Jelly mediating charge transfer from a battery to light up a LED.

As mentioned in section 2.2, Ion Jellies were previously investigated by dielectric spectroscopy, mainly with the focus on the conductivity, and by pulsed-field NMR measurements, i.e., with both experimental techniques, translational dynamics of the ions were probed. Rotational time constants were also calculated from the step in the real part of the permittivity as measured by dielectric spectroscopy [127]. However, no attention was paid to the fact that the step could be at least partly due to the conductivity relaxation.

In contrast, dynamic light scattering measurements on an Ion Jelly were not performed before to the best of the author's knowledge. It is, however, known from *polarized* dynamic light scattering measurements on gelatin-based gels without IL that information about the mesh size of the gelatin network can be obtained from the diffusive concentration fluctuations [354, 355]. It seems that depolarized light scattering measurements were not performed on gelatin-based gels before. If only water is mixed with gelatin, the reorientational motions which could be probed by depolarized light scattering are the ones from the water molecules. Thus the scattering intensity is very low, rendering such measurements difficult. However, in the case

of the Ion Jelly of this work, the scattering intensity of $[C_4C_1Im][DCA]$ is high, so it could be hoped to see the reorientational dynamics of these ions in the light scattering spectrum. Since it is known from DSC measurements in the literature that Ion Jellies based on $[C_4C_1Im][DCA]$ could be supercooled [127], the dynamics could not only be investigated over the whole temperature range down to the glass transition but also calorimetric time constants of the gel could be obtained by DSC measurements. Moreover, through cooperation with Johan Mattsson from the University of Leeds, United Kingdom, additional rheological data on the Ion Jelly was provided.⁸ By combining these experimental techniques, the complex interplay between the translational and rotational dynamics of the ions with the nanoscopic motions of the gelatin network and the macroscopic shear behavior of the gel could be investigated.

At first, a depolarized light scattering spectrum of the Ion Jelly is compared to the IL-water mixture without gelatin at 180 K in figure 6.17. At the beginning of this work, it was unclear whether it was possible at all to obtain a depolarized light scattering spectrum of the Ion Jelly. It turned out that it is easily possible. The only experimental obstacle is the vacuum tightness of the sample cell. This is because when air is pulled out of the sample cell, bubbles build up in the gel, which cannot ascend due to the high viscosity of the gel. Therefore, they get stuck in the sample and may render a measurement impossible in cases of too many bubbles or if the bubbles are located in the laser beam area. Venting the sample cell may help reduce the bubbles to a certain extent due to the self-healing properties of the Ion Jelly.

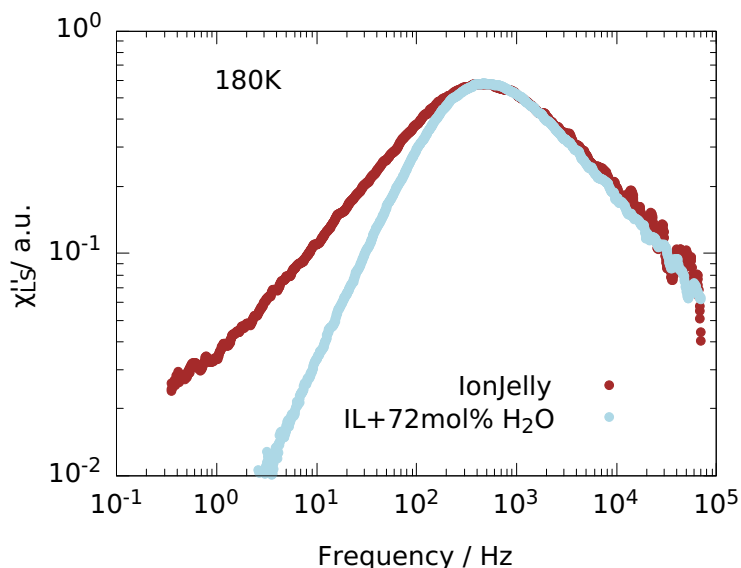


Figure 6.17.: Comparison of the light scattering spectrum of the Ion Jelly to the mixture of $[C_4C_1Im][DCA]$ with 72 mol% water. The spectra are only shifted vertically to superimpose.

When inspecting the light scattering spectra shown in figure 6.17, where the data is only shifted along the y-axis to superimpose, it gets immediately apparent that the peak frequency is identical for the Ion Jelly and the IL-water mixture. This means that the most probable

⁸data shown in figure B.4 in the appendix

relaxation time determined by the peak position is unchanged upon the addition of gelatin. This is rather surprising since it means that the rotational motions of most of the ions inside the gel matrix are not affected by the gelatin. Additionally, the high-frequency flank of both data sets is also very similar. In contrast, the low frequency flank of the Ion Jelly spectrum is markedly broadened in comparison to the IL-water mixture, where the usual ω^1 -behavior is found. The attempt to fit the Ion Jelly spectrum with a common model function like the one proposed by Havriliak and Negami, which is able to describe slopes of the low-frequency flank different from ω^1 , failed. This is because the peak is relatively narrow, while the broadening starts only at frequencies well below the peak. Since the crossover to an ω^1 -behavior is not observed and expected to occur outside the frequency window, it is possible to fit the spectra with a sum of a CD and an HN function. However, there is no evidence that the spectrum becomes bimodal at any temperature under investigation. Instead, it is more likely that just the low-frequency flank of the α -relaxation is broadened so that it becomes impossible to model it by a single common fit function. Therefore, some possible explanations for this low-frequency broadening should be discussed in the following.

The Ion Jelly displayed thermo-irreversibility, i.e., the gel did not liquefy upon heating. Moreover, after preparing the gelatin-water-IL solution, it was not necessary to cool it down to obtain a gel. Instead, gelation occurred even at elevated temperatures and under permanent stirring. In cases where only water is mixed with gelatin, thus without IL, the mixture has to be cooled down for gelation and liquefies upon heating, as is well known from using gelatin in deserts. This points into the direction that probably chemical cross-links are formed by the IL, similar to a previous observation where caffeic acid was used as a cross-linking agent [356]. However, the discrimination between chemical and physical cross-links is not straightforward [357], and beyond the scope of the present work.

In either way, one interpretation of the low frequency broadening of the spectra could be that some of the ions in the gel participate in the cross-linking process and are thus not as free in their movement as the ions not participating in cross-linking. Thus, while all ions participate in the α -process of the IL-water mixture, in the IJ, some of the ions are connected to the gelatin matrix. Therefore, the orientational correlation function measured by depolarized light scattering does not decay to zero in the course of the rotation of the free ions. Instead, slow dynamics due to the rotationally hindered ions are observed, which only decays to zero when the gel network relaxes, which is outside the accessible frequency window. Although such an explanation seems straightforward at the first sight, it has several problems: First, it is not clear how the cross-linked ions, which presumably all are trapped in a similar fashion can produce such a broad relaxation time distribution in the light scattering spectra. Second, and more importantly, a rough calculation of the number of ions participating in the slow relaxation gives values as high as 10 to 15 %, depending on the temperature, when comparing the area between the spectrum of the Ion Jelly and the area of the IL-water mixture. This value seems too high for two reasons: First, this amount of ions bonded to the gelatin matrix is difficult to reconcile with the unchanged peak position, which should shift significantly when the ratio of mobile IL and water molecules is altered. Second, the cross-link density ρ_x of the Ion Jelly can be estimated from the shear modulus value G' in the rubbery plateau region of the rheology data, which are shown in figure B.4 in the appendix, via $\rho_x \approx G'/(RT)$ [358]. There, R is the universal gas constant and T is the temperature. This gives a value of $\rho_x \approx 0.3 \text{ mol/m}^3$

at 300 K, which is below 0.01 % of the ion density in the system. Thus, the number of ions acting as cross-linker in the Ion Jelly does not suffice by far to explain the total amount of the observed slow contribution. Therefore, a different mechanism must be at work to explain the low-frequency broadening.

One could think of two possibilities for rotational motions appearing at slower time scales than the rotation of the free ions: On the one hand, optical anisotropic side chains of the gelatin might exhibit rotational motions which are detectable, for example, the pyrrolidine groups. On the other hand, some ions might be slowed down by a "slaving" of molecules in proximity to the gel matrix, like it was found for polymer-solvent mixtures [242, 359]. Both explanations involve the presence of slow rotational dynamics closely connected to the gelatin chain movements. Instead of actual slow molecules giving rise to the low-frequency flank of the light scattering spectrum, dynamic cross-correlations may be the reason, which were very recently identified in depolarized light scattering measurements of a concentrated polymer solution [243]: There, a pronounced broadening of the low-frequency flank of the solvent α -relaxation in DLS spectra was found. In that system, the effect could be attributed to orientational cross-correlations of the solvent molecules, which arise due to preferred orientations of the solvent molecules in the proximity of the polymer chain. These cross-correlations were found to decay only on the time scale of the polymer relaxation. Thus, no slow solvent molecules actually exist despite the observed slow relaxation mode. On lowering the temperature, the low-frequency broadening of the solvent relaxation increases (as is the case for the Ion Jelly) due to the increasing influence of the cross-correlation process. Thus, it might be possible that a similar mechanism is responsible for the low frequency broadening observed in the Ion Jelly. However, in the latter case, the complete decay of cross-correlations can not be observed since the polymer network does not fully relax in the temperature range studied due to the cross-linking of the gel.

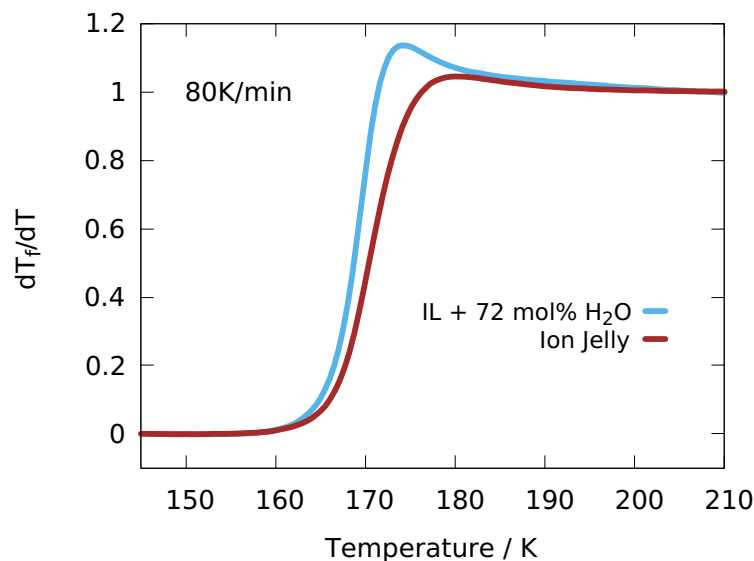


Figure 6.18.: Glass transition steps of the Ion Jelly and the mixture of $[C_4C_1Im][DCA]$ with 72 mol% water as measured by DSC.

In order to determine if indeed, slow molecules or slow molecular parts of the gelatin exist

or if, instead, cross-correlations are responsible for the low-frequency broadening of the low-frequency flank, a first hint might come from DSC measurements. This is because slow dynamics are expected to affect the glass transition step, while cross-correlations are not expected to be active in DSC measurements like it is well known for the Debye-process in monohydroxy alcohols [41, 42, 43]. Therefore, the glass transition step of the IJ and the IL-water mixture, both measured at a heating rate of 80 K/min are compared in figure 6.18 in the dT_f/dT representation. It can be seen that the slope of the glass transition step is steeper in the case of the IL-water mixture than for the IJ, leading to a broader glass transition step in the latter case. The differences between the two data sets are most prominent in the high-temperature region of the glass transition step, where the contribution from the slow dynamics would be expected. Thus, it seems that indeed slow molecules, or slow molecular parts, might be present and that the broadening of the low-frequency flank of the light scattering spectrum is not due to cross-correlations. Support for this interpretation comes from the fact that also in the macroscopic rheology spectra, a broadening of the low-frequency flank of the shear modulus is observed, as seen in figure B.4 in the appendix, reminiscent of the light scattering spectrum. However, to clarify the nature of the slow process, experiments are required that exclusively monitor the self part of the reorientational correlation function, such as certain NMR techniques, to exclude cross-correlations. Additionally, the dynamics of water molecules and ions could probably be measured separately by NMR to check if these molecules contribute to the slow relaxation.

As a next step, the invariance of the dynamics upon addition of gelatin, as indicated by the unaltered peak position between the IJ and the IL-water mixture seen in figure 6.17, should be explored further. Therefore, temperature-dependent light scattering correlation times from above room temperature down to the glass transition of both samples are compared in figure 6.19. It can be seen that the relaxation times are almost identical between the two samples over the whole temperature range. To check how the translational motions are affected by the presence of the gelatin matrix, the DC-conductivity of the IJ and the IL-water mixture are compared in the same figure. Again, they are almost identical for both samples. That means that the rotational, as well as the translational dynamics, are not affected by the presence of the gelatin.

This is a very interesting finding regarding possible applications of the Ion Jelly since mechanical stability is obtained, preventing any leakage, but without losing the high mobility of the ions. Bearing in mind the huge number of ionic liquids available, together with the fact that other liquids in these gels could replace water, this opens up the possibility of tailoring an Ion Jelly that fits the needs of specific applications.

Apart from the DC-conductivity, information about the conductivity relaxation time constants and the dipolar reorientation should be obtained from the dielectric spectra in analogy to the mixtures from the two preceding sections. Therefore, master plots of the dielectric data in $\epsilon''_{\text{der}}(\omega)$ and $M''(\omega)$ are shown in figure 6.20. It can be seen that the bimodality in $\epsilon''_{\text{der}}(\omega)$ is less pronounced than it was the case in the IL-water mixture. However, the change in the shape of the modulus spectra with temperature is similar to the one of the mixture without gelatin. At the lowest temperature, one can even see that a shoulder at the high-frequency flank of the dominant peak develops. This is reminiscent of the modulus spectrum at the lowest temperature of the 1-propanol-IL mixture shown in figure 6.12. Based on the discussion of these

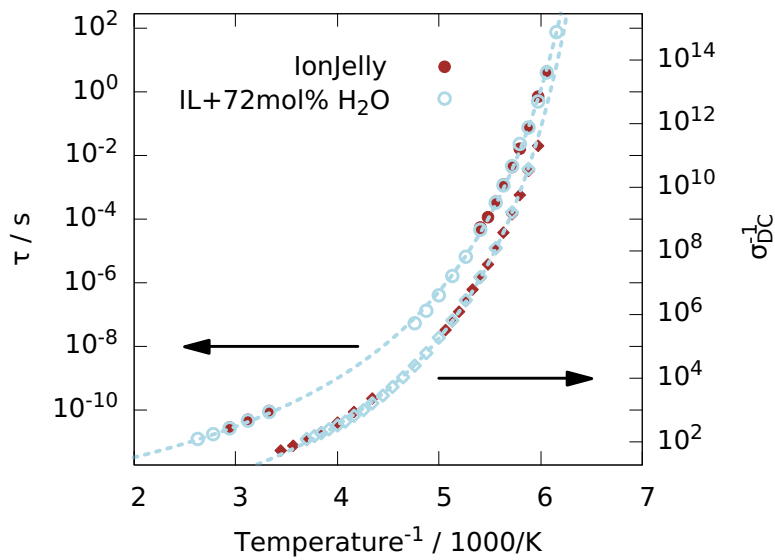


Figure 6.19.: Arrhenius plot of the light scattering time constants of the Ion Jelly and the mixture of $[\text{C}_4\text{C}_1\text{Im}][\text{DCA}]$ with 72 mol% water. Also, the inverse DC-conductivity of these two samples are shown.

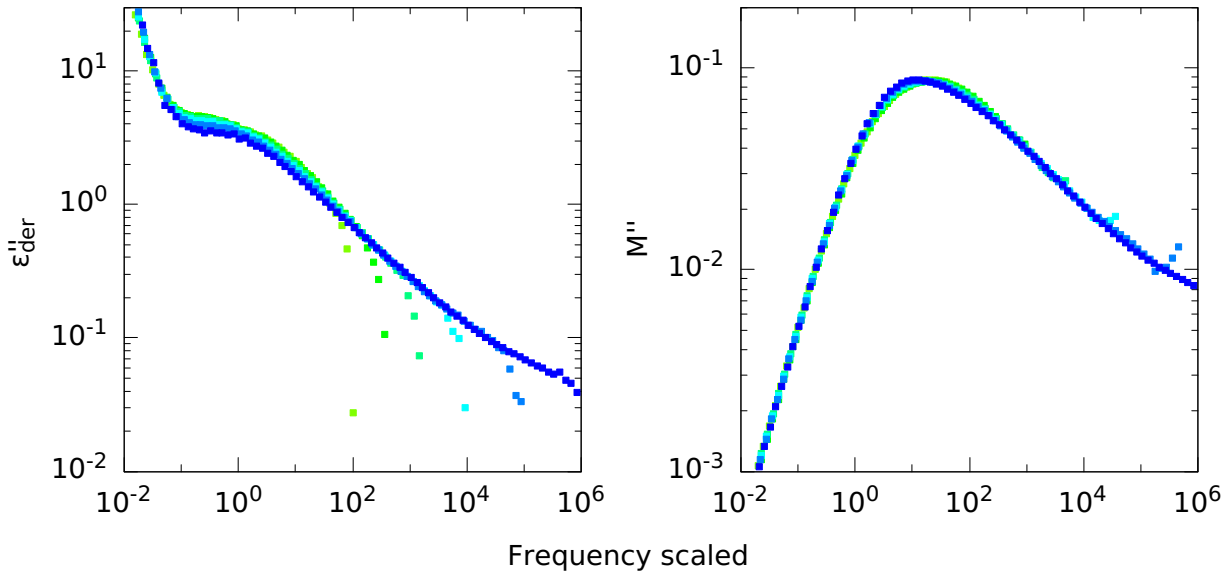


Figure 6.20.: Temperature dependent dielectric data of the Ion Jelly shown as a master plot in two representations.

spectra, it can be concluded that the conductivity relaxation is located at lower frequencies than the dipolar relaxation in the spectra of the Ion Jelly, just like it was assumed for the IL-water mixture. Thus, the data is fitted again with a MIGRATION model for the slow conductivity relaxation and a CD function for the dipolar reorientation, where the latter is probably due to

the reorientation of water molecules. Before comparing the time constants from these fits to the one from depolarized light scattering, data of polarized light scattering should be addressed first.

Since it is known from the literature that information about the mesh size of the gelatin matrix can be obtained by measuring polarized light scattering spectra of gels in general [354, 355], such measurements were performed here on the Ion Jelly in dependence of the temperature and the scattering angle θ . An example of the normalized field autocorrelation function at 300 K and $\theta = 90^\circ$ is shown in figure 6.21. A single KWW function (see equation 2.4), as commonly used to model such correlation decays, is not able to give a satisfactory description of the data. Therefore, a sum of a monoexponential decay, i.e. $\beta_{\text{KWW}} = 1$ and a KWW function with $\beta_{\text{KWW}} = 0.65$ is used to describe the correlation decay. This procedure was applied previously in the literature to polarized light scattering data of gels [354, 355]. The overall fit is shown as a solid black line in figure 6.21, and the monoexponential part as a green dashed line and the KWW contribution as a yellow dashed line, respectively.

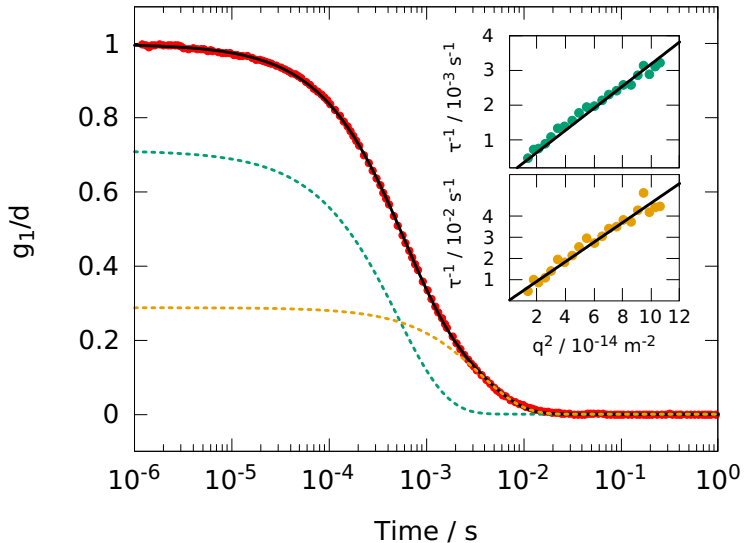


Figure 6.21.: Correlation decay of polarized light scattering measurements. A fit with a sum of a mono-exponential and a stretched exponential function is necessary to describe the data. Both are shown as dashed lines. Both decays obey a q^2 -behavior as can be seen in the insets.

The inset shows the inverse time constants τ_{KWW} for the fast and the slow decay as a function of the squared scattering vector, which is given by equation 3.4. The refractive index of the gel, necessary for calculating the scattering vector, was approximated by assuming ideal mixing [325] between water ($n = 1.33$) and $[\text{C}_4\text{C}_1\text{Im}][\text{DCA}]$ ($n = 1.51$) [326] for an IL-water mixture with a water concentration of 72 mol% $\hat{=} 19.16$ vol%. As it is obvious from the solid black lines in the insets, the dependence of the correlation time on the squared scattering vector is linear, indicating a diffusive behavior for both modes. This fit directly determines the diffusion constant via $Dq^2 = 1/\tau$. Using the diffusion constant of the mono-exponential process together

with the viscosity of the IL-water mixture,⁹ it is possible to calculate a correlation length ξ via the Stokes-Einstein equation, which is found to be $\xi = 10.5$ nm. This length-scale is of the same order of magnitude as the one found for hydrogels [354, 355], and attributed to the mesh size of the network in the literature, i.e., the fast process is due to a cooperative diffusion of chain segments between connection points of the gelatin matrix [360]. Accepting this interpretation, it is possible to compare this value of the mesh size to the distance between cross-linking points calculated from the rheological data. This distance ξ_{rheo} is used in the literature to obtain an estimate of the mesh size of the gel network by assuming that the density of cross-linking points, as calculated above from the shear modulus, can be translated into the distance between cross-linking points via

$$\xi_{\text{rheo}} = \sqrt[3]{\frac{3}{4\pi} \frac{RT}{G' N_A}}$$
 (6.1)

where ξ_{rheo} is the radius of a sphere representing the mesh size of the network. At 300 K a value of 11 nm is calculated, which is in excellent agreement with the value obtained from the diffusion constant of the fast relaxation observed by polarized light scattering.

On the other hand, the physical picture behind the slow mode in the polarized light scattering data, which has been observed in several gel systems, is controversial in the literature, see references [354, 360] and references therein. One interpretation attributes the slow mode to incomplete gelation, while other authors attribute it to cooperative rearrangements of larger areas of the network. Therefore, more work is needed to clarify the origin of this process. Here, it should just be mentioned that the slow process has a different temperature dependence than the fast process, so it could be followed only over a narrower temperature range. All time constants from the VV and VH light scattering measurements are compiled with the one from dielectric and DSC measurements in figure 6.22.

Dashed lines are fits to the respective data, indicated by matching colors, where the fits of the depolarized light scattering data and the conductivity relaxation are VFT-functions. The fit to the fast diffusive process from polarized light scattering is performed with an Arrhenius equation. It can be seen that the calorimetric time constants coincide once more with the conductivity relaxation times. The dipolar relaxation times from dielectric spectroscopy agree very well with the correlation times from depolarized light scattering. This might indicate that the reorientational motions of the water molecules, which are supposed to be seen in the dielectric spectra, are highly coupled to those from the ions, which are monitored by depolarized light scattering. This is slightly different from the situation found in the IL-water mixture discussed in section 6.1, where the dipolar relaxation was found to be slightly faster than the light scattering relaxation. However, the differences are marginal and should thus not be overinterpreted.

The data of the cooperative diffusion of chain segments, as described by the Arrhenius equation, would intersect with the VFT-curve of the other relaxation times at around 10 s, i.e., in the glass transition region. Similar observations have been made in polymer-solvent systems, where the concentration fluctuations intersect with reorientational time constants at the glass transition

⁹ $\eta = 7.31$ mPa at 298 K, as determined during the master thesis of Jennifer Kraus by Sebastian Stock, TU Darmstadt, with a rheometer.

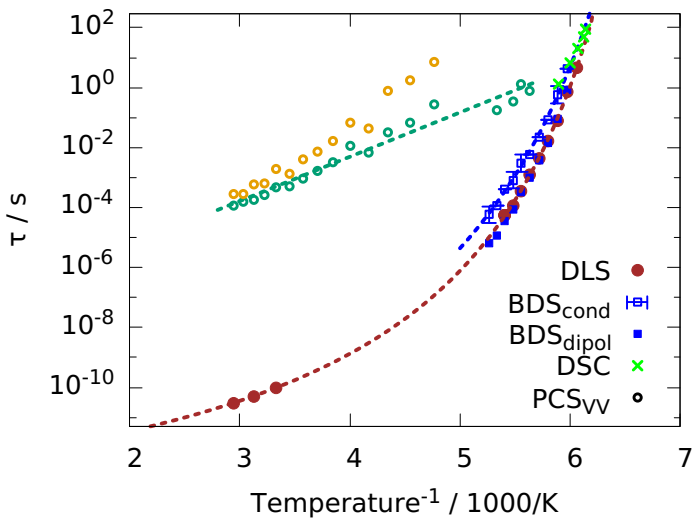


Figure 6.22.: Arrhenius plot of all time constants of the Ion Jelly.

temperature [361]. The reason for the diffusive motions exhibiting Arrhenius-type behavior while all other relaxation times show VFT-behavior is not reported in the literature to the best of the author's knowledge and should be studied in the future. While the temperature dependence of the faster process found in VV light scattering can be identified as Arrhenius-like, the temperature dependence of the slow process is not identified as easily. It is either Arrhenius-like with slightly higher activation energy than the faster process or VFT-like. Discrimination could not be made because the process left the accessible experimental time window at low temperatures.

In summary, it has been shown for the first time that reorientational dynamics of the ions in an Ion Jelly could be monitored with depolarized light scattering. It got apparent by the comparison with the IL-water mixture of the same concentration ratio just without gelatin that the time scale of the rotational dynamics is unaffected by the presence of the gelatin matrix. The same holds for the DC-conductivity, which was reported previously. The shear modulus spectrum resembles the broadening of the low-frequency flank of the depolarized light scattering spectra, and also, the glass transition step, as measured by DSC, is found to be broader than for the IL-water mixture. This might indicate that slow molecules or parts of the gelatin matrix might be responsible for these slow contributions. Additionally, mesh sizes calculated from polarized light scattering measurements and the shear modulus agree well. Thus, it has been shown that a combination of these different experimental methods can give insights into the complex interplay of rotational and translational motions of single molecules with the macroscopic dynamics of the gel. Therefore, a goal for the future might be to explore the limits of rigidity introduced by increasing the gelatin concentration without losing the high mobility of the ions.

7. Summary

The complex relaxation spectra of ionic liquids were addressed in the present work with the objective to disentangle the various dynamic contributions and to reveal their microscopic origins. Mainly two experimental methods were employed, namely depolarized light scattering (DLS) and broadband dielectric spectroscopy (BDS). In order to be able to monitor the dynamics over as wide a frequency range as possible, a third light scattering setup was implemented giving access to the terahertz regime. In BDS spectra of ionic liquids the rotational motion of the ions as well as their translational motions can be monitored. In contrast, DLS measurements gives access to rotational dynamics only, which makes the combination of both methods powerful for discriminating these contributions.

It has been shown that the conductivity relaxation, i.e., the translational motions, is ubiquitous in dielectric spectra of ionic liquids but often overlooked in the literature. It is described by the MIGRATION model in this work, which was rarely used before to describe dielectric spectra of ionic liquids but gives an excellent fit of the data. In some ionic liquids, an additional relaxational contribution showed up in the BDS spectrum, which was identified as dipolar reorientation of the cations by comparison with DLS spectra. Its visibility depends not only on the magnitude of the permanent dipole moment of the ions, but also on the degree of separation from the conductivity relaxation. This contribution was sometimes assigned to the dynamics of nanoscale aggregates of cations in the literature. However, it could be shown here that the high pressure responsiveness of this dynamic contribution is not connected to the one of the nanostructure signature from literature X-ray data. Furthermore, its time scale does not coincide with the one of a dynamic process observed by DLS, which could indeed be ascribed to the dynamics of aggregates by comparing with temperature dependent X-ray data from the literature.

A detailed analysis of DLS spectra revealed that cation and anion dynamics can be visible as two separated relaxation processes in cases of a marked difference in size of the two ion species. Strongest evidence for this assignment came from measurements of ionic liquids where the cation is the same but the anion is varied such that it is either optical isotropic or anisotropic. Only in the case of the anisotropic anion the second contribution is seen. A similar picture was obtained by measuring a non-ionic liquid where the molecular structure resembles the one of the cations under study. However, in those non-ionic cyclic compounds, also a bimodality was found in the light scattering spectrum in cases where the alkyl-chain attached to the ring was sufficiently long. The faster relaxation was ascribed to the ring reorientation independent of the rest of the molecule. It could be excluded that such a phenomenon alone is able to explain the fast relaxation in the spectra of the ionic liquids, but the anion reorientation appears on time scales similar to the one of the ring rotation. Due to the Coulombic interaction of the ring and the anion, this is reasonable. A separate contribution of cations and anions

to the relaxation spectra is only very rarely considered in the literature, and intramolecular reorientations, like the ring dynamics, seem not be reported before for high temperature light scattering measurements.

A mixtures of an ionic liquid with 72 mol% water was also investigated. The added water has no impact on the shape of the depolarized light scattering spectrum, which was ascribed to the low optical anisotropy of water molecules on the one hand and similar time scales of reorientation of water molecules and ions on the other hand. The latter was confirmed by differential scanning calorimetry measurements of the glass transition step, where no broadening in comparison to the neat ionic liquid was found. Additionally, polarized dynamic light scattering measurements were performed. They were intended to show translational motions of nanoscale water clusters. However, the hydrodynamic radius connected with these motions was found to deviate greatly from the size of the water clusters. Therefore, the observed correlation decay was ascribed to concentration fluctuations, from which it was deduced that the water molecules diffuse faster than expected through the ionic liquid matrix. This is in qualitative accordance with measurements from the literature employing different experimental techniques.

In the dielectric spectra, only a faint hint of the water dynamics was observed, although neat water exhibits a strong dielectric loss. Since higher water concentrations could not be measured due to insetting crystallization, 1-propanol was chosen instead as an admixture. In this way the full concentration range of a hydrogen-bonding solvent and an ionic liquid could be explored. From these measurements it became clear that the prominent Debye-process, which is thought to arise due to dipolar cross-correlations, already vanishes at an ionic liquid concentration around 10 mol%. This finding rationalizes the weak water contribution in the IL-water mixture since it is discussed also for water that the dielectric loss is dominated by a Debye-process.

The IL-water mixture was additionally mixed with gelatin to form an ionogel. Although mechanical rigidity was introduced in this way, the molecular dynamics, both translational and rotational, hardly changed. This might be interesting for electrolyte applications since the high ionic conductivity of a liquid is combined with quasi-solid properties in this way. It was possible to obtain mesh-sizes of the gelatin matrix from polarized light scattering measurements, which are in favorable agreement with those calculated from rheology measurements. However, some features of the relaxation spectra are not conclusively clarified, yet. For example, the low frequency broadening observed in the depolarized light scattering spectra was tentatively ascribed to ions slowed down by the gelatin matrix, but the exact mechanism still needs further research.

During the work on ionic liquids, two more fundamental questions regarding the relaxation spectra have emerged, which were addressed. One is whether it is possible to combine dynamic information of the scattered light with the intensity information in order to be able to connect relaxation processes to the anisotropy parameter of the molecules based on the scattering intensity. The experimental foundations for this were established, and the correct equation, relating the scattering intensity to the optical anisotropy, was identified from various ones available in the literature. The latter was done by comparing experimental optical ansiotropy parameters from the literature, obtained with different equations, to values from quantum chemical calculations. As a result, it is now possible to obtain depolarized light scattering spectra with the correct intensity information, which can be compared to calculated anisotropy parameters. They can be used, for example, to identify the relaxational contributions of

different molecules to the spectrum by comparison of the respective scattering intensity with the optical anisotropy parameters of the molecules under study. This is especially useful in ionic liquids, where the two ionic species can, of course, not be measured separately.

The second fundamental question which was addressed in this work concerns the shape of the rotational spectra from DLS and BDS. Since the origin of the non-exponentially of the α -relaxation is still an open question in glass physics, experimentalists usually search for correlations between different features of glassy dynamics or a universal relaxation pattern. In the case of BDS spectra, it is well known that no universal relaxation shape exists and it instead varies largely among different liquids. However, it has been shown here that the different shapes of the BDS spectra can be explained by dynamic cross-correlation contributions. These are absent in weakly polar substances or in dilute solutions, and also rarely seem to have impact on the DLS spectrum. In these cases, a generic shape is observed, which is characterized by an $\omega^{-1/2}$ slope of the high frequency flank of the relaxation peak. In systems with orientational cross-correlations, an additional Debye-like process arises in the BDS spectrum, rendering the combined peak consisting of the α -relaxation and the Debye-process narrower than the generic shape.

A. Samples and Preparation

The chemical names of the samples used in this work are listed together with the abbreviations, manufacturers, and specified purity in table A.1. The references from which density data was taken are indicated.

All ionic liquids, DC704 and DC705, were dried in a vacuum oven at 60 °C for at least 24 h before usage. Samples for light scattering measurements were filtered previously with a syringe filter with a pore size of 200 nm or 450 nm, depending on the viscosity, in order to reduce dust.

Sample	Abbreviation	Manufacturer	Purity	Lit.
1-Methyl-3-propylimidazolium bis(trifluoromethylsulfonyl)imide	[C ₃ C ₁ Im][NTf ₂]	IoLiTec GmbH	99%	[362]
1-Hexyl-3-methylimidazolium bis(trifluoromethylsulfonyl)imide	[C ₆ C ₁ Im][NTf ₂]	IoLiTec GmbH	99.5%	
1-Methyl-3-octadecylimidazolium bis(trifluoromethylsulfonyl)imide	[C ₈ C ₁ Im][NTf ₂]	IoLiTec GmbH	>98%	[103]
1-Decyl-3-methylimidazolium bis(trifluoromethylsulfonyl)imide	[C ₁₀ C ₁ Im][NTf ₂]	IoLiTec GmbH	98%	
1-Dodecyl-3-methylimidazolium bis(trifluoromethylsulfonyl)imide	[C ₁₂ C ₁ Im][NTf ₂]	IoLiTec GmbH	98%	[363]
1-Butyl-3-methylimidazolium dicyanamide	[C ₄ C ₁ Im][DCA]	IoLiTec GmbH	>98%	
1-Methyl-3-octadecylimidazolium tetrafluoroborate	[C ₈ C ₁ Im][BF ₄]	IoLiTec GmbH	>98%	[364]
1-Dodecyl-3-methylimidazolium tetrafluoroborate	[C ₁₂ C ₁ Im][BF ₄]	IoLiTec GmbH	>98%	
Octyltriethylammonium bis(trifluoromethylsulfonyl)imide	[N _{2,2,2,8}][NTf ₂]	IoLiTec GmbH	>98%	
Methyltriocetylammonium bis(trifluoromethylsulfonyl)imide	[N _{8,8,8,1}][NTf ₂]	IoLiTec GmbH	99%	
N,N-Diethyl-N-methyl-N-(2-methoxyethyl)ammonium bis(trifluoromethylsulfonyl)imide	[N _{2,2,1,2O1}][NTf ₂]	IoLiTec GmbH	99%	
1-Methyl-1-octylpyrrolidinium bis(trifluoromethylsulfonyl)imide	[Pyrr ₈][NTf ₂]	IoLiTec GmbH	99%	
Trihexyltetradecylphosphonium chloride	[P _{14,6,6,6}][Cl]	IoLiTec GmbH	≥95%	
1-Octylimidazole	C ₈ Im	IoLiTec GmbH	>98%	

1-Dodecylimidazole	C ₁₂ Im	IoLiTec GmbH	>98%	
Tributyl phosphate	TBP	Sigma Aldrich	>99%	[365]
trans-Decalin	t-decalin	Sigma Aldrich	99%	[366]
Toluene	Toluene	Acros Organics	99.8%	[367]
Propylene carbonate	PC	Karl Roth	≥99.7%	[368]
Squalane	SquaA	Acros Organics	99%	[369]
Squalene	SquE	Sigma Aldrich	≥98%	[370]
Di-n-octyl phthalate	DOP	Alfa Aesar	98%	[371]
n-Pentane	C5	Acros Organics	99+%	
n-Octane	C8	Acros Organics	99+%	[372]
Pentadecane	C15	Sigma Aldrich	≥99%	[373]
1-Phenyloctane	P8	Acros Organics	99%	[374]
p-Cymene	p-Cymene	Sigma Aldrich	99%	[375]
ortho-Terphenyl	OTP	Sigma Aldrich	99%	[154]
1,1,5,5-Tetraphenyl- 1,3,3,5-tetramethylsiloxane	DC704	fluorochem	–	[376]
1,3,5-Trimethyl- 1,1,3,5,5-pentaphenyltrisiloxane	DC705	Dow Corning	–	[376]
1-Propanol	1-propanol	Alfa Aesar	99.9%	
2-Ethyl-1-hexanol	2E1H	Alfa Aesar	99%	
5-Methyl-2-hexanol	5M2H	Sigma Aldrich	98%	
3-Phenyl-1-Propanol	3P1P	Alfa Aesar	99%	
Propylene Glycol	PG			
Glycerol	Gly	Karl Roth	99.7%	
Triphenyl phosphite	TPhP	Alfa Aesar	97%	
Water	H ₂ O	Milli-Q	–	

Table A.1.: Chemical names, abbreviations, manufacturers, and specified purity of the samples used in this work.

B. Additional data

In this chapter of the appendix some additional data is show. At first, some plots, which are related to the discussion of the main part of this work. After that, depolarized light scattering intensities of linear alkanes are addressed since they were found to behave differently than other classes of liquids. At last, refractive indices of substances used in this work are tabulated, which were measured in order to be able to calculate experimental optical anisotropies via equation 4.14.

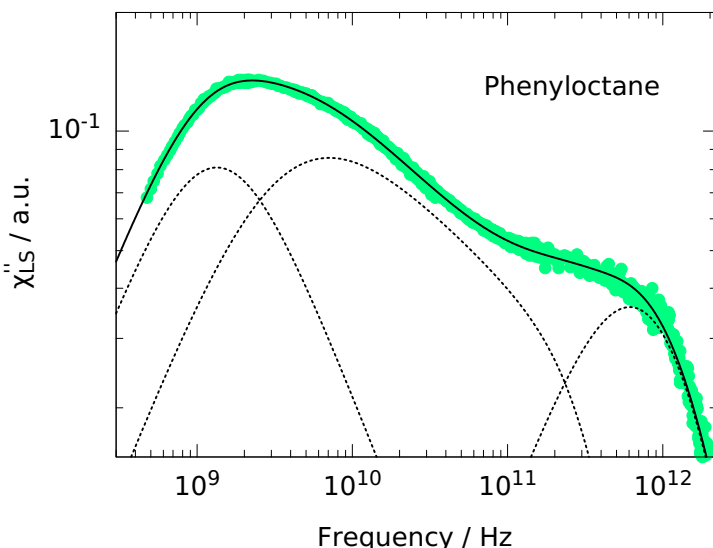


Figure B.1.: Light scattering spectrum of 1-phenyloctane at 300 K. A bimodality of the main peak can be seen, where the faster process is ascribed to the rotation of the phenylring. This is similar to the case of imidazolium-based cations. However, the optical anisotropy of the imidazolium-ring is markedly lower, which leads to a less pronounced fast relaxational process.

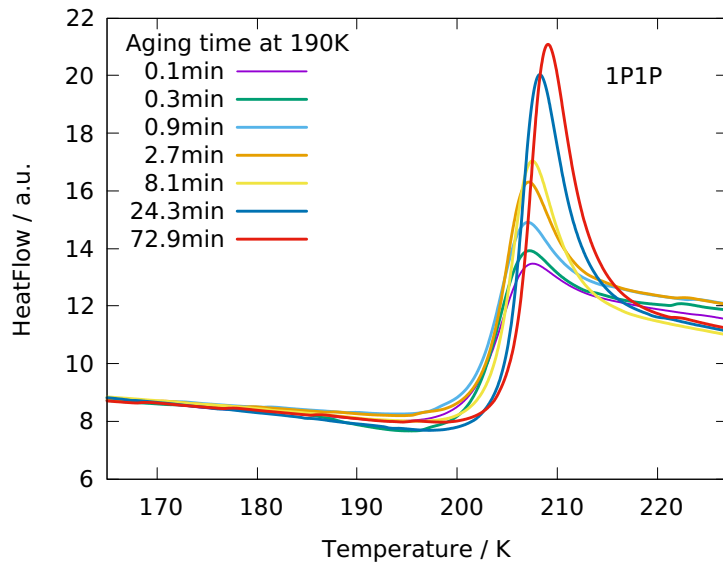


Figure B.2.: DSC curves in dependence of the aging time. The enthalpy overshoot increases as expected, underscoring the discussion of the DSC data of $[P_{14,6,6,6}][Cl]$.

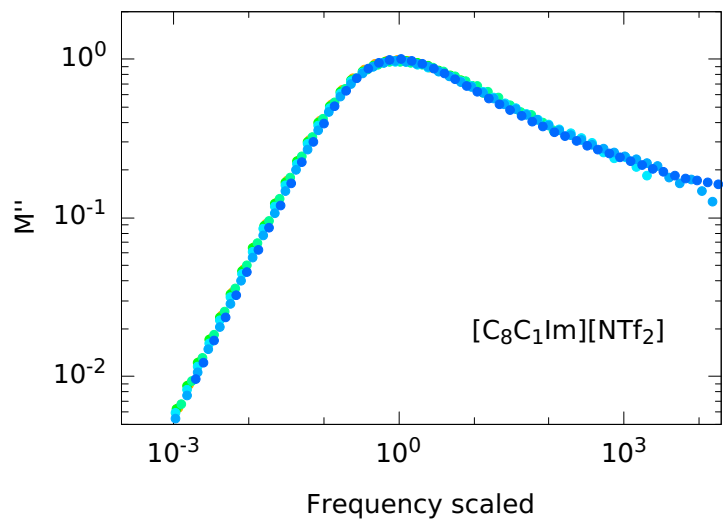


Figure B.3.: Master plot of dielectric data in the modulus representation for $[C_8C_1Im][NTf_2]$ to demonstrate that no change in the shape occurs over the whole temperature range, although a notable change in the spectrum is visible in the $\epsilon''_{der}(\omega)$ representation. This is in contrast to the data of the mixtures discussed in chapter 6, where a markedly change in the $M''(\omega)$ spectra is observed.

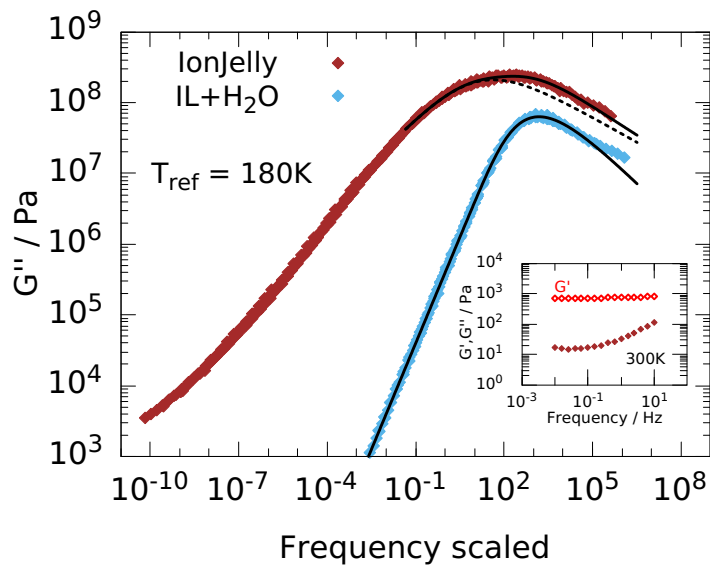


Figure B.4.: Rheology data of the Ion Jelly and the mixture of $[\text{C}_4\text{C}_1\text{Im}][\text{DCA}]$ with 72 mol% water as master plots, measured by Matthew Reynolds from the group of Johan Mattson, University of Leed, United Kingdom. Inset shows the real and imaginary part of the shear modulus at 300 K.

n-alkanes

As mentioned in section 4.1, the alkanes seemed to behave odd in respect to their light scattering intensity and should therefore be discussed here in more detail. A peculiarity of the n-alkanes was already observed decades before: The β -values of measurements in solution are only slightly different from those of the neat liquid, indicating no pronounced orientational ordering. However, the values from solution measurements of long alkanes differ significantly from gas phase measurements [377]. This is rather surprising, since they usually coincide for other molecules as shown by experiment [210] or – as in section 4.1 – by comparison with DFT calculations, which are gas phase values essentially. Therefore, it should be checked in the following how the different β -values from gas phase, solution and neat liquid measurements compare to the DFT values. Since alkanes are highly flexible, a plethora of conformers, often separated by only very small energy differences, exist for the longer chains. Therefore, a conformer search with the program CREST, as done for the other flexible molecules, is not feasible, since due to the small energy differences, rotamers are identified by the program as different conformers, which are actually the same conformer. Fortunately, a rich body of work has been dedicated to counting or identifying the conformers of n-alkanes. Here, the method by Tasi *et al.* is followed [378], who proposed the presence of five different C-C-C-C torsional angles and established simple rules to determine, which sequences of those angles are forbidden. The Tasi-notation is adapted here, where these angles are named as follows: $t : 180^\circ$, $g^+ : 60^\circ$, $g^- : -60^\circ$, $x^+ : 95^\circ$ and $x^- : -95^\circ$. A Python program was written where the Tasi rules were implemented and which gives an output file for the structure of each conformer, following those rules. These files were used as an input for the DFT calculations of the anisotropy parameters. No geometry optimization was performed, which might have destroyed the structure of the desired conformer, thus a larger error in the calculated β value than for the other molecules is expected. In order to construct the conformer ensemble, the relative energies of the conformers are needed. For this, the recent work of Stejfa *et al.* [379] is followed, where it was found that the energy penalty for a g and x conformer equals 2.5 kJ/mol and 8.7 kJ/mol, respectively, and a correction of -1.2 kJ/mol for a gg sequence was introduced. In this way, the $\langle \beta_{\text{DFT}} \rangle$ values from ethane to decane were calculated. For all substances, the complete conformer ensemble was taken into account, resulting in the case of decane in a total of 3375 conformers. This is done in order to be able to determine the lowest $\langle \beta_{\text{DFT}} \rangle$ value of all conformers. The calculated values are compared to the experimental ones, which were taken from the literature [380, 227]. In the case of the gas phase measurements, only depolarization ratios are given, which were transformed via equation 4.3 into anisotropy parameters using the isotropic polarizability α_0 from DFT calculations. The black solid line marks the equality of experimental and calculated values.

It is clear that the gas phase values follow this line most closely, while the values for the neat liquid and solution measurements have different slopes. However, the experimental gas phase values are slightly too high for the long chain alkanes. It should be noted that the authors of the study where the data was taken from, remarked that their most accurate values are those for butane, pentane and hexane, which agree very well with the calculated values, while the measurements on the longer alkanes are more difficult and thus less accurate. They also identified the value of heptane as being too high. Additionally, it has been shown that it is

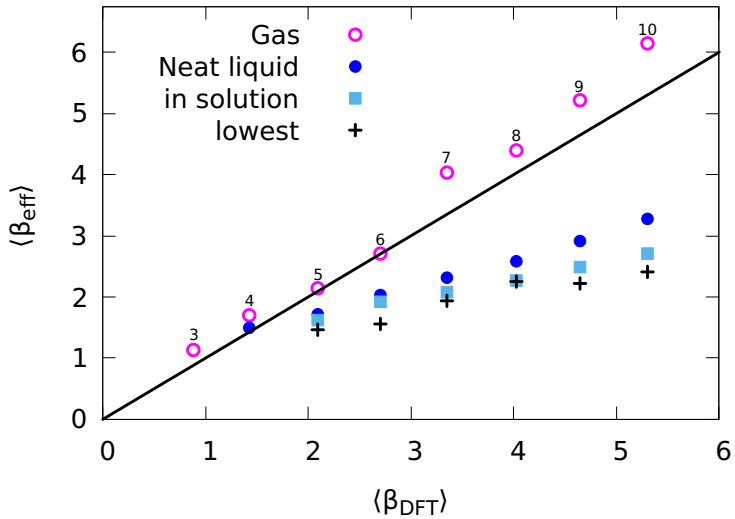


Figure B.5.: Comparison of experimental anisotropy parameters of n-alkanes from the literature [380, 227] and calculated ones. The number of carbon atoms in the chains are indicated. The lowest anisotropy parameters found in the conformer ensembles are also indicated.

crucial to eliminate stray light in order to get reliable depolarization ratios for these alkanes [381, 382]. Together, it seems that the experimental accuracy does not allow to conclude that the calculated conformer ensemble might not capture the actual one in the case of the alkanes longer than hexane.

Therefore, it is now discussed why the values from neat liquid or solution measurements deviate from the calculated or the gas phase values, respectively. One possible explanation one may think of is that the conformer ensemble for the alkanes in the liquid state is markedly different from that in the gas phase. Indeed, when extracting the conformer with the smallest β value from each ensemble and assuming it to be the energetically most stable one, the experimental values could be rationalized. This is shown in Figure B.5, where these lowest β values are included and one can see that they are slightly below all experimental values. However, this would mean that highly curled conformers with many g or x defects would have a notably lower energy than the all-trans conformer in the liquid. This is highly unlikely and a rich body of work, both experimental and theoretical, has shown that the conformer ensemble of alkanes hardly changes when going from the gas phase to the liquid phase or to solutions [383, 384, 385, 386, 387, 388].

Thus, another explanation must be found to explain the low anisotropy values in the liquid phase. Hence, the relative anisotropy parameter $\kappa = \beta/(3\alpha_0)$ is considered in the following. This allows one to see the increase in the anisotropy excluding the trivial increase of β due to the increasing α_0 with increasing volume of the molecules. In figure B.6 the κ values from the literature from gas phase and neat liquid measurements are shown in dependence of α_0 . Measurements performed during this work are included for $n = 8, 15$ as filled squares.

It can be seen that the relative anisotropy increases with increasing chain length in the case of

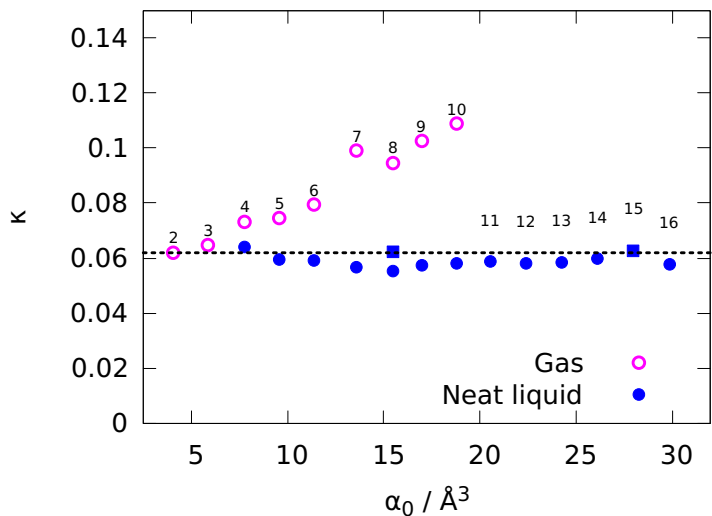


Figure B.6.: Experimental effective anisotropy parameters of n-alkanes from the literature (circles) [380, 227] and from measurements of this work (squares) in dependence of the isotropic polarizability. The number of carbon atoms in the chains are indicated.

the gas phase values, as expected when considering the all-trans conformers, the polarizability of which increases along the chain while it stays constant in the other two directions when increasing the chain length, thus the relative anisotropy increases naturally.

In contrast, the κ values of the neat liquid are constant in the limits of experimental uncertainty from butane up to hexadecane, which is the last alkane liquid at room temperature. This shows that the increase in β seen in Figure B.5 is just due to the trivial increase in α_0 with increasing chain length. Most interestingly, the constant value of κ is approximately equal to the gas phase value of ethane, as indicated by the dashes line. This points into the direction that light scattered by liquid alkanes should be considered as being scattered by isolated ethane segments, which are connected very flexibly so that the alkane molecule does not act as a joint scatterer. To support this view, further research is needed, supposedly MD simulations might help.

However, this shows that depolarized light scattering from liquids can in some cases not be directly related to the reorientation of the whole molecules. It is speculated that this is the case for highly flexible molecules consisting only of the same repeat units, like the alkanes or polymers, but is not the case as soon as symmetry breaking structures are present in the molecules, as for phenyloctane or squalane and squalene.

Refractive indices

An Abbe refractometer from Carl Zeiss, model A, is used for refractive index measurements. The temperature is controlled by pumping water at the right temperature through the instrument. A temperature calibration was made by placing a PT100 sensor between the prisms of the refractometer. The refractive index calibration was made with deionized water and 1-bromonaphthalene. The measurements were performed at two different wavelength: At the standard sodium D line (589 nm) using white light and at 532 nm using a Semrock bandpass filter with a FWHM of 2 nm placed between the white light and the refractometer.

	283.15 K	293.15 K	303.15 K	313.15 K	323.15 K	333.15 K
C15	1.4356	1.4317	1.4275	1.4232	1.4190	1.4150
TBP	1.4269	1.4231	1.4190	1.4149	1.4108	1.4069
t-decalin	1.4735	1.4691	1.4650			
DC705	1.5839	1.5797	1.5756	1.5713	1.5671	1.5630
Toluene	1.5023	1.4966	1.4912	1.4859	1.4805	
PC	1.4242	1.4205	1.4169	1.4130	1.4092	1.4056
Squalane	1.4558	1.4520	1.4480	1.4441	1.4401	1.4361
Squalene	1.4994	1.4956	1.4917	1.4877	1.4835	1.4792
DOP	1.4874	1.4840	1.4805	1.4769	1.4728	1.4689
C8	1.4021	1.3978	1.3931	1.3886	1.3839	1.3789
P8	1.4888	1.4844	1.4800	1.4756	1.4711	1.4666
p-Cymene	1.4951	1.4908	1.4860	1.4809	1.4760	1.4709
SquA+Tol	1.4616	1.4572	1.4532	1.4492	1.4451	1.4410
TBP+PC	1.4259	1.4220	1.4181	1.4142	1.4102	1.4061
SquA+C15	1.4489	1.4449	1.4409	1.4370	1.4330	1.4291
DC704	1.5630	1.5590	1.5550	1.5509	1.5469	1.5429
[C ₈ C ₁ Im][BF ₄]	1.4361	1.4332	1.4306	1.4279	1.4250	1.4221
[C ₃ C ₁ Im][NTf ₂]	1.4289	1.4260	1.4230	1.4200	1.4170	1.4141
[C ₆ C ₁ Im][NTf ₂]	1.4341	1.4311	1.4280	1.4250	1.4220	1.4190
[C ₈ C ₁ Im][NTf ₂]	1.4370	1.4339	1.4309	1.4279	1.4245	1.4215
[C ₁₀ C ₁ Im][NTf ₂]	1.4399	1.4368	1.4337	1.4305	1.4271	1.4240
[C ₁₂ C ₁ Im][NTf ₂]	1.4422	1.4391	1.4360	1.4329	1.4293	1.4261
	338.15 K	343.15 K	348.15 K	353.15 K	358.15 K	
OTP	1.6200	1.6121	1.6148	1.6121	1.6098	

Table B.1.: Refractive indices measured with an Abbe refractometer at 589 nm.

The reading error of the refractive indexes is ± 0.0002 for the values at 589 nm and ± 0.0005 at 532 nm due to the reduced intensity of the incident light. The values read off the instrument at 532 nm were transformed to the actual values taking into account the dispersion of the glass prisms following the procedure detailed in reference [389]. To check the accuracy of the measurements, the refractive indexes obtained for toluene are compared to literature data

and it was found that they compare favorably well at both wavelengths within the limits of uncertainty [390, 391]. All data is shown in table B.1 for measurements performed at 589 nm and in table B.2 at 532 nm.

	283.15 K	293.15 K	303.15 K	313.15 K	323.15 K	333.15 K
C15	1.4379	1.4340	1.4294	1.4294	1.4212	1.4170
TBP	1.4288	1.4244	1.4207	1.4162	1.4123	1.4082
t-decalin	1.4761	1.4713	1.4670			
DC705	1.5905	1.5861	1.5819	1.5776	1.5734	1.5691
Toluene	1.5077	1.5013	1.4962	1.4906	1.4862	
PC	1.4261	1.4222	1.4183	1.4149	1.4114	1.4071
Squalane	1.4580	1.4541	1.4503	1.4462	1.4419	1.4382
Squalene	1.5031	1.4991	1.4952	1.4912	1.4872	1.4831
DOP	1.4910	1.4872	1.4841	1.4795	1.4760	1.4718
C8	1.4042	1.4002	1.3948	1.3903	1.3853	
P8	1.4921	1.4880	1.4836	1.4792	1.4748	1.4700
p-Cymene	1.4997	1.4951	1.4901	1.4851	1.4800	1.4750
SquA+Tol	1.4641	1.4597	1.4556	1.4516	1.4475	1.4433
TBP+PC	1.4281	1.4241	1.4201	1.4162	1.4121	1.4076
SquA+C15	1.4512	1.4471	1.4432	1.4392	1.4354	1.4314
DC704	1.5692	1.5651	1.5609	1.5567	1.5523	1.5481
[C ₈ C ₁ Im][BF ₄]	1.4388	1.4355	1.4330	1.4302	1.4272	1.4242
[C ₃ C ₁ Im][NTf ₂]	1.4312	1.4283	1.4253	1.4221	1.4191	1.4162
[C ₆ C ₁ Im][NTf ₂]	1.4363	1.4333	1.4302	1.4273	1.4243	1.4212
[C ₈ C ₁ Im][NTf ₂]	1.4394	1.4363	1.4333	1.4301	1.4266	1.4235
[C ₁₀ C ₁ Im][NTf ₂]	1.4422	1.4390	1.4357	1.4324	1.4292	1.4260
[C ₁₂ C ₁ Im][NTf ₂]	1.4445	1.4412	1.4382	1.4346	1.4313	1.4282
OTP	1.6292	1.6269	1.6241	1.6212	1.6187	

Table B.2.: Refractive indices measured with an Abbe refractometer at 532 nm.

Bibliography

- [1] P. Walden. "Über die Molekulargrösse und elektrische Leitfähigkeit einiger geschmolzener Salze". In: *Bull. Acad. Imp. Sci.* 8.6 (1914), pp. 405–422.
- [2] T. Welton. "Ionic liquids: a brief history". In: *Biophys. Rev.* 10.3 (2018), pp. 691–706.
- [3] E. F. Borra, O. Seddiki, R. Angel, D. Eisenstein, P. Hickson, K. R. Seddon, and S. P. Worden. "Deposition of metal films on an ionic liquid as a basis for a lunar telescope". In: *Nature* 447.7147 (2007), pp. 979–981.
- [4] A. H. Tullo. *The time is now for ionic liquids*. <https://cen.acs.org/materials/ionic-liquids/time-ionic-liquids/98/i5>. Accessed: 2022-01-18. 2020.
- [5] A. Einstein and R. Furth. *Investigation on the theory of Brownian motion*. 1956.
- [6] P. J. W. Debye. *Polar molecules*. Chemical Catalog Company, Incorporated, 1929.
- [7] R. Richert. "Heterogeneous dynamics in liquids: fluctuations in space and time". In: *J. Condens. Matter Phys.* 14.23 (2002), R703.
- [8] M. Becher. "NMR-Studien der molekularen Dynamik in ionischen Flüssigkeiten und Polymerelektrolyten". PhD thesis. Technische Universität Darmstadt, 2020.
- [9] J. C. Dyre. "Colloquium: The glass transition and elastic models of glass-forming liquids". In: *Rev. Mod. Phys.* 78.3 (2006), p. 953.
- [10] R. Richert, J. P. Gabriel, and E. Thoms. "Structural relaxation and recovery: A dielectric approach". In: *J. Phys. Chem. Lett.* 12.35 (2021), pp. 8465–8469.
- [11] M. D. Ediger. "Spatially heterogeneous dynamics in supercooled liquids". In: *Annu. Rev. Phys. Chem.* 51.1 (2000), pp. 99–128.
- [12] L. Berthier and G. Biroli. "Theoretical perspective on the glass transition and amorphous materials". In: *Rev. Mod. Phys.* 83.2 (2011), p. 587.
- [13] P. Lunkenheimer, L. Pardo, M. Köhler, and A. Loidl. "Broadband dielectric spectroscopy on benzophenone: α relaxation, β relaxation, and mode coupling theory". In: *Phys. Rev. E* 77.3 (2008), p. 031506.
- [14] P. Lunkenheimer, U. Schneider, R. Brand, and A. Loidl. "Glassy dynamics". In: *Contemp. Phys.* 41.1 (2000), pp. 15–36.
- [15] U. Schneider, R. Brand, P. Lunkenheimer, and A. Loidl. "Scaling of broadband dielectric data of glass-forming liquids and plastic crystals". In: *Eur. Phys. J. E* 2.1 (2000), pp. 67–73.

- [16] B. Schmidtke, N. Petzold, B. Pötzschner, H. Weingärtner, and E. Rössler. “Relaxation Stretching, Fast Dynamics, and Activation Energy: A Comparison of Molecular and Ionic Liquids as Revealed by Depolarized Light Scattering”. In: *J. Phys. Chem. B* 118.25 (2014), pp. 7108–7118.
- [17] H. Cummins, G. Li, W. Du, J. Hernandez, and N. Tao. “Light scattering spectroscopy of the liquid-glass transition”. In: *J. Condens. Matter Phys.* 6.23A (1994), A51.
- [18] N. Petzold, B. Schmidtke, R. Kahlau, D. Bock, R. Meier, B. Micko, D. Kruk, and E. Rössler. “Evolution of the dynamic susceptibility in molecular glass formers: Results from light scattering, dielectric spectroscopy, and NMR”. In: *J. Chem. Phys.* 138.12 (2013), 12A510.
- [19] B. Schmidtke, N. Petzold, R. Kahlau, and E. Rössler. “Reorientational dynamics in molecular liquids as revealed by dynamic light scattering: From boiling point to glass transition temperature”. In: *J. Chem. Phys.* 139.8 (2013), p. 084504.
- [20] T. Blochowicz. *Broadband Dielectric Spectroscopy in Neat and Binary Molecular Glass Formers: Frequency and Time Domain Spectroscopy, Non-resonant Spectral Hole Burning*. Logos Verlag Berlin, 2003.
- [21] G. P. Johari and M. Goldstein. “Viscous liquids and the glass transition. II. Secondary relaxations in glasses of rigid molecules”. In: *J. Chem. Phys.* 53.6 (1970), pp. 2372–2388.
- [22] M. Vogel and E. Rössler. “On the nature of slow β -process in simple glass formers: a ^2H NMR study”. In: *J. Phys. Chem. B* 104.18 (2000), pp. 4285–4287.
- [23] C. Scalliet, B. Guiselin, and L. Berthier. “Excess wings and asymmetric relaxation spectra in a facilitated trap model”. In: *arXiv preprint arXiv:2106.01759* (2021).
- [24] C. Scalliet, B. Guiselin, and L. Berthier. “Microscopic origin of excess wings in the relaxation spectra of deeply supercooled liquids”. In: *Bull. Am. Phys. Soc.* (2021).
- [25] C. Gainaru, H. Nelson, J. Huebinger, M. Grabenbauer, and R. Böhmer. “Suppression of Orientational Correlations in the Viscous-Liquid State of Hyperquenched Pressure-Densified Glycerol”. In: *Phys. Rev. Lett.* 125.6 (2020), p. 065503.
- [26] T. Blochowicz and E. Rössler. “Beta relaxation versus high frequency wing in the dielectric spectra of a binary molecular glass former”. In: *Phys. Rev. Lett.* 92.22 (2004), p. 225701.
- [27] E. Donth. *The glass transition: relaxation dynamics in liquids and disordered materials*. Vol. 48. Springer Science & Business Media, 2013.
- [28] T. Hecksher, A. I. Nielsen, N. B. Olsen, and J. C. Dyre. “Little evidence for dynamic divergences in ultraviscous molecular liquids”. In: *Nat. Phys.* 4.9 (2008), pp. 737–741.
- [29] M. Uhl, J. Fischer, P. Sippel, H. Bunzen, P. Lunkenheimer, D. Volkmer, and A. Loidl. “Glycerol confined in zeolitic imidazolate frameworks: The temperature-dependent cooperativity length scale of glassy freezing”. In: *J. Chem. Phys.* 150.2 (2019), p. 024504.
- [30] L. Berthier, G. Biroli, J.-P. Bouchaud, L. Cipelletti, and W. van Saarloos. *Dynamical heterogeneities in glasses, colloids, and granular media*. Vol. 150. OUP Oxford, 2011.

- [31] A. Reiser, G. Kasper, and S. Hunklinger. “Pressure-induced isothermal glass transition of small organic molecules”. In: *Phys. Rev. B* 72.9 (2005), p. 094204.
- [32] E. R. López, A. S. Pensado, M. J. Comuñas, A. A. Pádua, J. Fernández, and K. R. Harris. “Density scaling of the transport properties of molecular and ionic liquids”. In: *J. Chem. Phys.* 134.14 (2011), p. 144507.
- [33] D. Fragiadakis and C. M. Roland. “On the density scaling of liquid dynamics”. In: *J. Chem. Phys.* 134.4 (2011), p. 044504.
- [34] H. W. Hansen, F. Lundin, K. Adrjanowicz, B. Frick, A. Matic, and K. Niss. “Density scaling of structure and dynamics of an ionic liquid”. In: *Phys. Chem. Chem. Phys.* 22.25 (2020), pp. 14169–14176.
- [35] F. Kremer and A. Loidl. *The scaling of relaxation processes*. Springer, 2018.
- [36] D. Coslovich and C. Roland. “Thermodynamic scaling of diffusion in supercooled Lennard-Jones liquids”. In: *J. Phys. Chem. B* 112.5 (2008), pp. 1329–1332.
- [37] T. B. Schröder, U. R. Pedersen, N. P. Bailey, S. Toxvaerd, and J. C. Dyre. “Hidden scale invariance in molecular van der Waals liquids: A simulation study”. In: *Phys. Rev. E* 80.4 (2009), p. 041502.
- [38] R. Casalini and T. C. Ransom. “On the experimental determination of the repulsive component of the potential from high pressure measurements: What is special about twelve?” In: *J. Chem. Phys.* 151.19 (2019), p. 194504.
- [39] M. Paluch, C. Roland, S. Pawlus, J. Zioło, and K. Ngai. “Does the Arrhenius temperature dependence of the Johari-Goldstein relaxation persist above T_g ?”. In: *Phys. Rev. Lett.* 91.11 (2003), p. 115701.
- [40] T. Fujima, H. Frusawa, and K. Ito. “Merging of α and slow β relaxation in supercooled liquids”. In: *Phys. Rev. E* 66.3 (2002), p. 031503.
- [41] D. Xu, S. Feng, J.-Q. Wang, L.-M. Wang, and R. Richert. “Entropic Nature of the Debye Relaxation in Glass-Forming Monoalcohols”. In: *J. Phys. Chem. Lett.* 11.14 (2020), pp. 5792–5797.
- [42] H. Huth, L.-M. Wang, C. Schick, and R. Richert. “Comparing calorimetric and dielectric polarization modes in viscous 2-ethyl-1-hexanol”. In: *J. Chem. Phys.* 126.10 (2007), p. 104503.
- [43] L.-M. Wang, Y. Tian, R. Liu, and R. Richert. “Calorimetric versus kinetic glass transitions in viscous monohydroxy alcohols”. In: *J. Chem. Phys.* 128.8 (2008), p. 084503.
- [44] J. Gabriel, F. Pabst, and T. Blochowicz. “Debye process and β -relaxation in 1-propanol probed by dielectric spectroscopy and depolarized dynamic light scattering”. In: *J. Phys. Chem. B* 121.37 (2017), pp. 8847–8853.
- [45] J. Gabriel, F. Pabst, A. Helbling, T. Böhmer, and T. Blochowicz. “Nature of the Debye-Process in Monohydroxy Alcohols: 5-Methyl-2-Hexanol Investigated by Depolarized Light Scattering and Dielectric Spectroscopy”. In: *Phys. Rev. Lett.* 121.3 (2018), p. 035501.

- [46] C. Gainaru, R. Figuli, T. Hecksher, B. Jakobsen, J. Dyre, M. Wilhelm, and R. Böhmer. “Shear-modulus investigations of monohydroxy alcohols: Evidence for a short-chain-polymer rheological response”. In: *Phys. Rev. Lett.* 112.9 (2014), p. 098301.
- [47] C. Gainaru, R. Meier, S. Schildmann, C. Lederle, W. Hiller, E. Rössler, and R. Böhmer. “Nuclear-magnetic-resonance measurements reveal the origin of the Debye process in monohydroxy alcohols”. In: *Phys. Rev. Lett.* 105.25 (2010), p. 258303.
- [48] T. Bauer, M. Michl, P. Lunkenheimer, and A. Loidl. “Nonlinear dielectric response of Debye, α , and β relaxation in 1-propanol”. In: *J. Non Cryst. Solids* 407 (2015), pp. 66–71.
- [49] P.-M. Déjardin. “Kinetic Yvon-Born-Green theory of the linear dielectric constant and complex permittivity of isotropic polar fluids”. In: *Phys. Rev. E* 105.2 (2022), p. 024109.
- [50] P.-M. Déjardin, F. Pabst, Y. Cornaton, A. Helbling, and T. Blochowicz. “Temperature dependence of the Kirkwood correlation factor and linear dielectric constant of simple isotropic polar fluids”. In: *Phys. Rev. E* 105.2 (2022), p. 024108.
- [51] V. Novikov and E. Rössler. “Correlation between glass transition temperature and molecular mass in non-polymeric and polymer glass formers”. In: *Polymer* 54.26 (2013), pp. 6987–6991.
- [52] T. Blochowicz, C. Karle, A. Kudlik, P. Medick, I. Roggatz, M. Vogel, C. Tschirwitz, J. Wolber, J. Senker, and E. Rössler. “Molecular dynamics in binary organic glass formers”. In: *J. Phys. Chem. B* 103.20 (1999), pp. 4032–4044.
- [53] K. Kessairi, S. Capaccioli, D. Prevosto, M. Lucchesi, and P. Rolla. “Relaxation dynamics in tert-butylpyridine/tristyrene mixture investigated by broadband dielectric spectroscopy”. In: *J. Chem. Phys.* 127.17 (2007), p. 174502.
- [54] M. F. Shears and G. Williams. “Molecular dynamics of the supercooled liquid state. A dielectric study of the low frequency motions of fluorenone in o-terphenyl and mixed solvents and of di-n-butyl phthalate in o-terphenyl”. In: *J. Chem. Soc.* 69 (1973), pp. 608–621.
- [55] G. Katana, E. W. Fischer, T. Hack, V. Abetz, and F. Kremer. “Influence of concentration fluctuations on the dielectric. Alpha.-relaxation in homogeneous Polymer mixtures”. In: *Macromolecules* 28.8 (1995), pp. 2714–2722.
- [56] T. Körber, R. Minikejew, B. Pötzschner, D. Bock, and E. Rössler. “Dynamically asymmetric binary glass formers studied by dielectric and NMR spectroscopy”. In: *Eur. Phys. J. E* 42.11 (2019), pp. 1–16.
- [57] S. P. Bierwirth, C. Gainaru, and R. Böhmer. “Coexistence of two structural relaxation processes in monohydroxy alcohol–alkyl halogen mixtures: Dielectric and rheological studies”. In: *J. Chem. Phys.* 149.4 (2018), p. 044509.
- [58] T. Körber, F. Krohn, C. Neuber, H.-W. Schmidt, and E. A. Rössler. “Reorientational dynamics of highly asymmetric binary non-polymeric mixtures—a dielectric spectroscopy study”. In: *Phys. Chem. Chem. Phys.* 23.12 (2021), pp. 7200–7212.

- [59] F. Howell, R. Bose, P. Macedo, and C. Moynihan. “Electrical relaxation in a glass-forming molten salt”. In: *J. Phys. Chem.* 78.6 (1974), pp. 639–648.
- [60] M. Paluch, Z. Wojnarowska, and S. Hensel-Bielowka. “Heterogeneous dynamics of prototypical ionic glass CKN monitored by physical aging”. In: *Phys. Rev. Lett.* 110.1 (2013), p. 015702.
- [61] E. Rhodes, W. Smith, and A. Ubbelohde. “Relaxation processes in super-cooled nitrate melts”. In: *Transact. Faraday Soc.* 63 (1967), pp. 1943–1952.
- [62] G. Li, W. Du, X. Chen, H. Cummins, and N. Tao. “Testing mode-coupling predictions for α and β relaxation in $\text{Ca}_{0.4}\text{K}_{0.6}(\text{NO}_3)_{1.4}$ near the liquid-glass transition by light scattering”. In: *Phys. Rev. A* 45.6 (1992), p. 3867.
- [63] J. Beerwerth, S. P. Bierwirth, J. Adam, C. Gainaru, and R. Böhmer. “Local and global dynamics of the viscous ion conductors $2\text{Ca}(\text{NO}_3)_2\text{-}3\text{KNO}_3$ and $2\text{Ca}(\text{NO}_3)_2\text{-}3\text{RbNO}_3$ probed by ^{87}Rb nuclear magnetic resonance and shear rheology”. In: *J. Chem. Phys.* 150.19 (2019), p. 194503.
- [64] S. Sen and J. Stebbins. “Heterogeneous NO_3^- Ion Dynamics near the Glass Transition in the Fragile Ionic Glass Former $\text{Ca}_{0.4}\text{K}_{0.6}(\text{NO}_3)_{1.4}$: A ^{15}N NMR Study”. In: *Phys. Rev. Lett.* 78.18 (1997), p. 3495.
- [65] P. J. Griffin, A. L. Agapov, and A. P. Sokolov. “Translation-rotation decoupling and nonexponentiality in room temperature ionic liquids”. In: *Phys. Rev. E* 86 (2 2012), p. 021508.
- [66] P. Griffin, A. L. Agapov, A. Kisliuk, X.-G. Sun, S. Dai, V. N. Novikov, and A. P. Sokolov. “Decoupling charge transport from the structural dynamics in room temperature ionic liquids”. In: *J. Chem. Phys.* 135.11 (2011), p. 114509.
- [67] Z. Wojnarowska, K. Kołodziejczyk, K. Paluch, L. Tajber, K. Grzybowska, K. Ngai, and M. Paluch. “Decoupling of conductivity relaxation from structural relaxation in protic ionic liquids and general properties”. In: *Phys. Chem. Chem. Phys.* 15.23 (2013), pp. 9205–9211.
- [68] J. R. Sangoro, C. Iacob, A. Agapov, Y. Wang, S. Berdzinski, H. Rexhausen, V. Strehmel, C. Friedrich, A. Sokolov, and F. Kremer. “Decoupling of ionic conductivity from structural dynamics in polymerized ionic liquids”. In: *Soft Matter* 10.20 (2014), pp. 3536–3540.
- [69] C. Gainaru, E. W. Stacy, V. Bocharova, M. Gobet, A. P. Holt, T. Saito, S. Greenbaum, and A. P. Sokolov. “Mechanism of conductivity relaxation in liquid and polymeric electrolytes: Direct link between conductivity and diffusivity”. In: *J. Phys. Chem. B* 120.42 (2016), pp. 11074–11083.
- [70] F. Wieland, A. P. Sokolov, R. Böhmer, and C. Gainaru. “Transient Nonlinear Response of Dynamically Decoupled Ionic Conductors”. In: *Phys. Rev. Lett.* 121.6 (2018), p. 064503.
- [71] K. Fumino and R. Ludwig. “Analyzing the interaction energies between cation and anion in ionic liquids: The subtle balance between Coulomb forces and hydrogen bonding”. In: *J. Mol. Liq.* 192 (2014), pp. 94–102.

- [72] J. N. Canongia Lopes and A. A. Padua. “Nanostructural organization in ionic liquids”. In: *J. Phys. Chem. B* 110.7 (2006), pp. 3330–3335.
- [73] A. Triolo, O. Russina, H.-J. Bleif, and E. Di Cola. “Nanoscale segregation in room temperature ionic liquids”. In: *J. Phys. Chem. B* 111.18 (2007), pp. 4641–4644.
- [74] T. Pott and P. Méléard. “New insight into the nanostructure of ionic liquids: a small angle X-ray scattering (SAXS) study on liquid tri-alkyl-methyl-ammonium bis (trifluoromethanesulfonyl) amides and their mixtures”. In: *Phys. Chem. Chem. Phys.* 11.26 (2009), pp. 5469–5475.
- [75] M. Kofu, M. Nagao, T. Ueki, Y. Kitazawa, Y. Nakamura, S. Sawamura, M. Watanabe, and O. Yamamuro. “Heterogeneous slow dynamics of imidazolium-based ionic liquids studied by neutron spin echo”. In: *J. Phys. Chem. B* 117.9 (2013), pp. 2773–2781.
- [76] H. V. Annapureddy, H. K. Kashyap, P. M. De Biase, and C. J. Margulis. “What is the origin of the prepeak in the x-ray scattering of imidazolium-based room-temperature ionic liquids?” In: *J. Phys. Chem. B* 114.50 (2010), pp. 16838–16846.
- [77] K. Nakamura and T. Shikata. “Systematic Dielectric and NMR Study of the Ionic Liquid 1-Alkyl-3-Methyl Imidazolium”. In: *ChemPhysChem* 11.1 (2010), pp. 285–294.
- [78] E. Heid, B. Docampo-Álvarez, L. M. Varela, K. Prosenz, O. Steinhauser, and C. Schröder. “Langevin behavior of the dielectric decrement in ionic liquid water mixtures”. In: *Phys. Chem. Chem. Phys.* 20.22 (2018), pp. 15106–15117.
- [79] T. Sonnleitner, D. A. Turton, S. Waselikowski, J. Hunger, A. Stoppa, M. Walther, K. Wynne, and R. Buchner. “Dynamics of RTILs: A comparative dielectric and OKE study”. In: *J. Mol. Liq.* 192 (2014), pp. 19–25.
- [80] T. Sonnleitner, D. A. Turton, G. Hefter, A. Ortner, S. Waselikowski, M. Walther, K. Wynne, and R. Buchner. “Ultra-broadband dielectric and optical Kerr-effect study of the ionic liquids ethyl and propylammonium nitrate”. In: *J. Phys. Chem. B* 119.29 (2015), pp. 8826–8841.
- [81] J. Hunger, A. Stoppa, S. Schroedle, G. Hefter, and R. Buchner. “Temperature dependence of the dielectric properties and dynamics of ionic liquids”. In: *ChemPhysChem* 10.4 (2009), pp. 723–733.
- [82] A. Wulf, R. Ludwig, P. Sasisanker, and H. Weingärtner. “Molecular reorientation in ionic liquids: A comparative dielectric and magnetic relaxation study”. In: *Chem. Phys. Lett.* 439.4 (2007), pp. 323–326.
- [83] J. Hunger, T. Sonnleitner, L. Liu, R. Buchner, M. Bonn, and H. J. Bakker. “Hydrogen-bond dynamics in a protic ionic liquid: evidence of large-angle jumps”. In: *J. Phys. Chem. Lett.* 3.20 (2012), pp. 3034–3038.
- [84] C. Schröder, C. Wakai, H. Weingärtner, and O. Steinhauser. “Collective rotational dynamics in ionic liquids: A computational and experimental study of 1-butyl-3-methylimidazolium tetrafluoroborate”. In: *J. Chem. Phys.* 126.8 (2007), p. 084511.
- [85] T. Yamaguchi and S. Koda. “Dielectric and shear relaxations of ionic liquid composed of symmetric ions”. In: *J. Chem. Phys.* 141.14 (2014), p. 144503.

- [86] C. Schröder, M. Haberler, and O. Steinhauser. “On the computation and contribution of conductivity in molecular ionic liquids”. In: *J. Chem. Phys.* 128.13 (2008), p. 134501.
- [87] K. Hayamizu, S. Tsuzuki, S. Seki, and Y. Umebayashi. “Multinuclear NMR studies on translational and rotational motion for two ionic liquids composed of BF₄ anion”. In: *J. Phys. Chem. B* 116.36 (2012), pp. 11284–11291.
- [88] E. Steinrücken, M. Becher, and M. Vogel. “On the molecular mechanisms of α and β relaxations in ionic liquids”. In: *J. Chem. Phys.* 153.10 (2020), p. 104507.
- [89] M. Becher, E. Steinrücken, and M. Vogel. “On the relation between reorientation and diffusion in glass-forming ionic liquids with micro-heterogeneous structures”. In: *J. Chem. Phys.* 151.19 (2019), p. 194503.
- [90] F. Pabst, J. Gabriel, P. Weigl, and T. Blochowicz. “Molecular dynamics of supercooled ionic liquids studied by light scattering and dielectric spectroscopy”. In: *Chem. Phys.* 494 (2017), pp. 103–110.
- [91] P. Sippel, S. Krohns, D. Reuter, P. Lunkenheimer, and A. Loidl. “Importance of reorientational dynamics for the charge transport in ionic liquids”. In: *Phys. Rev. E* 98.5 (2018), p. 052605.
- [92] W. Zhao, F. Leroy, B. Heggen, S. Zahn, B. Kirchner, S. Balasubramanian, and F. Müller-Plathe. “Are there stable ion-pairs in room-temperature ionic liquids? Molecular dynamics simulations of 1-n-butyl-3-methylimidazolium hexafluorophosphate”. In: *J. Am. Chem. Soc.* 131.43 (2009), pp. 15825–15833.
- [93] H. Weingärtner. “The static dielectric constant of ionic liquids”. In: *Z. Phys. Chem.* 220.10 (2006), pp. 1395–1405.
- [94] F. S. Howell, C. T. Moynihan, and P. B. Macedo. “Electrical relaxations in mixtures of lithium chloride and glycerol”. In: *Bull. Chem. Soc. Jpn.* 57.3 (1984), pp. 652–661.
- [95] P. J. Griffin, A. P. Holt, K. Tsunashima, J. R. Sangoro, F. Kremer, and A. P. Sokolov. “Ion transport and structural dynamics in homologous ammonium and phosphonium-based room temperature ionic liquids”. In: *J. Chem. Phys.* 142.8 (2015), p. 084501.
- [96] T. Cosby, Z. Vicars, E. U. Mapesa, K. Tsunashima, and J. Sangoro. “Charge transport and dipolar relaxations in phosphonium-based ionic liquids”. In: *J. Chem. Phys.* 147.23 (2017), p. 234504.
- [97] K. Funke, M. Mutke, A. Šantić, R. D. Banhatti, and W. Wrobel. “Broadband Conductivities and Fluidities of Fragile Ionic Liquids”. In: *Electrochemistry* 77.8 (2009), pp. 573–581.
- [98] T. Cosby, Z. Vicars, Y. Wang, and J. Sangoro. “Dynamic-Mechanical and Dielectric Evidence of Long-Lived Mesoscale Organization in Ionic Liquids”. In: *The J. Phys. Chem. Lett.* 8.15 (2017), pp. 3544–3548.
- [99] J. Sangoro, A. Serghei, S. Naumov, P. Galvosas, J. Kärger, C. Wespe, F. Bordusa, and F. Kremer. “Charge transport and mass transport in imidazolium-based ionic liquids”. In: *Phys. Rev. E* 77.5 (2008), p. 051202.

- [100] J. Sangoro, C. Jacob, S. Naumov, R. Valiullin, H. Rexhausen, J. Hunger, R. Buchner, V. Strehmel, J. Kärger, and F. Kremer. “Diffusion in ionic liquids: the interplay between molecular structure and dynamics”. In: *Soft Matter* 7.5 (2011), pp. 1678–1681.
- [101] J. R. Sangoro and F. Kremer. “Charge transport and glassy dynamics in ionic liquids”. In: *Acc. Chem. Res.* 45.4 (2012), pp. 525–532.
- [102] E. W. Stacy, C. P. Gainaru, M. Gobet, Z. Wojnarowska, V. Bocharova, S. G. Greenbaum, and A. P. Sokolov. “Fundamental Limitations of Ionic Conductivity in Polymerized Ionic Liquids”. In: *Macromolecules* 51.21 (2018), pp. 8637–8645.
- [103] H. Tokuda, K. Hayamizu, K. Ishii, M. A. B. H. Susan, and M. Watanabe. “Physicochemical properties and structures of room temperature ionic liquids. 2. Variation of alkyl chain length in imidazolium cation”. In: *J. Phys. Chem. B* 109.13 (2005), pp. 6103–6110.
- [104] R. Markiewicz, A. Klimaszyk, M. Jarek, M. Taube, P. Florczak, M. Kempka, Z. Fojud, and S. Jurga. “Influence of Alkyl Chain Length on Thermal Properties, Structure, and Self-Diffusion Coefficients of Alkyltriethylammonium-Based Ionic Liquids”. In: *Int. J. Mol. Sci.* 22.11 (2021), p. 5935.
- [105] T. Cosby, Z. Vicars, M. Heres, K. Tsunashima, and J. Sangoro. “Dynamic and structural evidence of mesoscopic aggregation in phosphonium ionic liquids”. In: *J. Chem. Phys.* 148.19 (2018), p. 193815.
- [106] P. J. Griffin, A. P. Holt, Y. Wang, V. N. Novikov, J. R. Sangoro, F. Kremer, and A. P. Sokolov. “Interplay between hydrophobic aggregation and charge transport in the ionic liquid methyltriocetylammonium bis (trifluoromethylsulfonyl) imide”. In: *J. Phys. Chem. B* 118.3 (2014), pp. 783–790.
- [107] P. J. Griffin, Y. Wang, A. P. Holt, and A. P. Sokolov. “Communication: Influence of nanophase segregation on ion transport in room temperature ionic liquids”. In: *J. Chem. Phys.* 144 (2016), p. 151104.
- [108] D. A. Turton, J. Hunger, A. Stoppa, G. Hefter, A. Thoman, M. Walther, R. Buchner, and K. Wynne. “Dynamics of imidazolium ionic liquids from a combined dielectric relaxation and optical Kerr effect study: evidence for mesoscopic aggregation”. In: *J. Am. Chem. Soc.* 131.31 (2009), pp. 11140–11146.
- [109] J. Jacquemin, P. Husson, A. A. Padua, and V. Majer. “Density and viscosity of several pure and water-saturated ionic liquids”. In: *Green Chem.* 8.2 (2006), pp. 172–180.
- [110] P. Sippel, V. Dietrich, D. Reuter, M. Aumüller, P. Lunkenheimer, A. Loidl, and S. Krohns. “Impact of water on the charge transport of a glass-forming ionic liquid”. In: *J. Mol. Liq.* 223 (2016), pp. 635–642.
- [111] O. Palumbo, F. Trequattrini, J.-B. Brubach, P. Roy, and A. Paolone. “Crystallization of mixtures of hydrophilic ionic liquids and water: Evidence of microscopic inhomogeneities”. In: *J. Colloid Interface Sci.* 552 (2019), pp. 43–50.
- [112] J. Vila, P. Gines, E. Rilo, O. Cabeza, and L. Varela. “Great increase of the electrical conductivity of ionic liquids in aqueous solutions”. In: *Fluid Phase Equilibr.* 247.1-2 (2006), pp. 32–39.

- [113] U. Schröder, J. D. Wadhawan, R. G. Compton, F. Marken, P. A. Suarez, C. S. Consorti, R. F. de Souza, and J. Dupont. “Water-induced accelerated ion diffusion: voltammetric studies in 1-methyl-3-[2, 6-(S)-dimethylocten-2-yl] imidazolium tetrafluoroborate, 1-butyl-3-methylimidazolium tetrafluoroborate and hexafluorophosphate ionic liquids”. In: *New J. Chem.* 24.12 (2000), pp. 1009–1015.
- [114] A. Stoppa, J. Hunger, and R. Buchner. “Conductivities of binary mixtures of ionic liquids with polar solvents”. In: *J. Chem. Eng. Data* 54.2 (2009), pp. 472–479.
- [115] M. Koeberg, C.-C. Wu, D. Kim, and M. Bonn. “THz dielectric relaxation of ionic liquid: water mixtures”. In: *Chem. Phys. Lett.* 439.1-3 (2007), pp. 60–64.
- [116] C. Schröder, J. Hunger, A. Stoppa, R. Buchner, and O. Steinhauser. “On the collective network of ionic liquid/water mixtures. II. Decomposition and interpretation of dielectric spectra”. In: *J. Chem. Phys.* 129.18 (2008), p. 184501.
- [117] H. Abe, T. Takekiyo, M. Shigemi, Y. Yoshimura, S. Tsuge, T. Hanasaki, K. Ohishi, S. Takata, and J.-i. Suzuki. “Direct evidence of confined water in room-temperature ionic liquids by complementary use of small-angle X-ray and neutron scattering”. In: *J. Phys. Chem. Lett.* 5.7 (2014), pp. 1175–1180.
- [118] J. Gao and N. J. Wagner. “Water nanocluster formation in the ionic liquid 1-Butyl-3-Methylimidazolium Tetrafluoroborate ($[C_4mim][BF_4]$)–D₂O mixtures”. In: *Langmuir* 32.20 (2016), pp. 5078–5084.
- [119] B. Fazio, A. Triolo, and G. Di Marco. “Local organization of water and its effect on the structural heterogeneities in room-temperature ionic liquid/H₂O mixtures”. In: *J. Raman Spectrosc.* 39.2 (2008), pp. 233–237.
- [120] J. Kausteklis, M. Talaikis, V. Alekša, and V. Balevičius. “Raman spectroscopy study of water confinement in ionic liquid 1-butyl-3-methylimidazolium nitrate”. In: *J. Mol. Liq.* 271 (2018), pp. 747–755.
- [121] K. Saihara, Y. Yoshimura, S. Ohta, and A. Shimizu. “Properties of water confined in ionic liquids”. In: *Sci. Rep.* 5.1 (2015), pp. 1–10.
- [122] M. H. Kowsari and S. M. Torabi. “Molecular Dynamics Insights into the Nanoscale Structural Organization and Local Interaction of Aqueous Solutions of Ionic Liquid 1-Butyl-3-methylimidazolium Nitrate”. In: *J. Phys. Chem. B* 124.32 (2020), pp. 6972–6985.
- [123] A. Verma, J. P. Stoppelman, and J. G. McDaniel. “Tuning Water Networks via Ionic Liquid/Water Mixtures”. In: *Int. J. Mol. Sci.* 21.2 (2020), p. 403.
- [124] M. Zhao, B. Wu, and E. W. Castner Jr. “Mixtures of octanol and an ionic liquid: Structure and transport”. In: *J. Chem. Phys.* 153.21 (2020), p. 214501.
- [125] T. Mendez-Morales, J. Carrete, M. Garcia, O. Cabeza, L. J. Gallego, and L. M. Varela. “Dynamical properties of alcohol+ 1-hexyl-3-methylimidazolium ionic liquid mixtures: a computer simulation study”. In: *J. Phys. Chem. B* 115.51 (2011), pp. 15313–15322.

- [126] A. Ordikhani Seyedlar, J. P. d. A. Martins, P. J. Sebastião, M. J. Jardim Beira, S. Stapf, F. Vaca Chavez, and C. Mattea. “Dynamics of binary mixtures of an ionic liquid and ethanol by NMR”. In: *Magn- Reson. Chem.* 56.2 (2018), pp. 108–112.
- [127] T. Carvalho, V. Augusto, A. R. Bras, N. M. Lourenço, C. Afonso, S. Barreiros, N. Correia, P. Vidinha, E. J. Cabrita, C. J. Dias, et al. “Understanding the ion jelly conductivity mechanism”. In: *J. Phys. Chem. B* 116.9 (2012), pp. 2664–2676.
- [128] R. Leones, F. Sentanin, L. C. Rodrigues, R. A. Ferreira, I. M. Marrucho, J. M. Esperança, A. Pawlicka, L. D. Carlos, and M. M. Silva. “Novel polymer electrolytes based on gelatin and ionic liquids”. In: *Opt.* 35.2 (2012), pp. 187–195.
- [129] T. Carvalho, P. Vidinha, B. R. Vieira, R. W. Li, and J. Gruber. “Ion Jelly: a novel sensing material for gas sensors and electronic noses”. In: *J. Mater. Chem. C* 2.4 (2014), pp. 696–700.
- [130] R. M. Couto, T. Carvalho, L. A. Neves, R. M. Ruivo, P. Vidinha, A. Paiva, I. M. Coelhoso, S. Barreiros, and P. C. Simões. “Development of ion-jelly® membranes”. In: *Sep. Purif. Technol.* 106 (2013), pp. 22–31.
- [131] N. Lourenço, A. Nunes, C. Duarte, and P. Vidinha. “Ionic liquids gelation with polymeric materials: The ion jelly approach”. In: *Applications of Ionic Liquids in Science and Technology* (2011), pp. 155–172.
- [132] S. A. M. Noor, P. Bayley, M. Forsyth, and D. R. Macfarlane. “Ionogels based on ionic liquids as potential highly conductive solid state electrolytes”. In: *Electrochim. acta* 91 (2013), pp. 219–226.
- [133] P. Vidinha, N. M. Lourenço, C. Pinheiro, A. R. Bras, T. Carvalho, T. Santos-Silva, A. Mukhopadhyay, M. J. Romao, J. Parola, M. Dionisio, et al. “Ion jelly: a tailor-made conducting material for smart electrochemical devices”. In: *ChemComm* 44 (2008), pp. 5842–5844.
- [134] T. Carvalho, V. Augusto, A. Rocha, N. M. Lourenço, N. T. Correia, S. Barreiros, P. Vidinha, E. J. Cabrita, and M. Dionisio. “Ion jelly conductive properties using dicyanamide-based ionic liquids”. In: *J. Phys. Chem. B* 118.31 (2014), pp. 9445–9459.
- [135] R. Carvalho, S. Matias, N. Lourenço, and L. Fonseca. “SEM characterization of gelatin-ionic liquid functional polymers”. In: *Microsc. Microanal.* 19.S4 (2013), pp. 137–138.
- [136] J. W. Strutt. “XV. On the light from the sky, its polarization and colour”. In: *Lond. Edinb. Dublin Philos. Mag. J. Sci.* 41.271 (1871), pp. 107–120.
- [137] L. Rayleigh. “XXXIV. On the transmission of light through an atmosphere containing small particles in suspension, and on the origin of the blue of the sky”. In: *Lond. Edinb. Dublin Philos. Mag. J. Sci.* 47.287 (1899), pp. 375–384.
- [138] R. J. Strutt. “The light scattered by gases: its polarisation and intensity”. In: *Proc. R. Soc. Lond. A* 95.667 (1918), pp. 155–176.
- [139] R. Gans. “Asymmetrie von Gasmolekülen. Ein Beitrag zur Bestimmung der molekularen Form”. In: *Ann. Phys.* 370.10 (1921), pp. 97–123.

- [140] M. v. Smoluchowski. "Molekular-kinetische Theorie der Opaleszenz von Gasen im kritischen Zustande, sowie einiger verwandter Erscheinungen". In: *Ann. Phys.* 330.2 (1908), pp. 205–226.
- [141] A. Einstein. "Theorie der Opaleszenz von homogenen Flüssigkeiten und Flüssigkeitsgemischen in der Nähe des kritischen Zustandes". In: *Ann. Phys.* 338.16 (1910), pp. 1275–1298.
- [142] L. Brillouin. "Diffusion de la lumière et des rayons X par un corps transparent homogène". In: 9.17 (1922), pp. 88–122.
- [143] E. Gross. "Change of wave-length of light due to elastic heat waves at scattering in liquids". In: *Nature* 126.3171 (1930), pp. 201–202.
- [144] A. Smekal. "Zur quantentheorie der dispersion". In: *Naturwissenschaften* 11.43 (1923), pp. 873–875.
- [145] C. V. Raman. "A new radiation". In: *Indian J. Phys.* 2 (1928), pp. 387–398.
- [146] G. Landsberg. "Eine neue Erscheinung bei der Lichtzerstreuung in Krystallen". In: *Naturwissenschaften* 16 (1928), p. 558.
- [147] E. L. Feinberg. "The forefather (about Leonid Isaakovich Mandelstam)". In: *Physics-Uspekhi* 45.1 (2002), p. 81.
- [148] J. Cabannes and P. Daure. "Analyse spectroscopique de la lumière obtenue par diffusion moléculaire d'une radiation monochromatique au sein d'un fluide". In: *CR Acad. Sci., Paris* 186 (1928), p. 1533.
- [149] C. Raman and K. Krishnan. "Molecular spectra in the extreme infra-red". In: *Nature* 122.3069 (1928), pp. 278–278.
- [150] C. Raman and K. Krishnan. "Rotation of molecules induced by light". In: *Nature* 122.3084 (1928), pp. 882–882.
- [151] E. Gross and M. Vuks. "Quasi-Crystalline Structure of Liquids and the Raman Effect". In: *Nature* 135.3403 (1935), pp. 100–101.
- [152] I. L. Fabelinskii. *Molecular scattering of light*. Springer Science & Business Media, 2012.
- [153] L. Landau and G. Placzek. "Structure of the undisplaced scattering line". In: *Phys. Z. Sowiet. Un* 5 (1934), p. 172.
- [154] A. Patkowski, W. Steffen, H. Nilgens, E. W. Fischer, and R. Pecora. "Depolarized dynamic light scattering from three low molecular weight glass forming liquids: A test of the scattering mechanism". In: *J. Chem. Phys.* 106.20 (1997), pp. 8401–8408.
- [155] B. Berne and R. Pecora. *Dynamic Light Scattering: With Applications to Chemistry, Biology, and Physics*. Dover Books on Physics Series. Dover Publications, 1976. ISBN: 9780486411552.
- [156] R. Finsy. "Particle sizing by quasi-elastic light scattering". In: *Adv. Colloid Interface Sci.* 52 (1994), pp. 79–143.
- [157] K. Fischer and M. Schmidt. "Pitfalls and novel applications of particle sizing by dynamic light scattering". In: *Biomaterials* 98 (2016), pp. 79–91.

- [158] M. M. Marsilius. "Aufbau einer Lichtstreu-anlage zur Untersuchung der Dynamik niedermolekularer Glasbildner am Beispiel Propylen Carbonat und Oligo(methylmethacrylat)". Diplomarbeit. Technische Universität Darmstadt, 2007.
- [159] J. Gabriel. "Depolarisierte dynamische Lichtstreuung an Monohydroxy-Alkoholen". PhD thesis. Technische Universität Darmstadt, 2018.
- [160] A. Siegert. "On the fluctuations in signals returned by many independently moving scatterers". In: (1943).
- [161] P. Pusey and W. Van Megen. "Dynamic light scattering by non-ergodic media". In: *Phys. A: Stat. Mech. Appl.* 157.2 (1989), pp. 705–741.
- [162] L. G. Bremer, L. Deriemaeker, R. Finsy, E. Gelade, and J. G. Joosten. "Fiber optic dynamic light scattering, neither homodyne nor heterodyne". In: *Langmuir* 9.8 (1993), pp. 2008–2014.
- [163] T. Blochowicz, E. Gouirand, S. Schramm, and B. Stühn. "Density and confinement effects of glass forming m-toluidine in nanoporous Vycor investigated by depolarized dynamic light scattering". In: *J. Chem. Phys.* 138.11 (2013), p. 114501.
- [164] L. N. G. Filon. "On a quadrature formula for trigonometric integrals". In: *Proc. Roy. Soc. Edinburgh* 49.1 (1928), pp. 38–47.
- [165] S. Lindsay, M. Anderson, and J. Sandercock. "Construction and alignment of a high performance multipass vernier tandem Fabry–Perot interferometer". In: *Rev. Sci. Instrum.* 52.10 (1981), pp. 1478–1486.
- [166] *TANDEM FABRY-PEROT INTERFEROMETER TFP-1*. JRS Scientific Instruments, 1998.
- [167] N. Surovtsev, J. Wiedersich, V. Novikov, E. Rössler, and A. Sokolov. "Light-scattering spectra of fast relaxation in glasses". In: *Phys. Rev. B* 58.22 (1998), p. 14888.
- [168] H. Barshilia, G. Li, G. Shen, and H. Cummins. "Depolarized light scattering spectroscopy of $\text{Ca}_{0.4}\text{K}_{0.6}(\text{NO}_3)_{1.4}$: A reexamination of the "knee"". In: *Phys. Rev. E* 59.5 (1999), p. 5625.
- [169] J. Gapiński, W. Steffen, A. Patkowski, A. Sokolov, A. Kisliuk, U. Buchenau, M. Russina, F. Mezei, and H. Schober. "Spectrum of fast dynamics in glass forming liquids: Does the knee exist?" In: *J. Chem. Phys.* 110.5 (1999), pp. 2312–2315.
- [170] R. Kubo. "Statistical-mechanical theory of irreversible processes. I. General theory and simple applications to magnetic and conduction problems". In: *J. Phys. Soc. Japan* 12.6 (1957), pp. 570–586.
- [171] H. B. Callen and T. A. Welton. "Irreversibility and generalized noise". In: *Phys. Rev.* 83.1 (1951), p. 34.
- [172] A. Brodin and E. A. Rössler. "Depolarized light scattering study of glycerol". In: *Eur. Phys. J. B-Condensed Matter and Complex Systems* 44.1 (2005), pp. 3–14.
- [173] R. N. Favors, Y. Jiang, Y. L. Loethen, and D. Ben-Amotz. "External Raman standard for absolute intensity and concentration measurements". In: *Rev. Sci. Instrum.* 76.3 (2005), p. 033108.

- [174] ASTM International West Conshohocken. “Standard guide for Raman shift standards for spectrometer calibration, ASTM E1840–96”. In: (2014).
- [175] C. Böttcher, O. van Belle, P. Bordewijk, and A. Rip. *Theory of electric polarization*. Vol. 1. Elsevier Scientific Pub. Co., 1978.
- [176] C. Böttcher, O. van Belle, P. Bordewijk, and A. Rip. *Theory of electric polarization*. Vol. 2. Elsevier Scientific Pub. Co., 1978.
- [177] F. Kremer and A. Schönhals, eds. *Broadband Dielectric Spectroscopy*. 2003rd ed. Springer, 2002. ISBN: 9783540434078.
- [178] G. Williams, M. Cook, and P. Hains. “Molecular motion in amorphous polymers. Consideration of the mechanism for α , β and $(\alpha\beta)$ dielectric relaxations”. In: *J. Chem. Soc. Faraday Trans.* 68 (1972), pp. 1045–1050.
- [179] J. Gabriel, F. Pabst, A. Helbling, T. Böhmer, and T. Blochowicz. “Depolarized Dynamic Light Scattering and Dielectric Spectroscopy: Two Perspectives on Molecular Reorientation in Supercooled Liquids”. In: *The Scaling of Relaxation Processes*. Springer, 2018, pp. 203–245.
- [180] G. Diezemann, H. Sillescu, G. Hinze, and R. Böhmer. “Rotational correlation functions and apparently enhanced translational diffusion in a free-energy landscape model for the α relaxation in glass-forming liquids”. In: *Phys. Rev. E* 57.4 (1998), p. 4398.
- [181] T. Blochowicz, A. Kudlik, S. Benkhof, J. Senker, E. Rössler, and G. Hinze. “The spectral density in simple organic glassformers: Comparison of dielectric and spin-lattice relaxation”. In: *J. Chem. Phys.* 110.24 (1999), pp. 12011–12022.
- [182] A. Brodin, R. Bergman, J. Mattsson, and E. Rössler. “Light scattering and dielectric manifestations of secondary relaxations in molecular glassformers”. In: *Eur. Phys. J. B-Condensed Matter and Complex Systems* 36.3 (2003), pp. 349–357.
- [183] M. Lebon, C. Dreyfus, Y. Guissani, R. Pick, and H. Cummins. “Light scattering and dielectric susceptibility spectra of glassforming liquids”. In: *Z. Phys. B* 103.3 (1997), pp. 433–439.
- [184] S. Gaisford, V. Kett, and P. Haines. *Principles of thermal analysis and calorimetry*. Royal society of chemistry, 2019.
- [185] P. G. Debenedetti and F. H. Stillinger. “Supercooled liquids and the glass transition”. In: *Nature* 410.6825 (2001), pp. 259–267.
- [186] Z. Wojnarowska, Y. Wang, J. Pionteck, K. Grzybowska, A. Sokolov, and M. Paluch. “High pressure as a key factor to identify the conductivity mechanism in protic ionic liquids”. In: *Phys. Rev. Lett.* 111.22 (2013), p. 225703.
- [187] I. M. Hodge. “Enthalpy relaxation and recovery in amorphous materials”. In: *J. Non-Cryst. Solids* 169.3 (1994), pp. 211–266.
- [188] F. Pabst, J. Gabriel, and T. Blochowicz. “Mesoscale Aggregates and Dynamic Asymmetry in Ionic Liquids: Evidence from Depolarized Dynamic Light Scattering”. In: *J. Phys. Chem. Lett.* 10.9 (2019), pp. 2130–2134.

- [189] T. Wu, X. Jin, M. K. Saini, Y. D. Liu, K. Ngai, and L.-M. Wang. “Presence of global and local α -relaxations in an alkyl phosphate glass former”. In: *J. Chem. Phys.* 147.13 (2017), p. 134501.
- [190] A. Q. Tool. “Relation between inelastic deformability and thermal expansion of glass in its annealing range”. In: *J. Am. Ceram. Soc.* 29.9 (1946), pp. 240–253.
- [191] C. Moynihan, P. Macedo, C. Montrose, C. Montrose, P. Gupta, M. DeBolt, J. Dill, B. Dom, P. Drake, A. Easteal, et al. “Structural relaxation in vitreous materials”. In: *Ann. N. Y. Acad. Sci.* 279.1 (1976), pp. 15–35.
- [192] O. Narayanaswamy. “A model of structural relaxation in glass”. In: *J. Am. Ceram. Soc.* 54.10 (1971), pp. 491–498.
- [193] I. M. Hodge and A. R. Berens. “Effects of annealing and prior history on enthalpy relaxation in glassy polymers. 2. Mathematical modeling”. In: *Macromolecules* 15.3 (1982), pp. 762–770.
- [194] C. T. Moynihan, A. J. Easteal, M. A. De BOLT, and J. Tucker. “Dependence of the fictive temperature of glass on cooling rate”. In: *J. Am. Ceram. Soc.* 59.1-2 (1976), pp. 12–16.
- [195] J. Hutchinson. “Determination of the glass transition temperature: methods correlation and structural heterogeneity”. In: *J. Therm. Anal. Calorim.* 98.3 (2009), pp. 579–589.
- [196] F. Neese. “The ORCA program system”. In: *Wiley Interdiscip. Rev. Comput. Mol. Sci.* 2.1 (2012), pp. 73–78.
- [197] F. Neese. “Software update: the ORCA program system, version 4.0”. In: *Wiley Interdiscip. Rev. Comput. Mol. Sci.* 8.1 (2018), e1327.
- [198] W. Koch and M. C. Holthausen. *A chemist’s guide to density functional theory*. John Wiley & Sons, 2015.
- [199] F. Weigend and R. Ahlrichs. “Balanced basis sets of split valence, triple zeta valence and quadruple zeta valence quality for H to Rn: Design and assessment of accuracy”. In: *Phys. Chem. Chem. Phys.* 7.18 (2005), pp. 3297–3305.
- [200] M. D. Hanwell, D. E. Curtis, D. C. Lonie, T. Vandermeersch, E. Zurek, and G. R. Hutchinson. “Avogadro: an advanced semantic chemical editor, visualization, and analysis platform”. In: *J. Cheminformatics* 4.1 (2012), pp. 1–17.
- [201] C. Bannwarth, S. Ehlert, and S. Grimme. “GFN2-xTB - An accurate and broadly parametrized self-consistent tight-binding quantum chemical method with multipole electrostatics and density-dependent dispersion contributions”. In: *J. Chem. Theory Comput.* 15.3 (2019), pp. 1652–1671.
- [202] P. Pracht, F. Bohle, and S. Grimme. “Automated exploration of the low-energy chemical space with fast quantum chemical methods”. In: *Phys. Chem. Chem. Phys.* 22.14 (2020), pp. 7169–7192.
- [203] M. Paluch, J. Knapik, Z. Wojnarowska, A. Grzybowski, and K. Ngai. “Universal behavior of dielectric responses of glass formers: role of dipole-dipole interactions”. In: *Phys. Rev. Lett.* 116.2 (2016), p. 025702.

- [204] M. Born. “Über die Zerstreuung des Lichtes in H₂, O₂ und N₂”. In: *Verh. Dtsch. Phys. Ges.* 20 (1918), pp. 16–32.
- [205] M. Kerker. *The scattering of light and other electromagnetic radiation: physical chemistry: a series of monographs*. Vol. 16. Academic press, 2013.
- [206] A. D. McNaught, A. Wilkinson, et al. *Compendium of chemical terminology*. Vol. 1669. Blackwell Science Oxford, 1997.
- [207] G. Floudas, A. Patkowski, G. Fytas, and M. Ballauff. “Optical anisotropies of nematogens from the depolarized Rayleigh spectra”. In: *J. Phys. Chem.* 94.7 (1990), pp. 3215–3219.
- [208] A. Burnham, G. Alms, and W. Flygare. “The local electric field. I. The effect on isotropic and anisotropic Rayleigh scattering”. In: *J. Chem. Phys.* 62.8 (1975), pp. 3289–3297.
- [209] H. Lorentz. *Theory of Electrons, 2nd edn.* (1915). Dover, New York, 1952.
- [210] D. Coumou, J. Hijmans, and E. Mackor. “Anisotropic light-scattering in pure liquids and in liquid mixtures”. In: *Trans. Faraday Soc.* 60 (1964), pp. 2244–2253.
- [211] D. Coumou. “Light scattering in pure liquids and the polarizability tensor of the molecules”. In: *Trans. Faraday Soc.* 65 (1969), pp. 2654–2662.
- [212] T. Keyes and B. M. Ladanyi. “The internal field problem in depolarized light scattering”. In: *Adv. Chem. Phys.* 56 (1984), pp. 411–465.
- [213] M. R. Battaglia, T. I. Cox, and P. A. Madden. “The orientational correlation parameter for liquid CS₂, C₆H₆ and C₆F₆”. In: *Mol. Phys.* 37.5 (1979), pp. 1413–1427.
- [214] J. McTague, P. Fleury, and D. DuPre. “Intermolecular light scattering in liquids”. In: *Phys. Rev.* 188.1 (1969), p. 303.
- [215] J. McTague and G. Birnbaum. “Collision-induced light scattering in gaseous Ar and Kr”. In: *Phys. Rev. Lett.* 21.10 (1968), p. 661.
- [216] S. Kielich. “Role of molecular interaction in anisotropic light scattering by liquids”. In: *J. Chem. Phys.* 46.10 (1967), pp. 4090–4099.
- [217] H. B. Levine and G. Birnbaum. “Collision-induced light scattering”. In: *Phys. Rev. Lett.* 20.9 (1968), p. 439.
- [218] G. Patterson and P. Flory. “Depolarized rayleigh scattering and the mean-squared optical anisotropies of n-alkanes in solution”. In: *J. Chem. Soc. Faraday Trans. 2* 68 (1972), pp. 1098–1110.
- [219] U. W. Suter and P. J. Flory. “Optical anisotropy of polystyrene and its low molecular analogues”. In: *J. Chem. Soc. Faraday Trans. 2* 73.7 (1977), pp. 1521–1537.
- [220] C. W. Carlson and P. J. Flory. “Separation of collision-induced from intrinsic molecular depolarized Rayleigh scattering optical anisotropy of the C-Cl bond”. In: *J. Chem. Soc. Faraday Trans. 2* 73.7 (1977), pp. 1505–1520.
- [221] J. G. Kirkwood. “The dielectric polarization of polar liquids”. In: *J. Chem. Phys.* 7.10 (1939), pp. 911–919.

- [222] P. J. Flory and P. Navard. “Optical anisotropies of alkylcyanobiphenyls, alkoxycyanobiphenyls and related compounds”. In: *J. Chem. Soc. Faraday Trans. 1* 82.11 (1986), pp. 3381–3390.
- [223] P. Navard and P. J. Flory. “Optical anisotropies of alkylcyanobicyclohexyls and related compounds”. In: *J. Chem. Soc. Faraday Trans. 1* 82.11 (1986), pp. 3367–3380.
- [224] E. Saiz, U. W. Suter, and P. J. Flory. “Optical anisotropies of para-halogenated polystyrenes and related molecules”. In: *J. Chem. Soc. Faraday Trans. 2* 73.7 (1977), pp. 1538–1552.
- [225] A. Unanué and P. Bothorel. “Étude de la structure électronique de molécules aromatiques substituées par diffusion Rayleigh dépolarisée”. In: *Bull. Soc. Chim. Fr.* 30 (1964), pp. 573–578.
- [226] A. Unanué and P. Bothorel. “Détermination des conformations du diphenyle et de quelques dérivés substitués par Diffusion Rayleigh Dépolarisée”. In: *Bull. Soc. Chim. Fr.* (1966), pp. 1640–1643.
- [227] C. Clément and P. Bothorel. “Étude de l'anisotropie optique moléculaire d' alcanes normaux, ramifiés et halogénés. Effet de solvant”. In: *J. Chim. Phys.* 61 (1964), pp. 878–883.
- [228] H. Wahid. “Role of molecular interaction in anisotropic Rayleigh scattering by pure liquids”. In: *J. Mol. Liq.* 55 (1993), pp. 19–34.
- [229] H. Wahid. “Measurements of anisotropic Rayleigh scattering of some pure liquids”. In: *J. Mol. Liq.* 51.3-4 (1992), pp. 219–230.
- [230] H. Wahid. “Molecular scattering of light in pure liquids”. In: *J. Opt.* 26.3 (1995), p. 109.
- [231] P. Bothorel, A. Unanué, C. Gardere, N. Buu-Hoi, P. Jacquignon, and F. Périn. “Anisotropie optique moléculaire et activité cancérogène de composés aromatiques azotés”. In: *Bull. Soc. Chim. Fr.* (1966), pp. 2920–1923.
- [232] T. Lavy, D. Harries, and A. Goldblum. “Molecular Properties from Conformational Ensembles. 1. Dipole Moments of Molecules with Multiple Internal Rotations”. In: *J. Phys. Chem. A* 115.23 (2011), pp. 5794–5809.
- [233] D. M. Hewett, S. Bocklitz, D. P. Tabor, E. L. Sibert III, M. A. Suhm, and T. S. Zwier. “Identifying the first folded alkylbenzene via ultraviolet, infrared, and Raman spectroscopy of pentylbenzene through decylbenzene”. In: *Chem. Sci.* 8.8 (2017), pp. 5305–5318.
- [234] A. Unanué and P. Bothorel. “Détermination des configurations de molécules polyphénoliques en solution par Diffusion Rayleigh Dépolarisée”. In: *Bull. Soc. Chim. Fr.* (1965), pp. 2827–2832.
- [235] K. Takahashi, A. Takano, S. Kinugasa, and H. Sakurai. “Determination of the Rayleigh Ratio with an Uncertainty Analysis by Static Light Scattering Measurements of Certified Reference Materials for Molecular Weight”. In: *Anal. Sci.* (2019), 19P103.
- [236] E. Pike, W. Pomeroy, and J. Vaughan. “Measurement of Rayleigh ratio for several pure liquids using a laser and monitored photon counting”. In: *J. Chem. Phys.* 62.8 (1975), pp. 3188–3192.

- [237] S. Eibl. "The highly fragile glass former decalin". PhD thesis. Université de Paris-Sud - Centre d'Orsay, 2009.
- [238] R. L. Schmidt. "Temperature dependence of rayleigh light scattering and depolarization in pure liquids". In: *J. Colloid Interface Sci.* 27.3 (1968), pp. 516–528.
- [239] A. J. Farrell, M. González-Jiménez, G. Ramakrishnan, and K. Wynne. "Low-frequency (gigahertz to terahertz) depolarized Raman scattering off n-alkanes, cycloalkanes, and six-membered rings: a physical interpretation". In: *J. Phys. Chem. B* 124.35 (2020), pp. 7611–7624.
- [240] T. Blochowicz, S. Lusceac, P. Gutfreund, S. Schramm, and B. Stuhn. "Two glass transitions and secondary relaxations of methyltetrahydrofuran in a binary mixture". In: *J. Phys. Chem. B* 115.7 (2011), pp. 1623–1637.
- [241] R. Kahlau, D. Bock, B. Schmidtke, and E. Rössler. "Dynamics of asymmetric binary glass formers. I. A dielectric and nuclear magnetic resonance spectroscopy study". In: *J. Chem. Phys.* 140.4 (2014), p. 044509.
- [242] T. Blochowicz, S. Schramm, S. Lusceac, M. Vogel, B. Stühn, P. Gutfreund, and B. Frick. "Signature of a type-a glass transition and intrinsic confinement effects in a binary glass-forming system". In: *Phys. Rev. Lett.* 109.3 (2012), p. 035702.
- [243] T. Böhmer, R. Horstmann, J. P. Gabriel, F. Pabst, M. Vogel, and T. Blochowicz. "Origin of Apparent Slow Solvent Dynamics in Concentrated Polymer Solutions". In: *Macromolecules* 54.22 (2021), pp. 10340–10349.
- [244] R. Böhmer, K. Ngai, C. A. Angell, and D. Plazek. "Nonexponential relaxations in strong and fragile glass formers". In: *J. Chem. Phys.* 99.5 (1993), pp. 4201–4209.
- [245] J. C. Dyre. "Ten themes of viscous liquid dynamics". In: *J. Phys. Condens. Matter* 19.20 (2007), p. 205105.
- [246] P. K. Gupta and J. C. Mauro. "Two factors governing fragility: Stretching exponent and configurational entropy". In: *Phys. Rev. E* 78.6 (2008), p. 062501.
- [247] K. Ngai. "Relation between some secondary relaxations and the α relaxations in glass-forming materials according to the coupling model". In: *J. Chem. Phys.* 109.16 (1998), pp. 6982–6994.
- [248] P. Bordat, F. Affouard, M. Descamps, and K. Ngai. "Does the interaction potential determine both the fragility of a liquid and the vibrational properties of its glassy state?" In: *Phys. rev. lett.* 93.10 (2004), p. 105502.
- [249] D. M. Petkovic, B. Kezele, and D. Rajic. "Dipole moments of some neutral organic phosphates". In: *J. Phys. Chem.* 77.7 (1973), pp. 922–924.
- [250] T. S. Ingebrigtsen, T. B. Schrøder, and J. C. Dyre. "What is a simple liquid?" In: *Phys. Rev. X* 2.1 (2012), p. 011011.
- [251] M. H. Jensen, C. Gainaru, C. Alba-Simionescu, T. Hecksher, and K. Niss. "Slow rheological mode in glycerol and glycerol–water mixtures". In: *Phys. Chem. Chem. Phys.* 20.3 (2018), pp. 1716–1723.

- [252] F. Pabst, J. P. Gabriel, T. Böhmer, P. Weigl, A. Helbling, T. Richter, P. Zourchang, T. Walther, and T. Blochowicz. “Generic Structural Relaxation in Supercooled Liquids”. In: *J. Phys. Chem. Lett.* 12.14 (2021), pp. 3685–3690.
- [253] F. Pabst, A. Helbling, J. Gabriel, P. Weigl, and T. Blochowicz. “Dipole-dipole correlations and the Debye process in the dielectric response of nonassociating glass forming liquids”. In: *Phys. Rev. E* 102.1 (2020), p. 010606.
- [254] T. Blochowicz, C. Tschirwitz, S. Benkhof, and E. Rössler. “Susceptibility functions for slow relaxation processes in supercooled liquids and the search for universal relaxation patterns”. In: *J. Chem. Phys.* 118.16 (2003), pp. 7544–7555.
- [255] J. C. Dyre. “Solidity of viscous liquids. III. α relaxation”. In: *Phys. Rev. E* 72.1 (2005), p. 011501.
- [256] J. C. Dyre. “Solidity of viscous liquids. IV. Density fluctuations”. In: *Phys. Rev. E* 74.2 (2006), p. 021502.
- [257] J. C. Dyre. “Solidity of viscous liquids. V. Long-wavelength dominance of the dynamics”. In: *Phys. Rev. E* 76.4 (2007), p. 041508.
- [258] A. I. Nielsen, T. Christensen, B. Jakobsen, K. Niss, N. B. Olsen, R. Richert, and J. C. Dyre. “Prevalence of approximate t relaxation for the dielectric α process in viscous organic liquids”. In: *J. Chem. Phys.* 130.15 (2009), p. 154508.
- [259] P.-M. Déjardin, S. V. Titov, and Y. Cornaton. “Linear complex susceptibility of long-range interacting dipoles with thermal agitation and weak external ac fields”. In: *Phys. Rev. B* 99.2 (2019), p. 024304.
- [260] B. Jakobsen, K. Niss, and N. B. Olsen. “Dielectric and shear mechanical alpha and beta relaxations in seven glass-forming liquids”. In: *J. Chem. Phys.* 123.23 (2005), p. 234511.
- [261] T. Körber, R. Stäglich, C. Gainaru, R. Böhmer, and E. A. Rössler. “Systematic differences in the relaxation stretching of polar molecular liquids probed by dielectric vs magnetic resonance and photon correlation spectroscopy”. In: *J. Chem. Phys.* 153.12 (2020), p. 124510.
- [262] Z. Wojnarowska and M. Paluch. “Two-step aging of highly polar glass”. In: *J. Phys. Chem. Lett.* 12.49 (2021), pp. 11779–11783.
- [263] M. Becher, T. Körber, A. Döß, G. Hinze, C. Gainaru, R. Böhmer, M. Vogel, and E. Rössler. “Nuclear Spin Relaxation in Viscous Liquids: Relaxation Stretching of Single-Particle Probes”. In: *J. Phys. Chem. B* 125.49 (2021), pp. 13519–13532.
- [264] K. Moch, P. Münzner, R. Böhmer, and C. Gainaru. “Evidence for the Collective Nature of the Glass Transition”. In: *arXiv preprint arXiv:2103.04624* (2021).
- [265] K. Ngai, Z. Wojnarowska, and M. Paluch. “Comparative analysis of dielectric, shear mechanical and light scattering response functions in polar supercooled liquids”. In: *Sci. Rep.* 11.1 (2021), pp. 1–15.

- [266] M. Becher, M. Flämig, and E. Rössler. “Field-cycling ^{31}P and ^1H NMR relaxometry studying the reorientational dynamics of glass forming organophosphates”. In: *J. Chem. Phys.* 156.7 (2022), p. 074502.
- [267] F. Pabst, Z. Wojnarowska, M. Paluch, and T. Blochowicz. “On the temperature and pressure dependence of dielectric relaxation processes in ionic liquids”. In: *Phys. Chem. Chem. Phys.* 23.26 (2021), pp. 14260–14275.
- [268] D. L. Sidebottom, B. Roling, and K. Funke. “Ionic conduction in solids: Comparing conductivity and modulus representations with regard to scaling properties”. In: *Phys. Rev. B* 63.2 (2000), p. 024301.
- [269] J. R. Macdonald. “Comments on the electric modulus formalism model and superior alternatives to it for the analysis of the frequency response of ionic conductors”. In: *J. Phys. Chem. Solids* 70.3-4 (2009), pp. 546–554.
- [270] J. Barton. “Dielectric relaxation of some ternary alkali-alkaline earth-silicate glasses”. In: *Verres Refract* 20.5 (1966), pp. 328–335.
- [271] H. Namikawa. “Characterization of the diffusion process in oxide glasses based on the correlation between electric conduction and dielectric relaxation”. In: *J. Non-Cryst. Solids* 18.2 (1975), pp. 173–195.
- [272] M. Wübbenhurst and J. van Turnhout. “Analysis of complex dielectric spectra. I. One-dimensional derivative techniques and three-dimensional modelling”. In: *J. Non-Cryst. Solids* 305.1-3 (2002), pp. 40–49.
- [273] J. C. Dyre and T. B. Schröder. “Universality of ac conduction in disordered solids”. In: *Rev. Mod. Phys.* 72.3 (2000), p. 873.
- [274] J. C. Dyre. “A simple model of ac hopping conductivity in disordered solids”. In: *Phys. Lett. A* 108.9 (1985), pp. 457–461.
- [275] T. B. Schröder and J. C. Dyre. “Ac hopping conduction at extreme disorder takes place on the percolating cluster”. In: *Phys. Rev. Lett.* 101.2 (2008), p. 025901.
- [276] F. Fan, Y. Wang, T. Hong, M. F. Heres, T. Saito, and A. P. Sokolov. “Ion conduction in polymerized ionic liquids with different pendant groups”. In: *Macromolecules* 48.13 (2015), pp. 4461–4470.
- [277] P. Münzner, L. Hoffmann, R. Böhmer, and C. Gainaru. “Deeply supercooled aqueous LiCl solution studied by frequency-resolved shear rheology”. In: *J. Chem. Phys.* 150.23 (2019), p. 234505.
- [278] K. Funke and R. Banhatti. “Modelling frequency-dependent conductivities and permittivities in the framework of the MIGRATION concept”. In: *Solid State Ion.* 169.1-4 (2004), pp. 1–8.
- [279] M. Mutke. “Dynamik der Ionen in ionischen Flüssigkeiten”. PhD thesis. Westfälische Wilhelms-Universität Münster, 2009.
- [280] K. Funke, R. D. Banhatti, D. M. Laughman, L. G. Badr, M. Mutke, A. Santic, W. Wrobel, E. Fellberg, and C. Biermann. “First and second universalities: Expeditions towards and beyond”. In: *Z. Phys. Chem.* 224.10-12 (2010), pp. 1891–1950.

- [281] C. S. Santos, N. S. Murthy, G. A. Baker, and E. W. Castner Jr. “Communication: X-ray scattering from ionic liquids with pyrrolidinium cations”. In: *J. Chem. Phys.* 134.12 (2011), p. 121101.
- [282] O. Russina, A. Triolo, L. Gontrani, R. Caminiti, D. Xiao, L. G. Hines Jr, R. A. Bartsch, E. L. Quitevis, N. Plechkova, and K. R. Seddon. “Morphology and intermolecular dynamics of 1-alkyl-3-methylimidazolium bis {(trifluoromethane) sulfonyl} amide ionic liquids: structural and dynamic evidence of nanoscale segregation”. In: *J. Phys. Condens. Matter* 21.42 (2009), p. 424121.
- [283] K. Shimizu, A. A. Pdua, and J. N. Canongia Lopes. “Nanostructure of trialkylmethyammonium bistriflamide ionic liquids studied by molecular dynamics”. In: *J. Phys. Chem. B* 114.47 (2010), pp. 15635–15641.
- [284] H. K. Kashyap, C. S. Santos, H. V. Annapureddy, N. S. Murthy, C. J. Margulis, and E. W. Castner Jr. “Temperature-dependent structure of ionic liquids: X-ray scattering and simulations”. In: *Faraday Discuss.* 154 (2012), pp. 133–143.
- [285] O. Russina, F. L. Celso, and A. Triolo. “Pressure-responsive mesoscopic structures in room temperature ionic liquids”. In: *Phys. Chem. Chem. Phys.* 17.44 (2015), pp. 29496–29500.
- [286] Y. Yoshimura, M. Shigemi, M. Takaku, M. Yamamura, T. Takekiyo, H. Abe, N. Hamaya, D. Wakabayashi, K. Nishida, N. Funamori, et al. “Stability of the liquid state of imidazolium-based ionic liquids under high pressure at room temperature”. In: *J. Phys. Chem. B* 119.25 (2015), pp. 8146–8153.
- [287] F. Lo Celso, A. Triolo, L. Gontrani, and O. Russina. “Communication: Anion-specific response of mesoscopic organization in ionic liquids upon pressurization”. In: *J. Chem. Phys.* 148.21 (2018), p. 211102.
- [288] Y. Yoshimura, T. Takekiyo, Y. Koyama, M. Takaku, M. Yamamura, N. Kikuchi, D. Wakabayashi, N. Funamori, K. Matsuishi, H. Abe, et al. “High-pressure glass formation of a series of 1-alkyl-3-methylimidazolium bis (trifluoromethanesulfonyl) imide homologues”. In: *Phys. Chem. Chem. Phys.* 20.1 (2018), pp. 199–205.
- [289] M. Drai, A. Mostefai, A. Paolone, B. Haddad, E. Belarbi, D. Villemin, S. Bresson, O. Abbas, Y. Chaker, and M. Rahmouni. “Synthesis, experimental and theoretical vibrational studies of 1-methyl and 1, 2-dimethyl, 3-propyl imidazolium bis (trifluoromethanesulfonyl) imide”. In: *J. Chem. Sci.* 129.6 (2017), pp. 707–719.
- [290] C. Schröder, T. Rudas, and O. Steinhauser. “Simulation studies of ionic liquids: Orientational correlations and static dielectric properties”. In: *J. Chem. Phys.* 125.24 (2006), p. 244506.
- [291] M. Miller, M. Jimenez-Ruiz, F. J. Bermejo, and N. O. Birge. “Comparison of the structural and orientational glass-transition dynamics in ethanol”. In: *Phys. Rev. B* 57.22 (1998), R13977.
- [292] O. Haida, H. Suga, and S. Seki. “Calorimetric study of the glassy state XII. Plural glass-transition phenomena of ethanol”. In: *J. Chem. Thermodyn.* 9.12 (1977), pp. 1133–1148.

- [293] F. J. Bermejo, A. Criado, R. Fayos, R. Fernández-Perea, H. Fischer, E. Suard, A. Guelylah, and J. Zuniga. “Structural correlations in disordered matter: An experimental separation of orientational and positional contributions”. In: *Phys. Rev. B* 56.18 (1997), p. 11536.
- [294] Z. Chen, L. Zhao, W. Tu, Z. Li, Y. Gao, and L.-M. Wang. “Dependence of calorimetric glass transition profiles on relaxation dynamics in non-polymeric glass formers”. In: *J. Non Cryst. Solids* 433 (2016), pp. 20–27.
- [295] M. J. Pikal, L. L. Chang, and X. C. Tang. “Evaluation of glassy-state dynamics from the width of the glass transition: Results from theoretical simulation of differential scanning calorimetry and comparisons with experiment”. In: *J. Pharm. Sci.* 93.4 (2004), pp. 981–994.
- [296] J. J. Hettige, J. C. Araque, H. K. Kashyap, and C. J. Margulis. “Communication: Nanoscale structure of tetradecyltrihexylphosphonium based ionic liquids”. In: *J. Chem. Phys.* 144.12 (2016), p. 121102.
- [297] Y.-L. Wang, B. Li, S. Sarman, and A. Laaksonen. “Microstructures and dynamics of tetraalkylphosphonium chloride ionic liquids”. In: *J. Chem. Phys.* 147.22 (2017), p. 224502.
- [298] L. Gontrani, O. Russina, F. Lo Celso, R. Caminiti, G. Annat, and A. Triolo. “Liquid structure of trihexyltetradecylphosphonium chloride at ambient temperature: An x-ray scattering and simulation study”. In: *J. Phys. Chem. B* 113.27 (2009), pp. 9235–9240.
- [299] T. K. Kottummal, S. Pilathottathil, M. S. Thayyil, P. M. Perumal, K. K. N. Sreekala, G. Guruswamy, S. V. Chaluvalappil, and N. N. M. Poovingal. “Dielectric relaxation and electrochemical studies on trihexyl tetradecyl phosphonium chloride [P14, 6, 6, 6][Cl] ionic liquid”. In: *J. Mol. Liq.* 252 (2018), pp. 488–494.
- [300] K. Thasneema, M. S. Thayyil, T. Rosalin, K. Elyas, T. Dipin, P. K. Sahu, N. K. Kumar, V. Saheer, M. Messali, and T. B. Hadda. “Thermal and spectroscopic investigations on three phosphonium based ionic liquids for industrial and biological applications”. In: *J. Mol. Liq.* 307 (2020), p. 112960.
- [301] C. Svanberg and R. Bergman. “Dielectric relaxation of Sorbitol revisited”. In: *Philosophical Magazine* 87.3-5 (2007), pp. 383–388.
- [302] C. Deferm, A. Van den Bossche, J. Luyten, H. Oosterhof, J. Fransaer, and K. Binnemans. “Thermal stability of trihexyl (tetradecyl) phosphonium chloride”. In: *Phys. Chem. Chem. Phys.* 20.4 (2018), pp. 2444–2456.
- [303] X. Monnier, S. Marina, X. Lopez de Pariza, H. Sardón, J. Martin, and D. Cangialosi. “Physical Aging Behavior of a Glassy Polyether”. In: *Polymers* 13.6 (2021), p. 954.
- [304] Y. Wang, N. A. Lane, C.-N. Sun, F. Fan, T. A. Zawodzinski, and A. P. Sokolov. “Ionic conductivity and glass transition of phosphoric acids”. In: *J. Phys. Chem. B* 117.26 (2013), pp. 8003–8009.

- [305] Z. Wojnarowska, M. Rams-Baron, J. Knapik-Kowalczuk, A. Połatyńska, M. Pochylski, J. Gapinski, A. Patkowski, P. Włodarczyk, and M. Paluch. “Experimental evidence of high pressure decoupling between charge transport and structural dynamics in a protic ionic glass-former”. In: *Sci. Rep.* 7.1 (2017), pp. 1–8.
- [306] J. Hachenberg, D. Bedorf, K. Samwer, R. Richert, A. Kahl, M. D. Demetriou, and W. L. Johnson. “Merging of the α and β relaxations and aging via the Johari–Goldstein modes in rapidly quenched metallic glasses”. In: *Appl. Phys. Lett.* 92.13 (2008), p. 131911.
- [307] A. Cassidy, M. R. V. Jørgensen, A. Glavic, V. Lauter, O. Plekan, and D. Field. “A mechanism for ageing in a deeply supercooled molecular glass”. In: *ChemComm* (2021).
- [308] C. Tanford. *The hydrophobic effect: formation of micelles and biological membranes 2d ed.* J. Wiley., 1980.
- [309] S. Arrese-Igor, A. Alegria, and J. Colmenero. “Multimodal character of shear viscosity response in hydrogen bonded liquids”. In: *Phys. Chem. Chem. Phys.* 20.44 (2018), pp. 27758–27765.
- [310] T. Yamaguchi. “Coupling between mesoscopic dynamics and shear stress of room-temperature ionic liquid”. In: *Phys. Chem. Chem. Phys.* 20 (2018), p. 17809.
- [311] J. P. Gabriel, P. Zourchang, F. Pabst, A. Helbling, P. Weigl, T. Böhmer, and T. Blochowicz. “Intermolecular cross-correlations in the dielectric response of glycerol”. In: *Phys. Chem. Chem. Phys.* 22.20 (2020), pp. 11644–11651.
- [312] S. Sharma, A. Gupta, and H. K. Kashyap. “How the structure of pyrrolidinium ionic liquids is susceptible to high pressure”. In: *J. Phys. Chem. B* 120.12 (2016), pp. 3206–3214.
- [313] B. Roling. “Scaling properties of the conductivity spectra of glasses and supercooled melts”. In: *Solid State Ion.* 105.1-4 (1998), pp. 185–193.
- [314] K. Fujii, T. Fujimori, T. Takamuku, R. Kanzaki, Y. Umebayashi, and S.-i. Ishiguro. “Conformational equilibrium of bis (trifluoromethanesulfonyl) imide anion of a room-temperature ionic liquid: Raman spectroscopic study and DFT calculations”. In: *J. Phys. Chem. B* 110.16 (2006), pp. 8179–8183.
- [315] T. Takekiyo, Y. Imai, H. Abe, and Y. Yoshimura. “Conformational analysis of quaternary ammonium-type ionic liquid cation, N, N-diethyl-N-methyl-N-(2-methoxyethyl) ammonium cation”. In: *Adv. Phys. Chem.* 2012 (2012).
- [316] D. L. Sidebottom. “Colloquium: Understanding ion motion in disordered solids from impedance spectroscopy scaling”. In: *Rev. Mod. Phys.* 81.3 (2009), p. 999.
- [317] F. Pabst, J. Kraus, S. Kloth, E. Steinrücken, M. Kruteva, A. Radulescu, M. Vogel, and T. Blochowicz. “Evidence of supercoolable nanoscale water clusters in an amorphous ionic liquid matrix”. In: *J. Chem. Phys.* 155.17 (2021), p. 174501.
- [318] S. Capaccioli and K. Ngai. “Resolving the controversy on the glass transition temperature of water?” In: *J. Chem. Phys.* 135.10 (2011), p. 104504.
- [319] U. Kaatze. “Complex permittivity of water as a function of frequency and temperature”. In: *J. Chem. Eng. Data* 34.4 (1989), pp. 371–374.

- [320] J. S. Hansen, A. Kisliuk, A. P. Sokolov, and C. Gainaru. “Identification of structural relaxation in the dielectric response of water”. In: *Phys. Rev. Lett.* 116.23 (2016), p. 237601.
- [321] P. Lunkenheimer, S. Emmert, R. Gulich, M. Köhler, M. Wolf, M. Schwab, and A. Loidl. “Electromagnetic-radiation absorption by water”. In: *Phys. Rev. E* 96.6 (2017), p. 062607.
- [322] C. Hözl, H. Forbert, and D. Marx. “Dielectric relaxation of water: assessing the impact of localized modes, translational diffusion, and collective dynamics”. In: *Phys. Chem. Chem. Phys.* 23.37 (2021), pp. 20875–20882.
- [323] I. Popov, P. B. Ishai, A. Khamzin, and Y. Feldman. “The mechanism of the dielectric relaxation in water”. In: *Phys. Chem. Chem. Phys.* 18.20 (2016), pp. 13941–13953.
- [324] J. M. Wimby and T. S. Berntsson. “Viscosity and density of aqueous solutions of lithium bromide, lithium chloride, zinc bromide, calcium chloride and lithium nitrate. 1. Single salt solutions”. In: *J. Chem. Eng. Data* 39.1 (1994), pp. 68–72.
- [325] J. C. R. Reis, I. M. Lampreia, Â. F. Santos, M. L. C. Moita, and G. Douhéret. “Refractive index of liquid mixtures: theory and experiment”. In: *ChemPhysChem* 11.17 (2010), pp. 3722–3733.
- [326] S. Xu. “Characterisation of ionic liquid-graphene interface: Sum frequency generation spectroscopy and electrochemical studies”. PhD-Thesis. University of Houston, 2014.
- [327] R. Finsy. “Use of One-Parameter Models for the Assessment of Particle Interactions by photon correlation spectroscopy”. In: *Part. Part. Syst. Charact.* 7.1-4 (1990), pp. 74–79.
- [328] B. Halle and M. Davidovic. “Biomolecular hydration: from water dynamics to hydrodynamics”. In: *PNAS* 100.21 (2003), pp. 12135–12140.
- [329] M. Kaszuba, D. McKnight, M. T. Connah, F. K. McNeil-Watson, and U. Nöbbmann. “Measuring sub nanometre sizes using dynamic light scattering”. In: *J. Nanopart. Res.* 10.5 (2008), pp. 823–829.
- [330] A. Kaintz, G. Baker, A. Benesi, and M. Maroncelli. “Solute diffusion in ionic liquids, NMR measurements and comparisons to conventional solvents”. In: *J. Phys. Chem. B* 117.39 (2013), pp. 11697–11708.
- [331] J. C. Araque, S. K. Yadav, M. Shadeck, M. Maroncelli, and C. J. Margulis. “How is diffusion of neutral and charged tracers related to the structure and dynamics of a room-temperature ionic liquid? Large deviations from Stokes–Einstein behavior explained”. In: *J. Phys. Chem. B* 119.23 (2015), pp. 7015–7029.
- [332] A. V. Bayles, C. S. Valentine, T. Überrück, S. P. Danielsen, S. Han, M. E. Helgeson, and T. M. Squires. “Anomalous solute diffusivity in ionic liquids: label-free visualization and physical origins”. In: *Phys. Rev. X* 9.1 (2019), p. 011048.

- [333] C. A. N. de Castro, E. Langa, A. L. Morais, M. L. M. Lopes, M. J. Lourenço, F. J. Santos, M. S. C. Santos, J. N. C. Lopes, H. I. Veiga, M. Macatrão, et al. “Studies on the density, heat capacity, surface tension and infinite dilution diffusion with the ionic liquids [C₄mim][NTf₂], [C₄mim][dca], [C₂mim][EtOSO₃] and [Aliquat][dca]”. In: *Fluid Phase Equilib.* 294.1-2 (2010), pp. 157–179.
- [334] Y. H. Zhao, M. H. Abraham, and A. M. Zissimos. “Fast calculation of van der Waals volume as a sum of atomic and bond contributions and its application to drug compounds”. In: *J. Org. Chem.* 68.19 (2003), pp. 7368–7373.
- [335] M. H. Rausch, J. Lehmann, A. Leipertz, and A. P. Fröba. “Mutual diffusion in binary mixtures of ionic liquids and molecular liquids by dynamic light scattering (DLS)”. In: *Phys. Chem. Chem. Phys.* 13.20 (2011), pp. 9525–9533.
- [336] S. M. Ali, A. Samanta, and S. K. Ghosh. “Mode coupling theory of self and cross diffusivity in a binary fluid mixture: Application to Lennard-Jones systems”. In: *J. Chem. Phys.* 114.23 (2001), pp. 10419–10429.
- [337] S. M. Green, M. E. Ries, J. Moffat, and T. Budtova. “NMR and rheological study of anion size influence on the properties of two imidazolium-based ionic liquids”. In: *Sci. Rep.* 7.1 (2017), pp. 1–12.
- [338] S. Schramm. “Konzentrationsfluktuationen und molekulare Dynamik in binären Glasbildnern”. PhD thesis. Technische Universität Darmstadt, 2011.
- [339] C. Hansen, F. Stickel, T. Berger, R. Richert, and E. W. Fischer. “Dynamics of glass-forming liquids. III. Comparing the dielectric α -and β -relaxation of 1-propanol and o-terphenyl”. In: *J. Chem. Phys.* 107.4 (1997), pp. 1086–1093.
- [340] P. Sillrén, A. Matic, M. Karlsson, M. Koza, M. Maccarini, P. Fouquet, M. Götz, T. Bauer, R. Gulich, P. Lunkenheimer, et al. “Liquid 1-propanol studied by neutron scattering, near-infrared, and dielectric spectroscopy”. In: *J. Chem. Phys.* 140.12 (2014), p. 124501.
- [341] S. Arrese-Igor, A. Alegria, A. Arbe, and J. Colmenero. “Insights into the non-exponential behavior of the dielectric Debye-like relaxation in monoalcohols”. In: *J. Mol. Liq.* 312 (2020), p. 113441.
- [342] M. A. Ramos, B. Kabtoul, and M. Hassaine. “Calorimetric and thermodynamic study of glass-forming monohydroxy alcohols”. In: *Philos. Mag.* 91.13-15 (2011), pp. 1847–1856.
- [343] A. Kraszewski, S. Kulinski, and M. Matuszewski. “Dielectric properties and a model of biphasic water suspension at 9.4 GHz”. In: *J. Appl. Phys. Lett.* 47.4 (1976), pp. 1275–1277.
- [344] C. Trivedi, V. Rana, et al. “Static permittivity, refractive index, density and related properties of binary mixtures of pyridine and 1-propanol at different temperatures”. In: *Indian J. Pure Appl. Phys. Lett.* 52.3 (2015), pp. 183–191.
- [345] A. A. Amooey. “Improved mixing rules for description of the permittivity of mixtures”. In: *J. Mol. Liq.* 180 (2013), pp. 31–33.

- [346] E. J. Gonzalez, A. Dominguez, and E. A. Macedo. “Physical and excess properties of eight binary mixtures containing water and ionic liquids”. In: *J. Chem. Eng. Data* 57.8 (2012), pp. 2165–2176.
- [347] M. Larriba, P. Navarro, J. García, and F. Rodriguez. “Liquid–liquid extraction of toluene from heptane using [emim][DCA],[bmim][DCA], and [emim][TCM] ionic liquids”. In: *Ind. Eng. Chem. Res.* 52.7 (2013), pp. 2714–2720.
- [348] R. Yusoff, M. K. Aroua, A. Shamiri, A. Ahmady, N. Jusoh, N. Asmuni, L. Bong, and S. Thee. “Density and viscosity of aqueous mixtures of N-methyldiethanolamines (MDEA) and ionic liquids”. In: *J. Chem. Eng. Data* 58.2 (2013), pp. 240–247.
- [349] N. Zec, M. Bešter-Rogač, M. Vraneš, and S. Gadžurić. “Volumetric and viscosimetric properties of [bmim][DCA] + γ -butyrolactone binary mixtures”. In: *J. Chem. Thermodyn.* 97 (2016), pp. 307–314.
- [350] A. P. Carneiro, C. Held, O. Rodriguez, G. Sadowski, and E. A. Macedo. “Solubility of sugars and sugar alcohols in ionic liquids: measurement and PC-SAFT modeling”. In: *J. Phys. Chem. B* 117.34 (2013), pp. 9980–9995.
- [351] R. D. Nelson Jr, D. R. Lide Jr, and A. A. Maryott. *Selected values of electric dipole moments for molecules in the gas phase*. Tech. rep. National Standard Reference Data System, 1967.
- [352] Y. Chua, A. Young-Gonzales, R. Richert, M. Ediger, and C. Schick. “Dynamics of super-cooled liquid and plastic crystalline ethanol: Dielectric relaxation and AC nanocalorimetry distinguish structural α -and Debye relaxation processes”. In: *J. Chem. Phys.* 147.1 (2017), p. 014502.
- [353] T. Richter, T. Böhmer, J. P. Gabriel, P. Weigl, F. Pabst, and T. Blochowicz. “Revealing the Non-Simplicity of the Dielectric α -Process in Monohydroxy Alcohols by Studying Octanol Isomers”. In: *to be submitted* (2022).
- [354] W. Wang and S. A. Sande. “A dynamic light scattering study of hydrogels with the addition of surfactant: a discussion of mesh size and correlation length”. In: *Polym. J.* 47.4 (2015), pp. 302–310.
- [355] T. Matsunaga and M. Shibayama. “Gel point determination of gelatin hydrogels by dynamic light scattering and rheological measurements”. In: *Phys. Rev. E* 76.3 (2007), p. 030401.
- [356] S. L. Kosaraju, A. Puvanenthiran, and P. Lillford. “Naturally crosslinked gelatin gels with modified material properties”. In: *Food Res. Int.* 43.10 (2010), pp. 2385–2389.
- [357] S. B. Ross-Murphy. “Reversible and irreversible biopolymer gels-structure and mechanical properties”. In: *Ber. Bunsenges.* 102.11 (1998), pp. 1534–1539.
- [358] L. Pescosolido, L. Feruglio, R. Farra, S. Fiorentino, I. Colombo, T. Coville, P. Matricardi, W. E. Hennink, T. Vermonden, and M. Grassi. “Mesh size distribution determination of interpenetrating polymer network hydrogels”. In: *Soft Matter* 8.29 (2012), pp. 7708–7715.

- [359] G. Floudas, G. Fytas, and W. Brown. "Solvent mobility in poly (methyl methacrylate)/toluene solutions by depolarized and polarized light scattering". In: *J. Chem. Phys.* 96.3 (1992), pp. 2164–2174.
- [360] J. Li, T. Ngai, and C. Wu. "The slow relaxation mode: from solutions to gel networks". In: *Polym. J.* 42.8 (2010), pp. 609–625.
- [361] S. Schramm, T. Blochowicz, E. Gouirand, R. Wipf, B. Stühn, and Y. Chushkin. "Concentration fluctuations in a binary glass former investigated by x-ray photon correlation spectroscopy". In: *J. Chem. Phys.* 132.22 (2010), p. 224505.
- [362] E. Gómez, N. Calvar, E. A. Macedo, and Á. Domínguez. "Effect of the temperature on the physical properties of pure 1-propyl 3-methylimidazolium bis (trifluoromethylsulfonyl) imide and characterization of its binary mixtures with alcohols". In: *J. Chem. Thermodyn.* 45.1 (2012), pp. 9–15.
- [363] U. Domańska and M. Włazło. "Thermodynamics and limiting activity coefficients measurements for organic solutes and water in the ionic liquid 1-dodecyl-3-methylimidazolium bis (trifluoromethylsulfonyl) imide". In: *J. Chem. Thermodyn.* 103 (2016), pp. 76–85.
- [364] B. Mokhtarani, M. M. Mojtabaei, H. R. Mortaheb, M. Mafi, F. Yazdani, and F. Sadeghian. "Densities, refractive indices, and viscosities of the ionic liquids 1-methyl-3-octylimidazolium tetrafluoroborate and 1-methyl-3-butylimidazolium perchlorate and their binary mixtures with ethanol at several temperatures". In: *J. Chem. Eng. Data* 53.3 (2008), pp. 677–682.
- [365] Q. Tian and H. Liu. "Densities and viscosities of binary mixtures of tributyl phosphate with hexane and dodecane from (298.15 to 328.15) K". In: *J. Chem. Eng. Data* 52.3 (2007), pp. 892–897.
- [366] W. Seyer and C. H. Davenport. "The Densities and Surface Tensions of cis-and trans-Decahydronaphthalene between -30 and 180°". In: *J. Am. Chem. Soc.* 63.9 (1941), pp. 2425–2427.
- [367] S.-J. Peng, H.-Y. Hou, C.-S. Zhou, and T. Yang. "Densities and excess volumes of binary mixtures of N, N-dimethylformamide with aromatic hydrocarbon at different temperature". In: *J. Chem. Thermodyn.* 39.3 (2007), pp. 474–482.
- [368] J. Barthel, R. Neueder, and H. Roch. "Density, relative permittivity, and viscosity of propylene carbonate + dimethoxyethane mixtures from 25° C to 125° C". In: *J. Chem. Eng. Data* 45.6 (2000), pp. 1007–1011.
- [369] G. H. Graaf, H. J. Smit, E. J. Stamhuis, and A. A. Beenackers. "Gas-liquid solubilities of the methanol synthesis components in various solvents". In: *J. Chem. Eng. Data* 37.2 (1992), pp. 146–158.
- [370] I. Tsujino and K. Kikuchi. "On lowering Boiling Fractions Obtained from Industrial Molecular Distillation of Basking Shark Liver Oil". In: *Journal of the Agricultural Chemical Society of Japan* 27.7 (1953), pp. 437–439.

- [371] J. N. Nayak, M. I. Aralaguppi, and T. M. Aminabhavi. “Density, viscosity, refractive index, and speed of sound in the binary mixtures of 1, 4-dioxane + ethyl acetoacetate, + diethyl oxalate, + diethyl phthalate, or + dioctyl phthalate at 298.15, 303.15, and 308.15 K”. In: *J. Chem. Eng. Data* 48.6 (2003), pp. 1489–1494.
- [372] T. M. Aminabhavi, M. I. Aralaguppi, G. Bindu, and R. S. Khinnavar. “Densities, shear viscosities, refractive indices, and speeds of sound of bis (2-methoxyethyl) ether with hexane, heptane, octane, and 2, 2, 4-trimethylpentane in the temperature interval 298.15–318.15 K”. In: *J. Chem. Eng. Data* 39.3 (1994), pp. 522–528.
- [373] E. Aicart, G. Tardajos, and M. D. Peña. “Isothermal compressibility of cyclohexane + n-tridecane and + n-pentadecane at 298.15, 308.15, 318.15, and 333.15 K”. In: *J. Chem. Thermodyn.* 13.8 (1981), pp. 783–788.
- [374] D. J. Luning Prak, P. J. Luning Prak, J. S. Cowart, and P. C. Trulove. “Densities and viscosities at 293.15–373.15 K, speeds of sound and bulk moduli at 293.15–333.15 K, surface tensions, and flash points of binary mixtures of n-hexadecane and alkylbenzenes at 0.1 MPa”. In: *J. Chem. Eng. Data* 62.5 (2017), pp. 1673–1688.
- [375] A. Ribeiro and G. Bernardo-Gil. “Densities and refractive indices of components of pine resin”. In: *J. Chem. Eng. Data* 35.2 (1990), pp. 204–206.
- [376] T. Hecksher. “Relaxation in Supercooled Liquids - Linear and Non-Linear Mechanical and Dielectric Studies of Molecular Liquids”. PhD thesis. Roskilde University, 2010.
- [377] J. V. Champion, A. Dandridge, and G. H. Meeten. “Optical investigation of motion of short chain liquid molecules”. In: *Faraday Discuss.* 66 (1978), pp. 266–276.
- [378] G. Tasi, F. Mizukami, J. Csontos, W. Győrffy, and I. Pálinkó. “Quantum algebraic-combinatoric study of the conformational properties of n-alkanes. II”. In: *J. Math. Chem.* 27.3 (2000), pp. 191–199.
- [379] V. Štejfa, M. Fulem, and K. Ružička. “First-principles calculation of ideal-gas thermodynamic properties of long-chain molecules by R1SM approach—Application to n-alkanes”. In: *J. Chem. Phys.* 150.22 (2019), p. 224101.
- [380] A. Massoulier. “Mesures de la dépolarisation de la lumière diffuseée (effet Rayleigh) par le xénon et par quelques alcanes gazeux”. In: *C. R. Acad. Sc. Paris* 267.2 (1968), pp. 132–134.
- [381] J. Powers, D. A. Keedy, and R. S. Stein. “Depolarization of Scattered Light by n-Paraffin Vapors and the Additivity of Bond Polarizability Tensors”. In: *J. Chem. Phys.* 35.1 (1961), pp. 376–377.
- [382] F. Dintzis and R. Stein. “Observations on Depolarization Ratios of Scattered Light by Some Low Molecular Weight Gases and n-Paraffin Vapors”. In: *J. Chem. Phys.* 40.5 (1964), pp. 1459–1460.
- [383] L. L. Thomas, T. J. Christakis, and W. L. Jorgensen. “Conformation of alkanes in the gas phase and pure liquids”. In: *J. Phys. Chem. B* 110.42 (2006), pp. 21198–21204.
- [384] F. Goodsaid-Zalduondo and D. Engelman. “Conformation of liquid N-alkanes”. In: *Biophys.* 35.3 (1981), pp. 587–594.

- [385] M. Dettenmaier. "Conformation of n-alkane molecules in the melt and in cyclohexane solution studied by small-angle neutron scattering". In: *J. Chem. Phys.* 68.5 (1978), pp. 2319–2322.
- [386] A. Habenschuss and A. Narten. "X-ray diffraction study of some liquid alkanes". In: *J. Chem. Phys.* 92.9 (1990), pp. 5692–5699.
- [387] P. Padilla and C. Vega. "Packing effects on the conformational equilibrium of alkanes". In: *Mol. Phys.* 84.2 (1995), pp. 435–450.
- [388] L. Van de Ven, J. De Haan, and A. Bucinska. "Conformational equilibria of normal alkanes, 1-alkenes, and some (E)-and (Z)-2-alkenes in neat liquids and in some selected solvents: a carbon-13 nuclear magnetic resonance study". In: *J. Phys. Chem.* 86.13 (1982), pp. 2516–2522.
- [389] J. Rheims, J. Köser, and T. Wriedt. "Refractive-index measurements in the near-IR using an Abbe refractometer". In: *Meas. Sci. Technol.* 8.6 (1997), p. 601.
- [390] G. Moumouzias and G. Ritzoulis. "Relative permittivities and refractive indices of propylene carbonate+ toluene mixtures from 283.15 K to 313.15 K". In: *J. Chem. Eng. Data* 42.4 (1997), pp. 710–713.
- [391] S. Kedenburg, M. Vieweg, T. Gissibl, and H. Giessen. "Linear refractive index and absorption measurements of nonlinear optical liquids in the visible and near-infrared spectral region". In: *Opt. Mater. Express* 2.11 (2012), pp. 1588–1611.

Supervised student theses

Master theses

- **Rolf Zeißler**,
Einfluss von intramolekularen Freiheitsgraden und Kettendynamik auf die spektrale Form des α -Prozesses
2022
- **Hannah Kirchhof**,
Temperatur- und konzentrationsabhängige Untersuchungen von Wasserstoffbrückenbindungen in 1-Propanol
2021
- **Jennifer Kraus**,
Struktur und Dynamik von Ionische Flüssigkeit-Wasser-Mischungen und Ionogelen
2020
- **Andreas Helbling**,
Dielektrische Spektroskopie an Tributylphosphat
2019
- **Stephan Bock**,
Aufbau eines Raman-Spektroskopie-Experiments zur Untersuchung molekularer Dynamik
2019

Bachelor theses

- **Jennifer Kraus**,
Dynamische Lichtstreuung und dielektrische Spektroskopie an Ionogelen
2018

Publications and conference contributions

Publications in peer reviewed international journals

- P.-M. Déjardin, **F. Pabst**, Y. Cornaton, A. Helbling, T. Blochowicz, *Temperature dependence of the Kirkwood correlation factor and linear dielectric constant of simple isotropic polar fluids*. Physical Review E, 105, 2 (2022)
- **F. Pabst**, J. Kraus, S. Kloth, E. Steinrücken, M. Kruteva, A. Radulescu, M. Vogel, T. Blochowicz, *Evidence of supercoolable nanoscale water clusters in an amorphous ionic liquid matrix*. The Journal of Chemical Physics, 155, 17 (2021)
- T. Böhmer, R. Horstmann, J.P. Gabriel, **F. Pabst**, M. Vogel, T. Blochowicz, *Origin of Apparent Slow Solvent Dynamics in Concentrated Polymer Solutions*. Macromolecules 54, 22 (2021)
- **F. Pabst**, J. P. Gabriel, T. Böhmer, P. Weigl, A. Helbling, T. Richter, P. Zourchang, T. Walther, T. Blochowicz, *Generic Structural Relaxation in Supercooled Liquids*. The Journal of Physical Chemistry Letters, 12, 14 (2021)
- J.H. Melillo, J.P. Gabriel, **F. Pabst**, T. Blochowicz, S. Cerveny, *Dynamics of aqueous peptide solutions in folded and disordered states examined by dynamic light scattering and dielectric spectroscopy*. Physical Chemistry Chemical Physics 23, 28 (2021)
- **F. Pabst**, Z. Wojnarowska, M. Paluch, T. Blochowicz, *On the temperature and pressure dependence of dielectric relaxation processes in ionic liquids*. Physical Chemistry Chemical Physics 23, 26 (2021)
- **F. Pabst**, A. Helbling, J.P. Gabriel, P. Weigl, T. Blochowicz *Dipole-dipole correlations and the Debye process in the dielectric response of nonassociating glass forming liquids*. Physical Review E 102, 1 (2020)
- J. P. Gabriel, P. Zourchang, **F. Pabst**, A. Helbling, P. Weigl, T. Böhmer, T. Blochowicz, *Intermolecular cross-correlations in the dielectric response of glycerol*. Physical Chemistry Chemical Physics 22, 20 (2020)
- T. Böhmer, J.P. Gabriel, T. Richter, **F. Pabst**, T. Blochowicz, *Influence of molecular architecture on the dynamics of H-bonded supramolecular structures in phenyl-propanols*. The Journal of Physical Chemistry B 123, 51 (2019)

- F. Pabst, J. Gabriel, T. Blochowicz, *Mesoscale Aggregates and Dynamic Asymmetry in Ionic Liquids: Evidence from Depolarized Dynamic Light Scattering*. The Journal of Physical Chemistry Letters 10, 9 (2019)
- P. Weigl, D. Koestel, F. Pabst, J.P. Gabriel, T. Walther, T. Blochowicz, *Local dielectric response in 1-propanol: α -relaxation versus relaxation of mesoscale structures*. Physical Chemistry Chemical Physics 21, 44 (2019)
- J. Gabriel, F. Pabst, A. Helbling, T. Böhmer, T. Blochowicz, *Nature of the Debye-process in monohydroxy alcohols: 5-methyl-2-hexanol investigated by depolarized light scattering and dielectric spectroscopy*. Physical Review Letters 121, 3 (2018)
- J. Gabriel, F. Pabst, T. Blochowicz, *Debye process and β -relaxation in 1-propanol probed by dielectric spectroscopy and depolarized dynamic light scattering*. The Journal of Physical Chemistry B 121, 37 (2017)
- F. Pabst, J. Gabriel, P. Weigl, T. Blochowicz, *Molecular dynamics of supercooled ionic liquids studied by light scattering and dielectric spectroscopy*. Chemical Physics 494 (2017)

Other publications

- J. Gabriel, F. Pabst, A. Helbling, T. Böhmer, T. Blochowicz, *Depolarized dynamic light scattering and dielectric spectroscopy: Two perspectives on molecular reorientation in supercooled liquids*. In: The Scaling of Relaxation Processes, Springer (2018)

Conference contributions

Talks

- F. Pabst, J.P. Gabriel, T. Böhmer, P. Weigl, A. Helbling, T. Richter, P. Zourchang, H. Kirchhof, R. Zeißler, T. Walther, T. Blochowicz, *The Generic α -Relaxation in Supercooled Liquids*. International Dielectric Society Online Workshop (2021)
- F. Pabst, J. Kraus, H. Kirchhof, T. Blochowicz, *Mixtures of an ionic liquid with water, gelatin or propanol*. AK-Meeting, online (2021)
- F. Pabst, J.P. Gabriel, T. Blochowicz, *Nanoscale Aggregates and Dynamic Asymmetry in Ionic Liquids*. AK-Meeting, Kloster Höchst, Germany (2019)
- F. Pabst, J.P. Gabriel, T. Blochowicz, *Dynamic Evidence of Nanostructures in Ionic Liquids?* 10th Conference on Broadband Dielectric Spectroscopy and its Applications, Brussels, Belgium (2018)
- F. Pabst, J.P. Gabriel, T. Blochowicz, *Molecular Dynamics in Ionic Liquids – What is special?*, AK-Meeting, Schloss Schney, Germany (2018)
- F. Pabst, J.P. Gabriel, T. Blochowicz, *Molecular dynamics in ionic liquids – Light scattering and dielectric spectroscopy*, AK-Meeting, Germany (2016)

Posters

- F. Pabst, J.P. Gabriel, P. Weigl, T. Blochowicz , *Molecular dynamics of supercooled ionic liquids studied by light scattering and dielectric spectroscopy*. 8th International Discussion Meeting on Relaxations in Complex Systems, Wisla, Poland (2018)
- F. Pabst, T. Blochowicz, *Molecular dynamics of ionic liquids studied by light scattering and dielectric spectroscopy*. Winter school on ionic liquids, Porto, Portugal (2017). Awarded best poster.

Danksagungen

Als erstes möchte ich mich ganz herzlich bei Thomas Blochowicz für die vielen spannenden Jahre bedanken, während derer er stets ein offenes Ohr für alle Fragen hatte, mir aber insbesondere auch sehr viel Freiheit für eigene Ideen gelassen hat.

Mein Dank geht auch an Michael Vogel, nicht nur für die Bereitschaft als Zweitgutachter zu fungieren, sondern auch für die gute Zusammenarbeit über die Grenzen der Arbeitsgruppen hinaus.

Meinen Kollegen Jenni, Till und Peter möchte ich für ihre Unterstützung in allen Belangen danken, darunter das Korrekturlesen dieser Arbeit. Aber auch darüber hinaus für die tolle Atmosphäre in der Arbeitsgruppe, wobei ich meinen ehemaligen Kollegen Jan ausdrücklich mit einschließen möchte.

Ein großer Dank geht auch an meine Masterstudierenden Rolf, Hannah, Andreas und Stephan für die tolle Arbeit, die sie geleistet haben.

Danke auch an alle Kollegen aus der AG Vogel für die gute Zusammenarbeit, insbesondere an Elisa und Manuel für die NMR-Messungen und an Sebastian und Robin für die Simulationen. Dabei darf natürlich auch Markus nicht fehlen, der immer eine große Hilfe bei allen Computerangelegenheiten war.

Auch möchte ich Barbara für die Unterstützung bei allen organisatorischen Dingen, Harald für seine Ideen und Umsetzungen von allerlei Konstruktionen, allen Mitgliedern der E-Werkstatt, insbesondere Klaus, für den Entwurf und den Bau von allem was mit Strom zu tun hatte, und den Mitgliedern der mechanischen Werkstatt für die zügige und präzise Umsetzung aller Metallarbeiten danken.

Last but not least, thanks to Pierre-Michel in France, Johan and Matthew in the UK, Zaneta and Marian in Poland and Margarita in Jülich for the great cooperation.